STATUS OF THESIS

Title of thesis	SYNTHESIZING AND EVALUATION OF NEW COPPER-TUNGSTEN BASED EDM ELECTRODE FOR MACHINING HARDENED MATERIALS

I AL TIDJANI ZAKARIA MAHAMAT

hereby allow my thesis to be placed at the Information Resource Center (IRC) of Universiti Teknologi PETRONAS (UTP) with the following conditions:

1. The thesis becomes the property of UTP
2. The IRC of UTP may make copies of the thesis for academic purposes only
3. This thesis is classified as

☐ Confidential

☐ Non-confidential

If this thesis is confidential, please state the reason:

______

______

______

The content of the thesis will remain confidential for _______ years.

Remarks on disclosure:

______

Endorsed by

Signature of Author	Signature of Supervisor
Permanent address: Avenue Mobutu Po box 1117 N'Djamena, CHAD	Assoc. Prof. Dr Ahmad Majdi
Date:____________	Date:____________

UNIVERSITI TEKNOLOGI PETRONAS

SYNTHESIZING AND EVALUATION OF NEW COPPER-TUNGSTEN BASED EDM ELECTRODE FOR MACHINING HARDENED MATERIALS

by

AL TIDJANI ZAKARIA MAHAMAT

The undersigned certify that they have read, and recommend to The Postgraduate Studies Programme for acceptance this thesis for the fulfillment of the requirements for the degree of Master of Science in Mechanical Engineering.

Signature: ____
Main Supervisor: Assoc. Prof. Dr. Ahmad Majdi Abdul Rani

Signature: ____
Co-Supervisor: Assoc. Prof. Dr. Patthi Husain

Signature: Ir. Dr. Masri Bin Baharom
Head of Department: ____

Date: ____

SYNTHESIZING AND EVALUATION OF NEW COPPER-TUNGSTEN BASED EDM ELECTRODE FOR MACHINING HARDENED MATERIALS

By

AL TIDJANI ZAKARIA MAHAMAT

A Thesis

Submitted to the Postgraduate Studies Programme

As a Requirement for the Degree of

DOCTOR OF PHILOSOPHY

MECHANICAL ENGINEERING DEPARTMENT

UNIVERSITI TEKNOLOGI PETRONAS

BANDAR SERI ISKANDAR,

PERAK

September, 2012

DECLARATION OF THESIS

Title of thesis

SYNTHESIZING AND EVALUATION OF NEW COPPER-TUNGSTEN BASED EDM ELECTRODE FOR MACHINING HARDENED MATERIALS

I AL TIDJANI ZAKARIA MAHAMAT

Hereby declare at the thesis is based on my original work except for quotations and citations which have been duly acknowledged. I also declare that it has not been previously or concurrently submitted for any other degree at UTP or other institutions.

Witnessed by

Signature of Author	Signature of Supervisor
Permanent address: Avenue Mobutu N'Djamena / CHAD Po box 1117	Assoc. Prof. Dr. Ahmad Majdi Abdul Rani
Date:	Date:

ACKNOWLEDGEMENT

I would like to thank my supervisor Assoc. Prof. Dr. Ahmad Majdi and my Co-Supervisor Assoc. Prof. Dr. Patthi Husain. Without their guidance and support this thesis would never successfully completed.

Further, I would like to thank the staff members at the Mechanical Engineering Department for their great cooperation and help.

I would like to thank the staff and the Dean of Centre for Graduate Studies (CGS) for their support and financial assistance.

Last but not the least, I wish to express my greatest gratitude to my wife and my two daughters for their love, patient and moral support, where they gave me the strongest motivation to accomplish this work.

AL TIDJANI ZAKARIA MAHAMAT

Universiti Terknologi PETRONAS
Mechanical Engineering

2012

ABSTRACT

By using Electrical discharge machining (EDM) it is possible to machine any materials that are difficult to machine by using conventional machining technique as long as it is electrically conductive. The performance of EDM is highly depending on the type of electrode being used, the power supply system, and the dielectric system. Copper-Tungsten electrode is the higher in wear resistance but it is difficult to manufacture due to variation of melting point and zero miscibility of copper (Cu) with Tungsten (W). Thus, new modified Copper-Tungsten electrodes were synthesized taking into consideration the variety of melting point and zero miscibility. Ball milling was used to synthesize the new electrode material and Taguchi method is used to design and analyse the experiment. Material removal rate (MRR) and electrode wear (EW) are the main parameters used for testing the performance between the existing Copper-Tungsten (Cu-W) electrode and the new developed electrode. Machining variables selection show that the gap voltage, peak current and pulse on time are the most important ones that contribute on material removal rate, electrode wear and surface roughness (Ra). Results of milling process indicate a clear change in the thickness of crystalline and d-spacing of the milled powder after five hours milling time. The performance of Cu-WC-Si electrode shows an improvement in MRR by an average of 22.5% when milled for 5 to10 hours. The EW of 10 to 20 hours milled Cu-WC-Si improved by an average of 62 % from that achieved by using Cu-W electrode. The performance of Cu-WC-Ti and Cu-WC-Ti-Si electrode show clear improvement in the electrode wear but at the expense of MRR. It is reduced by an average of 86% for Cu-WC-Ti and by 70.1% compared with that achieved by using Cu-W electrode. Si additive improve TWR of Cu-WC-Si electrode where it shows the lowest TWR (10%) compared with that achieved by Cu-WC-Ti (466%) and Cu-WC-Ti-Si (37%). The contribution of milling variables on the performance of the new developed electrodes shows that milling time is the most important variable.

ABSTRAK

Penggunaan Electrical Discharge Machining (EDM) membolehkan pemesinan apa-apa bahan yang sukar untuk dimesin melalui teknik pemesinan konvensional selagi ia elektrik konduktif. Prestasi EDM adalah sangat bergantung kepada jenis elektrod yang digunakan, sistem bekalan kuasa, dan sistem dielektrik. Copper-elektrod tungsten adalah lebih tinggi dalam kebolehupayaan rintangan tetapi ia adalah sukar untuk dihasilkan kerana perubahan takat lebur dan kebolehcampuran sifar Cu dengan W. Oleh itu, pengubahsuaian tembaga-elektrod tungsten telah dihasilkan dengan mengambil kira pelbagai titik lebur dan sifar kebolehcampuran. Bebola penggiling telah digunakan untuk menghasilkan bahan elektrod baru dan kaedah Taguchi digunakan untuk mereka bentuk dan menganalisis eksperimen. Kadar pembuangan bahan (MRR) dan memakai elektrod (EW) adalah parameter utama yang digunakan untuk menguji prestasi antara sedia ada Cu-W dan elektrod baru yang dibangunkan. Pembolehubah Pemesinan pemilihan menunjukkan bahawa voltan jurang, semasa puncak dan nadi pada masanya adalah pembolehubah yang paling penting menyumbang pada kadar pembuangan bahan, memakai elektrod dan kekasaran permukaan (Ra). Keputusan Pengilangan menunjukkan perubahan yang jelas dalam ketebalan kristal dan d jarak serbuk gilingan selepas lima jam masa pengilangan. Prestasi elektrod Cu-WC-Si menunjukkan peningkatan dalam MRR oleh purata sebanyak 22.5% apabila gilingan untuk to10h 5h. 15h dan 20hb EW gilingan Cu-WC-Si diperbaiki dengan purata sebanyak 62% daripada yang dicapai dengan menggunakan elektrod-W Cu. Prestasi Cu-WC-Ti dan elektrod Cu-WC-Ti-Si menunjukkan peningkatan yang jelas dalam pemakaian elektrod tetapi pada perbelanjaan MRR; ia dikurangkan oleh purata 86% bagi Cu-WC-Ti dan 70.1% berbanding dengan yang dicapai dengan menggunakan elektrod-W Cu. Tambahan Si meningkatkan TWR elektrod Cu-WC-Si mana ia menunjukkan TWR terendah (10%) berbanding dengan yang dicapai oleh Cu-WC-Ti (466%) dan Cu-WC-Ti-Si (37%). Sumbangan pengilangan pembolehubah prestasi elektrod maju baru menunjukkan bahawa masa pengilangan adalah pembolehubah yang paling penting.

TABLE OF CONTENT

LIST OF FIGURES

LIST OF TABLES

NOMENCLATURES AND ABBREVIATIONS

ANOVA	Analysis of Variance
AUX	Auxiliary power
$B_{1/2}$	full width at half maximum
BPR	Ball to Powder Ratio
CI	Interval of Confidence
CNC	computer numerical control
Cu-W	Copper-Tungsten
Cu-WC-Si	Copper-Tungsten carbide-Silicon
Cu-WC-Ti	Copper-Tungsten carbide-Titanium
Cu-WC-Ti-Si	Copper-Tungsten carbide- Titanium-Silicon
DEP	Dielectric pressure
DMLS	Direct Metal LASER Sintering
DOE	Design of Experiment
EDM	Electrical Discharge Machining
EDMG	Electrical Discharge Machining With Grinding
EDX	Energy-dispersive X-Ray
EW	Electrode Wear Rate
FESEM	field emission scanning electron microscope
GAP	Gap voltage
HE	hole enlargement
HEL	Heat Effected Layer
HIP	Hot Isostatic Pressing
HK	Hardness Rockwell K
H_{max}	maximum hardness
HP	Hot Pressing
HRB	Hardness Rockwell B
H_V	Vickers Hardness
IACS	International Annealed Copper Standard

IP	Peak current
J_D	Jump down time
J_S	Electric discharge stability
J_U	Jump up distance
MPa	Mega Pascal
MRR	Material removal rate
OA	Orthogonal Array
OC	Over Cut
P/M	Powder Metallurgy
PCAs	Process control agents
PCAs	Process control agents
POL	Polarity
R/P	Rapid Prototyping
Ra	Surface roughness parameter
SLS	Selective LASER Sintering
SS	Sum of Square
SSt	Total Sum of Square
SV	Servo voltage
T_{off}	Pulse of time
T_{on}	Pulse On-time
TWR	Tool Wear Ration
W	Tungsten
WC-Co	Cemented Tungsten Carbide
WLT	White Layer Thickness
XRD	X-Ray Diffraction
Θ_B	Bragg angle

CHAPTER 1

INTRODUCTION

1.1.Background of the Study

Machining process is among the most important in the manufacturing process because all the steps after the material selection need material removal process. The machining process referred to the material removal processes to produce the desired shape using cutting tool to remove material from a workpiece. Preparation of the work-piece for machining should pass through several stages such as cutting and shaping before finally machined to the desired shape. Machining process can be divided into two main categories, the conventional and Un-conventional machining. In conventional machining, parts of the material are removed mechanically from the workpiece using physical machining tool to change it to final shape. The main demand in conventional machining is that the tool must be harder than the workpiece and must resist all types of mechanical stress.

The machining rate and the quality of the machined surface strongly depend on the relative motion between the tool and the workpiece. Conventional machining may not be feasible when the workpiece material is harder than the tool electrode material or when low-rigidity structures with tight tolerances and fine surface quality are required. Therefore, there is an urgent need to use Un-conventional machining technique to overcome these limitations. Electrical discharge machining (EDM) is one of the most applicable Un-conventional machining techniques used for die and tool manufacturing because no restriction is imposed by the mechanical properties of workpiece material such as brittleness, toughness as long as it is electrically conductive. Additionally it has an advantage when a complex shape with sharp edges, holes, and the packet is required. Proper selection of EDM variables and the optimal setting of these variables is the first step to improve the material removal rate MRR; the electrodes wear EW and the surface roughness Ra.

1.2.Advantages and Limitation of EDM

EDM like any other technique have some advantages and limitations. The main advantages of this technique are the capability of machining a complex shape with code, channel, split or sharp corner on a very hard material. It is also possible to machine a very small work pieces because no direct contact between tool and work piece. With proper selection of the tool electrode material and optimal machining variables setting, the geometric limitations can be manipulated and the quality characteristic can be controlled.

The main disadvantage of this technique is the limitation to the conductive material, low material removal rate MRR, and the negative effect of electrode wears EW on machining process and surface quality. The electrode manufacturing is a time consuming process leading to the high cost of EDM electrode. Heat concentration can affect the microstructure and may cause cracks, which is undesirable. Machining of large areas is not normally possible and in some cases, the risk of the direct contact with debris and fine powder is high.

1.3.EDM Tool Electrode

EDM electrode is the physical cutting tool. It is important to keep in mind that the shape of the produced cavity (die) is the negative of the tool electrode shape. Thus, the electrode wear reduction must be the first consideration during design electrode manufacturing. As EDM is a non-contact machining process, the mechanical property is not the first priority in electrode manufacturing. Since the system converts an electric energy into heat energy by the series of sparking, the electrode material must have a high electrical and thermal conductivity. The high electrical conductivity makes the discharge more easily and reduces the bulk heating. For the same heat load but at different thermal conductivity, the localized temperature will rise at different rates due to differences in heat conduction leading to a localized melting of the electrode material and therefore the tool wear can be reduced with higher thermal conductivity for the same melting point material. The material removed by fusion and evaporation mechanism and due to this, it is important to use a high melting point material. During sparking, both the electrode and the workpiece eroded and to reduce the volume wear and as a consequence, less tool wear and less dimensional inaccuracy. Thus, the electrode material must have high density. Ease of manufacturing and low price are other important points which should be considered in EDM electrode industry.

It is impossible to find a single material in nature that can offer these entire requirements. Currently, the commonly used materials as electrodes are Copper, Copper alloy, Graphite, Tungsten and Copper-Tungsten. Each of these electrodes has advantages and disadvantages. Copper is good in electrical and thermal conductivity, but very poor in wear resistance. Tungsten on the other side the best in wear resistance but relatively low conductivity and very expensive. Graphite electrodes are good in wear resistance and not expensive. It has low electrical and thermal conductivity with low oxidation temperature as its main disadvantages. Furthermore, Graphite particles have been observed in the working gap. These particles can affect the dielectric conditions and even can produce undesirable electrical short cut.

Copper-Tungsten electrode combines the high electrical conductivity of Copper with the high wear resistance of Tungsten (high melting point). The main disadvantages of this electrode are;

- The high cost of the electrode due to the high-price of Tungsten
- Powder metallurgy is the only possible manufacturing technique because Copper and Tungsten are immiscible even in liquid phase and due to the variation of melting point.
- Infiltration is the only way to achieve full density. This point limits the selection of Tungsten particle size to a few µm.
- The early stage Copper erosion in combination with the relatively large particle size might leads to a rough electrode surface.
- The MRR rate of this electrode is only half of Copper electrode due to the low electrical conductivity of Tungsten.

1.4.Problem Statement

The selection of the EDM electrode material is most important in the process plan for any diesinker EDM process. Despite the fact that EDM is a zero force process, the sparks can exert a significant pressure on the electrode material at high temperature. The response of the electrode material to the sparking attacks on its surface depends on the electrode material. Impingement of electrode surface by high-energy ion will create an electrode wear, which can significantly affect the discharge efficiency and the machined surface quality. The commonly used EDM electrode materials are; Copper Kern and Khan [1, 2], Copper- Tungsten composite Lee [3] , and Graphite Aas [4] and Tang [5].

Copper-Tungsten (Cu-W) is one of the most used electrodes in machining of cemented Tungsten carbide. Copper-Tungsten electrode shows the highest thermal wear resistance. The main problems associated with this electrode are the difficulties of manufacturing due to the variation in melting temperature, zero miscibility of Cu and W and also the high cost due to the expensive nature of Tungsten. This electrode shows lower material removal rate in comparison with Copper due to lower conductivity. The basic demands during electrode material selection are the high melting point, good electrical and thermal conductivity, chemical stability, machinability, burr formation, and low price. It is impossible to find a single material that can offer all these properties. Therefore, development of new EDM tool electrode materials has become vital.

This research hypothesised that it is possible to use a new modified Cu-W electrode to overcome some of these problems. In the new modified electrode, the Tungsten in Cu-80%W is replaced with Tungsten carbide (less than 50 %) and intruding a suitable additive that have a good solubility with Copper and Tungsten such as Silicon and Titanium. Silicon can form silicide with Copper and Tungsten which is an intermetallic compound that has properties which is intermediate between metal and an alloy. Electroforming industries are using Titanium-Copper compound as electrode materials, which combine the corrosion resistance of Titanium with good electrical conductivity of Copper. The expected intermetallic bonding of these additives with Copper and Tungsten are electrically conductive.

1.5.Research Objectives

The main objectives of this research are;

1- To create standard machining data using Cu-W electrode

2- To synthesize and characterize a new EDM electrode material using ball milling.

3- To evaluate the performance of the new developed tool electrode material.

In order to achieve the above objectives, the following major activities are conducted.

- Preliminary analysis of machining process using Copper and Copper-Tungsten electrode on machining of cast iron, cemented tungsten carbide steel, and hardened die. This step is important for proper selection of the most important parameters that can affect the machining process and to analyse and identify the optimal parameters setting for material removal rate, electrodes wear, and surface roughness.

- Taguchi techniques adopted for the design and analysis of experiment (DOE) due to it is the ability of solving multivariable problems (high complexity) using a small number of experiments. By this technique, the percentage contribution parameter on the quality of the product measured and the optimal setting of parameter can be predicted.

- Characterization of the electrode and work-piece material before and after machining using field emission scanning electron microscope FESEM due it is high magnification range (up to 500,000X) where a nanostructures surface can thus be visualized and analysed. FESEM can give a high resolution images with less electrostatic distortion.

- Characterization of the powder before and after ball milling using X-ray diffraction XRD, FESEM, and the transmission electron microscope TEM. XRD used due to the advantages in identification the change of crystal structure during phase formation in polycrystalline powder (partly crystalline and partly amorphous). Transmission Electron Microscope TEM is used to determine the nanoparticle size and the crystalline structure distribution of ball-milled samples.

- Consolidation of the modified Cu-W electrode is carried out using two different approaches as follows;

  1. Cold pressing at 740 MPa followed by sintering at 950^{o}C for 2h in argon gas environment. Loose powder can be cold deformed to near fully densities under certain conditions but higher pressures can severe die wear and possible tool damage. Full density typically requires pressure rang of five to eight times the yield strength of the material under compaction. It is difficult and expensive to find tools that can resist such stresses. Thus, high-pressure cold compaction is applied to low strength materials. The concerns of cold compaction and sintering are the forming and densification of the powders.

  2. Hot pressing (HP) at 33 MPa and 850°C for 90 minutes in vacuum; High densities are possible via high sintering temperatures, but with a possible loss of precision and accuracy. The cold product can be further densified by repressing and re-sintering but for larger shapes require hot pressing or forging. In hot pressing, plastic flow occurs when the stress exceeds the yield strength at the compaction temperature. Thus, the densification will occurs at lower stresses simultaneously by elastic deformation and diffusion along grain boundaries or through the lattice combines with the stress to give densification in a process similar to creep.

- Selection and optimization of the most important machining variables setting using conventional Cu and Cu-W electrode on machining of cast iron, cemented Tungsten carbide, and hardened die steel. The predicted value of the machining results was tested experimentally to measure and establish the variation of the confirmation to measure the degree of confidence. Taguchi design of experiment is adopted for design and analysis the machining experiment

- The performance of the new developed EDM electrode material is tested in diesinker EDM by machining of hardened material using the selected variables at the optimal setting. Each electrode is tested at the same machining variable parameters setting for high material removal rate, low electrode wear and surface roughness Ra. Taguchi design of experiment is adopted for design and analysis the machining experiment

1.6.Scope of Study

The main focus of this study is the synthesizing and characterization of a new EDM electrode material. The materials to be synthesized using ball milling are Cu-WC-Si, Cu-WC-Ti, and Cu-WC-Ti-Si metal matrix composite due to their hypothesized suitability. This material can be used as diesinker EDM and spot welding electrode.

The study focuses on the application of diesinker EDM as the main Un-conventional machining technique in tools and dies manufacturing. It is applied on three different workpiece materials. The selected workpiece materials are the gray cast iron, cemented Tungsten carbide, and hardened die steel. Gray cast iron used for preliminary machining variables selection due to the ease of machining without poor formation. Tungsten carbide is the harder and high melting point material which cannot be machined by conventional machining process. The common material used for die and mold manufacturing is the hardened die steel. Machining of gray cast iron and machine cemented Tungsten carbide achieved by using Copper electrode. The advance analysis of machining variables (optimization) carried out by using Cu-W electrode to give better understanding of the advantage and limitation of diesinker EDM process.

1.7.Outline of the Thesis

This research work embarks on synthesizing and characterization of new EDM electrode material using ball milling. In order to carry out the research, six chapters are compiled as follows. The second chapter discusses the state of the art of advanced EDM equipment, electrode-manufacturing technique, the performance of new developed EDM electrode, synthesizing of EDM electrode material using mechanical alloying and ball milling. This survey gives significant information about the most effective variables on EDM, the main difficulties associated with this technique and the trend of current research to improve the machining process. It also gives good understanding of the relationship between material science, powder metallurgy and EDM electrode and manufacturing.

The third chapter explains the theoretical background, where the basic principal of EDM including power supply, dielectric role and EDM electrode are highlighted. The mathematical model of the quality characteristic of machining of material removal rate and surface roughness are explained.

The fourth chapter describe the methodology. In this chapter, the outline of the preliminary study as well as the experimental approach of synthesizing and characterization the newly developed material is shown. Optimization of the selected machining variable using Taguchi technique is also explained. Finally the performance the newly developed electrode during machining of the hardened die steel under the optimal setting was demonstrated.

Chapter five present the detailed discussion of the study results. The performance of the new electrode material on machining of die steel was analysed and compared with that of Cu-W electrode test.

The main points concluded from this research are concluded in chapter six. The results show that the performance of the newly developed electrode in MRR and EW is acceptable, but not on.

CHAPTER 2

LITERATURE REVIEW

2.1. Introduction

The high demand for the new EDM tool electrode materials in advance application creates some challenges in die and mould manufacturing industry. These challenges are for the ease of design and manufacturing, the electrode performance, cost reduction and the ability to provide a complex shape electrode with sharp edges and pockets. The literature review gave an overview about the advance in Electric discharge machining as one of the most applicable machining processes in die and mould manufacturing industry. Electric discharge machining requires close tolerance, relatively high material removal rate MRR, electrode wear resistance and good surface quality. These goals are unachievable by simple machining parameters setting. However, its performance can be improved and optimized by variable adjustment and setting. Optimization via parameters setting is very sensitive due to the high number of machining variables and the possibility of interaction between the arrays of combination of these variables. Uncontrollable variables such as dielectric conditions and electrode wear have substantial effect on the machining process and machining quality.

The major problems with this technique include low electrical conductive material, low material removal rate, and the thermal electrode wear. In general, as MRR increases the electrode wear, surface roughness increases. The aim of this review is to enumerate the research trend in Electrical discharge machining. Recently, a number of researchers have explored various methodologies in order to improve machining rate, electrode wear resistance and surface quality. Some successes have been recorded in the area of facilitating the machining process using an external energy source such as vibration and LASER. Research on developing a new EDM electrode material is still ongoing. Special attentions are given to;

- Advancement in EDM equipment
- Newly developed EDM tool electrode material
- EDM electrode manufacturing technique
- The effect of machining variables setting on machining output

The strategy used in this literature review was first to make a general study of the advancement in EDM research within the past decade so that the importance of this research and how it linked to the global EDM research problem becomes clear. In doing so, special attention was given to the advances in diesinker EDM including machining variable optimization and the new assisted EDM machine.

Furthermore, the second part of the review concentrates on the current available electrode materials and manufacturing technique such as rapid prototyping.

The third part of this review focused on the effect of machining variables on machining output

In the fourth part, special emphasis was given to synthesizing of the new EDM tool electrode material using mechanical alloying and ball milling. Ball mill is a promising technique in the area of synthesizing new tool electrode material.

Finally, the literature review is summarized to show the current research trend on advance of EDM and the need for developing a new EDM electrode material.

2.2. Advancement in EDM

Within the past fifteen years, EDM researchers have tried to find a solution to the contradiction between machining output goals by using a combination of process thereby increasing the material removal rate without affecting the machining quality.

2.2.1. Ultrasonic Vibration Assisted EDM

A number of research studies were conducted between 2004 and 2008 on developing an ultrasonic vibration assisted electrical discharge machining (UEDM). Kunieda [6] used piezoelectric actuator to control the discharge gap in dry EDM. The research showed that using piezoelectric servo system balances the gap control, thereby inducing significant rise in material removal rate. The simulation revealed that conventional EDM is stable with no piezoelectric servo system as a result of the increase in the gap distance than dry EDM. He states that “This conclusion supports our view about the increasing of operational parameters by more variable and can create some difficulties in case of controlling the machining in general”.

A mathematical model for material removal rate and electrode of ultrasonic vibration assisted electrical discharge machining in gas was developed by Zhang [7]. The experimental result shows that by using gas as dielectric medium, the MRR of UEDM is twice as much as the MRR of normal EDM. The mathematical model used for material removal rate and the surface roughness (Ra) is as follows:

$$MRR = \frac{\mu(I_e U_e t_s)}{(t_s + t_i)} \tag{2.1}$$

$$R_a = \zeta(I_e U_e t_s)^{1/3} \tag{2.2}$$

Where: t_i is the idle time, t_s is the pulse duration, I_e is the discharge current, U_e is the discharge voltage; μ and ζ are the proportional constants.

Another investigation of ultrasonic vibration assisted EDM was conducted by Abdullah [8] where Ultrasonically vibrated Copper electrode was used on machining of cemented Tungsten carbide (WC-Co). They discovered that ultrasonic vibration of the tool electrode when working at low discharge currents and low pulse times is very effective in attaining a high material removal rate MRR. The ratio of surface roughness to tool wear was greater when ultrasonic vibration was used. The vibration improves the machining stability due to the reduction in the undesirable arcing.

Endo [9] studied the effects of vibration-assisted on EDM by using a range of amplitudes and frequencies. The results obtained from the experiments show that a remarkable reduction of the machining time could be attained. The inference that could be drawn from the work is that shorter machining times are obtained from higher frequency and larger amplitude of vibration. The experimental results also show that the stiffness of the workplace affects the machining time. They provided necessary information about the improvement of machining process using ultrasonic vibration assisted EDM. All the experimental results confirmed the understanding that the material removal rate is improved by the presence of ultrasonic vibration. The technique is affected by the normal EDM parameters such as peak current, pulse On-time and off-time, gap voltage in addition to the vibration amplitude and frequency, dielectric type and the wall thickness of the pipe electrode. The direction of vibration and the stiffness of the workpiece also affect the machining process.

Combining of electrical discharge machining with grinding (EDMG) was investigated by Shu [10]. An empirical relation between MRR and current was obtained. The relation between MRR and the working current in ampere (A) is given by the following formula.

$$MRR = e^{(0.659A - 2.077)} \tag{2.3}$$

This relation shows that if the working current is greater than 3.2 ampere, the material removal rate will increase exponentially. EDMG gave up to 3-7 times of MRR under appropriate conditions of electrode rotating speed, SiC particle size, and current more than the normal EDM.

Also, they investigated the advantages and disadvantages of machining by using air and oxygen in replacement of dielectric liquid. However, as they mentioned, the technique is very sensitive to the gas speed; gas-fleshing mode and gas due to additional sensitive variables introduced. The presence of the critical value of peak current and gap voltage can be the cause of the breakdown of the dielectric properties.

2.2.2. Laser-EDM Drilling

Li [11] found that the novel combined laser and EDM drilling technique reduce drilling time by 70%, cost reduced by 42% and production capacity increased by 90% without compromising the whole quality as compared to standard EDM drilling. By this technique a final hole diameter of 137-140µm was achieved. Consequently, Laser-EDM drilling is better than standard EDM drilling in the reduction of radial gap.

2.2.3. Dry and Near Dry EDM

Dry and near dry electrical discharge machining process using air, mixed gas and a mixture of liquid with gas was studied by Kunieda [12] The author stated that using air; the solidified debris can be removed and flushed out of the working gap by the high-velocity air flow without being reattached to the electrode surfaces. If the air is replaced by pure oxygen the material removal rate will be doubled. He also found that oxygen is better than air, water and oil due to it is low viscosity and high cooling rate, which makes the interaction between debris and gas faster. The effect of the reaction with gas on surface chemistry and microstructure was not mentioned.

Another study was carried out by Kao [13] using liquid and gas mixture as the two phase dielectric fluids for near dry electrical discharge machining. Near dry EDM improve the material removal rate, and eliminated the problem of debris deposition. Equation 2.4 shows that the minimum discharge gap required for gap voltage to make a breakdown of the dielectric fluid is inversely proportional to the dielectric strength and the dynamic viscosity. This relation provided a quantitative prediction of the gap distance of wet, dry and near dry EDM.

$$d = \frac{\alpha}{(s_w - s_a)\sigma^m + s_a} + \beta((\eta_w - \eta_\alpha)(1-(1-\sigma)^n) + \eta_a) \tag{2.4}$$

Where: *d* is the gap distance, S_w and S_a is the direct strength of water and air,η_w and η_a is the dynamic viscosity of water and air *m, n, α* and *β* are the four unknown variables.

The dry and near-dry electrical discharge machining (EDM) processes was equally investigated by Tao [14]. The experimental results indicate that the oxygen-assisted dry EDM is capable of providing high MRR 39 (mm^3/min) and low tool wear. The mechanism of the enhanced MRR is attributed to the rapid exothermic oxidation stimulated by the oxygen environment and high discharge energy density. The dry and near-dry EDM milling is exploited for the finishing process.

2.2.4. Magnetic Force Assisted EDM

Magnetic force assisted Electrical discharge machining technique on SKD 61 steel in kerosene dielectric was studied by Lin [15]. Peak current and pulse duration were the selected variables to characterize the machining process in terms of material removal rate, electrode wear rate (EW), and surface roughness.

The experimental results show that: -

- The MRR of the magnetic force-assisted EDM increases with peak current and pulse duration, and the MRR reached a peak value at 20 A peak current and 350 ms pulse duration. Moreover, the MRR increased rapidly during 20–160 ms pulse durations but grew more smoothly under 160–350 ms pulse durations.
- The EW of the magnetic force-assisted EDM became low upon increasing the pulse duration. The EW became negative at 350 ms pulse duration with 15 and 20 A peak currents.
- The surface roughness of the magnetic force-assisted EDM increased with peak current. Furthermore, initially the surface roughness increased with increase in pulse duration, and then decreased upon increase in the pulse duration.
- The surface cracks became more noticeable in the conventional EDM than in the magnetic force-assisted EDM. Since the magnetic force-assisted EDM could facilitate the expulsion of machining debris to reduce the probability of abnormal electrical discharge, so the surface cracks were relatively less seen on the machined surface.”

Similar study on the effects of magnetic force assisted EDM on machining characteristics was carried out by Lin [16] . The experiment was designed using L18 Taguchi orthogonal array as fractional factorial design. The selected controlled variables are; machining polarity, peak current, pulse duration, high-voltage auxiliary current, no-load voltage and servo reference voltage. The results show machining characteristics for material removal rate (MRR) and surface roughness (SR).

The analysis of experiment data shows that the material removal rate of magnetic force assisted EDM is three times higher than that of standard EDM under the same conditions. Not only that, the result indicates lower electrode wear ratio, and a smaller surface roughness campaign with standard EDM. Also, it was concluded [16] that machining polarity (P) and peak current (Ip) were the major parameters affecting MRR in conjunction with the magnetic force assisted EDM. In the conclusion, he states that the lager discharge craters were achieved during machining with the standard EDM than those obtained during magnetic force assisted EDM process.

However, the paper did not explain how the magnetic field affects the machining process and if the advantages are limited to the magneto material or any material. The common magnetic metals such as iron and steel can lose the magnetic properties at high temperature. The most effective viable mentioned here is not different from that of normal EDM.

2.3. Fabrication Techniques of EDM Electrode

Fundamentally in EDM the electrical discharge machining rate, machining cost and surface quality depend strongly on the tool electrodes material, the servo-system, the machining parameters and the dielectric flushing system. The main factors associated with the electrode system are the electrode material, electrode wear (uncontrollable), electrode jumping distance, and jumping frequency. Research works are still on-going to develop a new EDM tool electrode material that can combine the high thermal and electrical conductivity with high melting point to improve mainly the electrode wear resistance. it is impossible to find single material that can offers all these properties, this prompting EDM researcher to find a combination of materials and innovative technique to reach this goal. The machining process and reducing the electrode wear.

2.3.1. Powder Metallurgy (P/M) Electrode

Powder metallurgy is one of the main techniques used to synthesize and manufacture a new EDM electrode. The performance of powder metallurgy electrode on the quality of the machined component was studied by Konieda [6]. The quality of the electrode was controlled over a wide range of properties by adjusting the compaction and sintering conditions. P/M electrode performance is found to be more sensitive to the pulse current and pulse duration than conventional solid electrodes. Not only that, electrodes can cause negative material removal rate. The machined surface contamination caused by the eroded particles from the electrode is a function of the manufacturing parameters of P/M electrodes. Lower currents and higher frequencies are responsible for low metal removal. This is, in no small way, due to the surface structure of P/M electrodes. In contrast to the conventional solid electrodes, P/M electrodes possess more asperities on the working surface since they are more porous nature.

Various compositions of Cu-ZrB_2 and Cu-TiSi P/M EDM electrode prepared and developed by Zaw [17] using Solid-state sintering and liquid phase sintering. Electrode materials such as Graphite, Copper, Copper alloys, Copper-Tungsten, brass, silver-Tungsten and steel have some advantages and disadvantages in respect to machining performance. The performance of the newly formed material was compared with that of conventional Cu, Graphite and Cu-W electrode.

The poor bonding strength among ZrB2 and Cu particles reduces the thermal wear resistance. Prior to melting the material through spark erosion, the bond strength is easily broken down. EDM electrodes made of TiSi/Cu compound were useable because they exhibit too high wear rate and they tend to damage the surface of the workpiece. Zaw also mentioned that if bonding problems could be solved by the addition of some fluxing elements and via laser melting, then ZrB2 may be an effective contributor to good machinability and provide increased in wear resistance. Generally, Copper-Tungsten EDM electrodes are used in die and mould industry because its combine the high thermal and electrical conductivity of Cu element with the high melting point of Tungsten W.

Some of the good qualities of Titanium carbide (TiC) include high melting point and high thermal and abrasion wear resistance, while Nickel (Ni) is highly soluble in copper (Cu). Due to these factors they were selected for use by Li [18], who studied the effect of Nickel (Ni) and Titanium carbide (TiC) additives in sintered behaviour and electrode performance. The experimental results show that densification of sintered material was improved by Nickel (Ni) and the reduction in particle size improved with increasing TiC. In addition, to that the tool material showed good performance with TiC additive. The relative density and the electrical conductivity of sintered electrode show an increase and then decrease with increasing TiC. Meanwhile, He concludes that surface roughness manifestly decreased with the increase in relative density. He therefore, proposes that 15% TiC show the best EDM with the highest relative density and lowest electrical resistivity.

The performance of Copper powders containing resin blended with chromium powders as electrodes was investigated by Tsai [19]. The electrode material is bonded in a hot mounting machine at 20 MPa compaction pressure and 200 °C temperature. The effect of mixing ratio and compaction pressure in addition to the machining variables (such as polarity, peak current, and pulse duration) were used to investigate the machining process in terms of material removal rate (MRR), electrode wear rate (EW), surface roughness, and thickness of the recast layer.

The experimental results show that under positive electrode polarity, Copper powders containing resin show a higher MRR than the Cu–Cr composite electrodes; but relatively the EW is higher. The high electrode wear is responsible for the weak bonding strength of Cu–Cr composite electrodes because of low sintering pressure and temperature. Instantaneous drop of Cu and Cr particles out of the electrode leads to unstable discharge condition during the EDM process. The drop out of Cu and Cr particles in the discharge gap affects the machining process and the surface quality whenever the particles stick to the machined surfaces. The author suggests that using such composite electrodes as tool electrode may improve the resistance of work piece surfaces to corrosion.

The reviewed paper about powder metallurgy EDM electrodes shows that P/M technique is a promising simple technique that can be used to develop and fabricate a new tool electrode material. The main problems with this technique are the low bonding strength of the components and the difficulties in achieving full density material.

2.3.2. Rapid Prototyping (R/P) Electrode

2.3.2.1.Selective LASER Sintering (SLS)

The use of selective laser sintering technique to fabricate EDM-electrodes was investigated by Durr [20]. In this Rapid Tooling technique, a bronze-nickel electrode was built layer by layer. Moving speed and the sintering strategy show a big impact on the quality of the sintered electrodes. Slower scanning speed gives the higher particle density and lower roughness. On the other hand, A 90° direction rotation after every layer (called jitter scanning) leads to an increase in strength and a decrease in porosity compared to the alternate scanning (no rotation). The electrodes wear and material removal rate have been investigated and the results indicate that the wear behaviour leads to an unacceptable change of the shape of the electrodes in addition to workpiece. The investigation so far conducted demonstrated that electrodes with lower porosity manifest decreased electrode wear with higher workpiece removal. Electrodes after-treatment by infiltrating them with silver-containing solder results in an almost fully dense tool body and consequently, a decrease in relative electrode wear by 30-50%.

Similar research using Selective laser sintering (SLS) technique was conducted by Zhao [21]. The study involved manufacturing an EDM rapid prototype electrode. Infiltration was used to improve the density and the mechanical performance of selective laser-sintering electrode. The results indicate that the electrode made by SLS can be used as an EDM electrodeCu reinforced WC-10% Co metal matrix composites electrode material prepared by Gu [22] using direct metal laser sintering (DMLS). The focus of the research was on investigation of laser power scan speed, layer thickness on microstructures and properties of the laser sintered samples. The experimental results show that below 700W, the higher the laser power, the greater the densification with improved bonding capacity between the reinforcement and the matrix. It was also observed that a critical scan speed of 0.04 m/s creates the transition of pushing to trapping of particulates by the advancing solid/liquid interface. Increasing the scan speed above the critical value can improve the distribution homogeneity of the reinforcing particulates.

The main disadvantages of SLS are the need for an additional treatment such as infiltration to achieve a full density due to the high porosity and the surface quality of the product parts influenced by powder particles. In addition, the scanning rate and scanning strategy are additional very important variables. The process is time-consuming due to the need for heating up and cooling down process.

2.3.2.2.Stereo Lithography (SL) and Electroforming

In his studies of the viability of using rapid prototyping techniques in the manufacture of EDM electrodes, [23]used an electroformed shell of Copper, backed with a suitable material as an EDM electrode and he concluded that electroformed Copper electrodes seem to possess an excellent potential to be used as EDM tools. The use of rapid prototyping electrode for EDM was also researched Dimla [24] using stereo lithography Copper coated models and Copper coating of direct metal laser sintering (DMLS) models. He stated that that variability of Copper thickness of the rapid prototyped electrodes is clearly a big concern. Due to variations in coating thickness, the machining process was found to be unsuitable. The need for a consistent layer of Copper on the SL and EDM electrodes is another reason that makes these RP electrodes unfit.

Further study on the development and performance of electroforming EDM electrode was undertaken by Rennie [25] using electroforming as a rapid prototyping technique to fabricate a complex EDM electrodes. The results show that it is possible to use electroformed electrode for machining. The performance of this rapid prototype R/P electrode depends on the wall thickness of the front faces and edges of the electrode. It was stated that a major advantage arising from the the use of electroforms in this application is that the electroforming process is such that several electroforms may be grown concurrently, although a single electrode may only be able to erode 6 mm of die steel.

New electrical discharge machining electrode was developed and tested by Monzon [26]. The electrode manufactured using rapid prototyping followed by electroforming technologies. The electrode performance has been tested in an EDM machine and the results compared with conventional electrolytic Copper electrodes.

The results show that both the electroformed and the conventional electrodes can operate with the same parameters and conditions, except when under strong work intensity. In general, the roughness and cavities produced by electroformed electrodes is higher than that obtained with conventional electrolytic electrodes. Another important study about the performance of a newly manufactured die-sinking EDM electrodes was done by Hsu [27]. He used rapid prototyping system based on nickel electrolysis plating and copper electroforming. This method shortens the electrode manufacturability as well as the cost of electrodes. The electrode prototype using stereo lithography and the electrolysis plating was then performed. Test results indicates the critical step in pre-treatment engineering for electrolysis plating is surface roughening but no crack was found on the electrode and that the electrical discharge machining effects are promising. The most effective factors are the electroforming current density, the ratio of depth over the width of the hole in the plating material, the concentration of the plating solution, and the direction of current. It was also established that the machining time is lower at low machining current and the electrode wear ratio seems to increase with current. The advantage of this technique is clear when an electrode with complex 3D geometry is needed. However, the electrode strength and cost are negatively affected.

2.3.2.3.Thermo Jet 3D Printing

Another rapid prototyping technique used to manufacture EDM electrode is Thermo Jet 3D printing. Ferrera [28] studied the application of indirect rapid tooling technology to manufacture EDM Copper electrodes from investment casting, using prototypes of wax made by Thermo Jet 3D printing. The results show that there was parity in the machining efficiency exhibited by both the Copper RT electrodes and the conventional machined solid Copper electrodes. The suitability of these electrodes lean towards roughing or semi-finishing cuts in die sinking EDM. The present electrodes show better electrode wear ratio (EW) compared with that of electrolytic Copper (standard) ". Generally, lead-time and the associated costs in the metalworking industry are greatly reduced during the manufacturing process of complex 3D shapes by the integration of reverse engineering methodology with additive rapid prototyping and tooling techniques.

2.4. Machining Variables

Electrical discharge machining system consists of three main subsystems. The three main subsystems are the tool electrode, power supply and the dielectric system. Each of these subsystems contributes significantly on the machining process, surface quality, and precision. To some extent variables such as electrode polarity, peak current, pulse duration, and dielectric pressure can be controlled while, variables such as electrode wear and dielectric condition are uncontrollable.

Leonardo [29] studied the influence of electrode material, flushing, electrode dimension, depth of cut and planetary motion on EDM performance. Machining was conducted using both Copper and Graphite electrodes on a Cr, Mo, and V steel. The experiments show that the electrode material is the primary variable influencing tool wear and surface roughness. The electrode size also affects productivity and electrode wear.

The effect of open-circuit voltage, the discharge voltage, the peak discharge current, the pulse-on duration, the duty factor and the dielectric flushing pressure on various machining characteristic such as MRR, TWR, the workpiece surface roughness and the average white layer thickness were studied by Ferreira [30]. The observations from planetary electrical discharge machining of full-hardened AISI H13 with Copper-Tungsten Cu-W electrodes are that the material removal rate increases with increasing peak current and W content. The Cu+80%W composition gives the highest MRR of 0.09 mm3/min at 4.0 A, followed by Cu+75%W and Cu+70%W compositions respectively. However, the relative tool wear ratios (TWR) decreased marginally as peak current rises and broadly speaking, the relative TWR is between 19% - 24% for all of the Cu-W compositions studied, while the Cu+80%W composition gave the lowest average of TWR of 20%. For die steel machined using planetary EDM, using Cu-W as the cathode and the workpiece as the anode gave a better machining performance. In the same vein, negative tool polarity produces a near-constant relative TWR over a wide range peak current and pulse on duration. The relation between surface roughness (Ra) and the energy per discharge (W_e) given by the following empirical formula in equation 2.5.

$$R_a = 0.0252(W_e)^{0.4473} \tag{2.5}$$

The effect of dielectric liquid and electrode type on white layer structure was studied by Ekmeksi [31] focusing on retaining austenite and residual stresses using X-ray diffraction method. The machining tests were conducted by using Copper and Graphite tool electrodes. The dielectric liquid used are; kerosene and de-ionized water under the same operating conditions. The research of Ekmeksi [31] demonstrates that regardless of the tool electrode material, the machines surface would always be saturated in so far as a hydrocarbon based liquid is used as the dielectric medium. Also, the quantity of the austenite phase is increased within the white layer as result of carbon supply from the graphite electrodes, when machining with deionized water as the dielectric. Micro cracks become visible on the machined surface when the stresses on the machined surface exceed the fracture strength of the material.

Employing the six-factor, three-level experiment using L_{27} orthogonal array, Govendan [32] studied the effect of machining variables such as Gap voltage, Discharge current, Pulse Off-time , Oxygen pressure, Electrode speed and shielding clearance on MRR, TWR, oversize and compositional variation across the machined cross-sections in dry electrical discharge drilling. The results show that: discharge current, rotational speed and gap voltage had major influence on MRR; TWR was found close to zero in most of the experiments due to the deposition of molten material from the workpiece on the electrode surface; compositional analysis of machined surface shows a migration of tool and shielding material into the work material and dry EDM as compared to the conventional liquid dielectric EDM show larger MRR and crater radius.

Mohri [33] investigated the electrode wear phenomena in electrical discharge machining. It was found that the edge wears is higher at the beginning of machining. It was also observed that the black carbon layer on the electrode surface influence the spark erosion in EDM. Therefore, zero wear of electrodes will be realized with very long pulse duration taking into account the equilibrium of the removal rate with precipitation and piled substance on the electrode. The effect of carbon black layer on the surface of W-Cu electrodes in machining process was investigated by Marafona [34]. The machining process carried out at two-stage EDM process technique. The results show that with the two-stage EDM process, it is possible to improve the material removal rate for a given tool wear ratio. It was also observed that the percentage of carbon in the ‘black’ layer is very vital for EDM performance improvement.

The possibility of machining Tungsten carbide and the operating parameter optimization was studied by Lee [35]. An EDM process was characterized in terms of the material removal rate, the surface finish quality of the workpiece produced and the relative wear ratio. The results show that for higher material removal rate and lower tool wear, the negative polarity electrode, high discharge current intensity and high open-circuit voltage is necessary for Tungsten carbide due to its high melting point and high hardness value. It was also observed that relatively low dielectric flushing pressure of 0.5 MPa is found to be better for machining optimization. Not all the conflicting goals can be achieved in single optimal parameters setting. Thus, the best machining results are obtained, by taking the goals independently in different phases of work with different emphasis.

as mentioned by Mohri [36] and Garg [37]; can be used on machining of hard and high melting point material such as metal matrix composite and also to fabricate a thin micro-tool. Where a rod electrode is driven through the centre of a controlled slit formed between two electrically isolated metal plates to provide a critical path for the rod electrode tool during the process. A thin bar of 20 µm in diameter is fabricated by this technique.

Li [11] use a combination of Laser and EDM Micro-drilling to make high quality holes of diameters less than 145µm for the manufacturing of next generation diesel fuel injection nozzles for improved combustion efficiency and reduction of emission to the environment.

Ekmeksi [38] use optical microscopy, scanning electron microscopy (SEM), and XRD to investigate the machining characteristics of electric discharge machined surfaces of normalized, quenched, and tempered steels employing kerosene and deionized-water as the dielectric liquids. Their work revealed that cracks within the white layer are created mainly because of non-homogeneity from the white layer. Carbon Uptake from the dielectric liquid leads to the development of martensite and complex iron carbides in a retained austenite matrix. This leads to high transformational stresses that exceeding the material ultimate strength during solidification. The research pointed out further that penetrating cracks are started because of shrinkage of the recast structure joined to the circumferential edges of a crater rim that is separated from the base with molten material soon after cessation of the discharge. Also, crack penetration depth is showed to be proportional the applied pulse energy. The incidence of such cracks mainly depends on mechanical and thermal properties of the base material.

In a separate study, Ekmeksi [39] employed layer removal method was to measure the residual stress profile with respect to its depth underneath the surface caused by die sinking type EDM. Cracking and its consequences on residual stresses were also studied on samples machined at long pulse durations.

High tensile residual stresses are generated by EDM and increased from the surface and reached maximum value. This maximum value is close to the ultimate tensile strength of the material. Compressive stresses depend on the sample thickness since residual stresses within plastically deformed layers are proportionately countered with elastic stresses in the core of the material. Consequently, the pattern of residual stress distribution at different pulse durations and currents is always the same except when cracking network is developed. The location of tensile peak stress and the spark energy share a direct relationship. The peak stress intensity remains unchanged.

The effect of key operating factors on output measures was investigated by Simao [40] They used L8 Taguchi orthogonal array to design an experiment and to analysis the effect of key operating factors on output measures. The experiment conducted in hydrocarbon oil die sink EDM using partially sintered WC-Co electrodes on AISI H13 hot work die steel. What was demonstrated from this research is that partially sintered electrodes made from WC-Co caused the development of a layer of uniformly formed alloyed/ modified surface with few microcracks. The results of the confirmation experiment showed an increase in workpiece surface microhardness from ~640 to 1319 HK (0.025) using the EDM operating parameter levels suggested by the main effects plot. Similarly, the effect voltage on workpiece microhardness was not as marked as had been expected. This could be inferred from the fact that not all combinations of factors were tested using the Taguchi methodology.

Lee [41] conducted an all-inclusive study of the surface integrity of the machined Tungsten carbide workpiece in (EDM) process, using peak current and pulse duration as variable. The machined surface morphology was examined with SEM. Surface hardness was determined with a macro-hardness tester. The results show a clear damaged layer on the machined Tungsten carbide workpiece surface and the concentration of WC grains within the damaged layer decreased from the internal structure to the top surface. Cracks were also observed and number increased with increase in the variables measured. Lower levels of peak current and pulse duration yielded little or no cracks at all.

The effects of low wear rate Cu-W electrodes on the EDM parameters were established through the study done by Lee [42] when they monitored the variation of surface integrity of AISI 1045 carbon steel machined by EDM. The research used a Hole-Drilling Strain-Gage Method to measure the residual stress emanating from by the EDM process. This study determined the relationship between the EDM parameters and various aspects of the surface integrity, namely the MRR, Ra, hole enlargement (HE), average white layer thickness (WLT), the presence of cracks, and the degree of induced residual stress. The main conclusions of this study may be summarized as follows:

- In general, the values of the MRR, surface roughness SR, and heat affected layer HE evaluation indices increase for higher values of pulse current. However, an excessive pulse-on duration results in an expansion of the electric plasma channel, which results in a reduction in both the MRR and the SR.

- Obvious cracks always appear in thick white layers. When the WLT is less than 3µm, virtually no cracks were evident. Increasing the pulse current (i.e. larger than 8A) while shortening the pulse-on duration (i.e. smaller than 12 µs) is effective in reducing surface crack.

- The pulse current affects the surface crack density, while the pulse-on duration influences the degree of crack opening. When the pulse current is too small (i.e. 1 A), the surface cracks density increases.

- EDM drilling induces residual compressive stress, whose value increases at higher values of pulse current and pulse-on duration. The linear relationship between the maximum principal stress (σ_{max}) and the average WLT is given follow; $\sigma_{max}(MPa) = -14.15 * WLT(\mu m)$. Adjusting the pulse-on duration is an effective means of controlling the magnitude of the residual stress.

2.5. Mechanical Alloying and Ball Milling

The need for new tool electrode material that can combine high electrical conductivity, thermal conductivity and high melting point for good wear resistance requires a special technique. Mechanical alloying by ball milling is one of the most practical and dependable techniques to synthesize alloy from material that are immiscible at low temperature or when the vibration of melting temperature is very high such as Copper and Tungsten. Soni [43]

2.5.1. Ball Milling

Copper-Tungsten exhibits total absence of solubility in both solid and liquid state. Mechanical alloying (MA) as a solid state, non-equilibrium process can be beneficial to the processing of such an immiscible system with the added features of refinement of the structure. Raghu [44] synthesized an ultrafine Cu-W microcomposite structure by mechanical alloying using ball milling. He affirmed that the milling behaviour depends on the composition, milling time and milling atmosphere. Metastable solid solubility in the system was also confirmed and the crystal sizes were found in the Nanocrystalline region. This result was confirmed by the lattice parameter analyses of Copper and Tungsten elements. They report that the conversion of milling energy effectively to create deformed surfaces, which resulted in metastable solid solubility and Nanocrystalline structure, was assisted by the oxygen available in the milling atmosphere. Li [45] used the thermo-mechanical approach to produce W-Cu composite powder by using high temperature oxidation, small amount of time, high-energy milling and reduction. The outcomes revealed that the oxygen content of W-Cu composite powder decreases with the increase of milling time, while the specific surface of final powder increases with the milling time

The sintered sample produced by thermo-mechanical process showed nearly full density as a result of sintering at 1200 °C for one hour without the addition of the sintering activator due to the high specific surface area and homogeneous microstructures of W–Cu powder that are beneficial to the sintering of products.

Synthesizing of Cu-W Nanocomposite by mechanical alloying was also investigated by Alan [46]. He found that the crystallite size of Tungsten is around 15 nm and that of Copper is 40 nm after 20 h of milling. Because Tungsten is brittle, it has lower crystallite sizes than Copper during milling and Copper imparts good cushioning effect due to their ductility. Also, Tungsten crystallite sizes are relatively higher in the milled W-Cu samples when the fraction of Copper is more in W-Cu system. Li [47] investigated the milling of the oxide of Tungsten–Copper oxides to produce a fine particle size distributed Cu-W composite powder. The paper concluded that milling of the oxide precursors in alcohol leads to reduced Tungsten-Copper composite powder and gave better particle size distributions than the other two processes of dry milling and water milling and produce near full density W–Cu composite at lower sintering temperature.

Yusof [48] studies the mechanical alloying of nanostructure Cu-WC by mixing the elemental powders of Copper (Cu), Tungsten (W) and Graphite (C) using planetary ball milling for different milling durations in the range (0 to 60 h) and compacted and sintered in order to precipitate hard Tungsten carbide particles into a Copper matrix. Characterization of milled powder by X-ray diffraction (XRD) did not show any carbide peak in the powder mixtures after milling. WC and W_2C phases were precipitated only in the sintered composite. Hardness of the composite was enhanced but electrical conductivity reduced with increasing milling time.

Yamamoto [49] studies the vaporization of carbon components from Cu-WC base contact during electric discharge in vacuum. The analysis of the deposits on the contact holders carried out using Auger electron spectrometer and X-ray photo-electron spectrometer and the results show that C and W which have extremely low vapor pressures were observed in the spectrum as well as Cu. The author conclude that the superheated Cu-WC at the contact surface induce the vaporization of carbon.

Shunmugam [50] studies the improvement of electrode wear resistance of EDM using WC powder metallurgy electrode. Electrical discharge machining using powder metallurgy electrode with reverse polarity were used to modify the surface properties of a machined surface. The author mentioned that by using a WC which is wear-resistant material in the compact, the wear resistance of the resultant surface can be improved, the wear resistance show considerable improvement.

Jamaludin [51] synthesize and studies the performance of Cu-WC spot welding electrode using mechanical alloying and powder forging. High density and electrically conductivity composites were obtained after mechanical alloying. In contrast, the hardness of the composite is higher when longer time mechanical alloying is used. The strength decreases with milling time as a result of higher density and electrical conductivity. The wear behavior of the composite showed that there was increase in deformation of the spot weld electrode as the milling time increased.

Hydrogen-reduction and sintering procedure was used by Ahmadi [52] to synthesize W-15 wt% Cu nanocomposite. Hydrogen-reduction was carried out at 600°C, 650°C, 700°C and 750°C for 15-90 min and sintering was performed at 1100°C, 1150°C, 1200°C and 1250°C for 60 min. The results show that at the first reduction step, CuO reduced to Cu according to the reaction: CuO --> Cu + 1/2O_2, which took place at 400^{o}C and the reduction of WO_3 to W occurred at 750^{o}C. The specimens sintered at 1200^{o}C for 60 min had a higher densification than those sintered at other temperatures.

Baikalova [53] investigated Cu-W-C system using high-energy ball milling and then annealing at 820-940°C in an argon atmosphere. Copper matrix with the composition of W+50%C was milled. The results show that high Tungsten content is found to retard WC synthesis and W_2C becomes the dominant product. Low Tungsten content causes the enhancement of WC in the products. Furthermore, a composition of Cu+3%W+3%C helped to achieve decrease in product grain size, with refinement down to the submicron level with a rise in preliminary mechanical treatment. Besides, grain size of carbides and Copper was less than 0.5 mm, with the samples of material having uniformly distributed grains of Tungsten carbide in the Copper matrix, resulting in improved microhardness.

Large numbers of nanocomposite materials were synthesized using high-energy ball milling. An amorphous of Cu-Ti and Cu-Zr was successfully synthesized by Hen [54]. The structure and thermal behaviour of these alloys show that the replacement of Ti by Zr can enhance the amorphization rate. These may be attributed to a more negative mixing enthalpy by adding zirconium to the Cu-Ti system, providing a larger chemical driving force of solid state reaction.

The influence of Ti and Zr embedded in Cu matrix on the shear strength between Cu-Ti and Cu-Zr alloys and carbon rod (or fibre) were studied by Sebo [55]. As the work concluded, the interface between carbon fibre with Cu-Ti alloys and Cu-Zr alloys can be optimized by controlling the amount of Titanium and zirconium in Cu-Ti and Cu-Zr alloys.

Evirgen [56] study revealed that Al-Cu-WC system can be mechanically alloyed in a high energy milled for 1 h, 2 h, 3 h and 5 h milling duration Powder characterizations were carried out with SEM and XRD analyses. In the work, the author sintered the mechanically alloyed powder pellets under inert Argon atmosphere at 650°C for 4 h. Examinations of these mechanically alloyed sintered powders revealed that the decomposition of WC after 450°C resulted in the creation of $Al_{12}W$ intermetallic. It is this intermetallic that provided high strength composites. The microhardness of sintered samples increased with the increase of MA duration.

Guilemani [57] studied the effect of planetary ball milling parameters on WC-Co powder using Taguchi method. The selected milling variables are; powder ratio, size of milling balls, type of medium, volume of milling medium and rotation speed. The results show that using ethanol and a combination of 12 + 18 mm ball size improves the grain size reduction of WC. While using distilled water and a ball size combination of 10 + 12 mm could accelerate the particle size reduction. It was also found that after the ball to powder ratio, all other factors are very significant, and the volume of ball milling medium and the rotation speed offer the largest and the second largest contributions in the SSA reduction. After 10 h of ball milling with the optimized parameters, the WC grain size of the WC–Co powder are about 400 nm and 10 nm, respectively. Feng [58] mentioned that mechanical alloying promoted the formation of a solid solution of elemental powders and the barrier energy of the formation of the compound could be exceeded easily. The author also added that, a decrease in the ball milling time will improve the efficiency of mechanical alloying, and prevent the formation of amorphous phase.

On the other hand, the compressibility and sintering behaviour are directly related to the properties of the milled powder. Gan [59] researched the relation between powder morphology of the milled powder and compressibility of Cu/SiC powder under cold compaction. It was found that the density of composites decreases with increasing milling time. With increasing milling time, the dendrite Copper powder became flattened which successively changed to spherical composite powder. The morphology and hardening effects during ball milling have an important influence on compressibility of the powders.

Wang [60] study the mechanically alloyed W–Ti system using high-energy milling and the powders were characterized by scanning electron microscopy and X-ray diffraction. This alloy is widely used in the microelectronics field as diffusion barrier layer. The conclusion drawn by the other can be summarized as follow: W-Ti alloy prepared by MA show neither a coherent structure nor a nanocomposite of W and Ti. The pre-alloyed powders synthesized are beneficial to improve the properties and microstructure of W–Ti alloy.

Lee [61] in another study used high-energy ball milling to synthesize a mechanical alloyed Ti-Si and TiH1.924-Si system. Mechanical alloying of a mixture of elemental Ti and Si powders resulted in the creation of $TiSi_2$ equilibrium compound, whereas, commencing the process from a Si + TiH1.924 combination resulted in the formation of metastable phase. When the mechanically alloyed powder is annealed at temperatures above 800 °C, the metastable phase is completely transformed to TiSi2. This is most likely attributable to the formation of a metastable phase, which is kinetically more favoured than the stable $TiSi_2$.

Kosroshahi [62] used Ti-50Al atomic weight percent (at %) and Ti-48Al-2.4Si at % compositional powder to study the effect of Si on Mechanical Alloying process of Ti-Al (γ) intermetallic compound. In this work, the mechanical alloying was carried out using ball mill in inert argon atmosphere and the structural examination was carried out using XRD and SEM. The outcome of the work showed that elemental powders were transformed into Nanocrystalline Ti solid solution and amorphous phases with time, during the MA process. The time required for the Ti solid solution or amorphous phase development was longer in powders that contained Si. Sticking of powder mixtures to milling tools was significantly increased during the formation of solid solution phase. In general, the adhesion tendency of Si containing powders was considerably lower than those of Si free powders.

Fundamental understandings of high energy milling studied by Yang [63] where he applied the technique to synthesize nanostructure Si_3N_4 /SiC composites. It was shown that the high energy milling of Silicon and Graphite mixtures produced nanostructure Si_3N_4/SiC composites. At the early stage of milling (within ~10 h of milling) a significant refinement of particles and crystallites occurs. The introduced defects and absorbed nitrogen enhance the compound formation. This enhancement is believed to be related to the defect structure generated during milling and the mechanical excitation during ball collisions.

In parallel to this, an important result about mechanical alloying using high energy ball milling was published by Tian [64]. He mentioned that during milling the grain size decreases and strain increases with time until steady state is reached. He averred that at steady condition, the grain size increases weaklyas the temperature is increased. The observed weak dependence of the grain-growth term temperature is consistent with nonequilibrium vacancy production. Another important point mentioned by the author is that the stored enthalpy first decreases to a minimum value and subsequently increases toward a steady state, while at high temperatures it decreases monotonically.

Schaefer [65] applied the dry and wet milling to investigate the effect of high-energy ball milling of powders on sintering behaviour. The dry and wet milling was applied for 1, 2 and 3 h in alcohol medium and were sintered at 1000, 1050 and 1100 °C temperatures . The experimental results showed that by improving the starting powders, it is possible to eliminate the enclosed pores and to improve the sintering process.

2.5.2. Combustion

Synthesizing of the nanocomposite material can be achieved using combustion technique. Said [66] produced a (Ti,W)C in Ni-Ti reinforced Titanium matrix composites by combustion method. Different W-Ti-Ni was produced and the results show that solution of W in TiC was approved by XRD and SEM-EDS techniques. In addition, increasing W/Ti ratio of the starting materials increases W-exchange in the carbide phase. Depending on the Ni and Ti content, a critical W/Ti ratio exists above which the carbide phases were found to be WC+ (Ti, W) C, and below this critical value the carbide phase is (Ti, W) C. The critical W/Ti ratio decreases with increasing Ni content.

Hong [67] used combustion followed by hot pressing to produce TiB_2-40Cu-8Ni ceramic-metal composite at 1200^0C, 1250^0C and 1300^0C. Among the parameters investigated are the microstructure, deformation behaviour and mechanical properties. It was clear from the outcome of the investigation that the relative density and the flexural strength were enhanced considerably after hot pressing. TiB_2 ceramic grains of the combustion synthesized TiB_2–40Cu–8Ni composite transformed from near equal axis-like shape to rod-like shape after hot pressing. The cause of change in the morphology is not as result of elastic and plastic deformation, but is rather a consequence of diffusion growth of TiB_2 in high temperature.

Combustion followed by hot pressing approach was used by [68] to synthesize Al_2O_3-TiC-ZrO_2 Nanocomposite using TiO_2, Al, C and ZrO_2 as raw materials. The results show that an appropriate amount of ZrO_2 nanoparticle additive improves the mechanical properties. The flexural strength and fracture toughness of Al_2O_3-TiC-10 wt. percentage ZrO_2 composite were approximately 20% higher than that of Al_2O_3-TiC composite. The addition of ZrO_2 nanoparticle reduced the grain size and improved the distribution of different phases.

From the reviewed papers; three main directions in EDM research can be highlighted as shown in Table 2.1.

Table 2.1 Summary of the reviewed papers

	Author	Notes
Advancement in EDM by assisting machining process	(Zhang, Zhang et al. 2004, Prihandana, Mahardika et al. 2009, Xu, Zhang et al. 2009)	Ultrasonic assisted EDM are needed for increasing the material removal rate without degrading surface quality
	(Li 2006, Garg 2010)	LASER and EDM micro-drilling for next generation fuel injection nozzle manufacturing
	(Lin 2008, Lin 2009)	Magnetic force assisted EDM used to facilitate the machining process and drive the machining debris expelled from the machining gap.
Fabrication Techniques of EDM Electrode	(Tang, Hong et al. 2005, Ferreira 2007, Hsu 2008, Zhang and Liu 2009)	Rapid Prototyping technique such as selective LASER sintering and 3D thermo-jet printing is used to fabricate EDM electrodes.
	(Shunmugam, Philip et al. 1994, Samuel and Philip 1997, El-Taweel 2009)	EDM Electrode mainly fabricated by using Powder Metallurgy technique
Mechanical Alloying and Ball Milling	(Li 2001)	TiC is an extremely hard refractory material with a high melting temperature, and abrasion resistance is used to reinforce copper.
	(Tsai 2003)	Chromium used to improve the wear and corrosion resistance of copper. Such electrode can be used to modify surface layer of work piece.
	(Gan 2008, Jamaludin 2009, Wang 2009, Evirgen 2010)	Mechanical alloying by ball milling is used to synthesize Cu-SiC, Cu-WC, W–15 %Ti, and Al-2 % Cu alloy reinforced with WC composite.
	(Yusoff, Othman et al. 2011)	Cu-W-C were mechanically alloyed using ball mill for (0–60 h). The formation of WC began and the Hardness of the composite was enhanced but electrical conductivity reduced with increasing milling time.

CHAPTER 3

THEORETICAL BACKGROUND

3.1. Introduction

Electro discharge machining is an electro-thermal non-traditional machining process. The main types of EDM include diesinker EDM (Electrical Discharge Grinding (EDG), multi-electrode and multi-lead machining), micro-hole EDM drilling, and wire-cut EDM (multiple-electrode and multiple-workpiece machining). All these types are operates based on power generation, dielectric function, and the tool electrode. Understanding the working principle of electro discharge machining is vital.

The main requirements of EDM electrode material and a simple mathematical modelling for machining characteristic also will be discussed in Section 3.3

The large numbers of variables and interaction between these variables make EDM a very sensitive machining process. Thus, the basic principle of Taguchi design of experiment techniques as fractional factorial design of experimental (DOE) adopted in this research will be discussed in Section 3.4. This is also important basic information for understanding the advantage and disadvantages of fractional design of experiment.

The theory of mechanical alloying and ball milling and consolidation will be given in detail in Section 3.5.

Full density achievement is one of the main problems associated with powder metallurgy. Thus, the main consolidation techniques namely hot isostatic pressing (HIP) and hot pressing (HP) will be discussed in Section 3.6 of this chapter

3.2. Non-Traditional Machining Process

The great improvements of new developed engineering materials has been achieved in addition to the shape that is more complex, low-rigidity structures, and micro-components with high surface tolerance and surface quality which have been difficult or even impossible to meet these demands using traditional cutting and abrasion machining.

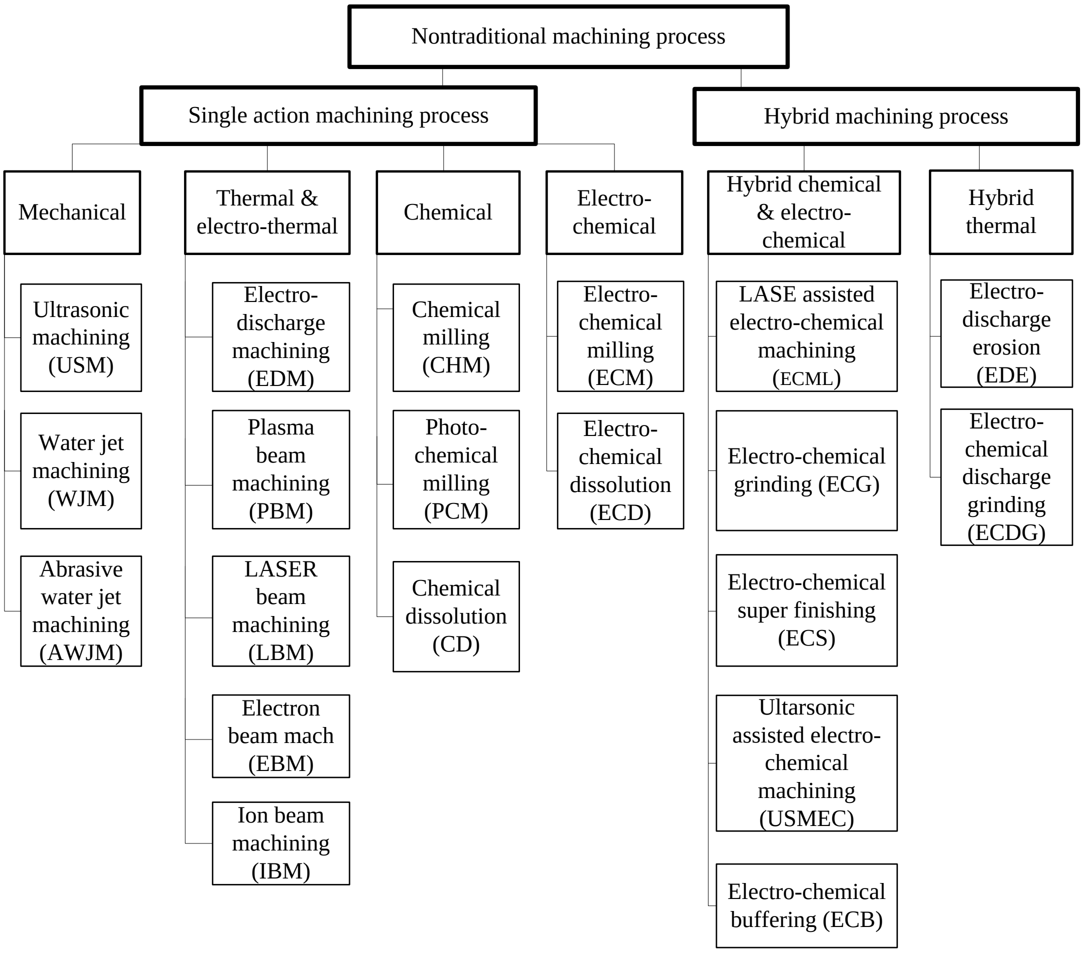

Figure 3.1 Categories of nontraditional machining processes El-Hofy [69]

In traditional machining, the tools must be harder than the workpiece meanwhile in many non-traditional machining processes such as EDM, the electrode hardened is not one of the main required properties. The new techniques provide a technological and economic advantage over traditional methods. The thermal and electrochemical process use thermal energy to remove material by melting or vaporizing the workpiece material. This includes electro discharge machining (EDM), plasma beam machining, laser beam and electron beam as well as ion beam machining. In electrode discharge, machining is sometimes called electrical erosion. [69, 70]

3.3. Electro Discharge Machining

Electrical discharge machining (EDM) is an electro thermal process that can erode any conductive workpiece by the formation of an electrical spark between an electrode and the workpiece. As a result, spark erosion, the shape of the electrode can be reproduced into the workpiece. The typical EDM machine consists of machine tool, EDM power supply, dielectric unit, and electrode servo control system as shown in Figure 3.2.

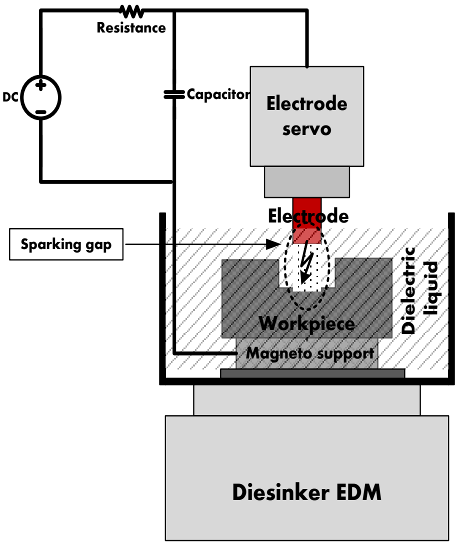

Figure 3.2 The basic concept of Diesinker EDM. Brown [71]

The electrode and workpiece immersed in a tank filled with a hydrocarbon dielectric (such as oil and kerosene) which can ionize in the presence of high electrical field. The frequencies of the sparks are in the range from 500 to 500,000 sparks per second and the material removal rate is in the range of fraction of one to around 3.9 (cm3/min). Since this is non-contact machining process, the hardness of the workpiece is no more a source of difficulty. The main EDM electrode materials include Tungsten, Tungsten carbide, Copper Tungsten, Graphite, Copper, brass, and zinc alloys. Ostwold [72].

The main disadvantages associated with Copper electrodes are the low thermal wear resistance and the material to machine or grind the burr formation. Tungsten due to the combination of its high density and melting point is the best choice if wear resistance is the main concern. Tungsten is seldom used as EDM electrode due to the low cutting speed, high and very low machinability. Copper-Tungsten on the other hand is incomparable for its high volume and corner wear resistance. The cost of

Copper-Tungsten electrode depends on Tungsten ration. Reducing Tungsten content would increase the corner wear, but enable smoother burning in addition to reducing the cost of the material. It is important to note that Copper-Tungsten typically cut only half as fast as a Copper.

3.3.1. Types of EDM

There are many types of machine using electrical discharges. These types include diesinker EDM, Electrical Discharge Grinding (EDG), multi-electrode and multi-lead EDM, wire-cut EDM (multiple-electrode and multiple-workpiece), micro-hole EDM drilling and Electrical Discharge Texturing (EDT).The electrical discharge grinder is different from a normal diesinker machine because the electrode remains stationary while the workpiece traverses under the rotating electrode.

In Multiple-electrode machining, multiple electrodes are used instead of a single electrode. When using the multiple-electrode technique, only one spark occurs at any moment and this can increases the spark Off-time and improve the debris removal where additional time is reserved. Since the next spark will occurs in area free from debris, the sparking efficiency will increases.

Wire cut EDM is used for contour cutting where a continuously moving wire travels along a path and cutting the workpiece with the discharge sparks between the wire and the electrical conductive workpiece. The tensioned wire is used when travelling from take-off to take-up spool while being guided to provide an accurate narrow slit. The horizontal movement of the worktable is numerically controlled to determine the path of the cut. Flushing nozzles should be as close as possible to avoid the wire breakage due to poor dielectric flushing. Deionized water exclusively used as a dielectric because of it is low viscosity. Sometimes ethylene glycol-based compounds and oils are used as dielectrics for wire cut EDM. Avallone [73].

Micro-hole EDM drilling can be used to drill a small hole. Pure Tungsten wire is the preferred electrode material for some users because of its exceptional wear resistance but also Tungsten carbide can be a good choice to form small holes in the 5-10 µm range. The electrode is typically rotated while cutting in order to promote flushing of residues. Grzesilk [74].

3.3.2. The Basic Working Principle Diesinker of EDM

Electro discharge machining is a machining process that can be used to machine any electrically conductive material by using controlled sparking pulses between the electrode and workpiece in the presence of dielectric liquid. The basic principle of EDM process can be described as shown in the schematic diagram of Figure 3.3. The tool electrode and the workpiece immersed in dielectric liquid that is mostly kerosene and oil and connected to the power supply that can generate waveforms pulses. The tool electrode must always be at distance from the workpiece, known as sparking gap. When the electrode is moved close to the workpiece very close to the closest points between them, the potential differences between the electrode and the workpiece will rise up to around 170 volt. This voltage is called open-circuit voltage. When applying waveform voltage at a distance equal to 0.025mm, the dielectric fluid will ionize and changes from insulator to conductor. Filming and Jamison [75, 76].

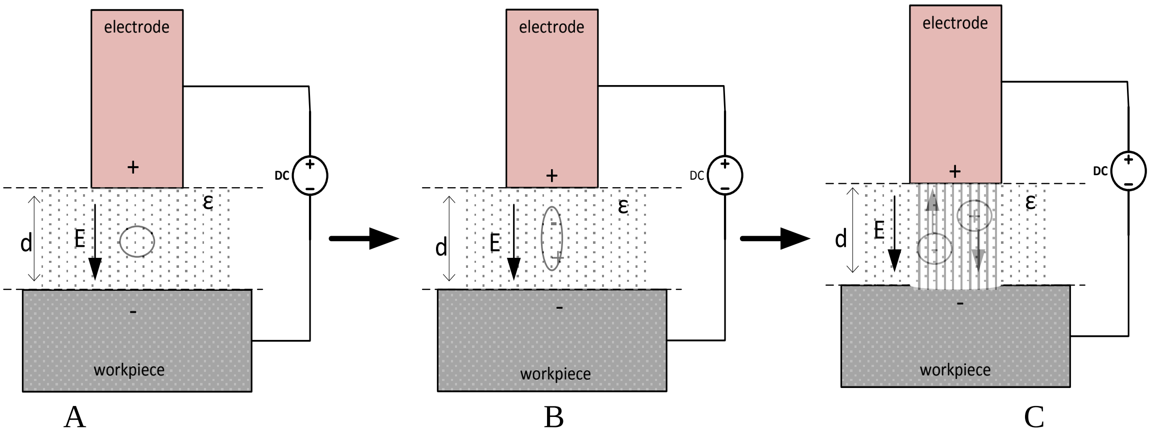

Figure 3.3 Schematic diagram showing the main steps of sparking including polarization and ionization. Jameson [76]

After ionization of the dielectric fluid, the electricity flow between the electrode and the workpiece will be in a waveform. Due to the thermal energy of the sparking, there will be gradual machining of the workpiece. Thus if we have a cylindrical tool electrode, the exact opposite shape of the electrode will be machined in the workpiece and finally the cylindrical hole will be produced on the workpiece. In similar manner, any shape can be machined by using EDM.

3.3.2.1. The Main Characteristic of EDM

Electrical discharge machining is used to machine any workpiece material regardless of its hardness. This characteristic is different from turning machining operation where the mechanical properties of workpiece, such as the strengths, ductility, brittleness, hardness are very important. Any material is possible to be machined using EDM if it is electrically conductive. The technique is not applicable in nonconductive material because it is not easy to supply free electrons or the movement of the free electron is very low.

The material removal rate in electrical discharge machining mainly depends on the thermal properties of the workpiece such as the specific heat capacity, the thermal conductivity as well as the melting temperature. Therefore, how much melting will occurs depend on these properties. The volumetric material removal rate on the other hand depends on the density of the workpiece material where higher density material show lower volume removal rate.

In Electro-discharge machining, electrode plate is a physical tool similar to that used in turning machining. This is different from other Un-conventional machining technique such as abrasive water jet machining where there is a water jet but no solid tool. Thus, the geometry to be machined on the workpiece is the negative image of the tool geometry.

The tool has to be electrically conductive. Otherwise, a higher voltage must be applied to pull out the electrons during the cold emission so one of the main constraints on the electrode material is that it should be highly conductive electrically.

On the other hand, tool wear does not depend on the mechanical properties such as stiffness, young modulus, hardness, and yield strength. The tool wear depends on the thermal properties and also the material removal rate.

Due to the intense heating by high-energy electrons, the local temperature rise of the tool electrode on workpiece will be very high. But that pulse On-time is in the range of microsecond to millisecond. Because of that, whatever heat is generated at the site of impact of the electron does not get enough time to diffuse in the workpiece and there is very low increase in the bulk temperature. Thus, in electrode discharge machining process because of very short pulse on time, the heat-affected zone is very limited. Typically, it is in the range of 2 to 4 µms of the spark crater and this constitutes a major advantage for EDM process. During EDM, the rapid heating and cooling rate can make local metrological changes on the surface. This surface hardening quite often is desirable. Brown and Jameson [71, 76].

3.3.2.2. Sparking

The application of high potential difference can develop an electric field between the electrode and the workpiece. The most important physical quantities that influence the spark initiation are the effective work function of the electrode surface, the local field strength, and the ionization energy of the liquid. The strength of this electric field depends on the discharge gap and the dielectric constant of the dielectric fluid (ε).

If the pulsed voltage applied between the electrode and workpiece exceed a certain barrier which related to the dielectric strength, the dielectric can lose its insulation ability and become electrically conductive. The electrical breakdown will occur only for a short time in a very small fraction of the dielectric liquid. The fluid will recover the previous conditions rapidly and resume its insulating function. This ability to recover from failure makes the dielectric fluids very useful in high frequency discharge application.

The tool and the workpiece, both, should be electrically conductive material, and they should have enough amounts of free electrons. When the electric filed is launched, the free electrons will be drifted because they will experience a strong electrostatic force. If the work function of tool material is less than the field strength, then this electrode will come out in large numbers due to the presence of electric field. This is called the cold mission of electrons. After the electrons have been emitted within this particular space between the tool and workpiece, then these electrons will be accelerated from the negative tool electrode toward the positive workpiece because there is an electric field.

The electrons will enter the dielectric liquid at various favourable sites from the electrode surface. Because the medium between the tool and the workpiece is filled with dielectric fluid; there will be collision of electrons with the dielectric molecules.

As collision occurs with the dielectric molecule, some of the electrons will be energetic enough to ionize the dielectric molecules. Once ionization of the dielectric molecules occurs, the accelerated ions will undergo collision with the dielectric molecules leading to generation of more ions and more electrons. If the electron is not sufficiently energetic, then it may lead to elastic or inelastic college. There will also be a secondary and tertiary electron collision.

The electrons are generated because all primary collision will again be accelerated and undergo new collision leading to huge number increase in the concentration of ions and electrons around the tool on the warped piece. After converting their energies with the molecules of the liquid, these electrons will form clusters that slowly drifted across the discharge gap. This leads to establishment of something called plasma channel between the tool and the workpiece. The high energetic electrons will cause some chemical changes due to ionization and the stream of electrons will gradually raise the local temperature of both the metal and the fluid in the close neighbourhood of the injection sites. Because of this, the low-density regions will form at the injection sites. Jameson [71].

When this plasma channel is established, there will be avalanche motion of electrons because the resistivity of plasma channel is very low. The avalanche discharge of plasma channel will be seen as a spark generally known as electrode discharge machining called spark erosion machining. During sparking, the surface of the discharge channel becomes unstable leading to the formation of a gaseous discharge channel, which is characterized by an emission of high intensity light and disintegration of molecular liquids. At the end of the discharge phase, the conductivity and the temperature of the discharge channel are reduced due to the recombination of charge carriers. According to Bartnikas [77], If an alternating voltage, V, is applied to C a current I is flowing which is given by;

$$I = C\frac{dV}{dt} + \frac{V}{R} \tag{3.1}$$

The first term is the dielectric displacement current and the second term is the conduction current. In vector notation the current density J, in SI units can be written in vector notation as shown in equation 3.2 where, first term represents the conduction current density component and the second term is the displacement current density component, $\vec{E}$ represents the electric field vector, ε_r is the relative permittivity, and ε_0 is the permittivity in a vacuum.

$$\vec{J} = \sigma\vec{E} + \varepsilon_r\varepsilon_0 \frac{\partial\vec{E}}{\partial t} \qquad (3.2)$$

The dielectric constant is related to the atomic or molecular structure of the liquid, and it indicates whether the atoms or molecules possess an electric dipole moment or not. The current density j for any medium except vacuum according to Vasili [78] is given by equation 3.3 where n_i is the ith type charges concentration, q_i is the charge, μ_i is the mobility of charge carriers.

$$j = n_i q_i \mu_i E \qquad (3.3)$$

The concentration of the charge carrier given by equation 3.4 where n the density of molecules is, v is the frequency of electron vibrations in the molecule (~1014 s^{-1}), W is the ionization energy, k is the Boltzmann constant, and T is the temperature.

$$n_i = (n.v \,/\, k_r)^{1/2}.e^{-W/2kT} \qquad (3.4)$$

The relation between polarization and relative permittivity is given by Clausius-Mossotti in equation 3.5 where, T is the absolute temperature, α is the electronic polarization, and μ is the dipole moment, and is the number density.

$$\frac{\varepsilon_r - 1}{\varepsilon_r + 1} = \frac{n}{3\varepsilon_0}\left(\alpha + \frac{\mu^2}{3T}\right) \qquad (3.5)$$

This equation shows that the ionized liquids exhibit a wide range of dielectric constants depending mainly on the dipole moment.

Table 3.1 Examples of dielectric constants, polarizability, and dipole moments for selected dielectric liquid. Bartnikas [77].

Liquid	T(k)	ε_r	$\alpha *10^{24}$ (cm^3)	$\mu *10^{30}$ (cm)
Transformer oil	293.00	2.20	-	0.00
Methane	100.00	1.70	2.60	0.00
Benzene	293.00	2.28	10.30	0.00
Methanol	298.00	32.63	3.90	1.70
Ethanol	298.00	24.30	5.40	1.70
Ammonia	239.60	22.40	2.40	1.44
Helium	4.20	1.05	0.22	0.00
Nitrogen	77.00	-	1.76	0.00
Water	298.00	78.50	1.50	1.84

3.3.2.3. The electric pulse generator

The power supply can generate and supply the power into the dielectric fluid in the discharge gap. The power supply contains current and potential difference indicator to monitor the sparking conditions. The reading of the voltmeter before sparking indicates the potential difference between the electrode and workpiece, which is called the open circuit voltage and the reading during machining operation is called working voltage. The power supply also includes servo-system that can adjust the motion and position of the electrode relative to the workpiece. Jamiuson [76]. There are different types of EDM power generators that can store energy in an intermediate storage (capacitance) and discharge it as an electrical energy into a load in a single short pulse. These include the RC-type generator, rotary impulse trigger generator, electronic pulse generator and hybrid EDM generator. The theory of RC-type generator is a very simple and can be explained by the schematics diagram shown below. The working principle of this pulse generator depends on storing of D-C energy in a capacitor (charging face) and the transferring of this energy into the discharge gap as shown in Figure 3.4. A. Lissaman [70]

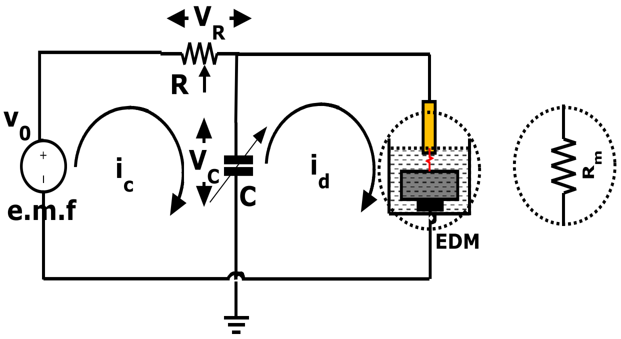

Figure 3.4 an electric circuit represent the R-C type pulse generator. Jameson [76]

During charging, the energy transfer from the source (e.m.f) and stored into the capacitor where the charging current gradually grows in the capacitor as;

$$i_C = C\,\frac{dV}{dt} \tag{3.6}$$

According to Kirchhoff's law; $V_R + V_C = V_0$ and If we take $V_R = iR$ and the charging current as $i_C = \frac{V_O - V_C}{R}$, then the charging equation during charging time t_C in an integral form can be written as follow;

$$\int_o^{V_C^*} \frac{dV}{[V_o - V\ ]} = \frac{-1}{RC}\int_o^{t_c} dt \tag{3.7}$$

By Integrating of this equation will give the following expression for the potential difference of capacitor during charging V_C and the charging current i_C .

$$V_C^* = V_o[1 - e^{-\frac{t_c}{RC}}] \tag{3.8}$$

$$i_C^* = \frac{V_O}{R}e^{-\frac{t_c}{RC}} = i_m e^{-\frac{t_c}{RC}} \tag{3.9}$$

Referring to Figure 3.5, after the capacitance is fully charged to V_c^* , the charging current will drop to zero and the discharge cycle will start. At the beginning of discharge cycle, the capacitor is at the value V_c^* . Taking the discharging current as i_d and the matching resistance (dielectric, tool electrode and the workpiece) as R_m , then the discharge current through the machine is $i_d = \frac{V_c}{R_m}$ and through the capacitor the discharge current is;

$$i_d = C\,\frac{dV_c}{dt}\,. \tag{3.10}$$

Integrating $$\int_{V_c^*}^{V_d} \frac{dV_c}{V_c} = -\frac{1}{R_m C}\int_0^{t_d} dt \tag{3.11}$$

$$i_d = \frac{V_d}{R_m} = \frac{V_c^*}{R_m}.e^{-\frac{t}{R_m C}} \tag{3.12}$$

This current is the EDM current and can be controlled through the capacitor C which is related to the pulse generator and R_m which is related to the dielectric properties. If the electrode material is not highly conductive then, the electrode resistance will be added to this R_m. The Spark energy of the single pulse can be determined as follow;

$$E_{discharge} = \int_0^{t_d} i_d^2 R_m dt = \int_0^{t_d} \frac{V_c^2}{R_m^2} R_m e^{\frac{-2t}{R_M C}} dt \tag{3.13}$$

The input pulse signal, the V_C voltage pulse shape and the discharge current are shown in Figure 3.5 as a function of time. The capacitor gradually charged from the e.m.f until it reaches the maximum value V_C*.

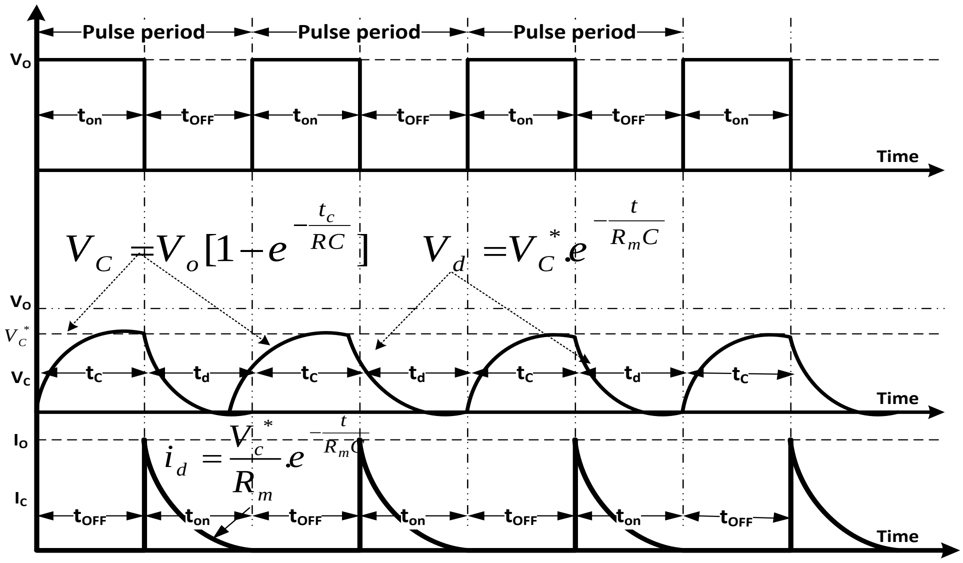

Figure 3.5 Applied voltage V_O, charging voltages V_C, and discharge current I_C of R-C type pulse generator. Jameson [76]

During charging, the discharge current is zero. After fully charged, the capacitance will discharge this energy in the load resistance of the machine (Rm) taking the discharge time as equal to t_d. At the beginning the discharge current is the maximum value i_c^* and gradually decreases and drop to zero at the end of t_d. The charging will remain zero during the next charging time t_c and jump again to maximum when the discharge cycle starts again. According to the second law of thermodynamics, the energy transfer cannot reach hundred percent and that is why the maximum potential difference between the electrode and the workpiece during discharge V_C^* which is called the working voltage is less than V_0 which is called the open circuit voltage. The frequency f of this RC type generator at the maximum output power gain when $V_c^* = 0.716V_0$ can be controlled by R_c and C as shown in the following expressions. Saha [79].

$$f = \frac{1}{[t_c + t_d]} = \frac{1}{[R_C C ln(1 - \frac{V_c^*}{V_c}) + R_m C ln(\frac{V_d}{V_c^*})]} \tag{3.14}$$

By integrating equation 3.14 with respect to V_C we will get

$$E_{discharge} = \frac{1}{2} C V_c^{*2} \tag{3.15}$$

During machining, the average machining amperes is determined from the ratio of spark- ON to -Off-time by using the following equation.

$$I_a = I_0 (\frac{t_{on}}{t_{on} + t_{off}}) \tag{3.16}$$

Where: I_a is the average amperes, I_0 is the peak amperes, t_{on} is the Pulse On-time and t_{off} is the Pulse Off-time.

In transistor pulse generator; there is an electromotive force source which is supplied by a steady voltage V_o. So if we apply the driving pulse to the base of this transistor, then the transistor will allow the steady voltage to come out in the shape of the driving pulse. Here, the pulse is used to trigger the applied voltage given in an EDM pulse form like that shown in Figure 3.5. The main advantage of this generator is the signal amplification and because the output signal is driven by the input signal at the base of the transistor, it's also possible to control the pulse On-time and the pulse off-time.

Hybrid electronic pulse generator is different from the standard electronic pulse generator because it has combined the standard RC-type pulse generator. This will make it easy not only to control the peak current, pulse On-time and pulse Off-time but also by proper selection of R, C and the switching circuit we can control also the pulse shape to get trapezoid waveform which is much better than the square waveform. For more types of pulse generator, Rodulf F. Graf [80].

3.3.2.4. Dielectric Fluid

Referring to Figure 3.2 the tool electrode and the workpiece are both immersed in dielectric fluid. If a potential difference is applied between the tools and the workpiece, there will be a spark and machining via spark erosion. The material removal occurs mainly due to thermal evaporation and melting. One of the main role of dielectric is to prevent oxidation which can led to flaming. The oxidation is undesirable because oxidation would lead to oxide burning which reduces the surface electrical conductivity and this will affect the machining process.

Thus, oxidation has to be prevented and this is the first role of dielectric fluid. The dielectric should have two conflict electrical properties; it should have strong dielectric resistance so that when a potential difference is applied, it should not breakdown very easily. But at the same time the dielectric should ionize to get a plasma channel. Because the spark is violence from the thermal point of view, the dielectric should not breakdown it should be thermally resistant. It should not dissociate due to high temperature of the spark.

The commonly used dielectric fluids in diesinker EDM are the hydrocarbon fluids such as kerosene, lamp oil or other commercial oil such as Rustlick EDM-30. These types of dielectric are easy to find and relatively low in cost. Depending on the type of dielectric used, the dielectric constant becomes a parameter. Tap water cannot be used as dielectric liquid because it will experience some contamination like salt and it will ionize easily because it does not have enough dielectric constant or resistance and the process will breakdown.

The dielectric fluid must be forced (flushed) continuously using so that at all the time the dielectric between the electrode and the workpiece is replenished. Dielectric flushing can be applied in different way as shown if Figure 3.6.

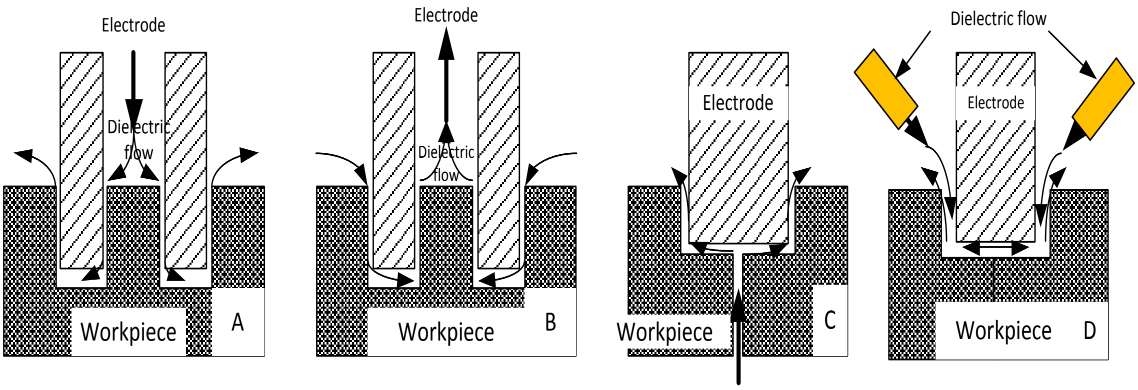

Figure 3.6 Examples of dielectric flushed through electrode (A), Suction flushes through electrode (B), Pressure flushes through workpiece (C), External suction flush (D). Brown [71] and Filming [75]

Thus, external flashing through the sparking is also an important parameter in electro-discharge machining. As a conclusion, EDM dielectric fluids should provide:

1. A known electrical barrier between the electrode and workpiece so that at the beginning of pulse on time, the dielectric fluid remain insulator until the voltage break the dielectric strengths to make the fluid change into an electrical conductor. The point when the fluid changes from an insulator into a conductor is called the ionization point.
2. A high cooling rate to dissipate the heat generated by the spark within the electrode and workpiece material. The dielectric fluid helps in carrying away this heat from the electrode and workpiece surface. Sometimes cooling the dielectric fluid is recommended.
3. Cooling of the vaporized material and debris removal from the sparking gap. When spark occurs, the vaporized material from the electrode and workpiece in the sparking-gap area is cooled by the dielectric fluid and solidifies to form the debris. EDM debris must be removed from the sparking area at the same rate as they are generated to prevent any accumulation of chips in the sparking gap.
4. Controlling the discharge gap conditions by shielding the sparking gap and preventing inflammation or oxidation.

the electric energy per unit volume of a dielectric material in static dielectric is given by Frohlich [81] as follow;

$$E_S = \varepsilon_S \frac{E^2}{8\pi} \tag{3.17}$$

Where; E is an electric field and ε_s is the static dielectric constant. Equation 3.17 suggests that the dielectric constant is static and the electric field is constant. Assuming that ε_s depends on temperature.

3.3.2.5. Dielectric Liquid in Electric Field

The basic principle of electromagnetic theory gives the influx of energy into the dielectric material in an electric field if the displacement D is increased by the small amount dD as follow $\frac{1}{4p} EdD$. By using the first and second law of thermodynamic with the help of Helmholtz free energy, the properties of dielectric in static electric field can be explained as shown in equation 3.18. Raju [82].

$$dQ = dU + \frac{1}{4p} EdD \tag{3.18}$$

$$dS = \frac{dQ}{T} \tag{3.19}$$

$$F = U - TS \tag{3.20}$$

Assuming that ε depends on temperature but is independent on electric field.

$$dD = d(\varepsilon E) = \varepsilon dE + E \frac{\partial e}{\partial T} dT \tag{3.21}$$

$$dQ = dU + \frac{1}{4\pi} E(\varepsilon dE + E \frac{\partial e}{\partial T} dT) \tag{3.22}$$

Taking T and E_2 as independent variables, the change in the infinitesimal energy and entropy can be written as follow;

$$dU = \frac{\partial U}{\partial T} dT + \partial \frac{\partial U}{\partial (E^2)} d(E^2) \tag{3.23}$$

$$dS = \frac{\partial S}{\partial T}dT + \partial \frac{\partial S}{\partial (E^2)}d(E^2) \qquad (3.24)$$

Taking $dS = A(T,E^2) + B(T,E^2)$ (3.25)

Where; $\frac{\partial B}{\partial T} = \frac{\partial A}{\partial (E^2)}$ (3.26)

$$dS = \frac{dQ}{T} = \frac{1}{T}[\{ \frac{\partial U}{\partial T}dT + \partial \frac{\partial U}{\partial (E^2)}d(E^2)\} - \{ \frac{\varepsilon}{8\pi}d(E^2) + E^2 \frac{\partial \varepsilon}{\partial T}dT\}] \qquad (3.27)$$

$$dS = \frac{dQ}{T} = \frac{1}{T}(\frac{\partial U}{\partial T} - E^2 \frac{\partial \varepsilon}{\partial T})dT + (\partial \frac{\partial U}{\partial (E^2)} - \frac{\varepsilon}{8\pi})d(E^2) \qquad (3.28)$$

$$\frac{\partial}{\partial (E^2)}\{ \frac{1}{T}(\frac{\partial U}{\partial T} - E^2 \frac{\partial e}{\partial T})\} = \frac{\partial}{\partial T}\{ \frac{1}{T}(\partial \frac{\partial U}{\partial (E^2)} - \frac{\varepsilon}{8\pi})\} \qquad (3.29)$$

Differentiation and integrating with respect to E2 we can find that;

$$U = U_0(T) + (\varepsilon_S + T \frac{\partial e_S}{\partial T}) \frac{E^2}{8\pi} \qquad (3.30)$$

$$S = S_0(T) + \frac{\partial \varepsilon_s}{\partial T} \frac{E^2}{8\pi} \qquad (3.31)$$

$$F = F_0(T) + \frac{\varepsilon_S E^2}{8\pi} \qquad (3.32)$$

Where; $U_0(T)$, $S_0(T)$ and $F_0(T)$ are the internal energy, the entropy and the free energy in the absence of a field respectively. The free energy shows that the amount of electric energy available in an isothermal reversible process is equal to $\frac{\varepsilon_S E^2}{8\pi}$. The increase of entropy which is the measure of the molecular disorder due to the presence of electric field depends on $\frac{\partial \varepsilon_s}{\partial T}$. If this quantity is negative, then the entropy is decreased. If the external field creates order in dipolar dielectric liquids, then ε_s will decrease with increasing T. the change in the internal energy due to the presence of electric field equal to $\frac{\varepsilon_S E^2}{8\pi}$ for substance that have dielectric independence on temperature such as dilute dipolar gases. The dependence of ε_s on temperature will increase the internal energy due to the presence of the external field by $(T\frac{\partial \varepsilon_S}{\partial T})\frac{E^2}{8\pi}$. For time-dependent electric field such as that produced by high-frequency pulse generator. Considering an isothermal case, then the internal energy U of the dielectric cannot change because the temperature is kept constant. Thus the first law of thermodynamic can be written in an integral form as follow;

$$\int dQ = -\frac{1}{4\pi}\int EdD = -\frac{1}{4\pi}\int_0^{2p/w} E\,\partial\frac{\partial D}{\partial t}dt \tag{3.33}$$

By integrating periodical electric field, the rate of energy loss L from the electric field is proportional to the frequency ω and can be given by the following expression;

$$L = \frac{\varepsilon E_0^2}{8\pi}\omega \tag{3.34}$$

Equation 3.34 shows that the energy stored in the dielectric fluid at the presence of time varying electric field is merely depends on the strength of the electric field but also affected by the dielectric constant and the frequency of the field.

3.3.2.6. The Material Removal Mechanism

The EDM process removes material by thermal energy. Once the spark is launched, the workpiece surface continuously impinged by high-energy ions or electron depending on the workpiece polarity. The accelerated ions and electrons having very high kinetic- energy and that kinetic energy will be converted into thermal energy leading to a high temperature on the warped piece. This high temperature on the workpiece cause a localized melting and evaporation and we get material removal rate. When sparking electricity is turned OFF, the vapour cloud is cooled to form EDM debris. This process is repeated thousands of times every second in various points on the workpiece and therefore, the electrode gradually goes down under the servo system control. Typical removal rate ranges from 0.1 to 400 mm^3/min. The material removal rate not only depends on current and melting point of the workpiece, but also the other workpiece properties, the tool electrode material, pulse energy, and the dielectric. Jameson [76].

1. Beside the melting temperature, the workpiece properties that can affect the MRR include; the thermal properties of the workpiece because when the spark strike the workpiece, it is generate thermal energy. Therefore, how much localized melting that will occur depends on what are the thermal properties of the workpiece such as specific heat capacity and the thermal conductivity. The density also cam affect the machining rate. The mechanical properties of the workpiece material are much more important in the case of conventional machining.

2. The tool electrode properties have a big impact on material removal rate by virtue of the material type, electrode shape and electrode size, electrical and thermal conductivity.

3. Pulse energy conditions such as pulse duration (including On-time , Off-time and duty factor), peak current, potential difference and pulse signal shape, all can affect the machining rate

4. The dielectric is the machining medium where the ions generated can affect the MRR from different point of view. First the ease and the amount of ion can be generated which depends on the dielectric strength as mentioned before. The dielectric also plays an important role, the cooling rate of the vaporized material which is related to the physical properties of the dielectric such as the heat capacity, thermal conductivity and viscosity. The rate of debris removal depends on the dielectric velocity, pressure, and plashing mode.

3.3.3. EDM Tool Electrode

Absolutely, the tool materials will affect the machining process, surface tolerance, and surface roughness, therefore the properties of tool material should be taken into consideration. As an example if a rectangular hole is desired but the electrode experiences high wear then, finally the result may be an elliptical cross-section hole due to the corner wear. Therefore, the first constraint towards the electrode material selection is that the electrode should not experience high wear when it is impinged by the high-energy ions from the plasma.

During discharge, there will be a localized temperature rise that cannot be avoided but in some way, this temperature rise should be reduced to the level that is manageable. This can be achieved either by manipulating machining variable setting or by properly choosing the tool material. The selection of the tool material properties depends on other constraints such that during the temperature rise there should not be any melting or evaporation. The selection of electrode material in diesinker EDM should be the key decision before any experimental plan. Kern [1] and Jameson [76].

Depending on the constraint mentioned before, the electrode materials should provide the following properties.

1. The electrode should not experience high wear when it is bombarded by the high-energy ions from the plasma.
2. During machining, the temperature rise should not result in any melting or evaporation
3. The electrode material should have a high electrical conductivity, because higher electrical conductivity (lower resistivity) can improve the cutting efficiency.
4. Since EDM is a thermal process, the selection of the tool material properties should take into account the melting point of the electrode material. The electrode material should have a high melting point for better electrode wear ratio.
5. The electrode should also have high thermal conductivity because if it is having a high thermal conductivity for the same heating input the heat cannot be carried

away from the heated zone. Thus, if the thermal conductivity is high then the local temperature rise will be less and this is good for the electrode.

6. The electrode material also should have an ability to be easily machined. The main factors that can increase the difficulty of electrodes manufacturing include machinability, stability, burr formation, and burr removal.
7. The electrode material should also have high density because for the higher density the dimensional loss will be less. If the density is a higher for the same weight-loss it is dimensional loss will be less and this is an important property for good surface tolerance.
8. The electrode should be cheap because EDM required many tools.
9. The mechanical properties of electrode materials such as tensile strength and hardness also can affect the fabrication of the electrode and the electrode performance during machining.
10. Sparking process is usually occurs with a remarkable force and energy which can exert a considerable stress on the electrode material at high temperature. The response of electrode material to these attacks is a significant factor spatially for powder metallurgy electrode.

No single electrode material can offers all the requirements highlighted in section 3.3.3. The materials used as an electrode for die-sinking machines can be divided into metallic electrode and Graphite electrodes. Some of the metallic electrodes used in Sinker EDM applications include brass, Copper, Tungsten, Copper –Tungsten, silver, silver-Tungsten, Tungsten carbide as well as Titanium alloy.

Metallic electrode is important in machining when a small hole and sharp corner are required. Electrical conductivity and mechanical integrity are the advantages of metallic electrode materials. The main disadvantages of metallic electrodes are difficulty in fabrication and low cutting speeds as shown in Table 3.2 assuming that Copper on Steel is 100%. Kern [1].

Table 3.2 Cutting speeds for various electrodes on steel for a given surface finish based on assumption that Copper on Steel is 100%. Kern [1]

Copper-Tungsten on Carbide	25%
Copper-Tungsten on Steel	50%
Copper on Steel	100%
Graphite Positive on Steel	200%
Graphite Negative on Steel	400%

3.3.3.1. Brass

Brass is inexpensive and easy to machine but rarely used as an electrode material in modern sinker EDMs, due to its high wear rate. Brass shows a good wear ratio when machining steel and a very high wear ratio when machining Tungsten carbide. It is not recommended for resistance-capacitance pulse generator (R-C-Type) but if wear is not a main concern, brass can be used, since it shows a higher degree of stiffness and is easier to machine. Brass, however, is one of the most commonly used electrode materials for EDM super drill.

3.3.3.2. Copper

Copper is the best metallic electrode material for the transistor pulse generator. This is due to its structural integrity and highly resistant to the direct current (DC) arcing. Copper can produce very fine surface finishes and is preferred as material for small hole applications required in aerospace alloys as well as carbide. The main disadvantages of Copper electrodes are the slow machining rate in comparing with Graphite electrodes, difficult to machine or grind and Copper is very difficult material to de-burr. Copper regularly is used for R-C-type pulse generator.

3.3.3.3. Copper-Tungsten

Copper-Tungsten is a powder metallurgy electrode material made by sintering of up to 70% Tungsten ratio followed by infiltration with Copper. It combines the high electrical and thermal conductivity of Copper with the high thermal wear resistance of Tungsten. Due to this, Copper-Tungsten has very good wear characteristics and are-used as the main electrode for machining Tungsten carbide. Generally, a higher Tungsten content is better to increase the wear resistance but at the expense of lower cutting stability and higher cost.

3.3.3.4. Graphite

Graphite electrodes are manufactured from compaction of powder/binder mixture followed by a series of thermal treatments that convert the carbon to Graphite. The density of this material depends on powder particle size used and the strategy of compaction. Graphite is available in grain sizes ranging from 100 µms for a coarse grade, down to one µm for fine-grade material. Graphite sublimes at a temperature that is approximately equal to the melting temperature of Tungsten. Graphite is used as the main diesinker EDM electrode due to its high machining rate and the ease of manufacturing over metallic electrode materials.

3.3.4. The Electrode Wear

Electrode wear occurs as a result of ion bombardments, where the negative electrode is bombarded by positive ions and the positive electrode is bombarded by negative ions. The accelerated ions will lose its kinetic energy ($1/2*mv^2$) as heat when it is crashed onto the surface of the electrode. The heat generated due to this bombardment is enough to vaporize the electrode material and a small amount of electrode material is removed.

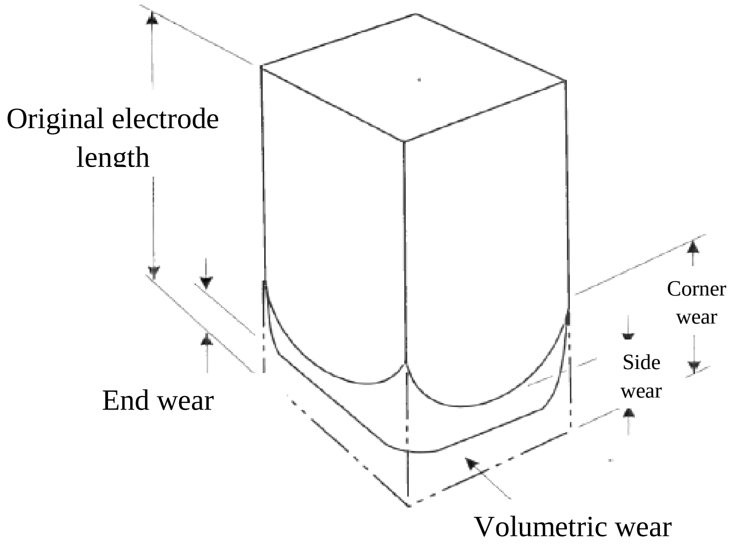

Figure 3.7 The different kinds of electrode wear. Jameson [76]

The ion mass and volume is much bigger than the electron but the electron velocity is much higher than that of the positive ions. Thus, removal of material from the electrode surface depends on the electrode polarity. The main types of the electrode wear are the corner wear, end wear, side wear, and volumetric wear. Figure

3.7 show the different kinds of electrode wear. The number of sparks originating from a point on the electrode surface determines electrode wear. The corner of the electrode suffer more than the front because it was exposed to more attacks from the front, sides and edges, due to that more material is removed from the corner than the flat surface leading to higher corner wear. Jameson [76].

3.3.5. Modeling of Material Removal Rate

Developing a model can give better understanding about what can happen if the process parameters changed before going onto the experiment details. Suppose that a single spark can create a single hemispherical crater on the workpiece as shown Figure 3.8. If the radius of this hemispherical is r, then the volume of this hemispherical crater is $V_{hs} = \frac{2}{3} pr^3$. The size of this crater in some manner can relate to the spark energy $E_S = VIt_{on}$ where; t_{on} is the pulse on time. Part of this energy that is converted to heat on the workpiece is proportional to the sparking energy and can be given as $E_w \alpha E_s$. The rest of this energy dissipated in the discharge medium as heating of the dielectric medium, electromagnetic energy, and sound energy and heating of the electrode.

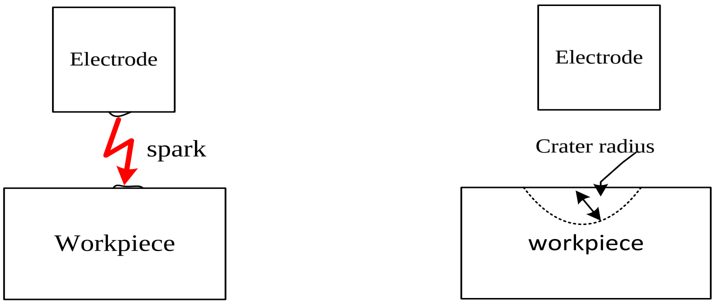

Figure 3.8 single crater generated by single sparking. Jameson [76]

Thus, the working energy is $E_w = kE_s$ where, k is the proportionality constant. The volume removal of material from the workpiece by a single spark is proportional to the sparking in energy. Then we can write the material removal rate as the volume of the crater created by a singular spark divided by the total time of the spark, which is the pulse duration, saha [79].

$$MRR = \frac{\beta E_w}{[t_{on} + t_{off}]} = \frac{\beta' V I t_{on}}{[t_{on} + t_{off}]} = \frac{\beta' V I}{[1 + (\frac{t_{off}}{t_{on}})]} \tag{3.35}$$

Where β and β' are the proportional constants. Equation 3.35 indicates that, higher material removal rate which is one of the main goals of EDM improvement can be achieved with high current I , high potential difference V and also by increasing the Pulse On-time t_{on} and decreasing the Pulse Off-time t_{off} .

The volumetric material removal rate in (mm3/min) was described in El. Hofy [69] as a function of melting point of the workpiece material and the discharge current as follow;

$$MRR = (4x10^4).i.T_w^{1.23} \tag{3.36}$$

Where, i is the discharge current and T_w is the melting point of the workpiece material (°C). Another model is established by Rahman [83] to give the relations between the different EDM process parameters and the MRR using is the response surface methodology (SRM).

$$Y = C_0 + \sum_{i=1}^{n} C_i x^2 + \sum_{i=1}^{n} C_{ii} X_i^2 + \sum_{i=1}^{n-1} \sum_{j=1}^{n} C_{ij} X_{ij} \tag{3.37}$$

Where, Y is the response (MRR), n in the number of variables, X is the EDM process variables, i & j are levels of nth variables, and the terms $C_{0,} C_i , C_{ii}$ and C_{ij} are the second order regression coefficients. The application of this model shows that the materials removal rate is given as follow;

$$\begin{aligned} MRR = {} & 0.901 + 0.87 I_P + 0.41 t_{on} - 0.076 t_{off} + 0.24 I_P^2 - \\ & 0.24 t_{on}^2 - 0.040 t_{off}^2 + 0.23 I_P t_{on} - 0.025 I_P t_{off} - 0.05 t_{on} t_{off} \end{aligned} \tag{3.38}$$

Where I_P is the peak current, t_{on} is the pulse On-time and t_{off} is the pulse off-time.

3.3.6. Modeling of Surface Roughness

Let us assume that the sparking the maximum surface roughness R_a is equal to the radius of the hemispherical crater. Then the surface roughness is equal to

$$r = R_a = [\frac{3}{2}V_s]^{1/3} = [\frac{3}{2}bE_s]^{1/3} = [\frac{3}{2}bVIt_{on}]^{1/3} \tag{3.39}$$

This equation indicates that, surface roughness does not depend on pulse Off-time t_{off} . In order to reduce surface roughness, the potential difference V , the peak current I , and Pulse On-time t_{on} must be decreases. By contrast, reducing any of the three terms will also reduce the material removal rate which is undesirable. Referring to equations 40 and 44, reducing the surface roughness without redusing the material removal rate can be achieved by reducing t_{on} and t_{off} simultaneously. However, there is a limit to reducing t_{off} because if it is reduced too much, then there will be unstable sparking, Saha [79].

3.4. Design of Experiment (DOE)

3.4.1. Introduction

Within the 1970s, Dr. Taguchi proposed a new theory of quality loss function, which state that in any system, a departure from nominal was pricey and that it is possible to optimize designs if the noise within the system in which the product would operate is taken into cognisance during the stage of the product design. Taguchi compiled methods to support his theory, which are today called the “Taguchi method”, named after him. The method is also sometimes called robust design or quality engineering Roy[84]. The Taguchi’s method is a statistical approach to experimental design system, which employs about 18 standard orthogonal arrays to layout experimental designs. An orthogonal array has been defined in El-Hayk [85] as a fractional factorial experimental matrix that is vertical and balanced. Taguchi advanced an excellent philosophy for quality control in the manufacturing industry. The philosophy of Taguchi technique depends on three simple fundamental concepts. Roy [86].

1. The quality should be designed into the product and not inspected into it.
2. Quality is best achieved by minimizing the deviation from a target.
3. The cost of quality should be measured as a function of deviation from the standard and the losses should be measured.

The experimental data of Taguchi method are analysed to achieve one or more of the following three objectives:

1. To establish the best or the optimum condition for a product or a process
2. To estimate the contribution of individual factors
3. To estimate the response under the optimum conditions

In Figure 3.9 (A), the average value of the parameter deviates from the target value; the range of value (variation) is also excessive. Figure 1.9 (B) shows the average on target but the variation is still excessive. Figure 3.9 (C) illustrates the desired characteristic- on target and with narrow variation.

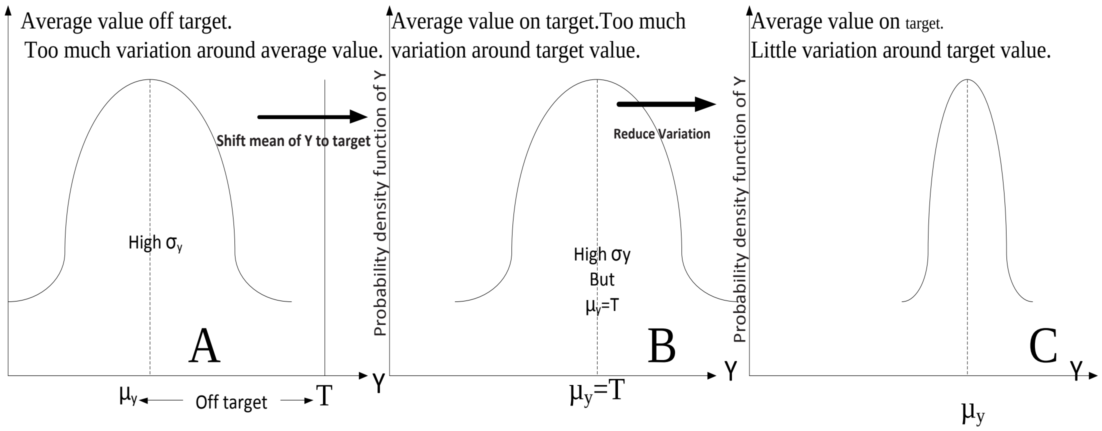

Figure 3.9 Typical quality distributions showing the variation from targeted value. Roy [86]

In Taguchi method, the quality loss function is a basic starting point and given as follow

$$L = kE(Y - T)^2 = k(m_y - T)^2 + ks_y^2 \tag{3.40}$$

Where; L is quality loss, k is quality loss coefficient, E is the expected value, and T is target value of Y. , which is the mean value of performance level Y, and is the variance of performance level Y.

3.4.2. Taguchi Orthogonal Array

There is the need to enhance the quality of products and processes if their design is dependent on many factors. This is what the Taguchi method is designed and aims to achieve. For experimental plans in engineering that involve many factors, the number of possible combinations is too large. Many methods meant to reduce the number of test combinations have been established. Amongst such methods is the partial factorial experimental design. Taguchi made a construct of special set of general designs, consisting of orthogonal arrays for factorial experiments which could be employed in many applications. The use of these arrays helps determine the least number of experiments needed for a given set of factors. The orthogonal arrays (OAs) provide a technique for fractional factorial experiments which satisfy a number of situations. When a fixed number of levels for all factors are involved and the interactions are unimportant, standard OAs will satisfy most experimental design needs. When mixed levels and interactions are present, a modification of the OAs is necessary. Roy [86]. Taguchi experimental set up are represented by 18 standard orthogonal arrays. These orthogonal arrays represent selected experiments in balanced (fractional factorial) from the full factorial experimental design as shown in Table 3.3. The design should satisfy some objectives.

- Known the factors that can affect the quality of the product are important.
- The number of trials must be determined.
- The conditions for each trial must be specified.

The proper selection of the suitable orthogonal array depends on the previous points.

The procedure of Taguchi experimental design follows the following three-step:

- Find out the total degree of freedom (DOF).
- Selection of suitable orthogonal array
- The number of runs in the orthogonal array should be ≥ total DOF.
- Placing factors in the appropriate columns
- Assign interactions according to the linear graph and interaction Table.

Table 3.3 L8 Taguchi orthogonal array selected from 27 experiments. Roy [86]

FULL FACTORIAL EXPERIMENT				A1				A2			
				B1		B2		B1		B2	
				C1	C2	C1	C2	C1	C2	C1	C2
D1	E1	F1	G1	T-1							
			G2								
		F2	G1								
			G2				T-3				
	E2	F1	G1								
			G2						T-5		
		F2	G1							T-7	
			G2								
D2	E1	F1	G1								
			G2							T-8	
		F2	G1						T-6		
			G2								
	E2	F1	G1				T-4				
			G2								
		F2	G1								
			G2	T-2							

Table 3.4 Trial runs and conditions of L8 Taguchi orthogonal array with seven variables at two levels. Roy [86]

	1	2	3	4	5	6	7
	A	B	C	D	E	F	G
T-1	1	1	1	1	1	1	1
T-2	1	1	1	2	2	2	2
T-3	1	2	2	1	1	2	2
T-4	1	2	2	2	2	1	1
T-5	2	1	2	1	2	1	2
T-6	2	1	2	2	1	2	1
T-7	2	2	1	1	2	2	1
T-8	2	2	1	2	1	1	2

Table 3.5 Compression of full factorial and Taguchi design in terms of number of runs. Roy [86]

Factors	Levels	Total Number Of Experiment	
		Factorial	Taguchi
2	2	4 (2^2)	4
3	2	8 (2^3)	4
4	2	16 (2^4)	8
7	2	128 (2^7)	8
15	2	32,768 (2^{15})	16
4	3	81 (3^4)	9

3.4.3. Taguchi Experiment Data Analysis

Usually, Taguchi orthogonal array is only a sample of the full experiment. The implication of this is that in analyzing the partial experiment, it is important to analyse the degree of confidence that can be placed in the results. The technique determines the variance of the data from the target. The data analysis requires three very important statistical tools.

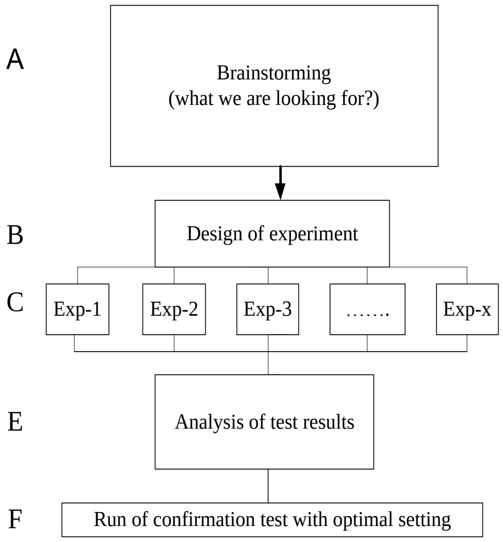

Figure 3.10 Taguchi experiments flow diagram. Roy [86]

3.4.3.1. *Analysis of Variance (ANOVA)*

Computation of the degree of freedom is important in order to carry out analysis of the experimental data. The same goes for the the sums of squares and the mean squares. If the experimental variables are *A, B, C…*etc. and the number of levels for each variable is n_A, n_B, n_C…etc respectively. Then, the degree of freedom for factor $A= (n_A - 1)$, for factor B= $(n_B - 1)$... etc.

The degree of freedom of interaction AB= (nA - 1) (nB - 1). The first step of ANOVA is the calculation of the sum of squares using equations 45 where; k is the levels, N is the total number of runs, n is the number of replication, and yij are the individual observations.

$$SS = \frac{k}{N * n}\sum_{i=1}^{k} T^2{}_i - \frac{T_t^2}{N * n} \qquad (3.41)$$

Therefore, the total percentage contribution of all variable is given by the following equation. Where SS_t is the total sum of square

$$SS_T = \sum_{J=1}^{N} \sum_{i=1}^{n} y^2{}_{ji} - \frac{T_t^2}{N * n} \tag{3.42}$$

$$\frac{SS_A}{SS_T} + \frac{SS_B}{SS_T} + \frac{SS_C}{SS_T} + ... + \frac{SS_{error}}{SS_T} = 100\% \tag{3.43}$$

3.4.3.2. Main-Effects and Interaction Chart

The chart of average responses versus the factor levels is called the main-effects chart. Plots of main-effect charts in Taguchi experimental data analysis are the same as in classical experimental data Analysis.

3.4.3.3. Optimization

Optimization in the Taguchi experiment requires determination of the combination of factor level that can give the optimal response. To do this, it is necessary to analyze the experimental results using standard analysis from the mean average of results or by using the signal to noise ratio (S/N). The conversion of a set of results into S/N (single number) required first to calculate the mean square deviation (MSD) from the target of the quality characteristic and then use it to calculate the S/N ratio by the following equation. El. Haik [85].

$$S / N = -10log_{10}(MSD) \tag{3.44}$$

The S/N ratio provides guidance for levels optimization base on the least variation from the target and from the average value closest to the target value. MSD have different definition depending on the quality characteristic considered. Nominal is the best quality characteristic for a set of observations with targeted value $\overline{y}$ is given as

$$MSD = \frac{1}{n-1} \sum_{i=1}^{n} (y_i - \overline{y}) \tag{3.45}$$

For smaller is better, the MSD from the target value 0 is defined as;

$$MSD = \frac{1}{n}\sum_{i=1}^{n} y_i^2 \tag{3.46}$$

For larger is better it is given as;

$$MSD = \frac{1}{n}\sum_{i=1}^{n} \frac{1}{y_i^2} \tag{3.47}$$

3.4.3.4. Prediction and Confirmation Test

Prediction of the results at optimal variable setting to verify the improvements of the performance characteristic are very important. The predicted value of responses at optimal setting Y_p measured by using the equation 3.48. Where Y_t is total mean of S/N ratio, $\overline{Y}$ is the mean of S/N ratio at the optimal level, and n is the number of variables that significantly affect the performance.

$$Y_p = Y_t + \sum_{i=1}^{n} (\overline{Y_i} - Y_t) \tag{3.48}$$

A confirmatory test is required for the design of experiments and this is done as the final step in the first round of the design of the experiments. The pupose of the confirmation experiment is to attest to the validity of the outcomes obtained during the analysis phase. The confirmation experiment is carried out by conducting a test at the optimal factors levels previously evaluated. Esme [87].

3.5. Mechanical Alloying and Ball Milling

When powders of pure metals, intermetallic, or pre-alloyed powders are milled without any material transfer, then the process is called mechanical milling (MM). If material transfer occurs, then milling process is called mechanical alloying (MA). In mechanical alloying, the new crystalline structure can be different or can be the same as the base metal. This new structure can show different mechanical, chemical, or physical properties. Alloying of base metal with one or more chemical element is normally required to change the bulk or the surface characteristics of the base metal to make it easier to fabricate or perform better during application. As an example, the strength bulk material depends on plastic deformation when the slip of crystallographic planes occurs along the grains of the metal, thus it is important to increase the resistance to slip. Suryanarayana [88].

3.5.1. Mechanical Alloying

Since 1980s, mechanical alloying by ball milling are used to synthesize a variety of stable and metastable phases including supersaturated solid solutions, crystalline, quasicrystalline intermediate phases, and amorphous alloys. In addition, the procedure can be used to stimulate chemical (displacement) reactions in powder mixtures at room temperature or at least at much lower temperature than normally required. Metals, ceramics, polymers, and composite materials have benefited from the use of this technique; Mechanical alloying (MA) is a dry, high-energy ball-milling process for producing composite metallic powders with a controlled and fine microstructure. Elements that are incompatible in many ways can also be alloyed through mechanical. The main limitation on the powder particles mixing for mechanical alloying are the particle size range, high degree of oxidation, and the requirement of a binder for the other constituents during the process. Suryanarayana [89] and Davis [90]

3.5.2. Modeling of Mechanical Alloying

The behaviour of mechanical alloying process has been known qualitatively and some semi-empirical formula developed, but the mathematical statement of this process is complex due to the interference of many mechanics, mechanical behaviour, heat flow, thermodynamics and kinetics. Recently, some researchers develop interest in this direction for further understanding. Soni [43]

3.5.2.1. Deformation

During the collision, the kinetic energy of the balls is converted into deformation energy during the approach of their centres and the deformation within the contact area can be expressed as in equation 3.49. Where r is the distance from the centre of contact, R_b is the radius of the balls, v_0 is the relative velocity of the balls at impact, ρ is the density of medium balls and H_V is the powder hardness. Suryanarayana [91].

$$\alpha(r) = R_b v_0 \left(\frac{\rho}{H_v} \right)^{1/2} - \frac{r^2}{R_b} \qquad (3.49)$$

3.5.2.2. Coalescence

During plastic deformation the oxide layer present on the particle surface breaks leading to an increase in their surface area due to the effect of the bonding force acting at the surface contact. The bonding force given in equation 3.50 where σ_u is the tensile strength and A_w is the effective new surface area created.

$$F_w = A_w \sigma_u \qquad (3.50)$$

3.5.2.3. Fracture

Considering that the only mechanism of fracture is the forging fracture where the crack can reach a critical length. Then, the condition for forging fracture within the powder should exceed some critical strain over a given length. The critical strain can be expressed as in equation 3.51 where ε_c is the critical strain to fracture, R_w is the radius of the surface contact region, h_0 is the powder coating thickness, and f_s are the shape factor.

$$\frac{\alpha(r)}{h_0} = 1 - \left(1 - \frac{a_c^2 f_s^{2/3}}{4R_w^2} \right)^{0.5} exp(-\varepsilon_c) \qquad (3.51)$$

3.5.3. Ball milling

Ball milling is used to fracture metal powder particles when it is subjected to heavy plastic deformation. During ball milling, many factors should be taken into consideration. If ductile metal powder particles are used, cold welding phenomenon could prevent fragmentation of the particles or could be as rapid as fracturing. Another problem is the reactivity of the very fine particles. There are many types of high-energy milling equipment currently in use for MA/MM they include the Shaker mills, Planetary Ball Mills, and Attrition Mills.

The planetary ball mill owns its name from the planet-like movement of its vials. The centrifugal force is produced by the rotation of vials and the supporting disk in opposite directions at the same time. The impact energy during milling mainly depends on the speed of the planetary mill. As the speed is reduced, the grinding balls lose the impact energy, and when the energy is sufficiently low there is no grinding involved; only mixing occurs in the sample. Suryanarayana [91].

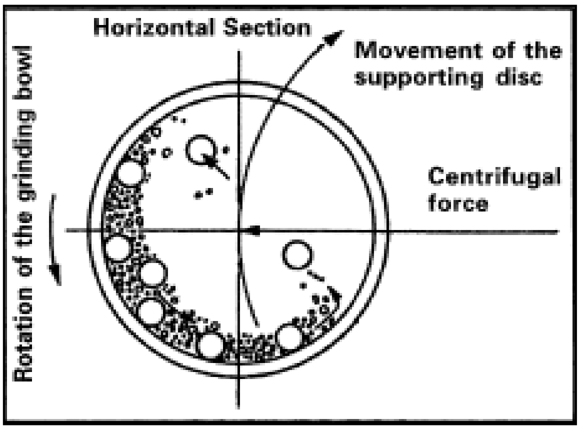

Figure 3.11 Schematic diagram of high-energy planetary ball mill. Iskandarany [92]

3.5.4. Process Variables in Milling

In ball milling there are many variables that affect the final constitution of the milled powder. The interaction between these variables is very important. For example, the optimal milling time depends on the type of mill. For a given composition of the powder, some of the important variables that have an important effect on the final constitution of the milled powder are as follows: [88, 91, 93]

3.5.4.1. Type of mill

There are many types of mills according to their capacity, speed of operation, and the ability to control the operation variables such as temperature, milling time, and milling environment. Table 3.6 shows the main mill type and their capacity.

Table 3.6 the capacity of main mills type. Suryanarayana [91].

Mill type	Sample weight
Mixer mills	2 Up to 20 g
Planetary mills	4 Up to 250 g
Attritors	0.5±100 kg
Uni-ball mill	4 Up to 2000 g

3.5.4.2. Milling container

The mechanical and chemical properties of milling medium material can affect the inner walls of the container leading to contaminate or change the chemistry of the milled powder. The main materials used as grinding medium are hardened steel, tool steel, hardened chromium steel, tempered steel, stainless steel, zirconia (ZrO2), cemented Tungsten carbide (WC±Co), and bearing steel. On the other hand, the shape of the container can affect the milling rate. It was found that at the higher rates occur in the flat-ended vial than in the round-ended container. Suryanarayana [91]

3.5.4.3. Milling speed

It is easy to understand that the faster the mill rotates the higher would be the energy input into the powder. This is related to the kinetic energy $E = ½ mv^2$ of the grinding medium. The first limitation on the effect of milling speed is that when the speed of rotation reaches a critical speed, the ball will pinned to the inner walls of the vial leading to zero impact motion. Thus, the maximum milling speed should be just lower than the critical value in order to make the balls fall down from the maximum height to produce the maximum collision energy.

The second limitation to the maximum speed is that at high intensity of milling (speed), the temperature of the milling medium may increase rapidly to reach a high value. This may be required to promote homogenization and mechanical alloying. The intensity of milling as a function of ball-to-powder weight ratio (BPR), and the maximum velocity and frequency of the balls given by Suryanarayana [91] as follow:

$$I = (\frac{M_b}{M_p})V_{max} f \tag{3.52}$$

Where M_b is the mass of the ball, Mp the mass of the powder, and f is the impact frequency. Thus, the milling intensity increases rapidly with the impact frequency, velocity, and mass of the balls. The intensity decreases with increasing milling time and increases at higher ball to powder ratio(BPR), Suryanarayana [91].

3.5.4.4. Milling time

The most important milling parameter is time of milling. It is important to choose a time that can achieve a steady state between the fracturing and cold welding of the powder particles. The time required depending on the type of mill, milling speed, the ball-to-powder ratio, milling temperature, and the properties of the milled powder as shown if Figure 3.12 and Figure 3.13. The determination of the suitable milling times depends on the combination of the above parameters for any particular powder system. Suryanarayana [91]

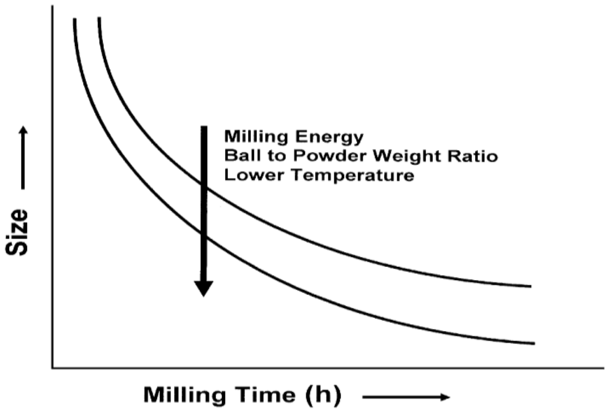

Figure 3.12 Refinement of particle/grain/crystallite size with milling time for mechanical alloying and milling. Suryanarayana [91]

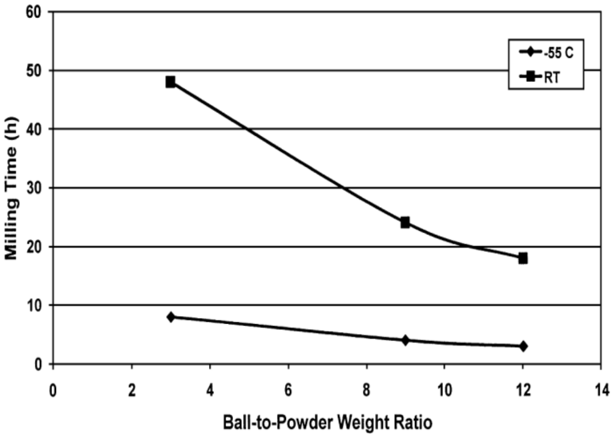

Figure 3.13 Effect of ball-to-powder weight ratio (BPR) and milling temperature on the time required to synthesize Titanium during reduction of TiCl4 with Mg. Suryanarayana [91]

3.5.4.5. Grinding medium

In general, the density of the milling medium should be high to create enough impact force. It is advisable to use milling medium made from the same material of milled powder to avoid encountering contamination. The large size container with high milling speed can be useful since more impact energy will be generated. It has also been reported that the ball size can affect the constitution of the milled powder. For example, when balls of 15 mm diameter were used to mill the blended elemental Ti±Al powder mixture, a solid solution of aluminum in Titanium was formed. Suryanarayana [91]

3.5.4.6. Ball-to-powder weight ratio

One very vital variable in the milling process is the ration of balls to the powder weight, which is also sometimes referred to as the charge ratio. Though some researchers have used different ratios, the commonly used one is 10:1, especially when milling powder in a small capacity mill such as the SPEX mill. This ration nonetheless varies with mill capacity. A milling process carried out in an attritor utilizes a ratio of up to 50:1 or even 100:1 is used. A higher ball to powder ration (BPR) or CR results in more number of collisions per unit time and consequently, more energy is transferred to the powder particles causing alloying to take place faster Suryanarayana [91].

3.5.4.7. Extent of filling the vial

Alloying phenomenon only takes place amongst the the powder particles due to forces of impact brought on them by the falling balls. For this reason, it is necessary to make for enough space within the milling container, for the balls and the powder particles to move around freely. Therefore, the degree of filling the vial with the powder and the balls is a major factor. If the quantity of the balls and the powder is very small, then the production rate and vice versa. Suryanarayana [91].

3.5.4.8. Milling atmosphere

According to literature [91], the main effects arising from the milling atmosphere are in regard to powder contamination. For this reason, containers used for milling powders must have been evacuated or filled with inert gas, for example, argon or helium. The use of nitrogen is not encouraged as it has been discovered to have interactions with metal powders. Argon with high purity level is readily and commonly used as the atmosphere to prevent oxidation or contamination or both during milling of powders. Normally, the loading and unloading of the powders into the vial is completed inside atmosphere-controlled glove boxes. Suryanarayana [91].

3.5.4.9. Process control agents (PCAs)

Whenever the powder particles being milled are ductile, their propensity to cold-weld to one another increase, due to the heavy plastic deformation they undergo during the milling process. Nonetheless, good alloying takes place amongst the powder particles when a good balance between cold-welding and fracturing of the particles is continuously maintained. The particles adsorb the surfactant on to their surface and lower the surface tension of the powder particles. This in turn lowers the surface energy. This reduction in surface energy leads to the decrease in time taken to mill the powders to the required particle size. Suryanarayana [91].

3.5.4.10. Temperature of milling

One other important factor in the determination of the milled powder constitution is the milling temperature. Expectedly, milling temperature plays considerable role in alloying system. There has been merely a couple of research reported in which the temperature of milling deliberately varied. It was made by either dripping liquid nitrogen within the milling container to reduce the temperature or electrically heating the milling vial to raise the temperature of milling. The extent of solid solubility was reported to lower at greater milling temperatures. Suryanarayana [91].

3.5.5. Milling Theory

Since the trapped powder particle is very small compared to the colliding bodies, it is possible to see the surfaces of the colliding bodies as a flat surface as shown in Figure 3.14.

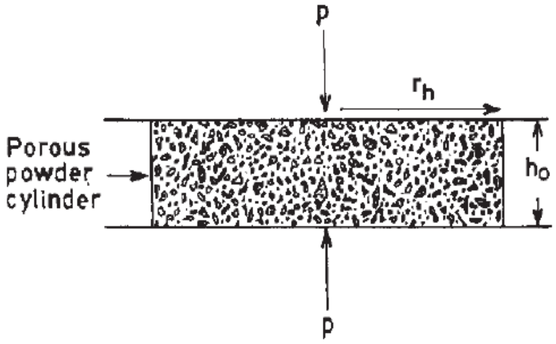

Figure 3.14 Cylindrical slugs of initial height, h_0, Hertz radius, r_h, entrapped between the colliding surfaces. Soni [43].

The collisions with powder can be seen as forging process between the two parallel plates. If the time between collisions t_c is estimated from $t_c = \lambda / v_0$ Where λ is the mean free path between collisions and v_0 is the relative velocity of the balls at impact, then the processing time for such system t_p to alloy, the material can be given as;

$$t_p = (V_p \varepsilon_c t_c) / (\varepsilon \pi r_h^2 h_0) \tag{3.53}$$

Where; v_p is the total powder volume, ε_c is the critical deformation strain, t_c is the time between impact events, h_0 is the initial height of cylindrical slug, and r_h Hertz radius.

The impact velocity in the case of a planetary mill can be calculated using the following relationship. [43]

$$v_0 = \left[\frac{\omega_n^3 \left(R_n - \frac{R_b}{2} \right)}{\omega_p} + \omega_p \omega_n R_p \right] \left(R_n - \frac{R_b}{2} \right) \tag{3.54}$$

Where ω_n and ω_p are the angular velocity of the vial and the plate, respectively, and R_n and R_b are the radius of the vial and the balls, respectively. The average pressure developed across the contracting surfaces at maximum compression can be expressed as

$$P_{max} = g_p n_0^{0.4} \left(\frac{\rho}{E} \right)^{0.2} E \tag{3.55}$$

Where g_p is also a geometrical constant, ρ is the ball density, and E is the tensile modulus of the colliding media.

3.6. Consolidation Technique

The MA powders have very fine cold welded particles with compressed layers and rough surfaces. This can reduce the mechanical deformation during cold compaction due to the high shear resistance. Thus, the compaction techniques of M/M or M/A powders will combine the effect of temperature, pressure and shear stress. The temperature can helps in softening the particles and improve the thermal diffusion bonding. The pressure, on the other hand, supports densification, at the same time shear can help in cleaning the powder surface and improve the bonding between particles. In M/A, degassing prior to consolidation is a necessary step due to the high amount of trapped gas and high degree surface oxidation. The grain growth of the mechanical alloyed powder during consolidation at high temperature can be given by the modified Arrhenius equation as follow. [43]

$$d^2 = d_0^2 + k_m t p^2 exp^{(-Q/RT)} \tag{3.56}$$

Where d_0 is the initial grain diameter, K_m is the material constant; p, T and t are the pressure, absolute temperature and time used for compaction, respectively, Q is the activation energy and R is the gas constant.

3.6.1. Cold Compaction

The Powder Densification during compaction starts by the particles sliding followed by particle deformation as shown in the simple sketch of die compaction in Figure 3.15. At low pressure the particles rearrange to eliminate large pores. Depending on the particle hardness, eventually the particles deform at high pressures and particle deformation dominates densification. German [94].

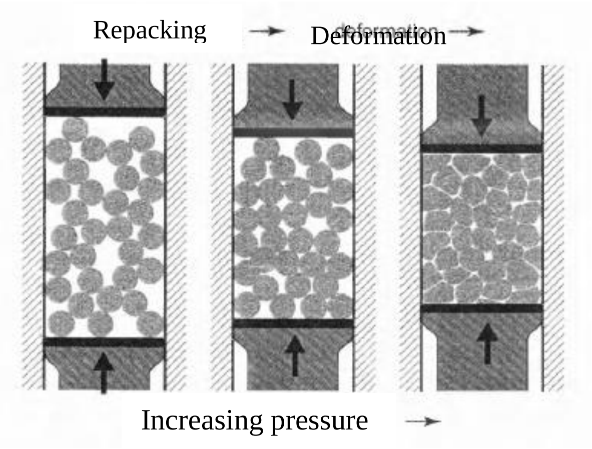

Figure 3.15 A view of the stages of powder under compaction. German [94].

Figure 3.16 shows that the densifications for five different metals with different hardness increase rapidly at low pressures. The Vickers hardness is listed for each material showing that softer materials are easier to compact to high density. It is clear that particle hardness is one of the most important parameters in compaction. The effect of compaction on densification rate is negligible after 800 MPa for all materials.

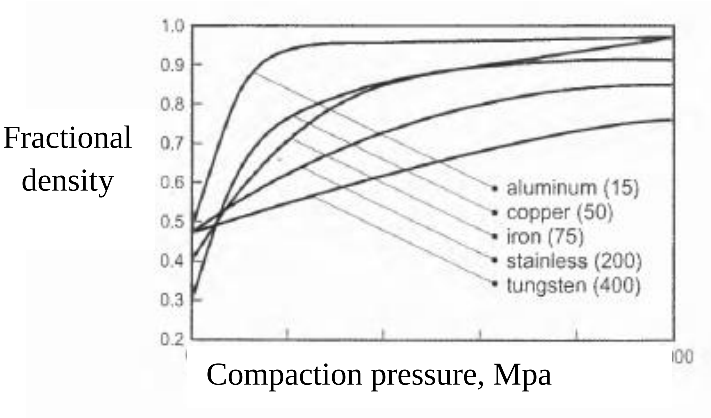

Figure 3.16 Compaction behaviour of several metals. German [94].

3.6.2. Compaction Theory

Figure 3.17 shows a cylindrical compact of diameter D and height H. Consider a thin section of height d_H under compaction. If the top pressure is P_T and the bottom pressure is P_B then, the pressure gradient on this thin section will exert a force on this thin section. The friction of powder with walls and the antiparticle friction resist this force and the balance of forces along the central axis can be expressed as in equation 3.57. Where F_N is the normal force, μ is the coefficient of friction between the powder and the die wall, and A is the cross sectional area. German [94].

$$\sum F = A(P_B - P_T) + \mu F_N = 0 \tag{3.57}$$

The normal force can be given in terms of the applied pressure with a proportionality factor β as follows;

$$F_N = \pi \beta P_T DdH \tag{3.58}$$

During compaction the die-wall friction force F_F is determined by the normal force acting against the die wall and the coefficient of friction μ as follows.

$$F_F = \pi\mu\beta P_T dH \tag{3.59}$$

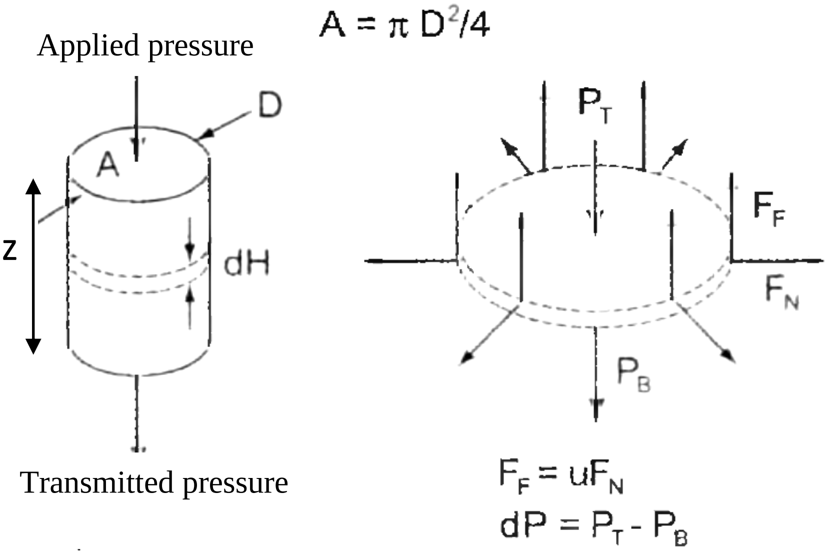

Figure 3.17 The balance of forces during die compaction. German [94].

Taking dP = P $_T$ - P$_B$ and rearrange the terms in equation 3.57, the pressure gradient on the this element as a function of the compact height can be written as;

$$dP = -\frac{F_F}{A} = -\frac{4\,\mu\beta P_T dH}{D} \tag{3.60}$$

By integrating equation 3.60 with respect to compact height, an expression for the pressure as a function of position z below the punch can be written as follows:

$$P(x) = P\exp\left(-\frac{4\,\mu\beta z}{D}\right) \tag{3.61}$$

Where, P is the applied pressure at the punch. The average green density in the compact depends on the mean pressure which at all time is less than the applied pressure The mean compaction for single-ended pressing pressure and for double-action compaction P$_M$ can be estimated respectively as;

$$P_M = P\left(1 - \frac{2\,\mu\beta H}{D}\right) \tag{3.62}$$

$$P_M = P\left(1 - \frac{\mu\beta H}{D}\right) \tag{3.63}$$

These equations show that mean pressure depends on the factor (H/D), the axial-to-radial pressure distribution via the factor z and the Die-wall friction via the factor μ.

3.6.3. Sintering theory

Sintering is a thermal process for consolidating powder particles into a coherent structure via mass transport on the atomic scale. Sintering theory is most accurate for single-phase powder sintering by solid-state diffusion. It is important to know that this model suffers from the limitation especially, when the particles are varying in shapes and sizes. The model suggests that the particles are spherical in shape with high purity. In reality, the powder particles do not have uniform shape, uniform density and 100% purity. Instead, they may have organic binders, lubricants, additives and other impurities from the sintering atmosphere. In general, powders have a curved surface and this curved surface always has some stress. Laplace gives the stress associated with a curved surface as shown in equation 3.64 where, γ is the surface energy and r_1 and r_2 are the principal radii of curvature for the surface. Sintering can be divided into initial, intermediate and final stage.

$$\sigma = \gamma\left(\frac{1}{r_1} - \frac{1}{r_2}\right) \tag{3.64}$$

During the initial stage, there is a neck formation between two touching spheres, which in the final stage culminates into small closed pores. The main sintering mechanisms are the evaporation and condensation, diffusion (surface, grain boundary and lattice), Plastic flow and viscous flow. Figure 3.18 is a schematic diagram showing the change in pore structure during initial, intermediate, and final sintering stages starting with three point particle contact.

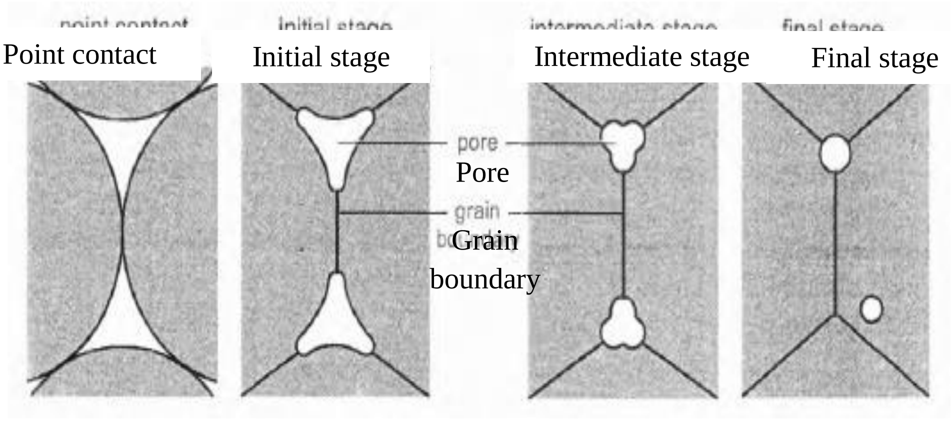

Figure 3.18 Schematic diagram showing the pore structure change during sintering starting with particles in point contact. German [94].

As the pore size decreases, the grain boundary increases leading to a spheroid shape. The three sintering stages can be given in details as follows;

3.6.3.1.Initial Stage

As sintering proceeds, a neck will grow between a sphere and a plane and there will be a large negative curvature of the neck. The neck growth in the initial stage for various material transport mechanisms from the particle surface given in German [94] by equation 3.65. Where, x is the radius of the neck, r is the sphere radius of the material, t is the isothermal sintering time and C is the constant, x/r is known as the neck size ratio. C can be expressed in the exponential form as in eqation 70

$$\left(\frac{x}{r}\right)^n = \frac{Ct}{r^m} \qquad (3.65)$$

The values of n and m depending on sintering mechanism are given in Table 3.7.

Table 3.7 The constant n & m of initial stage sintering taken from. Upahdyaya [95].

Mechanism	n	m
Viscous flow	2	1
Plastic flow	2	1
Evaporation-condensation	3	2
Lattice (Volume) diffusion	5	3
Grain boundary diffusion	6	4
Surface diffusion	7	4

$$C = C_0 exp\left(- \frac{Q}{RT} \right) \tag{3.66}$$

Where, C_o is the cumulative constant of a material at a particular temperature and given particle geometry, R is the gas constant, T is the absolute temperature and Q is the activation energy associated with the atomic transport process. Figure 3.19 is a schematic diagram representing the two-sphere model of densification mechanism during initial stage of sintering.

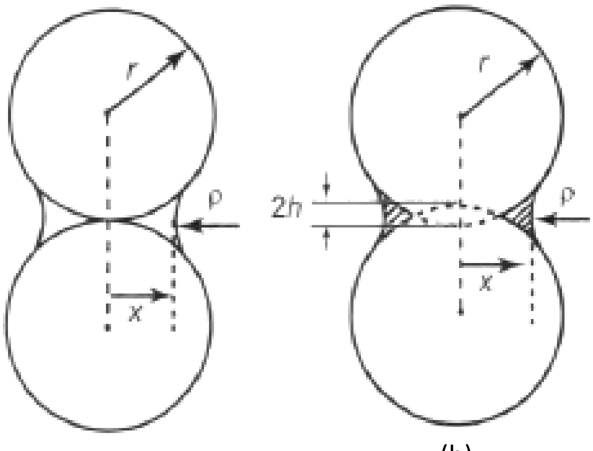

(a) (b)

Figure 3.19 Schematic two-sphere model showing (a) non-dandifying mechanism and (b) dandifying mechanism. Upadhyana [95].

The rate of pore elimination during this stage given by Schatt and co-workers as:

$$\frac{dV_p}{dt} = \frac{\sigma_e \Omega D_n}{kTL^2} \tag{3.67}$$

Where, V_p is the fractional volume of porosity, t is the time, σ_e is the effective surface stress, Ω is the atomic volume, D_n is the volume diffusion coefficient, k is the Boltzmann's constant, T is the absolute temperature and L is the mean distance between mobile dislocations.

3.6.3.2. Intermediate Stage

More than one sintering mechanism could be operated at the same time during the intermediate stage. In such cases, the rate of one mechanism influences the other. The interaction between the mechanisms is very important. In modelling this stage of sintering, it is assumed that the pore geometry is uniform and the chemical potential is the same everywhere on the pore surface. The densification mechanism will continue at the grain boundary mainly by lattice diffusion. By introducing a solution for the diffusion equation, Coble gives the rate of change of porosity as in equation 3.68.

$$\frac{dP}{dt} = -\frac{CD\gamma\Omega}{G^{3}kT} \tag{3.68}$$

Where, C is a constant and G is the edge length of a grain.

3.6.3.3.Final Stage

After prolonged sintering, the open pores become closed or isolated. They become spherical in shape and shrink by lattice or volume transport processes if they are connected to the grain boundaries. Spherical pores result when the pores are separate from the grain boundary. Ostwald ripening of solid grains makes the larger pore growth at the expense of smaller and less stable ones. The densification rate (pore removal rate) during the final stages of sintering depends on the balance between the surface energy and the pore gas pressure. The densification rate can be given as:

$$\frac{d\rho}{dt} = \frac{12D_{v}\Omega}{kTG^{2}}\left(\frac{\gamma}{r_{p}} - P_{g}\right) \tag{3.69}$$

Where, ρ is the fractional density, t is the sintering time, **Ω** is the atomic volume, D_v is volume or lattice diffusivity, k is the Boltzmann’s constant, T is the absolute temperature, G is the grain size, γ is the solid-vapour surface energy, r_p is the pore radius and Pg is the gas pressure within the pore. [95]

3.6.4. Hot Pressing (HP)

Hot pressing is a suitable method for dandifying materials with poor sintering behaviour. This technique, which combines powder pressing and sintering into one single operation, offers many advantages over conventional powder consolidation. Figure 3.20 shows the Schematic design of a hot pressing unit including the die system, heating system, vacuum unit, and the hydrostatic pressing system.

- It is feasible to achieve near theoretical density in a wide range of hard-to-work materials.
- The resistance of metal particles to plastic deformation decreases rapidly with increase in temperature
- Much lower pressures are required for consolidation by hot pressing.
- Densification by hot pressing is relatively less sensitive to powder characteristics such as shape, size and size distribution.

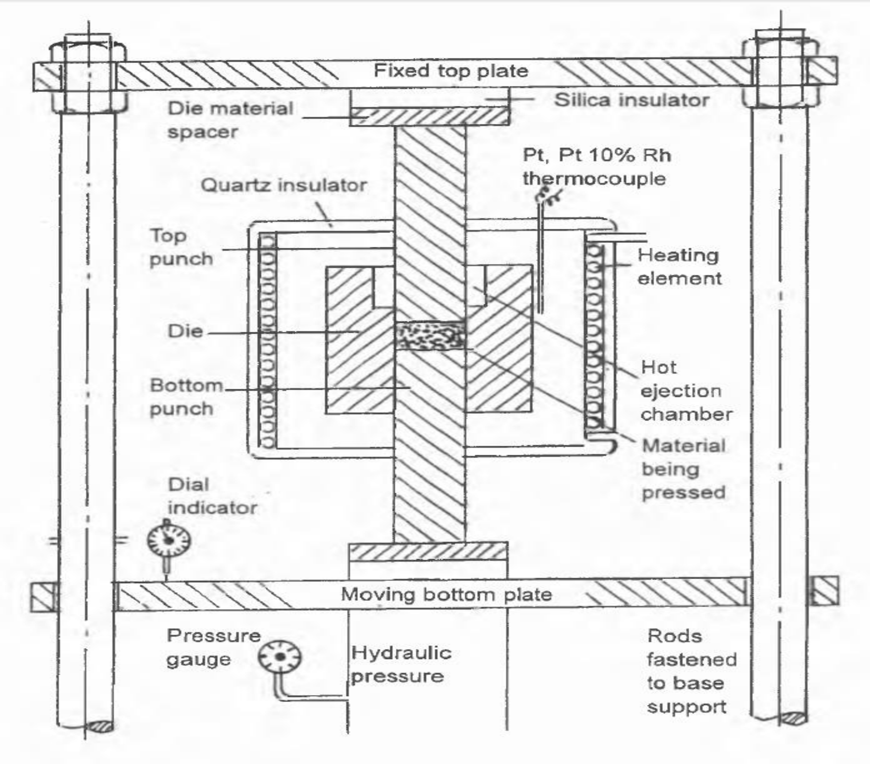

Figure 3.20 Schematic design of a hot pressing unit. Upadhayana [95].

The main hot pressing parameters are pressure, temperature, time and the working atmosphere. High-speed tool steels, super alloys, beryllium and the refractory metals are particularly amenable to hot pressing. Hot pressing is perhaps the only method of producing dense and fine-grained shapes of materials such as pure carbides, nitrides and borides which are otherwise difficult to sinter due to the lack of adequate atomic mobility at the sintering temperature. Many oxide and carbide ceramics can be hot pressed using die made from Graphite in the open atmosphere. However, the die life is limited due to severe oxidation at temperatures above 500°C. Hot compacting of refractory and reactive metal powders demands an inert atmosphere or vacuum. Using a vacuum instead of inert gas for hot pressing offers additional advantages of removing air from the powder body (Eliminating the possibility of air entrapment), and also degassing it during the initial heating up of the pressing cycle. This would enhance the activity of the powder and thus help in sintering. Graphite is the most common die material used for hot pressing, but other ceramics and refractory metals have also been used. Graphite strength increases with temperature, up to about 2500°C, beyond which it falls. The strength at 2500°C is almost twice that at room temperature. The low thermal expansion coefficients ease of machining and low cost make it a nearly ideal choice for die material, Upadhayaya [96].

3.6.5. Thermodynamics and phase diagram of Cu-WC-Si-Ti system

Tungsten, which also called Wolfram or Heavy Stone, is a metallic transition element. The high melting point characterizes it after carbon and relatively high thermal conductivity in compared to copper. The melting point of tungsten varies between 3387°C and 3422°C and the thermal conductivity varies between 167-190 W/m.k. The solubility of tungsten in the molten copper is negligible. Cu-W composite which is combining the beneficial properties of both metals, play an important role as electrical contact materials and electrode materials for spark erosion machines. The main properties of tungsten at room temperature are shown in Table 3.8. Lassner [97] and MATABASE [98].

Table 3.8 The main physical and mechanical properties of Tungsten at room temperature Lassner [97]

Quantity	Value	Unit
Young's modulus	360000 - 420000	MPa
Tensile strength	1490 - 4200	MPa
Thermal expansion	4 - 4.500	1^{-6}/K
Thermal conductivity	167 - 190	W/m.K
Specific heat	130 - 199	J/kg.K
Melting temperature	3200 - 3387	°C
Density	19300	g/cm^3
Resistivity	0.055	Ohm.mm^2/m

Copper

High-purity metals containing at least 99.3% Cu with small trace amounts of silver or phosphorus may be present. Neither element affects electrical conductivity significantly when present in such small concentrations. Electrical conductivity of copper is 100% IACS, while thermal conductivity can reach 391 W/m · K. Pure Coppers is a ductile material and cannot be hardened by heat treatment. Oxygen-free copper has the highest electrical and thermal conductivity among the cast copper alloys. The main copper properties are shown in Table 3.9. Davis [90]

Table 3.9 The main physical and mechanical properties of Copper at room temperature. Davis [90].

Quantity	Value	Unit
Nominal composition,	99.95-99.99	%
Tensile strength,	172	MPa
Yield strength,	62	MPa
Hardness	44	HRB
Electrical conductivity	100	%IACS
Thermal conductivity,	391	W/m.k

Silicon

Silicon is the second most abundant element after oxygen and comprises 25.7%. Silicon is mainly used in the glass as silicon dioxide. It used as a semiconductor and in solar cells, tools, cement, grease, and oil. Silicon is a relatively high melting temperature 1400^{o}C. Silicon density increases with temperature so that it is density in a liquid state is greater than a solid state, similar to how water. The thermal conductivity of silicon is 149 W/m·K and can form silicide with tungsten and copper at temperatures lower than the melting point of copper. Due to this, silicide is used as heat sink in semiconductors.

Tungsten silicide was used by Savrun [99] in improving the erosion-resistance of the protective coating layer for IR windows. Tungsten silicide also used as gate electrode and as a bottom electrode for storage capacitors and transistors. In both cases, thermal stability up to 780°C has been shown. Band discontinuities between the SiO_2 and WSi_2 were estimated from current-voltage measurements by Shell [100]. The electrical conductivity of tungsten disilicide is 33.4–54.9x10^6 W/m.k. Shackelford [101].

Titanium

Titanium is a corrosion resistant material with a high melting point and good thermal conductivity. On the other hand, Titanium electrical conductivity has been just 3.1% relative to copper which is considered to be 100%. From this point of view titanium is not advisable if the electrical conductivity is the prime factor. For comparison, stainless steel has a conductivity of 3.5% and aluminium has a conductivity of 30%. The main physical and mechanical properties of Titanium are shown in Table 3.10. There is no much information is available in the literature on the intermetallic compounds of titanium with tungsten, which are potential candidates for high temperature applications. [102-104]

Table 3.10 The main physical and mechanical properties of Titanium at room temperature Gummadi [104].

Quantity	Value	Unit
Temperature	20	°C
Thermal Conductivity	17	W/m.k
Electrical Resistivity	0.48	μΩ.cm
Specific Heat capacity	500	J/g.k
Elastic modulus	110	GPa

Copper-tungsten (Cu-W)

The binary phase diagram in Figure 3.21 shows that Tungsten is insoluble in liquid Copper when it is prepared by liquid phase sintering of mechanical mixtures of Cu and W powders at temperatures greater than the melting point of Cu. Based on the semi-empirical model mentioned given by Smolej [105].

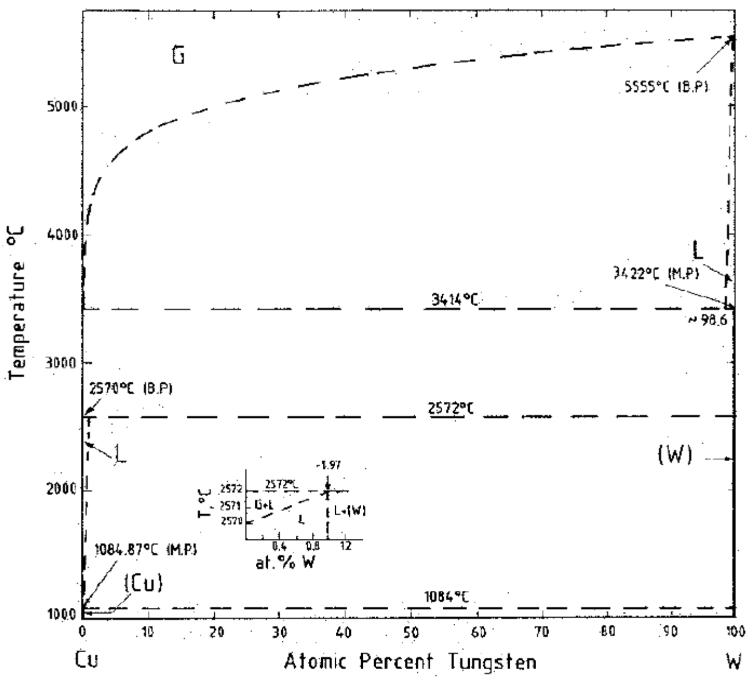

Figure 3.21 Schematic phase diagram of Cu-W calculated at one atmospheric total pressure (P = 1 atm.). Rao [106].

$$G^{ex}\left(L\right)= x\left(l - x\right)\left[101\,000 - 21\,OOOx\right]J\ /\ mol\ . \qquad (1)$$

Where; x is the atomic fraction of W. The heat of solution of W in liquid Cu is calculated to be 101 kJ /mol and that of Cu in liquid W is 80 kJ /mol. Because these values are very high, the solubility of Cu in liquid W and that of W in liquid Cu is expected to be extremely small.

The standard state is pure liquid Cu and pure liquid W. The quantities are in J/mol, T is in K, x is the atomic fraction of W, and mol refers to the atom as the elementary entity.

Tungsten-titanium (W-Ti)

The binary phase diagram of W-Ti is shown if Figure 3.22. The alloy W-10Ti is used as a sputtering target in the manufacture of microelectronics devices, such as VLSI, ULSI (very large and ultra-large-scale integration), and DRAM (dynamic random access memory) chips. Thin W-Ti layers are sputtered onto Silicon substrates and act as a diffusion barrier against aluminium (interconnect). W-10Ti alloy targets are produced by blending ultrapure Tungsten and Titanium powders obtained by vacuum melting and subsequent pulverizing, followed by pressure sintering. The impurity level has to be very low, in particular, with respect to radioactive elements (U, Th) and "mobile" alkaline metals (Na, K). Lasser [97].

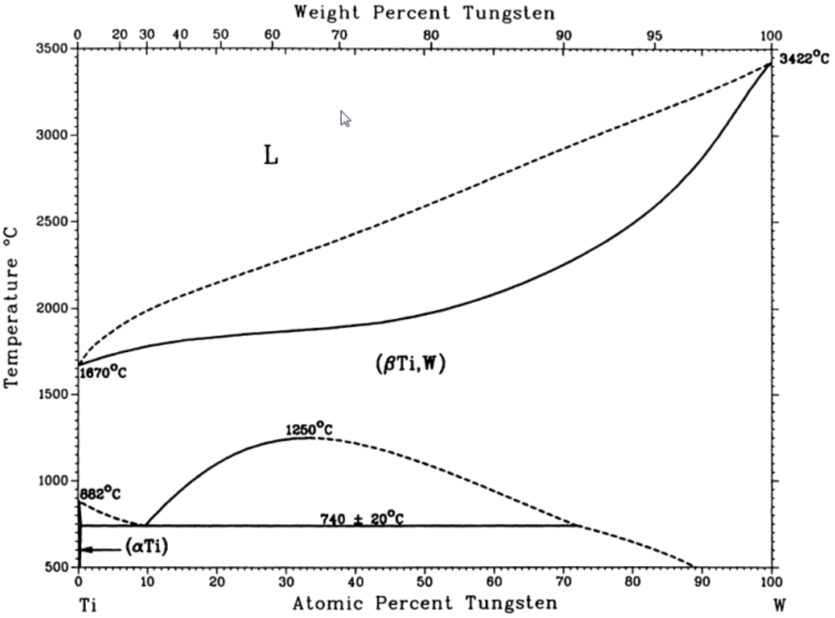

Figure 3.22 Schematic phase diagram of Ti-W (Titanium - Tungsten) binary phase diagrams. [107]

Tungsten carbide (WC)

The electrical conductivity of Tungsten carbide is in the same range as tool steel and carbon steel. Tungsten-carbon binary phase diagram in Figure 3.23 contains three intermediate compounds: W_2C (β), $WC_{1-}x$ (γ), and WC (δ), the latter being the main constituent in most of the commercial cemented carbides (hard metals). Besides, ternary and even more complex compounds exist which are of interest in alloyed steels and cemented carbides.

The tungsten carbide (W2C) can be produced in a pure state by mixing the appropriate amounts of Tungsten powder and carbon black or Graphite and subsequent heating in a hydrogen atmosphere to at least 1600^0C; alternatively, it can be easily produced by melting. The crystal structure of W2C can be described as a slightly distorted hexagonal close-packing of Tungsten atoms. The carbon atoms occupy half of the octahedral interstices. They may be distributed in an ordered manner, the type and degree of ordering depending on temperature. There exist 3 temperature dependent modifications: B, β', and β". The transition temperatures are:

β'-> β" 2100-2140^{0}C and β’ -> β 2490^{0}C

β is a hexagonal with a = 2.985-3.000 A, c = 4.716-4.730 A

β' is an orthorhombic with a = 4.728 A, b = 6.009 A, c = 5.193

β" is a hexagonal with a = 5.184A, c = 4.721 A [4.18

The WC1-x is a Cubic high-temperature modification; it undergoes a eutectoid decomposition at 2530-2535^{0}C into P (W$_2$C) + 8 (WC). At room temperature it can only be obtained by rapid quenching in liquid tin with a = 4.220 A (at 38 at% C). Tungsten monocarbide is the only stable Tungsten carbide at room temperature. It can be produced by the reaction of Tungsten trioxide with carbon in an inert atmosphere, Vapour phase deposition, or by electrolysis of fused salts. The crystal structure of WC is a Hexagonal with a = 2.906-2.9066 A, c = 2.8364-2.8374 A. Lassner [97].

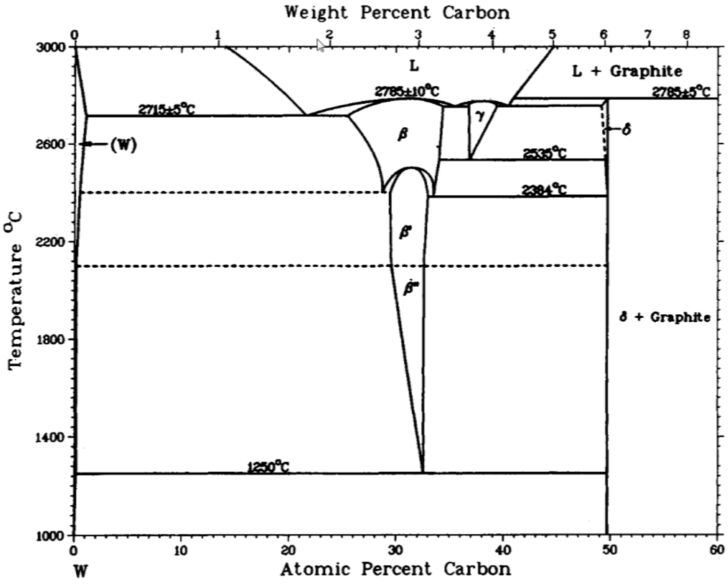

Figure 3.23 Tungsten-carbon phase diagram. lasser [97].

Tungsten-Silicon

Figure 3.24 shows that Tungsten can form with Silicon two types of silicide compounds: The Penta-Tungsten Trisilicide W_5Si_3 and Tungsten Disilicide WSi_2. These compounds can be produced by the reaction of the elements in powder form in a protective atmosphere, like argon or vacuum at elevated temperature. Tungsten silicides form a protective layer at the surface of Tungsten and prevent destructive oxidation at elevated temperatures. PentaTungsten Trisilicide: W_5Si_3 is a tetragonal with a = 9.601 A, c = 4.972 A. Meanwhile Tungsten Disilicide WSi_2 is a tetragonal cube, with a = 3.211 A, c = 7.868 A. [97]

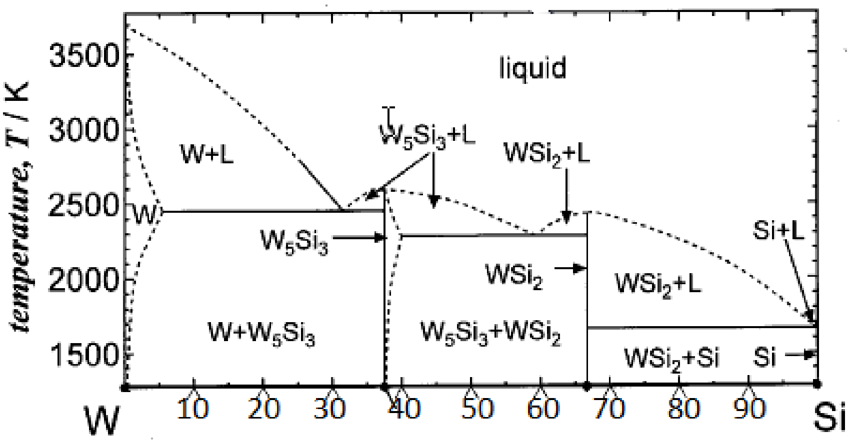

Figure 3.24 Phase diagram of W–Si binary system at 1373 K. [108]

Copper-Silicon

Cu-Si is a key system for several applications such as traditional silicon bronzes to catalysis, microelectronics, and recently in Li-ion batteries, Sufryd [109]. Figure 3.25 is the binary phase diagram of Cu-Si. These systems are used for several applications such as Silicon Bronzes, heat sink for electronic devises, and recently as Li-ion batteries. The Cu-Si intermediate phases are located in the Cu-rich part of the phase diagram, between 5 and 25 at % Si as shown in Figure 3.25.

The only congruent melting compound, Cu_3Si, is an intermediate solid solution with a small composition of Si at % in the range from 23 to 25 and a melting point of 859^0C. For this phase, three allotropic modifications denoted as h-Cu_3Si at high temperature, h0-Cu_3Si at intermediate temperature, and h00-Cu_3Si at low temperature have been reported in literature.

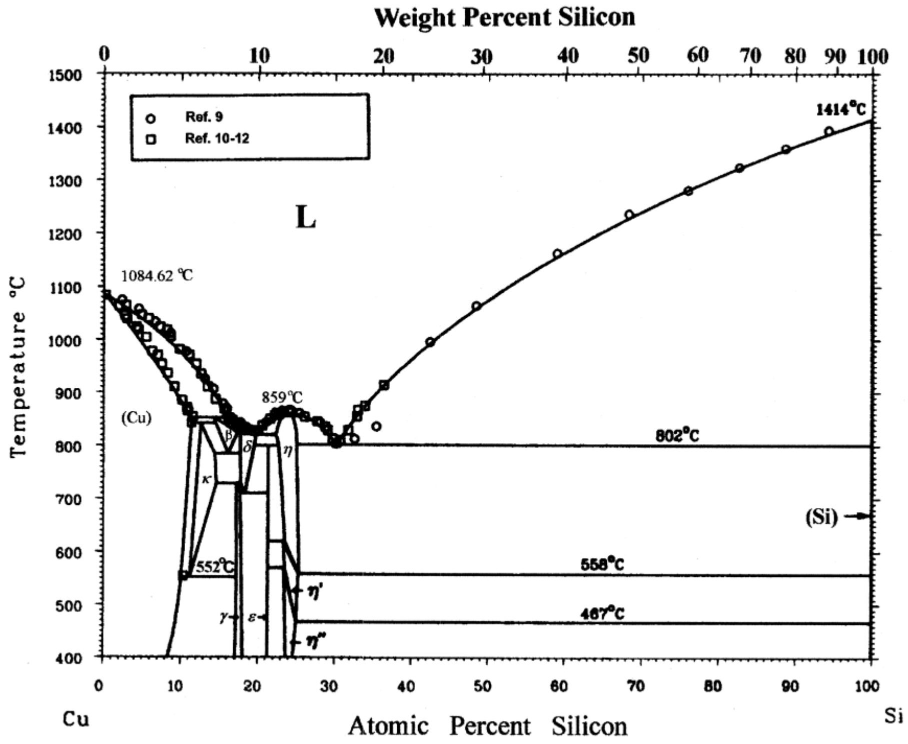

Figure 3.25 Cu-Si binary phase diagram. [109], [107] and [110]

Copper-Titanium

Copper also can form with titanium many compounds with titanium as shown in the binary phase diagram of Cu–Ti in Figure 3.26. Cu–Ti alloy is considered to be ultra-high strength conductive materials for applications such as conductive springs, interconnections, Hernandez [111].

It has been shown that Cu–Ti powders produced by the rapid solidification process (RSP) have better mechanical properties than alloys of the same chemical composition produced by standard melting and casting techniques which have been widely considered. Mechanical properties of Cu–Ti alloys are limited to intermediate temperatures up to 450 °C.

Unfortunately, these properties drop down at higher temperatures because of the coarsening of the β-phase precipitates with the nominal composition of Cu_4Ti. If dispersed phase which remains stable at higher temperatures without coarsening is introduced in the Cu–Ti matrix material it is possible to combine two different strengthening mechanisms: precipitation hardening and dispersion hardening. The choice of $TiSi_2$ as dispersed phase meets some of the basic rules for dispersion hardened systems: dispersed phase/matrix minimal coherency strain, complete insolubility of dispersed phase in the matrix, high melting point of dispersed phase compared to the matrix and good mechanical bonding between the matrix and dispersed phase. Bozic [112]

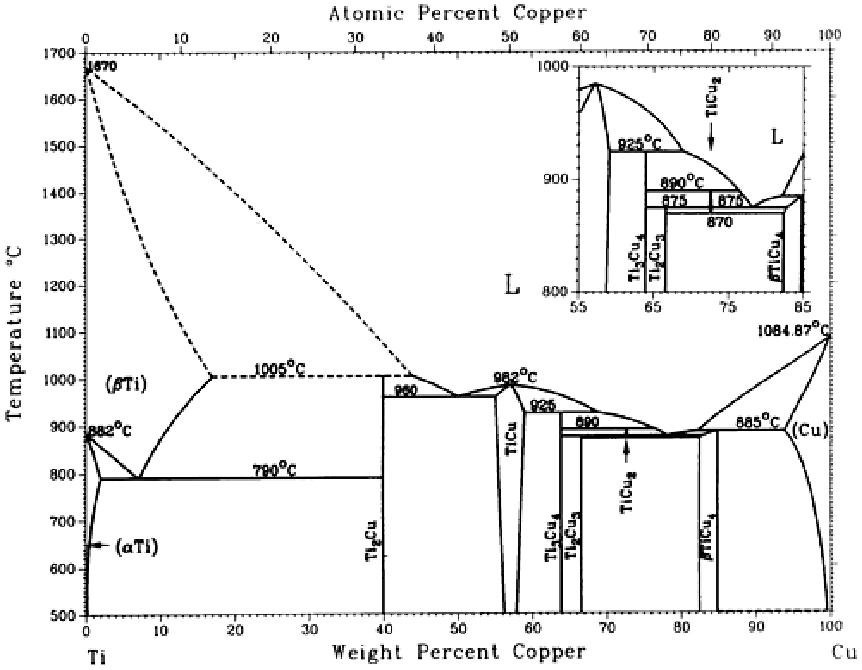

Figure 3.26 Equilibrium phase diagram of Cu-Ti phase diagram. ASM [107]

3.7. Summary

In Chapter 3, theoretical background, the basic working principal of EDM was discussed in details including modelling of MRR and surface roughness. The role and the properties of dielectric material liquid in electric field also discussed. The dielectric should have strong dielectric resistance and it should ionize. Cu-W and graphite EDM electrodes can only be manufactured using copper electrode.

Taguchi design of experiment is discussed in details in section 3.4. The main point can be concluded is that Taguchi's DOE is one of the main parameters technique optimization used when experimental design involving a large number of design factors but least number of experiments is important.

Mechanical alloying by ball milling can be influenced by milling medium, speed, time, milling atmosphere, ball to powder ration, temperature, and grinding medium. But the final density is directly related to the consolidation technique. Hot pressing and hot Isostatic pressing is the main candidate for to achieve a full density product.

CHAPTER 4

METHODOLOGY

4.1. Introduction

This chapter is divided into three sections. The first part is the preliminary study on machining two different materials using Copper electrodes. This part is relevant to the basic knowledge, selection of the most effective variables, and the current conditions of the equipment.

The second section focuses on machining of hardened steel tool using the conventional Copper-Tungsten electrodes. This area is important to optimize the selected machining variables and to create reference data for validation of the performance of the new modified electrode.

The third section is focused on the synthesizing and manufacturing methods of the new tool electrode material using high-energy ball mills and hot pressing. Characterization was carried out using an optical microscope, scanning electron microscope (SEM), X-ray diffraction (XRD) and transmission electron microscopy (TEM). All experiments were designed and analyzed using Taguchi technique.

The selection of electrode material is the first step to ensure machining process efficiency and surface quality. Thus, the tool electrode properties can be selected in diesinker EDM to meet the optimal machining efficiency. In order to enhance machining quality, the second option is the optimal setting of the most important variables to give high material removal rate without increasing the electrode wear and the surface roughness. Figure 4.1 shows the main of methodology used to carry out this research work where it divided into three main steps including parameter selection, optimization, manufacturing of the new EDM electrode using ball milling, and performance of new electrode on machining of hardened die steel.

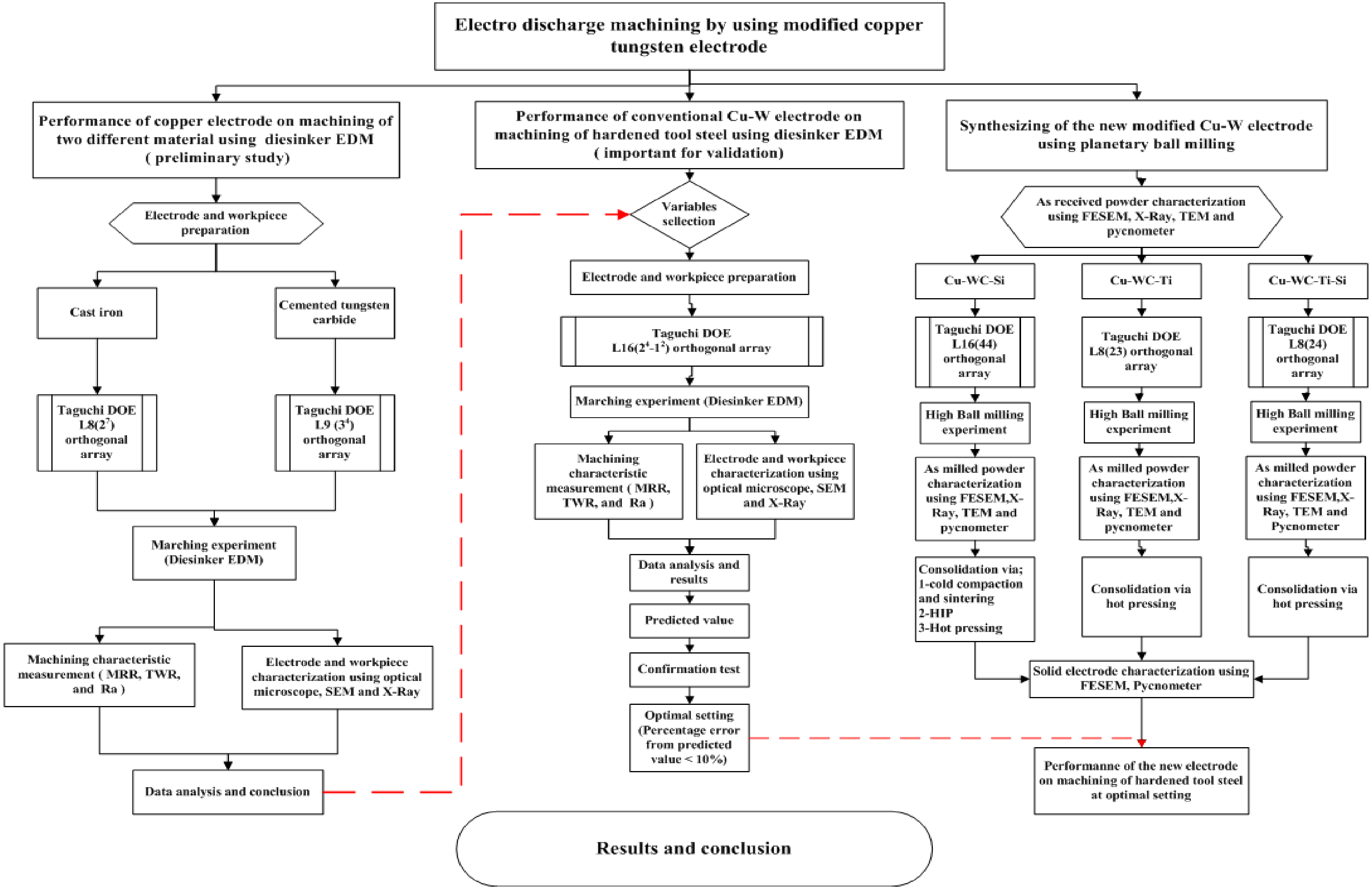

Figure 4.1 Research planned

The performance of diesinker EDM depends on how the electrode and workpiece material respond to the machining variables setting. Table 4.1 below summarizes key properties of the electrodes and workpiece material used in this research. The properties of the new powder metallurgy electrodes are expected to be hybrid of pure Copper electrode and the Cu-W electrode.

Table 4.1 Electrical, thermal, and mechanical properties of tool electrodes and workpiece materials at room temperature. [113], [114], [115],and [116]

Properties	Electrode material		Workpiece materials		
	Cu	Cu-W	Cast iron	Die steel	Cemented Tungsten carbide
Melting point (^{0}C)	1083.0	3422.00	1500.0	1400.0	2800
Electrical conductivity	100.0	34.00	2.0-	3.0-15.0	7.5-12
Thermal conductivity	401.0	130.00	46.0	16.7.0	45-80
Density (g/cm^3)	8.9	15.15	7.3	7,7	14.0-14.6
Hardness (HRB)	110.0	230.00	92.0	120.0	1660 (HV)
Thermal expansion	17.0	-	12.0	12.0-	5x10-4
Young modulus (Gpa)	90.0	230.00	80.0	140.0-	450 – 650

4.2. Preliminary Study

Preliminary study involves the selection of electrode and workpiece material, characterization of electrode and workpiece material, sample preparation for metallographic investigation, selection of machining variables, Design of experiments (DOE), conducting the experiments to study the effect of discharge parameters on the EDM roughing process, measuring of machining characteristic such as MRR, TWR, Ra and heat effected layer.

Since the machining process depends on the electrode and the workpiece material, characterization of electrode on workpiece material prior machining is important. Microstructures analysis was carried out for qualitative and quantitative description of the microstructure using size, shape, composition, and change of phases. This investigation was carried out using an optical microscope, FESEM, TEM and X-Ray.

4.2.1. Machining of Gray Cast Iron Using Conventional Copper Electrode

Machining of gray cast iron is carried out to find the most important machining variable and the optimal setting of these variables. All machining experiments were conducted on NC oil die-sinking EDM Machine (EA 8) from Mitsubishi electric corporation. This machine was programmed for X, Y, Z, and rotation around z-axis. The machining is having servo controls programmed to follow the NC code, inserted by the control panel. The servo system also controls the electrode jump up the distance and frequency.

These two are very important parameters are regarding the machining time, cooling rate and debris removal. During machining, the machining time and depth are displayed online on NC screen and machining can be programmed to stop at the targeted depth of cut. The power supply system was designed to produce an AC 3-Phase 200/220V 50/60Hz. The main pulse power generator circuit methods are the transistor pulse circuit (TP), slope control circuit (SC), fine surface finish circuit (SF), and mirror surface finish circuit (MSF). As shown in Figure 4.2, the numbers of diesinker EDM variables that can influence the machining process of diesinker EDM are very large and cannot be optimized by single setting.

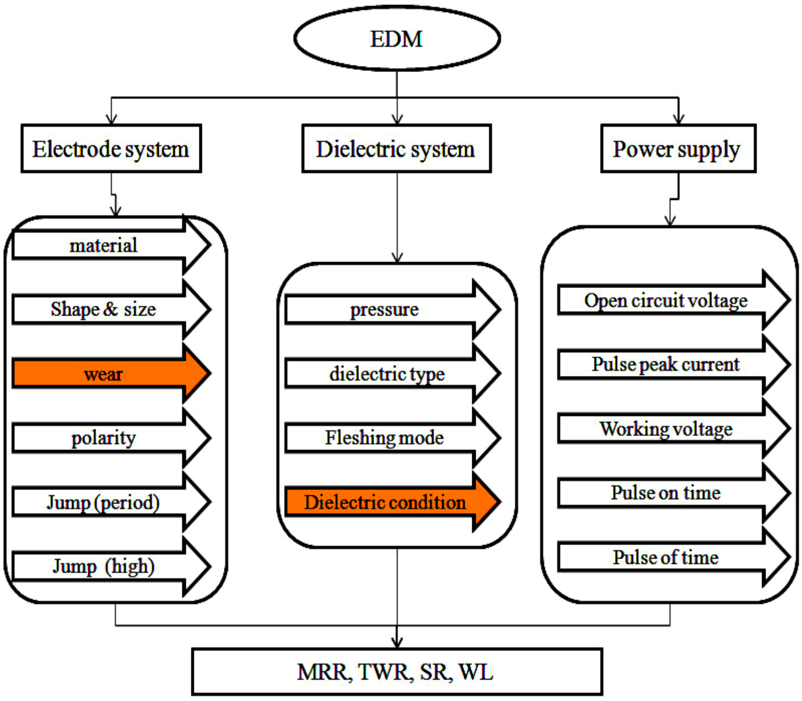

Figure 4.2 Schematic diagram shows the diesinker EDM parameters that can influence MRR, EW, Ra and heat effected layer, including uncontrolled variables.

4.2.1.1.Material Selection

The critical property of the electrode and workpiece material is the electrical conductivity [117].

1- Copper is the commonly used EDM electrode due to its high electrical conductivity [59,6x10^3 (cm.Ω)$^{-1}$] and low cost. It is a suitable material for preliminary study since the electrode wear can be seen clearly and high peak current can be used.

2- Cast iron is one of the frequently used materials in the industry, especially when the desired shape is small with very complex shape such as coins or trademark stamp on metal product. Since EDM involves a thermal erosion process, the main property of concern is the workpiece conductivity.

4.2.1.2.Metallographic study

a- Sectioning

Sectioning of specimens from a larger sample, is one of five major steps in the preparation of specimens for metallographic. In this work, the electrode and workpiece material were sectioned using wire cut EDM, lathe machining and grinding machining.

1- The electrode used for machining the gray cast iron workpiece was Cu cylinder cut from one meter length copper rod having a diameter of 21 mm. Each cylinder was then machined using lathe machine to 13 mm diameter and 70 mm length as shown in Figure 4.3.

2- The gray cast iron workpiece samples were sectioned from a car disk brake into 20x20x7mm rectangular prisms using wire cut EDM followed by milling machining as shown in Figure 4.4.

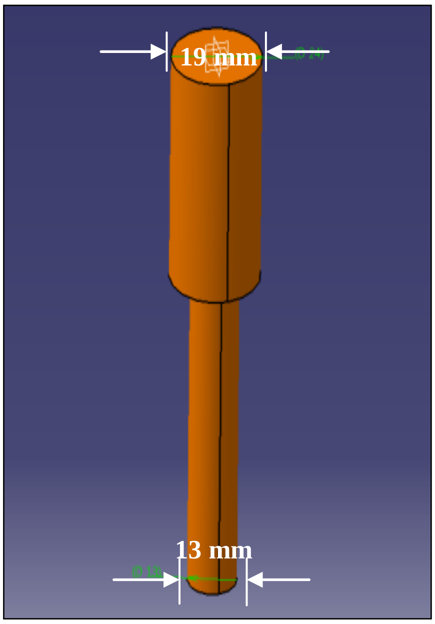

Figure 4.3 The 13 mm diameter Copper electrode

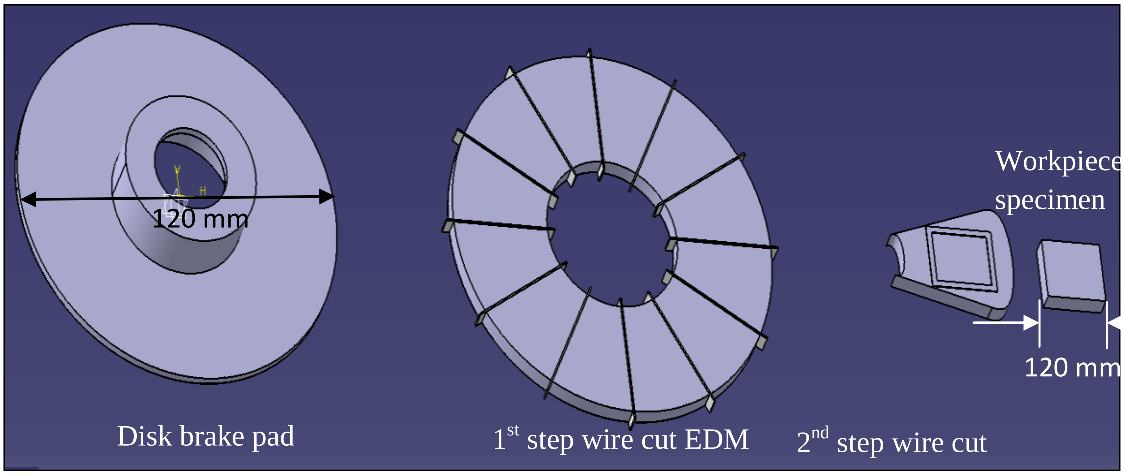

Figure 4.4 The steps of specimen sectioning from 22x22x6 mm gray cast iron disk brake pad

b- Mounting

Mounting of a specimen provides a safe handling of small and irregular samples. Mounting was carried out using [SIMPLIMENT 1000 auto mounting]. The specimen was placed on the rim face and then the ram is lowered into its lowest point. Epoxy powder was added and the mould closed. The epoxy was used because of low melting temperature, which cannot alter the microstructures of the workpiece. Finally, the cycle is operated at 4000 psi and 180°C for 10 minutes, including heating, holding, and cooling.

c- *Grinding and Polishing*

In order to investigate the structures of metallic samples that have been cut from a bulk specimen, the specimen surface is prepared to expose the structural features on this surface using optical microscope, SEM, and X-Ray. Achieving the desired surface finish requires grinding followed by abrasion using finer grades of abrasive followed by polishing processes. This requires a low speed with liquid coolant, to avoid heating of the specimen surface. Polishing was carried out using skid polishing with the cloth filled with an appropriate polishing fluid. The abrasive particles can produce fine scratches.

In this work, grinding and polishing were carried out in METASERY 2000 grinder and polisher using diamond abrasive disc at speed 246 rpm and the next steps with abrasive alumina papers with grade 400, 600, and 800. During grinding, the specimen was moved from centre to edge and rotated 90 degrees in each step. After each abrasive paper level, the specimen was washed with water. Rotation of the specimen by 45^0 during grinding is necessary. The removal of the remaining scratches and contamination from the grinding step plays a crucial role in the success or failure of producing a mirror like surface. Coarse polishing was achieved using polycrystalline diamond suspension from 6 to 1 µm. The Fine polishing was carried out using 0.3 and 0.05 µm alumina where it was distributed uniformly over the polishing cloth and the disc is rotated at speed of 246 rpm. During polishing, the sample rotated in a direction counter to the wheel rotation and washed with water after each abrasive paper level [118]. Since cemented Tungsten carbide is very hard, coarse grinding was carried out using an aggressive metal bonded diamond disc due to it is high material removal rate and low surface contamination.

d- *Etching*

Etching is used to reveal the micro structural contrast because the etchant reacts with the specimen. The selection of etchant depends on electrochemical characteristics of constituents. The common chemical etchant are the acids, bases, neutral solutions, mixtures of solutions, and salts. The main etching variables are etching time, etching temperature, cleaning material and technique. Etching times can be from several seconds to one hour depending on how etchant type reacts with the etched surface.

Etching temperature, on the other hand, can reduce etching time but in general heating is not advisable because the rate of reaction could rapidly increase leading to dark spots.

It is important to remove or halt any chemical reactions during etching. For example, etching of irons and steels using Copper containing compounds requires rinsing with alcohol first because Copper could precipitate on the specimen surface. In order to reduce the effects of etchants seeping from pores, cracks, or mounting clamp interfaces, ultrasonic cleaning was used. Also, a highly concentrated acid was used for etchant neutralization before rinsing and drying the specimen, especially with porous sample. Table 4.2 shows the main etchant used during this research for gray cast iron, cemented Tungsten carbide, and hardened die steel.

Table 4.2 Etchant used in this research. Perrin Walker [119].

Etchant name	Chemical composition	Time	Type of specimen
Nital	2 ml HNO_3 +98 ml ethanol	30-60 sec	Cast iron and die steel
Aqueous ferric chloride	10g $FeCl_3$+20ml HCl acid+ 80ml H_2O	30-60 sec	Copper electrode
Murakami's	10 grams $K_3Fe(CN)_6$ + 10 grams KOH + 100 ml Water	10-60 min	Cemented Tungsten carbide

4.2.1.3.Characterization

a- Optical Microscopy

The microstructure analyses of electrode specimen and workpiece material were carried out using Leica DM LMU Light Microscope. The top surface area of the specimen was positioned perpendicular to the optical axis and illuminated from above through the objective lenses. The X-Y movable platform was used to adjust the position of the specimen. Several images were taken at different areas for each magnification range (5x, 10 and 50x). The scale was taken by using micro hardness indenture on the same workpiece and then the image was cropped out from the indented area.

b- FESEM

The use of scanning electron microscope in the investigation is important to close the gap between the optical and the transmission electron microscope. SEM can reveal from one order of magnitude to approximately 100 nm or better. FESEM was used to revile the effect of discharge machining on surface structure.

Sample preparation for SEM required freeing the surface from any substance that changes from solid or liquid to a vapour in high vacuum such water, oil, or grease. Drying powder metallurgy sample is important to remove the trapped moist before putting it in vacuum room. Otherwise, low vacuum pressure will not be achieved. It is important to know that nonconductive material must be coated with a layer of electro-conductive material such as Pt, Au, and gold to prevent charging.

c- Energy-dispersive X-Ray (EDX)

SEM provided additional component like Energy-dispersive X-ray spectroscopy (EDX) that can be used for qualitative elemental **analysis** and chemical characterization **where** the presence and relative abundance of element can be determine. The intensity of the detected X-Ray energy is proportional to the mass fraction of element that produces it. Table 4.3 shows the mass fraction of element detected for Copper electrode, gray cast iron, and cemented Tungsten carbide. Examples of EDX profile of Copper electrodes material, gray cast iron workpiece, and cemented Tungsten carbide workpiece used are shown in Figures 4.5, 4.6, 4.7 respectively.

Table 4.3 EDX analysis of elements in electrode and workpiece

	No of Element	Element	Weight%	Atomic%
Copper electrode	1	Cu	100.00	100.00
Gray cast iron	1	Fe	92.51	77.27
	2	C	4.50	18.60
	3	Si	2.38	4.14
	4	Mn	0.61	0.37
Cemented Tungsten carbide	1	C	9.45	61.51
	2	W	90.55	38.49

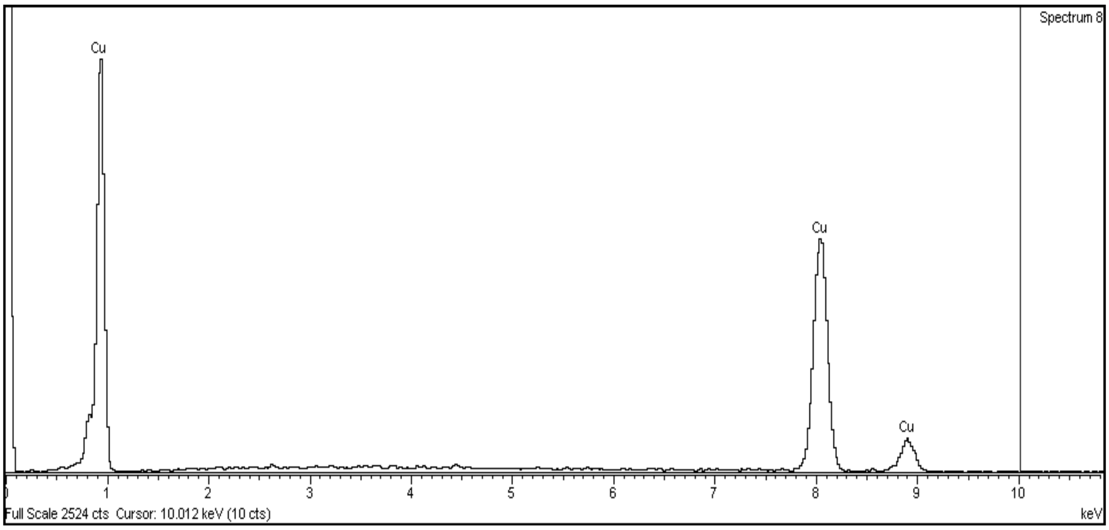

Figure 4.5 EDX spectrum of copper electrode

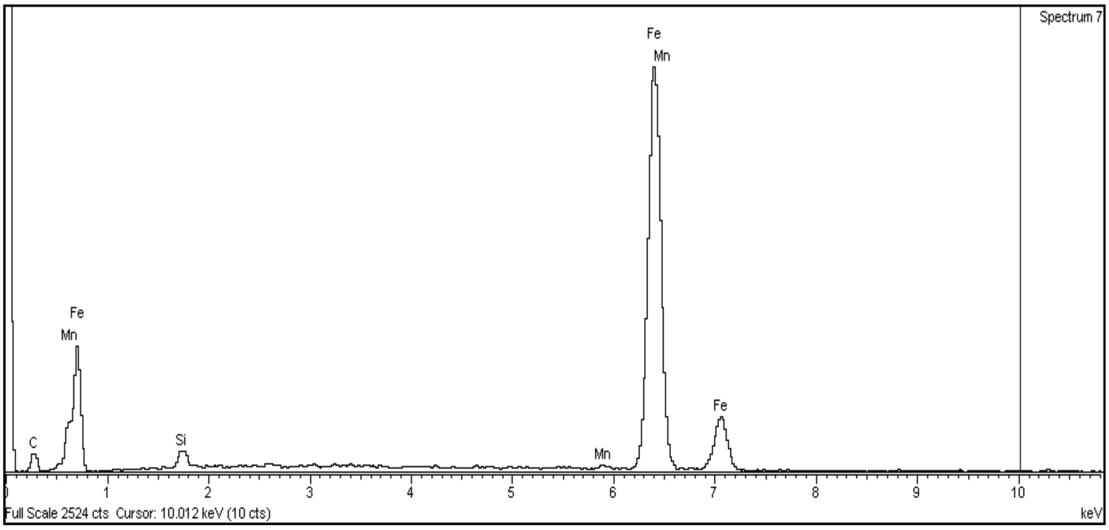

Figure 4.6 EDX spectrum of gray cast iron

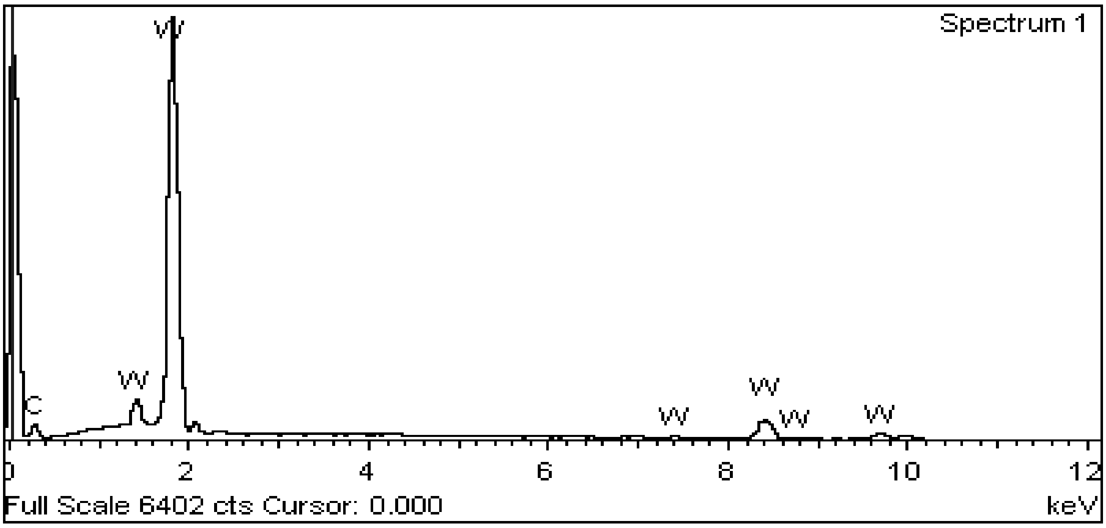

Figure 4.7 EDX spectra of cemented tungsten carbide

4.2.1.4.Taguchi Design of Experiment

An experiment was designed based on the most repeatedly used factors identified from the review. The design of experiments (DOE) is an important step in order to improve the machining processes. It is beneficial to determine which variables are important for controlling the machining process. The main advantages of this technique are; the reduction in number of experiments and the determination of the best combination (optimal setting) for optimal machining process.

a- Selection of Machining Variables

From the literature review, the most controlled variables repeatedly used to optimize the machining process are the peak current, pulse on time, pulse off-time, gap voltages, dielectric pressure, electrode jump distance, and electrode jump frequency. Thus, the design of experiments must depend on the most influencing variables keeping the rest of variables setting fixed. The material removal rates, electrode wear rate, surface roughness are important variables. Selection of variables must take into consideration the following points.

- In general, as the current peak increases, the machining speed will increase. However, the electrode wear and surface roughness also will increase.
- Longer pulse ON (pulse width) will decrease the electrode wear and increase the machining speed and the surface roughness will increase.
- Lower Pulse Off-time (Halt time) will increase the number of electrical discharges per unit time and consequently the machining speed will increase.
- The higher Gap voltage setting will improve the sludge discharge, prevent short-circuits, and stabilize the machining state.
- By moving the electrode up JU and down JD cycle during machining, the machining rate, and stability, cooling rate, and debris removal will be improved.
- Servo voltage sets the reference voltage of the servo operation to stabilize the voltage between the electrode and workpiece gap.

b- Taguchi Orthogonal Array

Taguchi DOE requires that the number of trials and the conditions for each trial must be specified. Full design of experiment using seven variables at two levels requires 2^7 Run (128 experiment). This is not manageable. It is a time consuming process to start from the preparation of electrode workpiece followed by conducting experiment, characterization, and lastly data analysis. Under low peak current and pulse on time, the machining of cemented Tungsten carbide using 13 mm diameter cylindrical Copper electrode to 4cm depth can takes over two days. Thus, Taguchi fraction of factorial design of experiment was used. The designed experiment using L8 orthogonal array by selecting seven variables at each two levels is shown in Table 4.4. This designed experiment should be run in a random order to avoid the influence of experimental setup.

Table 4.4 Design of experiment using L8 Taguchi orthogonal array for seven variables at two levels as mentioned in chapter 3.

	Peak current Code [ampere]	Pulse On-time Code [µs]	Pulse Off-time Code [µs]	Servo voltage code [Volt]	Jump up Code [mm]	Jump down code [ms]	Dielectric pressure (MPa)
Exp-1	2.5 [10]	3 [8]	3 [8]	2.5 [180]	4 [08]	2 [100]	0.02
Exp-2	2.5 [10]	3 [8]	3 [8]	4.5 [280]	7 [1.8]	4 [200]	0.04
Exp-3	2.5 [10]	7 [128]	5 [32]	2.5 [180]	4 [08]	4 [200]	0.04
Exp-4	2.5 [10]	7 [128]	5 [32	4.5 [280]	7 [1.8]	2 [100]	0.02
Exp-5	5.5 [35]	3 [8]	5 [32	2.5 [180]	7 [1.8]	4 [200]	0.02
Exp-7	5.5 [35]	3 [8]	5 [32	4.5 [280]	4 [08]	2 [100]	0.04
Exp-7	5.5 [35]	7 [128]	3 [8]	2.5 [180]	7 [1.8]	2 [100]	0.04
Exp-8	5.5 [35]	7 [128]	3 [8]	4.5 [280]	4 [08]	4 [200]	0.02

4.2.1.5.Machining conditions

The designed experiments were conducted following random order, oil diesinker EDM machine of type Mitsubishi AE series model brn-51748. The machining was conducted in rough machining setting using TP circuit. Before conducting the experiment, the mass of electrode and workpiece materials were weighed using microbalance up to four decimal with an error equal ±0.0005.The machining variable and their levels are shown in Table 4.5. The other machining parameters are kept constant as shown in Table 4.5.

Table 4.5 The full machining conditions including fixed and controlled variables

Machining factors	Code	Fixed variables	Controlled variables
Power circuit type	ES	TP	
Auxiliary power	AUX	0	
Polarity	POL	+	
Peak current	IP		Varied
Pulse On-time	ON		Varied
Pulse of time	OFF		Varied
Gap voltage	GAP	10	
Electric discharge	JS	11	
Jump up distance	JU		Varied
Jump down time	JD		Varied
Condenser selection	PICON	0	
Machining adjustment	GAIN	80	
Servo voltage	SV		Varied
OP sensitivity	OPAJ	1	
Dielectric pressure	DEP		Varied
Flashing angle		45^0	
Dielectric conditions		Uncontrolled	
Electrode wear	EW	Uncontrolled	

a- Machining Characteristics

The machining process was characterized by measuring MRR, EW from the weight loss during EDM process from the tool electrode and the workpiece using the following equations.

$$MRR(mg / min) = \frac{[(W_i)_w - (W_f)_w]}{t_m} x1000 \tag{4.1}$$

$$EW(mg / min) = \frac{[(W_i)_e - (W_f)_e]}{t_m} x1000 \tag{4.2}$$

Or directly from the volume loss of workpiece and tool, during EDM process in (cm^3/min) as;

$$MRR(cm^3 / min) = \frac{[(V_i)_w - (V_f)_w]}{t_m} x100 \tag{4.3}$$

$$EW(cm^3 / min) = \frac{[(V_i)_e - (V_f)_e]}{t_m} x100 \tag{4.4}$$

Where; $(W_i)_w$ is the initial weight of the workpiece before machining, $(W_f)_w$ is the final weight of the workpiece after machining, $(W_i)_e$ is the initial weight of the electrode before machining, $(W_f)_e$ is the final weight of the electrode after machining. σ_w is the density in g/cm^3 of the workpiece, ρ_e is the density of electrode material in g/cm^3, and t_m is the machining time in minutes.

According to Govindan [32] and Kung [120], the Tool Wear Ratio (TWR) can be measured as the ratio of the electrode wear rate to the material removal rate of the workpiece as follows;

$$TWR = (\frac{EW}{MRR}) x100 \tag{4.5}$$

Surface roughness was measured using Metotoyo surface roughness tester Model CS-3000. The average of ten readings was taken from the machined surface parallel to the electrode axis (side surface).

Over cut of the drilled holes was measured using Vernier calliper by taking an average of at least five readings taken at different rotation.

$$OC = \left(\frac{d_h - d_e}{2} \right) \tag{4.6}$$

Where; d_h is the hole diameter and d_e is the electrode diameter. [121]

b- Data Analysis

The main objectives of Taguchi analysis are to understand the optimum condition and the contribution of each factor to the results. Also to determine the deviation of expected result from the predicted values subjected to confirmation test with the goal of achieving minimum error when compared to the predicted value. In general, as MRR increases the EW and Ra also increase proportionately.

The preliminary analysis is important to show the percentage of the contribution of the factors and how these variables affect the targeted quality characteristic. The quality characteristic of MRR is “the higher is better”, for electrode wear, surface roughness and for over cut “the lower is better’. Table 4.6 shows the main steps used for Taguchi design and analysis of experimental. For further details Roy [86, 122]

Table 4.6 The calculation steps for Taguchi data analysis. El. Haik [85].

No	Steps	Details
1	Degree of freedom of factors	Number of levels of that factor (A) minus one
2	Replication	Number of repetition for each setting
3	Response	Machining results for each factor level combination
4	The average responses	Summation of the results equivalent to that factor level divided by the number of trials at that level trail
5	The quality characteristic	• The higher is better (MRR) • The lower is better (EW & Ra)
6	Analysis of variance (ANOVA)	• Computing the sum of squares (SS) • Computing the mean squares (MS) by dividing the SS by the degree of freedom
7	Relative contribution	• Computing the total sum of squares • Computing the percentage contribution
8	Main-effects chart of variables	The plot of average responses at different levels of a factor versus the factor levels
9	Optimization	The Best factor level setting for optimal performance depending on quality characteristics
10	Confirmation test	Analyzing the variation of confirmation test from the predicted values

4.2.2. Machining of Cemented Tungsten Carbide Using Copper Electrode

4.2.2.1.Material Selection

Since the electrode material is the key factor in die-sinker, Copper was kept as a tool electrode for machining to avoid any high variation of result due to different electrode wear rate. The selection of the same tool electrode will give a chance to make a comparative study by machining of two different materials. Cemented Tungsten carbide is one of the most challengeable materials for machining in engineering industries. This material mainly used as tool for tools milling and mining tools since it gives high levels of hardness and wear resistance. Cemented Tungsten carbide was chosen to replace expensive diamond wire drawing dies for Tungsten filaments. The main properties of this material are shown in Table 4.1. Upadhyasa [114].

4.2.2.2.Sectioning

The hardness and cutting characteristics of cemented Tungsten carbide make it impossible to be sectioned by conventional cutting. Tungsten carbide workpiece specimen was sectioned from a 100 mm x 50 mm rod using wire cut EDM Model FA10 in steps as shown in Figure 4.8. The Wire cut has the advantage of accurate cutting action and very thin heat effected layer, which can be removed during grinding.

High-energy setting of cutting parameters may cause a break in the wire leading to the termination of machining operation. The wire failures occur when the wire becomes in contact with one of the three surfaces (U shape). The electrode used for machining cemented Tungsten carbide workpiece was sectioned by using conventional lathe machining. Since machining of cemented Tungsten carbide required fleshing of dielectric through electrode, a 5 mm diameter cylindrical hole was made using lathe machining as shown in Figure 4.8.

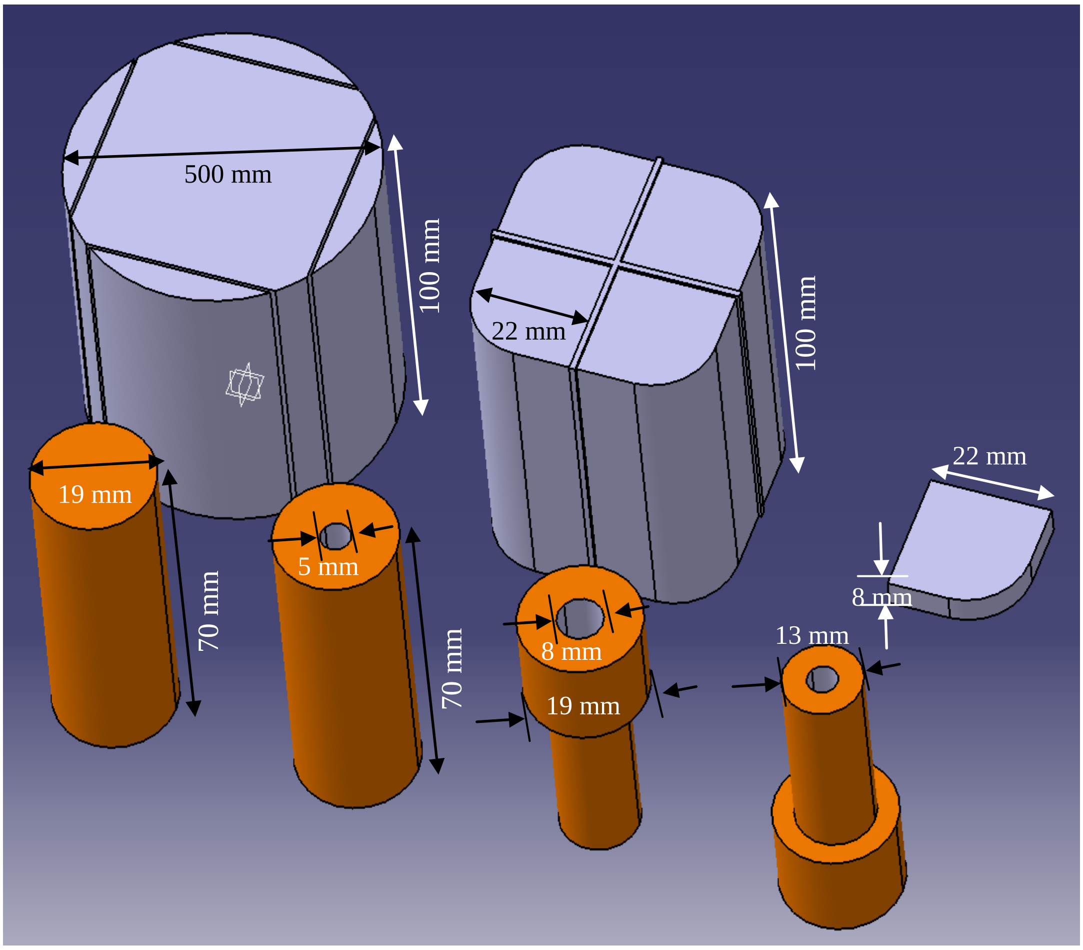

Figure 4.8 Copper electrode and cemented Tungsten carbide workpiece specimen preparation using lathe machining and wire cut EDM respectively.

4.2.2.3.Design of Experiment

Pre-experimental Taguchi design of experiment requires the selection of control factors and their levels. Control factors are machining variables that control to optimize the process. The selected machining variables are the peak-current, Pulse On-time, pulse Off-time and Gap-Voltage. Factors that cannot be control during machining process such as electrode wear and dielectric conditions are called uncontrolled factors (or noise).

Taguchi Design was developed according to the selected machining variables and setting as shown in the Table 4.7 where the unit of variables are displayed in code and unites (in-between bracket). The layout of the designed machining experiment using L9 Taguchi orthogonal array are shown if Table 4.8.

Table 4.7 Machining variables and there levels in codes unit and explicit unit (in between bracket)

levels	Peak-Current Code[Amp]	Pulse On-time Code[μs]	Pulse Off-time Code[μs]	Gap-Voltage Code[volt]
1	3.2 [12]	6 [64]	4 [16]	10 [80]
2	3.4 [14]	7 [128]	5 [32]	11 [110]
3	3.5 [15]	8 [256]	6 [64]	12 [150]

Table 4.8 L_9 Taguchi orthogonal array displayed in codes (explicit unit)

	L9 orthogonal array			
	Peak-Current Code[Amp]	Pulse On-time Code[μs]	Pulse Off-time Code[μs]	Gap-Voltage Code[volt]
Exp-1	3.2 [12]	6 [64]	4 [16]	10 [80]
Exp-2	3.2 [12]	7 [128]	5 [32]	11 [110]
Exp-3	3.2 [12]	8 [256]	6 [64]	12 [150]
Exp-4	3.4 [14]	6 [64]	5 [32]	12 [150]
Exp-5	3.4 [14]	7 [128]	6 [64]	10 [80]
Exp-6	3.4 [14]	8 [256]	4 [16]	11 [110]
Exp-7	3.5 [15]	6 [64]	6 [64]	11 [110]
Exp-8	3.5 [15]	7 [128]	4 [16]	12 [150]
Exp-9	3.5 [15]	8 [256]	5 [32]	10 [80]

4.2.2.4.Conducting the Experiments

The designed experiments were conducted in oil diesinker EDM machine of type Mitsubishi AE series model brn-51748 in the following order 1, 9, 2, 8, 3, 7, 4, 6 and 5. As remarked in section 4.2.1.10, the machining experiment was conducted in rough machining setting using TP power circuit. The machining variable settings are shown in Table 4.9.

Table 4.9 The full machining conditions including fixed and varied variables

Machining factors	Code	Fixed variables setting	Controlled variables
Power circuit type	ES	TP	
Auxiliary power	AUX	0	
Polarity	POL	+	
Peak current	IP		Varied
Pulse On-time	ON		Varied
Pulse of time	OFF		Varied
Gap voltage	GAP		Varied
Electric discharge	JS	11	
Jump up distance	JU	2	
Jump down time	JD	3	
Machining adjustment	GAIN	80	

4.2.2.5.Data Analysis

Taguchi data analysis requires the following two steps: the Analysis of variance (ANOVA) and main-effects chart. Assuming that the factors are A, B, C, and D and the factors level is k (here equal 3). If Yi represents the machining response corresponding to the ith level, then the total sum of response equivalent to that factor is $Y_t = \sum_i^k Y_i$ .Taking the number of runs as N (equal 9), and the number of replicates is n (equal 1), then the sum of squares (SS) for each factor can be calculated by using equation 4.7 given by Yang [85].

$$SS = \frac{k}{N * n} \sum_{i=1}^{k} Y_i^{\,2} - \frac{(\sum_i^k Y_i)^2}{N * n} \tag{4.7}$$

This calculation will be repeated for all other controlled variables for MRR, EW, and Ra. The total sum is the sum of sum of squares for all factors and is given by;

$$SS_t = SS_A + SS_B + SS_C + SS_D + SS_{Error} \tag{4.8}$$

The percentage contribution of any of these factors is computed by dividing the sum of that factor divided by the total sum of square multiply by 100.The total sum of the percentage contribution should be equal to 100 as follows;

$$100 = \frac{SS_A}{SS_t} x100 + \frac{SS_B}{SS_t} x100 + \frac{SS_C}{SS_t} x100 + \frac{SS_D}{SS_t} x100 + \frac{SS_{Error}}{SS_t} x100 \tag{4.9}$$

By arranging this from high to low, the percentage contribution of factors on any of responses such as MRR, EW, and Ra can be plotted to evaluate the relative importance of each effect. The factor with higher percentage contribution is considered to be more important. As an example, if factors D, A, C, and B contribute to MRR by 3, 7, 30 and 60, then the percentage contribution chart will be in the form;

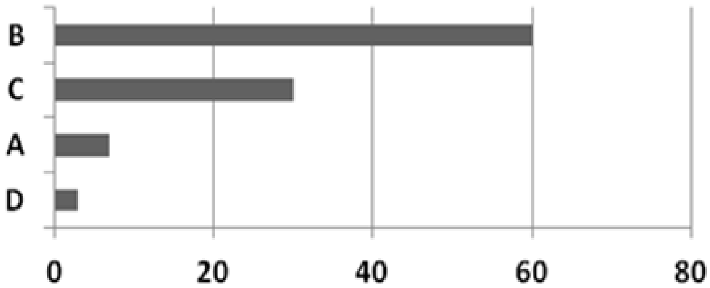

Figure 4.9 Example of percentage contribution chart. El. Haik [85].

4.3. Machining by Using Conventional Cu-80%W Electrode

Cu-W electrodes combine the high conductivity of Copper with thermal wear resistance of Tungsten. These electrodes exhibit very good wear properties and that is why they are mostly used for machining the high melting point material such as cemented Tungsten carbide or when a sharp corner is needed. The difficulties of manufacturing in addition to the high cost of Tungsten make Cu-W electrode very expensive.

Since the objective of this research is to develop a new modified Copper-Tungsten electrode, the performance of the new electrode will be compared with the performance of the current used Cu-W electrode. This is the main reason why this electrode is selected for validation.

4.3.1. Workpiece and Electrode Material Selection

EDM is Un-conventional machining technique recommended for any machining material that is difficult to be machined by conventional technique. The selected material is the high chromium vanadium cold work die steel type 2379/RCC Supra. This material is able to withstand high load. Due to the relatively low carbon content, this material prevents scaling or cracking which is the common problem in die and tool manufacturing. This material also shows a very high toughness after heat treatment and is recommended for abrasive tools, metal forming tools, cutting tools, punches, die for cold extrusion, and as a tool for cutting. Since the result of this step will be used as a data reference for validation, the electrode should be the currently used Cu-W electrode.

4.3.1.1.Characterization

In order to confirm the specification form supplier, characterization of the samples was carried out using X- ray diffraction, optical characterizations and scanning electron microscopy. XRD equipment is available in the Department of Mechanical Engineering and others are available in UTP Research center.

4.3.1.2.Hardening

The optimum hardening temperatures for 1.55 % C is 750 $\pm 10^0$C. Quenching is aimed at obtaining martensite with a fine-grain structure. Hardening is carried out by heating the work to 1050^0C for 90 minute and then quenching in air until a temperature slightly higher than A1 for steels is reached (around 750^0C) which is the optimum hardening temperatures of steel as shown in Figure 4.10. At this temperature, oil quenching was used to fix the optimal structure for high hardness, which is a mixture of very fine pearlite + cementite (iron carbide). The degree of hardening S is the ratio of the after quenching hardness (H) to the maximum hardness of the sample before hardening (H_{max}). Quantitatively, the degree of hardening is given by George [123] as follows;

$$S = \frac{H}{H_{max}} \tag{4.10}$$

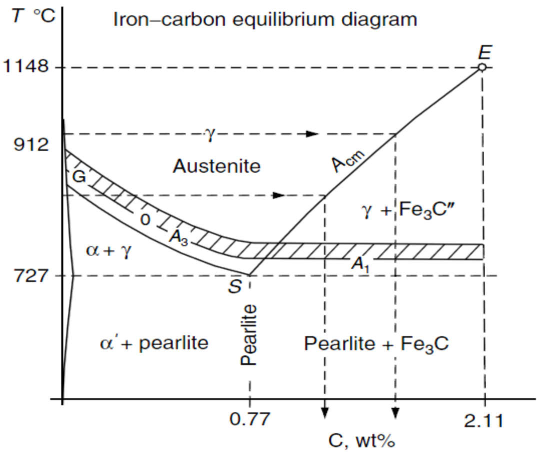

Figure 4.10 The range of optimum hardening temperatures. Totten [123].

Table 4. 10 Correlation between degree of hardening and percentage of martensite in the quenched structure. Totten [123].

Percent Martensite	Degree of Hardening S
50–60	0.70–0.74
60–70	0.74–0.76
70–80	0.76–0.78
80–85	0.78–0.81
85–90	0.81–0.86
90–95	0.86–0.91
95–97	0.91–0.95
97–100	0.95–1.00

4.3.1.3.Electrode and Workpiece Preparation

Figure 4.11 show the steps of workpiece specimen preparation from a 400 x 50 x 50 mm^3 bar using wire cut EDM. The bar was divided into four equal parts using abrasive cutting. After hardening, the 90 x 50 x50 mm^3 was sectioned using wire cut EDM. The final workpiece specimen is 24x24x7 mm^3 rectangular. Figure 4.12 shows the steps electrode manufacturing from 200 x 22 x 22 mm^3 Cu-W bar using wire cut. The 13 mm diameter was divided into 25 equal parts each is 7 mm high. This small electrode required special electrode clamper. The clamper is made from 21mm diameter Copper rod by creating a 20 mm hole of 15 mm diameter using lathe machining. Two parallel slots were made by using drilling. The electrode finally can, therefore, be clamped using the two parallel half cylinders and tightened using adjustable ring.

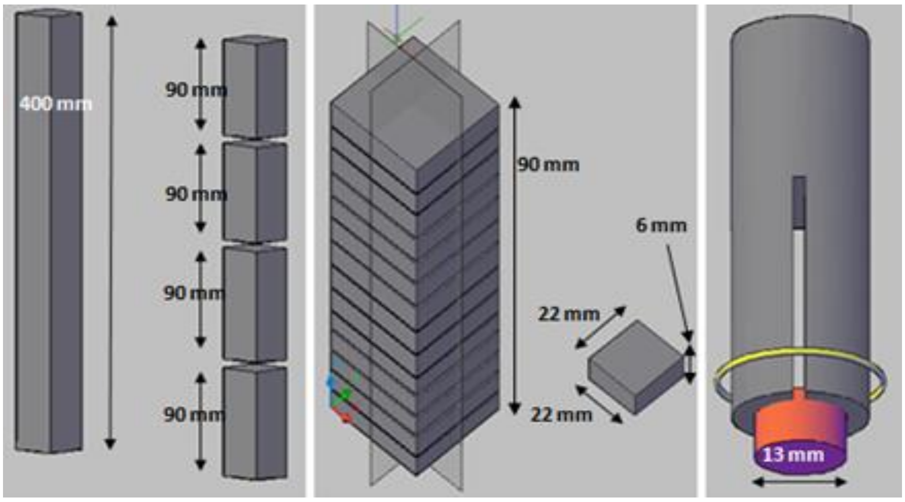

Figure 4.11 Preparation of workpiece from hardened die steel using wire cut EDM. The 7x13 mm^2 electrodes prepared using lathe machining and milling.

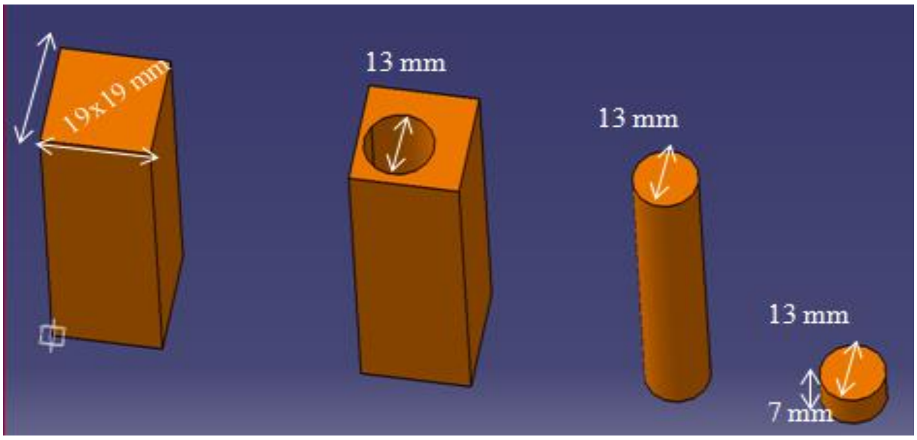

Figure 4.12 Preparation of Cu-W electrode using wire cut EDM

4.3.2. Machining

The machining was carried out using AE series model barn-51748 oil diesinker EDM machine of Mitsubishi type. The machining was conducted in a rough machining setting using TP power circuit by selecting the peak current, pulse On-time and gap voltage as controlled variables and the other variables were kept constant as shown in Table 4.11. The setting levels of the selected variables in CNC code and actual unit are given in Table 4.12. The gap voltage which is the potential difference between the electrode and workpiece before any discharge takes place is set at two levels.

Table 4.11 Variables setting including fixed and varied variables

Machining factors	Fixed variables	Controlled variables
Power circuit type (ES)	TP	
Auxiliary power (AUX)	0	
Polarity (POL)	+	
Peak current (IP)		Varied
Pulse On-time (ON)		Varied
Pulse of time (OFF)	4	Varied
Gap voltage (GAP)		
Electric discharge stability(JS) (JS)	11	
Jump up distance (JU)	2	
Jump down time (JD)	3	
Condenser selection (PICON)	0	
Machining adjustment (GAIN)	80	
Servo voltage (SV)	0	
OP sensitivity (OPAJ)	8	

Table 4.12 . The variables levels in codes and explicit unit

levels	Peak-Current Code [Amp]	Pulse On-time Code [µs]	Gap Voltage Code [volt]
1	1.5 [5.5]	4 [16]	0 [80]
2	2.5 [10]	5 [32]	1 [110]
3	3.5 [15]	6 [64]	
4	4.5 [25]	7 [128]	

4.3.2.1.Design of Experiment

Out of seven variables selected during the preliminary study, three variables were adopted as the machining variables for the rest of this research. Optimizations of these variables require a higher-level orthogonal array. The L16 Taguchi orthogonal array shown in Table 4.13 was used for mixed level design of experiment using two variables at four levels and one variable at two levels. The interactions among variables are not included in this design.

Table 4.13 Mixed two&4 levels L16 Taguchi orthogonal array

	Peak currant	Pulse On-time	Gap Voltage
Exp-1	1.5	4	0
Exp-2	1.5	5	0
Exp-3	1.5	6	1
Exp-4	1.5	7	1
Exp-5	2.5	4	0
Exp-6	2.5	5	0
Exp-7	2.5	6	1
Exp-8	2.5	7	1
Exp-9	3.5	4	1
Exp10	3.5	5	1
Ex-11	3.5	6	0
Exp12	3.5	7	0
Exp13	4.5	4	1
Exp14	4.5	5	1
Exp15	4.5	6	0
Exp16	4.5	7	0

4.3.2.2.Machining results and optimization

The machining process was characterized by the MRR, EW, and Ra. The electrode and workpiece weight were recorded before and after machining and with the knowledge of milling time, these quantities can be calculated using equations 76 and 77 respectively. The percentage of electrode wear EW relative to the MRR which is called tool wear ratio TWR measured because it gives better since about the wear resistance and can be measured as the percentage of ratio of EW/ MRR.

The machined clearance between the electrode corner and the workpiece side wall is known as overcut and it is an important EDM characteristic. It is calculated by dividing the difference between the diameter of the electrode before machining and the diameter of the machined hole on workpiece divided by 2.

The analysis of variance was used to plot the percentage contribution of factors and the main effects plot. The influence of factors and the optimal conditions were measured from the plot of factor average effect. This plot depends on the calculation of the average standard deviation, grand average and the factor averages.

4.3.2.3.Confirmation Test

The best setting of the selected factors for optimal targeted response (depends on the quality characteristic) was predicted from the plot of factor average effect of Taguchi experiment. The response tables and main effects plots were analysed to identify the factors and settings that have the greatest effects (reduce the variation). The predicted values of the responses at the selected combination of factors (optimal settings) are tested experimentally to determine how well the prediction matches the observed result.

Ultimately, the percentage error of the confirmation test from the predicted value was calculated. The effect of interactions between the observed results and predictions is not included in this analysis. If contribution of this interaction on machining results is high, then the deviation of the predicted values from the observed results will increase.

4.4. Synthesizing Cu-WC-Si, Cu-WC-Ti, and Cu-WC-Ti-Si nanocomposite

Figure 4.13 show the main steps of synthesising and characterization of Cu-WC-Si, Cu-WC-Ti, and Cu-WC-Ti-Si nanocomposite using high-energy ball mills. The first step prior to conducting the experiment is the selection of milling variables.

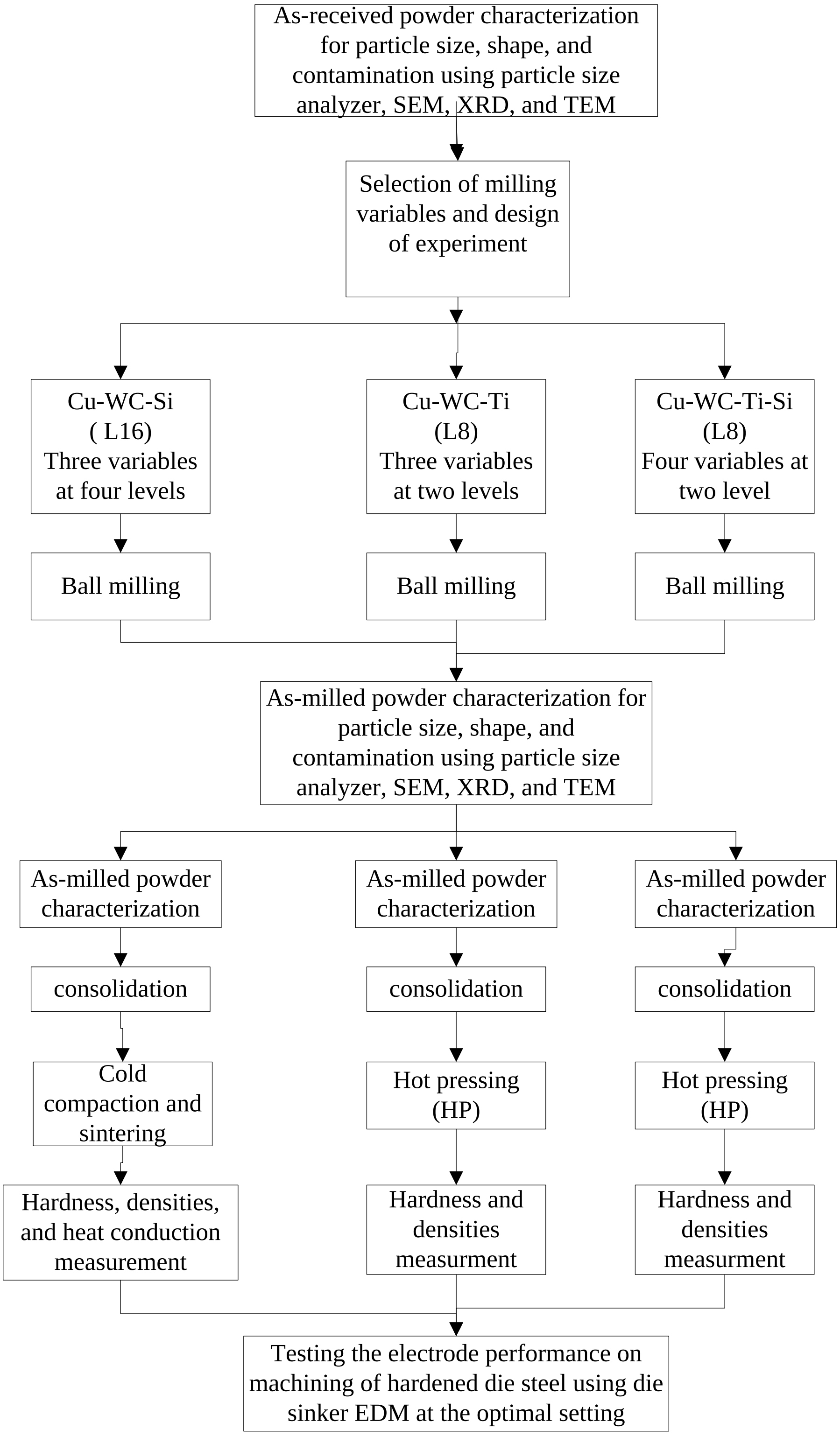

Figure 4.13 Schematic diagram the whole processing including synthesizing, characterization, and electrode performance.

4.4.1. Justification of new EDM electrode material selection

High-purity Copper containing small amounts of silver or phosphorus melts at 1083°C, which is relatively low value. The electrical conductivity of copper at room temperature according to International Annealed Copper Standard (IACS) is 100%, while thermal conductivity the oxygen-free copper is 391 W/m.K, which is the highest value among the cast copper alloys .

Tungsten is a metallic transition element characterized by the high melting temperature and relatively high thermal conductivity (144 W/m.K) compared to copper (445 W/m.K). The melting point of tungsten varies between 3387°C and 3422°C and the thermal conductivity varies between 167-190 W/m.K Lassner [97].

Copper-Tungsten Cu-W binary phase diagram in Figure 3.21 shows that Tungsten is insoluble in liquid Copper. Cu-W composite which combine the beneficial properties of both metals are used as main EDM electrode materials for machining cemented tungsten carbide. Rao [106].

Tungsten carbide is not only a hard material but also has a high melting point making it a suitable material to act as main filler for an EDM electrode. The electrical conductivity of WC is in the same range as tool steel and carbon steel, but the melting point is double as shown in Table 4.1. Tungsten carbide can be produced in a pure state by mixing the appropriate amounts of Tungsten powder with black carbon or Graphite and subsequently heating in hydrogen atmosphere to over 1600^0C. The high melting point, good conductivity, and manufacturability of WC can make it an alternative to replace tungsten in Cu-W electrode because electrical conductivity is not the only concerned property. The Tungsten monocarbide is the only stable Tungsten carbide at room temperature. It can be produced either through the reaction of Tungsten trioxide with carbon in an inert atmosphere, vapour phase deposition, or by electrolysis of fused salts.

Table 4.14 shows the main properties of materials that can create a metallic bonding with copper and tungsten resulting in relatively high melting point, high thermal conductivity and relatively good electrical. Any of these materials can be used as a binder for Copper-Tungsten composite but depending on the targeted properties.

Silicon is the second most abundant element after oxygen and used in glass as silicon dioxide, semiconductor, solar cells, tools, cement, grease and oil. Silicon has a relatively high melting temperature 1400^{o}C. Similar to water, Silicon density increases with temperature such that its density in liquid state is greater than in solid state. The thermal conductivity of silicon is 149 W/m.K and it is used as a heat sink in semiconductors. Silicon can form silicide with tungsten and copper at temperatures lower than the melting point of the component.

The two types of silicide compounds that can be formed by the reaction of Tungsten with Silicon are penta tungsten trisilicide W_5Si_3 and tungsten disilicide WSi_2. These compounds can be produced by the reaction of the elements in powder form in a protective atmosphere. Tungsten silicide forms a protective layer at the surface of Tungsten and prevents destructive oxidation at elevated temperatures.

The electrical conductive tungsten silicide was used to improve the erosion-resistance of protective coatings for infrared furnace windows. Tungsten silicide also used as gate electrode and as a bottom electrode for storage capacitors and transistors. In both cases, thermal stability up to 780°C with low leakage current has been shown. The electrical conductivity of tungsten disilicide is in the range (33.4–54.9) x10^{-6} W/m.k.

Copper-Silicon (Cu-Si) systems are used for several applications such as Silicon Bronzes, heat sink for electronic devises, and recently as Li-ion batteries. The Cu-Si intermediate phases are located in the Cu-rich part of the phase diagram, between 5 and 25 at % Si. The only congruent melting compound, Cu_3Si, is an intermediate solid solution with a small composition of Si atomic weight percent ranges from 23% to 25% and a melting point of 859^{0}C.

Titanium is a corrosion resistant material with a high melting point and good thermal conductivity but the electrical conductivity of Titanium is 3.9% relative to copper electrical conductivity. There is lack of information available in the literature on the intermetallic compounds of titanium with tungsten, which are potential candidates for high temperature applications.

Tungsten-titanium alloy is used as a sputtering target in the manufacture of microelectronics devices, such as very large and ultra-large-scale integration. Thin W-Ti layers are sputtered onto Silicon substrates and act as a diffusion barrier. W-10Ti alloy targets are produced by blending ultrapure Tungsten and Titanium powders obtained by vacuum melting and subsequent pulverizing, followed by pressure sintering.

Eagle refractory metal composite materials are a combination of tungsten or tungsten carbide with copper or silver which are manufactured by using sintering at high temperature followed by infiltration of copper or silver under controlled conditions. The composite show a superior arc and wear resistance, high physical properties at elevated temperatures, and good electrical and thermal conductivity. online data base [124].Table 4.15 shows the main mechanical and physical properties of different grade of copper tungsten and copper tungsten carbide composite materials.

Table 4.14 Main properties of materials that can creates metallic bonding with copper and tungsten [125], [126] and [101]

	Group name	Melting point ^0C	Density g/cm^3	Electrical resistivity k(Ω.cm)$^{-1}$	Thermal conductivity W.m^{-1}.K^{-1}	Vickers hardness MPa	Uses:	Atomic radius pm	Crystal structure
Copper Cu	Transition metals	1083	8.96	588.2	401	363	Electrical conduction	135	Cubic close packed
Tungsten W	Metalloids	3422	19.25	177.0	173	3430	Wear resistance materials	135	Body center cube
Tungsten carbide WC	Composite	2800	14.8-15.7	15.4	42	1300	Wear resistance materials	…	Hexagonal
Silicon Si	Transition metals	1414	2.33	0.1	149	982	Semiconductors	110	Diamond
Titanium Ti	Transition metals	1668	4.5	18.1	21.9	970	Resistance to corrosion	140	Hexagonal close
Zirconium Zr	Transition metals	1855	6.62	25.0	22.6	903	Nuclear application	155	Hexagonal close
Hafnium Hf	Transition metals	2233	13.3	28.2	23	1760	Plasma setting electrode	155	Hexagonal close
Iron Fe	Transition metals	1538	7.86	103.1	80	608	Steel	140	Body center cube
Tool Steel	-----	-----	7.6-7.89	19-52	13.6	252-780	-----	-----	----
Graphite		3650 (Sublimation)	2.25	0.17	24	-------	-----	-----	not isotropic
Chromium Cr	Transition metals	1907	7.15	58.8	94	1060	Stainless steel	140	Body center cube

Table 4.15 Main properties of different grade of Copper-tungsten and Copper-tungsten carbide composite materials [97, 124]

Properties at 20°C	Nominal composition in weight percent (%)						
	45Cu+55W	30Cu+70W	20Cu+80W	50Cu+50WC	44Cu+56WC	30Cu+ 70WC	30 Cu+70WC
Rockwell Hardness	79B	90B	98B	94B	99B	37C	47C
Electrical Conductivity % ACS	55	50	44	47	42	30	18
Ultimate Tensile Strength PSI	63000	85000	96000	70000	75000	85000	150000
Cross Breaking Strength PSI	110000	140000	170000	140000	160000	180000	220000
Density g/CC	12.6	14.18	15.58	11.27	11.67	12.6	12.6
Thermal Conductivity W/CM	2.4	2.01	1.82		--	--	--
Specific Heat /kg °C	251	214	188	--	--	--	--
Electro resistance	3.16	3.41	3.9	3.6	4.1	5.7	9.5

4.4.2. As-received Powder Characterization

Copper, Tungsten carbide, Titanium, and Silicon powders (> 99.5% purity) having an average particle size of 1μm were used for this study. The as-received powders were characterized for particle size, morphology, and contamination using MALVERN MASTERSIZER 2000 particle size analyser, FESEM, XRD, and TEM. The FESEM was used to observe powder morphology and particle size reduction. TEM was also used to observe the crystal structure before milling.

4.4.3. Selection of Milling Variables

Mechanical alloying and ball milling is complex processes due to the large number of variables. The selection of Taguchi orthogonal array depends largely on the number of factors selected as well as the time required by each experiment during preparation, conduction, and characterization. The importance of knowing the duration of the experiment as one of the basic requirements is that any experimental study must be limited by the project duration and it is millstone. Thus, the selected milling variables are the weight percent of WC, Ti, and Si content as well as milling time meanwhile, the other milling process variables were kept constant.

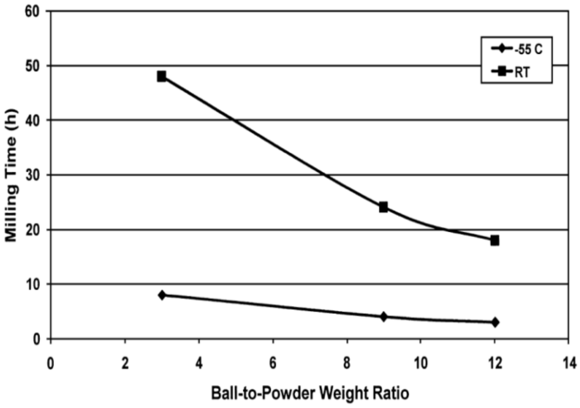

Figure 4.14 Ball-to-powder weight ratio and milling (h) at -55°C and room temperature (RT) required to synthesize Titanium during reduction of $TiCL_4$ with Mg Suryanarayana [91].

According to Suryanarayana [91], the required milling time for synthesizing depends on the ball to powder ratio and milling temperature as shown in Figure 4.14. For 12:1 ball to powder ratio, milling time ranges from 3 to 20 h. In general, milling time decreases with increasing weight ratio (BPR) and with decreasing temperature.

4.4.4. Design of Experiment

Taguchi design of experiments (DOE) technique is widely used to study the effect of several controlled factors on product and process improvement. Taguchi design of experiments was adopted for designing and analyzing the milling experiment. Table 4.16 shows the milling variables and levels used for designing the milling experiments.

Table 4.16 The selected variables for L_{16} and their levels

	Cu-WC-Si				Cu-WC-Ti		Cu-WC-Ti-Si	
Variables	Variable level				Variable level		Variable level	
	1	2.00	3.00	4.00	1	2	1	2
Time (h)	5	10.00	15.00	20.00	5	10	5	10
WC %	0	150.00	30.00	45.00	20	40	20	40
Si %	0	0.75	1.50	2.25			0	1
Ti %					5	10	10	20

The selected Taguchi orthogonal array has the following configuration. L16 Taguchi orthogonal array is shown in Table 4.17 represents the milling experiment configuration of Cu-WC-Si composite where all variables set at four levels. For Cu-WC-Ti and Cu-WC-Ti-Si composite, L8 Taguchi orthogonal arrays are used where all variables set up at two levels as shown in Tables 4.16 and 4.17.

Table 4.17 single level L16 Taguchi orthogonal array by three variables

	Milling time (h)	Tungsten Carbide (Wt. %)	Silicon (Wt. %)
Exp-1	5	0	0.00
Exp-2	5	15	0.75
Exp-3	5	30	1.50
Exp-4	5	45	2.25
Exp-5	10	0	0.75
Exp-6	10	15	0.00
Exp-7	10	30	2.25
Exp-8	10	45	1.50
Exp-9	15	0	1.50
Exp-10	15	15	2.25
Exp-11	15	30	0.00
Exp-12	15	45	0.75
Exp-13	20	0	2.25
Exp-14	20	15	1.50
Exp-15	20	30	0.75
Exp-16	20	45	0.00

Table 4.18 Single level L8 Taguchi orthogonal array by three variables all at two levels

	Milling Time (h)	Tungsten carbide (Wt %)	Titanium (Wt %)
Exp-1	5	20	5
Exp-2	5	20	5
Exp-3	5	40	10
Exp-4	5	40	10
Exp-5	10	20	10
Exp-6	10	20	10
Exp-7	10	40	5
Exp-8	10	40	5

Table 4.19 Single level L8 Taguchi orthogonal array by four variables all at two levels

	Milling time (h)	Tungsten carbide (Wt %)	Titanium (Wt %)	Silicon (Wt %)
Exp-1	5	20	10	0
Exp-2	5	20	20	1
Exp-3	5	40	10	1
Exp-4	5	40	20	0
Exp-5	10	20	10	1
Exp-6	10	20	20	0
Exp-7	10	40	10	0
Exp-8	10	40	20	1

4.4.5. Conduction of Milling Experiment

Table 4.18 shows the variables influencing the properties of the bal- milled powder for a given composition. Ball milling was carried out using PULVERISETTE 5 high-energy planetary ball mill. The as-received powders were weighed using a digital balance. In all experiments, the total amount of powder was 80 g and the ball- to-powder mass ratio was fixed at 12:1. The cemented Tungsten carbide ball of 10 mm diameter was loaded into a Tungsten carbide bowl vial (250 ml) under a dry air atmosphere. The weighed powder was poured over the balls and then the grinding bowl tightly and carefully sealed with surface sealing rubber ring. The grinding bowls with material and balls rotated around their own axis on a counter-rotating supporting disc. The other milling variables kept constant are as shown in a cylindrical die made of steel.

After every experiment, the bowl and balls were cleaned by milling with sand (silica) for 5 min to remove the cold-welded powder on the bowl and ball surfaces. The bowl containing the powder was then placed carefully in its position on the rotating disk and tightly closed. Pressure and temperature were kept constant for all the experiments. Milling time was divided into equal cycle of one hour separated by 15 minutes to cool down the milling medium.

Table 4.20 The most important variables influencing the properties of milled powder for a given powder composition.

Type of mill	High energy planetary ball milling
Milling container	Zirconium Oxide and Tungsten carbide
Milling speed	300 rev/min
Milling time	5, 10, 15, and 20 h
Grinding tools	Tungsten carbide, 250 ml bowls and grinding balls (10 and 20 mm)
Ball-to-powder ratio	1:12
Extent of filling the vial	1:3
Milling atmosphere	Air
Process	Dry milling
Milling temperature	Room temperature

4.4.6. As-milled Powder Characterization

After milling, the powder was characterized again to expose the effect of milling conditions of the morphology, particle size reduction, homogenization, the formation of any metastable phase, and crystalline change. Characterization was carried out using Pycnometer, XRD, FESEM, and TEM methods. Pycnometer was used to analyze the effect of milling variables on Tap density, and SSA. The Tap density and the green density were used to measure the effect of milling time on compressibility.

Scanning and transmission electron microscopy was employed to study the morphology and crystalline structure of as-milled powder samples. FESEM was used to observe the powder morphology, homogenization and particle size reduction. TEM techniques were used to analyze the nanosize powder morphology particle size reduction, and to measure the thickness of crystallization. The x-ray analysis was conducted using Philips and Bruker 5000 X-ray systems (A Cu-Ka target of 0.154 nm) for qualitative and quantitative XRD analysis. The analysis detects the materials chemistry, phase constitution, structure of milled powder samples and crystallite size.

The crystallite size broadening of a peak is correlated to the crystallite size through the Scherer equation. Lifshin [127].

$$t = (k * \lambda) / B_{1/2} * COS(\theta_B) \qquad (4.11)$$

Where t is the average thickness of crystalline particles, K is a constant depending on the crystalline shape (0.89), λ is the x-ray wavelength, and $B_{1/2}$ is the full width at half maximum, and Θ_B= Bragg angle. One of the main sources of error considered is the effect of internal strains on broadening.

4.4.7. Consolidation Techniques

The consolidation of milled powder by applying temperature and pressures is an important process used to fabricate the final products. Consolidation was carried out using three different techniques. The cold compaction, sintering, and the hot isostatic pressing were used for Cu-WC-Si. Instead, for Cu-WC-Ti and Cu-WC-Ti-Si hot pressing was used.

4.4.7.1.Consolidation of Cu-WC-Si

Consolidation of the milled Cu-WC-Si composite was carried out using uniaxial stainless steel die-pressed at 740 MPa to form 13 mm diameter cylindrical samples. Figure 4.19 shows that 600-800 MPa compaction pressure is enough to achieve up to 0.92 fractional densities for Copper and up to 0.7 fractional densities for Tungsten.

Sintering was carried out using high temperature sintering furnace model LINN term VMK-135-S at 950°C for 120 minimums in argon atmosphere. One of the three sintered samples from each experiment was re-sintered using HIP at 31 MPa in argon atmosphere to reveal the effect of re-sintering on final density. After compaction, the compressibility of the green compact was measured in terms of densification parameter, which is a measure of how much a green density achieved by the application of external pressure. This parameter is influenced by some factors such as hardness of powder, initial particle size and shape, interparticle friction and powder volume.

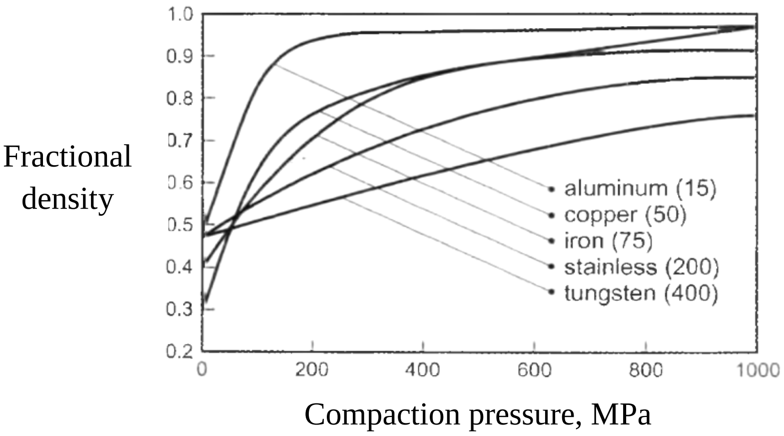

Figure 4.15 Cold Compaction behavior of different metals showing how the green density increases with pressure. German [94].

4.4.7.2.Consolidation of Cu-WC-Ti & Cu-WC-Ti-Si

Consolidation of Cu-WC-Ti and Cu-WC-Ti-Si carried out using resistance-heated hot pressing furnaces in Graphite dies as shown in Figure 4.16. Thin layer of boron nitride is used to cover the internal surface of the die before powder to simplify the removal of the product from the die after hot pressing. The punch was lowered until it makes physical contact with powder surface. After the furnace room was evacuated up to 10^{-5} torr (6.57×10^{-8} atmospheric pressure), heating started at the rate of 2^{o}C/min heating rate up to 850^{o}C and then 31 MPa pressure was applied for 90 minute. This pressure and time are selected according to the schematic diagram shown in Figure 4.17.

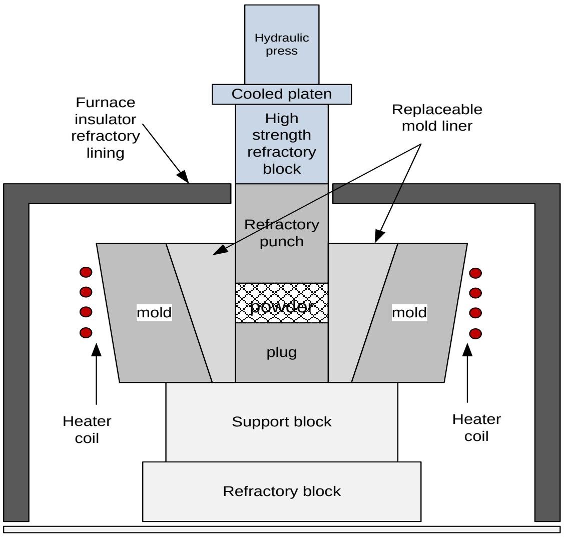

Figure 4.16 Schematic diagram showing the essential elements of uniaxial hot pressing

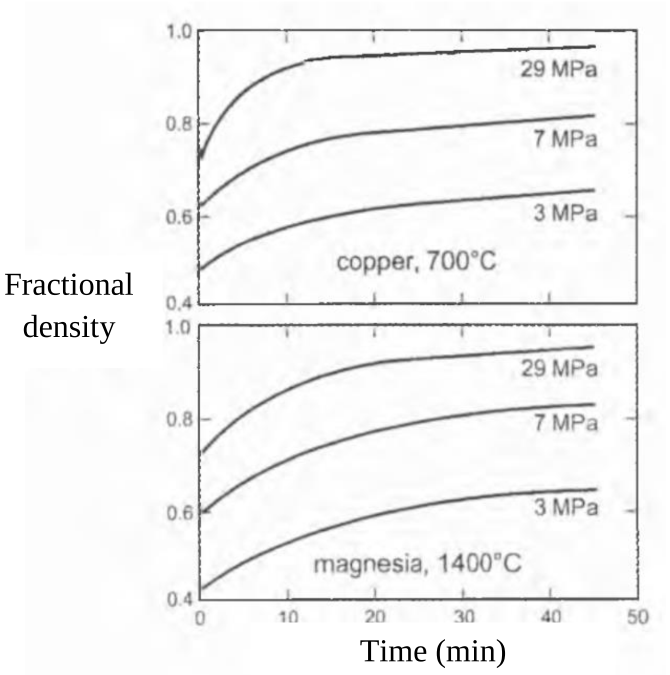

Figure 4.17 Hot pressing densification data for Copper and magnesia, showing the combined effects of time and pressure on density. German [94].

4.4.8. Densities and Volume Measurement

The densities and specific surface area of the powder was measured according to the gas adsorption principle using Ultrapycnometer 1000 version 2.2. Measurement was carried out using helium at 19-psi pressure and room temperature. The average of the last three reading out of five was recorded with variation less than 0.008 cm^3 for volume and less than 0.16 g/cm^3 for densities. The density and volume of solid samples were measured according to the gas adsorption principle as mentioned before and confirmed using Archimedes' principle. The density and volume measured by using Archimedes' principle by measuring the following as quantities follow;

1- Weight of sample in air (A)

2- Weight of samples in the auxiliary liquid (distilled water) (B)

3- Density of the distilled water (ρ_0 = 0.997 g/cm^3), the density of air ($\rho_{a=}$ 0.0012 g/cm^3), and α is the balance correction factor (0.99985)

Then, the density and volume were calculated using equation 4.12 and 3.13 respectively.

$$\rho = \frac{A}{A - B}(\rho_0 - \rho_a) - \rho_a \qquad (4.12)$$

$$V = \alpha \frac{A - B}{\rho_0 - \rho_a} \qquad (4.13)$$

The effect of milling variables of compressibility and densification was calculated from the measured green density, theoretical density, and the sintered densities. The compressibility and the densification measured are as follows.

$$compressibility = \frac{(\rho_{gr} - \rho_{ta})}{\rho_{ta}} x100 \qquad (4.14)$$

$$Densification = \frac{(\rho_{si} - \rho_{gr})}{(\rho_{th} - \rho_{gr})} x100 \qquad (4.15)$$

Where ρ_{ta} is the tap density, ρ_{gr} is the green density, ρ_{si} is the sintered density, and ρ_{th} the theoretical density.

4.4.9. Heat Conduction Measurement

The transfer of heat under unsteady state condition from the surface to the centre was measured using HT17 unsteady state heat transfer. The solid cylindrical sample of 13 mm diameter and 9 mm high was stabilized at initial temperature Ti (room temperature) before dropping into stabilized heated water at 80-90^{0}C (T_{max}). Due to the heat transfer from the bath to the centre, the temperature of the sample increases as a function of time and distance from the surface as T=T (r, t). Assuming that the dimensionless temperature θ is defined as;

$$\theta = \frac{T(r,t) - T_{max}}{T_i - T_{max}} \qquad (4.16)$$

according to Lumped model of transient heat conduction, the change in the dimensionless temperature as a function of time can be calculated from equation 4.17. Cengel [128].

$$\theta = \frac{T(r,t) - T_{max}}{T_i - T_{max}} = Ae^{-bt} \qquad (4.17)$$

The decay constant b is the reciprocal of the time constant and given as

$$b = \frac{\alpha h A_S}{k.V} = \frac{h A_S}{\rho V.c_p} \tag{4.19}$$

Where k is the thermal conductivity, V is the volume of mass m, A_s is the surface area, ρ is the density, and C_p is the specific heat capacity. The plot of Ө versus time t was used to study the effect of composition of electrode material and milling time on the rate of heat transfer rate (mode).

4.4.10. Hardness Test

Hardness is the ability of a material to resist deformation when it is in contact with an indenter under load. It is an important property especially in sample cutting and chapping. The hardness of samples varies depending on the composition, porosity, and consolidation technique. Due to this high variation in hardness, some of hardness reading is out of Vickers ranges and thus, Rockwell B was adopted as the hardness testing scale. This makes possible comparison between the hardness of as-sintered Cu-WC-Si and after HIP. Hardness testing was carried out using Rockwell hardness testing machine.

According to the standard of measurement ASM [129], initially the surface of a sample with two parallel surfaces was ground and polished to give a mirror like surface and then the load is applied. The load is applied for a specified period at a different point from the centre to the edge. The result is taken as an average of ten Rockwell B scale reading. Table of conversion was used to convert from Rockwell B to Rockwell C and Vickers.

4.4.11. The Setting for Performance Measurement

The electrode performance was tested on machining of hardened die steel using oil diesinker EDM machine of type Mitsubishi AE series. All machining experiments were conducted in a rough machining setting using Transistor-capacitor power circuit type TP.

CHAPTER 5

RESULTS AND DISCUSSION

5.1. Microstructure of electrode and workpiece

Figure 5.1 is the optical image of the nital-etched grey cast iron showing flake Graphite with an average of thickness equal to 3.5 µm imbedded in ferrite structure. Figure 5.2 is an optical micrograph of Copper electrode etched using ferric chloride -etchant showing different color of copper at different orientation with average size of 25±10 µm.

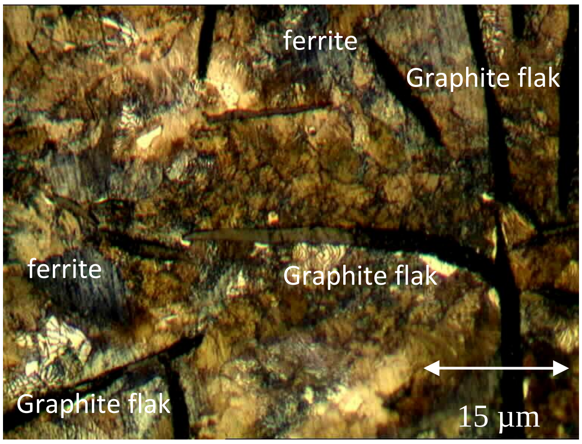

Figure 5.1 Optical micrograph of a nital-etched grey cast iron showing flake Graphite

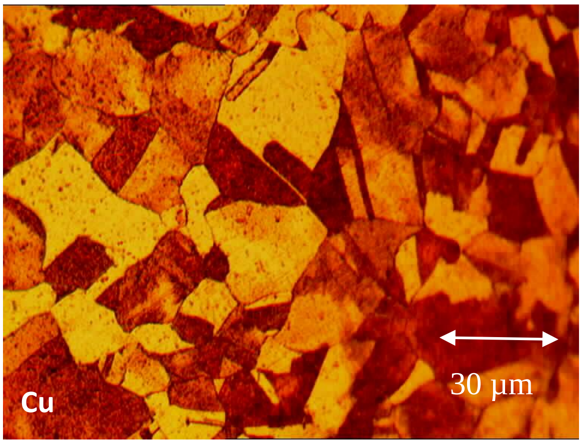

Figure 5.2 Optical micrograph of Copper electrode etched by ferric chloride

The FESEM images of the two workpieces of gray cast iron and cemented tungsten carbide are shown in Figures 5.3 and 5.4. The structure of cemented tungsten carbide shows the high value of tungsten content. The average particle size of tungsten particle in cemented tungsten carbide is around 2 µm.

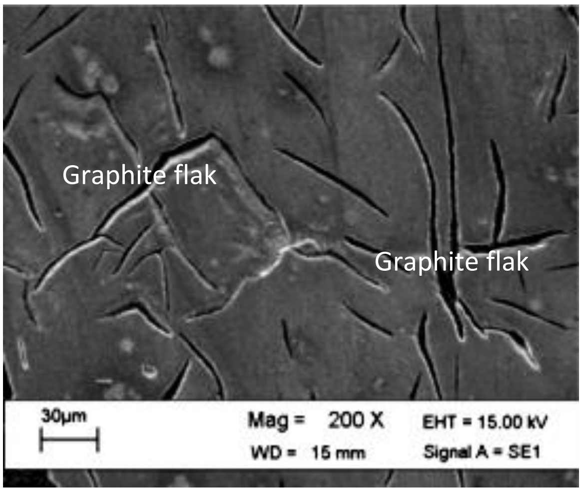

Figure 5.3 SEM micrograph of gray cast iron disk brake with Graphite flaks imbedded in pearlite grains

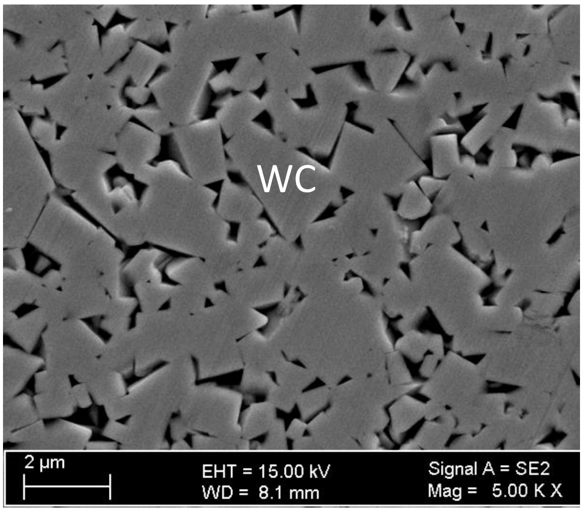

Figure 5.4 SEM micrograph of cemented Tungsten carbide workpiece

5.2. Machining of Gray Cast Iron using Copper Electrode

The machining experiment was performed using peak current, pulse On-time, Pulse Off-time, servo voltage, electrode jump up, dielectric pressure, and electrode jump down as input machining parameters. The machining results characterized by measuring the effect of machining variables setting on the material removal rate

MRR, electrode wear EW, and surface roughness Ra. The L8 Taguchi orthogonal array layout and the equivalent machining responses (results) are shown in Table 5.1.

Analysis of variance (ANOVA) was carried out based on measuring the sum of squares (SS) to identify the percentage contribution of each variable to the machining results as shown in Table 5.3. The effects of machining variables setting on machining results were analyzed using ANOVA and the results are shown in Table 5.2. This analysis is necessary to determine quantitatively the effect of machining variables setting on the machining result.

Table 5.1 Taguchi design of machining experiment with seven variables all at two levels including the machining results

No	L8 Taguchi orthogonal array by seven variables all at two levels (2^7)							Machining results			
	Peak current code[ampere]	Pulse On-time code[µs]	Pulse Off-time code[µs]	Servo voltage code[Volt]	Jump up code[mm]	Dielectric pressure (MPa)	Jump down code[ms]	MRR (mg/min)	EW (mg/min)	Ra (µm)	OC (mm)
Exp	2.5 [10]	3 [8]	3 [8]	2.5[180]	4[0.8]	0.02	2[100]	30.00	14.00	2.80	0.30
Exp	2.5 [10]	3 [8]	3 [8]	4.5[280]	7[1.8]	0.04	4[200]	8.00	3.70	2.90	0.06
Exp	2.5 [10]	7[128]	5[32]	2.5[180]	4[0.8]	0.04	4[200]	9.50	0.41	6.56	0.40
Exp	2.5 [10]	7[128]	5[32]	4.5[280]	7[1.8]	0.02	2[100]	2.60	0.26	7.25	0.20
Exp	5.5 [35]	3 [8]	5[32]	2.5[180]	7[1.8]	0.02	4[200]	22.50	42.70	3.33	0.42
Exp	5.5 [35]	3 [8]	5[32]	4.5[280]	4[0.8]	0.04	2[100]	3.60	6.00	3.00	0.12
Exp	5.5 [35]	7[128]	3 [8]	2.5[180]	7[1.8]	0.04	2[100]	147.00	1.80	11.30	0.56
Exp	5.5 [35]	7[128]	3 [8]	4.5[280]	4[0.8]	0.02	4[200]	27.00	0.40	11.20	0.62

Table 5.2 The values of the mean averages of MRR, EW, Ra, and OC versus machining variables setting

Mean of responses	Variables level	Peak current	Pulse On-time	Pulse Off-time	Gap-voltage	Jump up	Dielectric pressure	Jump down
MRR (mg/min)	1	12.50	16.00	53.00	52.30	17.50	20.50	45.80
	2	50.00	46.50	9.60	10.30	45.00	42.00	16.80
EW (mg/min)	1	4.60	16.60	5.00	14.70	5.20	14.30	5.50
	2	12.70	0.70	12.30	2.60	12.10	3.00	11.80
Ra (µm)	1	4.88	3.01	7.05	6.00	5.89	6.15	6.09
	2	7.21	9.08	5.04	6.09	6.20	5.94	6.00
OC (mm)	1	0.24	0.23	0.39	0.42	0.36	0.39	0.30
	2	0.43	0.45	0.29	0.25	0.31	0.29	0.38

Table 5.3 The sum of square (SS) and the percentage contribution (SS %) of variables on machining results

	MRR (mg/min)		EW (mg/min)		Ra (μ)		OC (mm)	
	SS	SS %	SS	SS %	SS	SS %	SS	SS %
Peak current	2812.50	17.67	132.28	13.12	10.86	27.42	0.072	35.70
Pulse On-time	1682.00	10.57	40.23	3.99	20.32	51.31	0.014	7.15
Pulse Off-time	3775.81	23.73	108.56	10.76	8.12	20.51	0.020	9.89
Gap voltage	3519.61	22.12	294.64	29.21	0.02	0.04	0.058	28.58
Jump up	1512.50	9.50	95.57	9.48	0.19	0.47	0.005	2.47
Dielectric pressure	924.50	5.81	258.21	25.60	0.08	0.21	0.020	9.89
Jump down	1687.81	10.61	79.07	7.84	0.02	0.04	0.013	6.33
Total	15914.72	100.00	1008.55	100.00	39.60	100.00	0.20	100.00

5.2.1. Material Remodel Rate (MRR in mg/min)

Tables 5.2 and 5.3 show the data analysis of the experimental results for MRR, EW, Ra, and OC. Figure 5.5 shows the percentage contribution of the machining variables on MRR (mg/min) of gray cast iron using Copper electrode. The results indicate that pulse off-time, gap voltage, and peak current are the most important variables that can determine the values of the MRR (mg/min). The effect of electrode jump up (distance) and jump down (frequency) also can affect the value of the MRR.

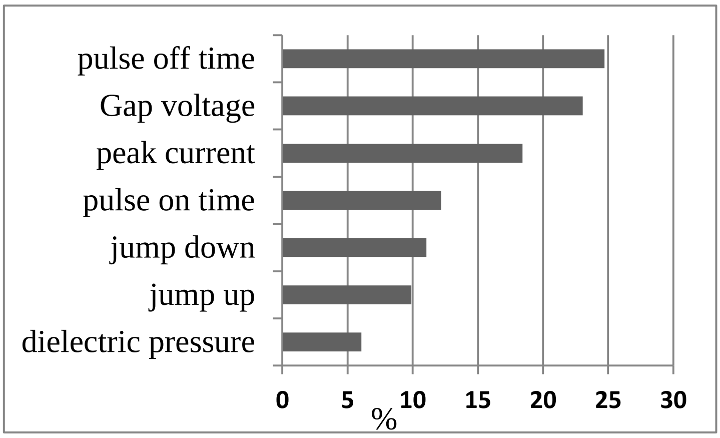

Figure 5.5 Contribution of machining variables on MRR (mg/min) for gray cast iron using Copper electrode

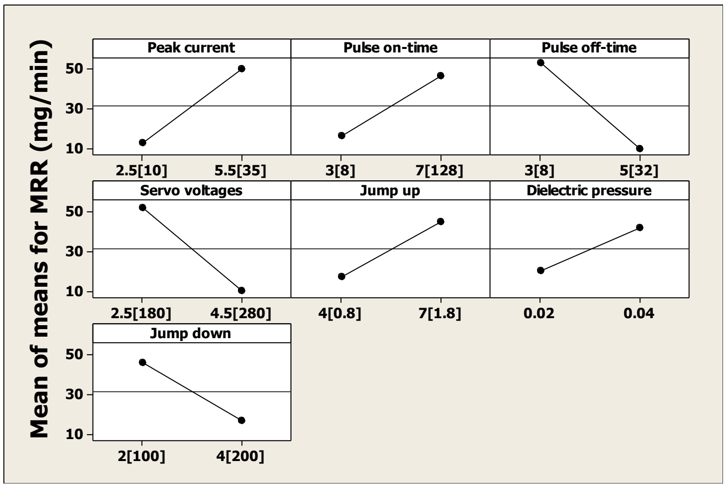

Figure 5.6 The main effects plot for mean MRR (mg/min) for gray cast iron using Copper electrode

Figure 5.6 is the main effect plot of MRR (mg/min) for gray cast iron using Copper electrode. The MRR increases with peak current, pulse On-time, electrode jump up (Ju), and dielectric pressure (DEP). Simultaneously, the MRR decreases with Pulse Off-time, servo voltage, and the electrode jump down. The servo voltage is the reference voltage used to stabilize the gap voltage between the electrode and the workpiece.

5.2.2. Electrode Wear (EW in mg/min)

The percentage contribution of variables and the main effect plot of the mean of EW (mg/min) are shown in Figures 5.7 and 5.8. The most significant factors influencing the values of the EW (mg/min) are the gap voltage, dielectric pressure, and peak current followed by pulse Off-time and the electrode jump up distance. The effect of other variables on Ra is negligible. The values of the Ra decrease with Pulse Off-time but conversely increased with Pulse On-time and peak current. The contributions of pulse Off-time on EW is negligible.

Figure 5.8 shows that the values of the EW (mg/min) increase with peak current, pulse off-time, the electrode jump up (distance), and the electrode jump down (frequency). Conversely, the EW decreases with pulse on-time, gap voltage, and the dielectric pressure. In general, the mean average of the EW remained in the range of 0.70 – 16.6 (mg/min).

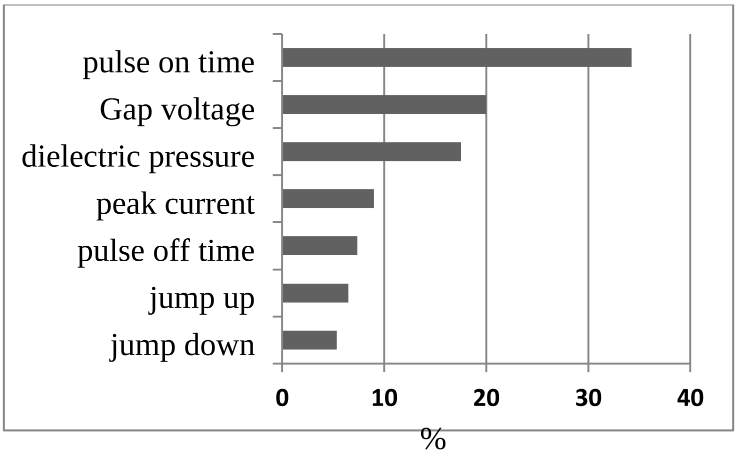

Figure 5.7 Contribution of machining variables on EW (mg/min) of gray cast iron using Copper electrode

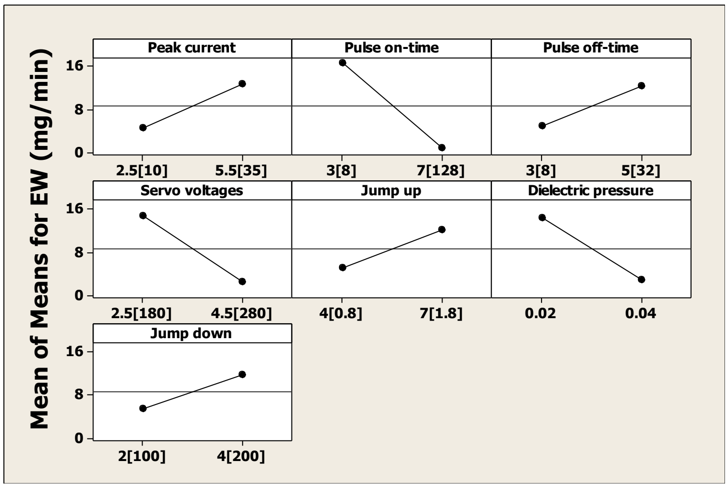

Figure 5.8 The main effects plot for mean EW (mg/min) for gray cast iron using Copper electrode

5.2.3. Surface Roughness (Ra in µm)

Figure 5.9 shows that the most significant factors influencing the Ra are the Pulse On-time, peak current, and pulse off time. The effect of other variables on Ra is negligible. It can be seen from Figure 5.10 that the values of the Ra decrease with Pulse Off-time but conversely increased with Pulse On-time and peak current. The discharge energy is related to the value of peak current and pulse on time. In order to achieve a low EW, it is necessary to set the peak current, Pulse On-time, electrode jump up, and dielectric pressure at low level. Meanwhile, the other variables can be set at higher level to speed up the machining rate.

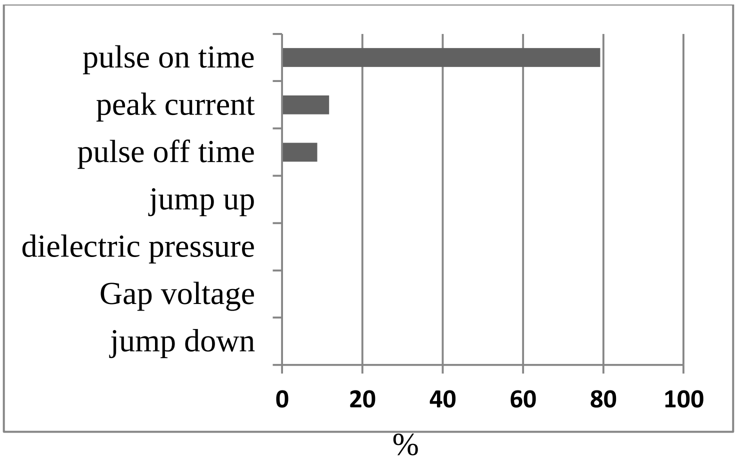

Figure 5.9 Contribution of machining variables on Ra (μm) of gray cast iron using Copper electrode

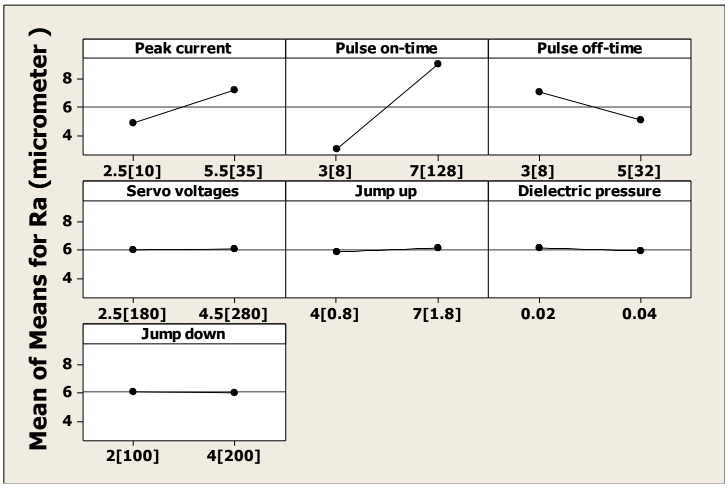

Figure 5.10 The main effects plot for mean Ra (μm) for gray cast iron using Copper electrode

5.2.4. Over Cut (OC in mm)

Measuring the value of over cut during machining is important and must be considered during die and mold manufacturing. Figure 5.11 shows that peak current, gap voltage, dielectric pressure and pulse Off-time are the most important variables that influence the value of overcut. Figure 5.12 is the main effect plot of OC during machining of gray cast iron using Copper electrode. The value of OC in mm increases with peak current, pulse on-time, and the electrode jump down frequency. On the other, the values of pulse off-time, gap voltage, the electrode jump up (distance), dielectric pressure must be set at higher level to reduce over cut.

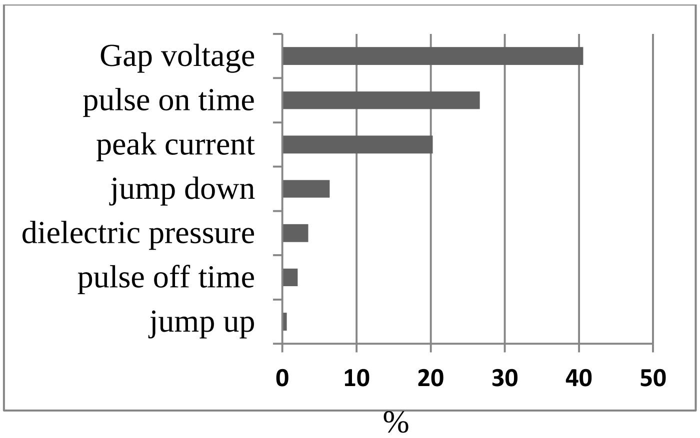

Figure 5.11 Contribution of machining variables on Over-cut (mm) of gray cast iron using Copper electrode

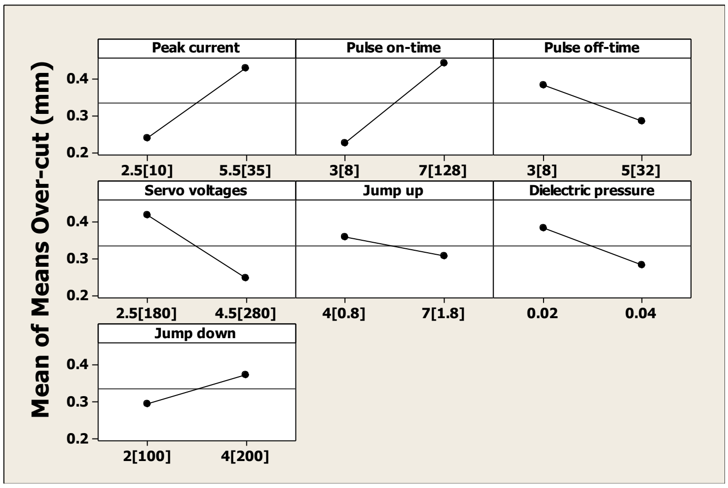

Figure 5.12 Contributions of machining variables and the main effects plot for mean of OC (mm)

5.2.5. Optical Microscopy

Figure 5.13 shows the surface layer derived from the re-solidified molten metal at tip of Copper electrode (A) and the cast iron workpiece surface (B) by redeposit of the molten metal (recast layer). The analysis shows a 50 µm thick layer at the electrode tip and 40-µm thick recast layer including the sputtered surface layer. The layer under the recast layer is called the heat-affected layer. This heat affected layer shows structure different from the unaffected part (base metal). These three layers can influence the quality of the surface integrity. The recast layer can be reduced by auto CNC machining conditions called finishing setting.

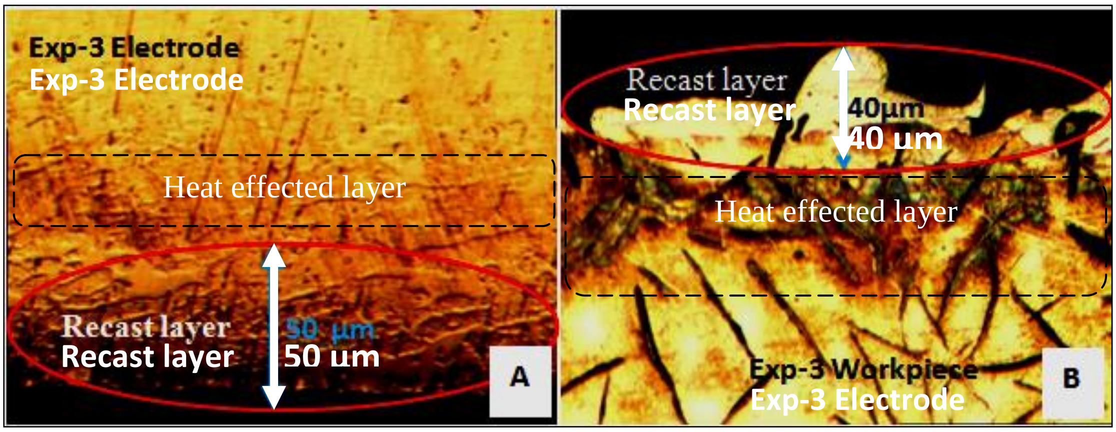

Figure 5.13 The heat effected layer on Copper electrode (A) and gray cast iron workpiece (B) including the recast layer

5.2.6. Scanning Electron Microscopy

The FESEM image in Figure 5.14 (A) shows the curved corner of the tool electrode due to the high corner wear of the tool electrode, which takes place at the early stage of machining. The radius of curvature is 1200 µm but is higher in x direction than y direction. This result is in agreement with the study done by Khan [2] where he studied the electrode wear along the cross-section of an electrode compared to the same along its length during EDM of aluminum and mild steel using Copper and brass electrodes. This result is also mentioned by Lo [130]. Figure 5.10 (B) shows the effect of the electrode corner wear on the shape of the machined cavity. The cavity shape obtained is the negative copy of the electrode shape but the radius of curvature is around 1000 µm.

The FESEM images C and D in Figure 5.14 show the structure of the sputtered layer, recast layer, and the heat effected layer of the gray cast iron machined by Copper electrode under the machining condition of Exp-3. The sputtered layer is characterized by uneven topography with small size debris and voids due to the rapid cooling rate. The layer underneath the sputtered layer is the recast layer, which was made from the re-deposited molten metal onto the surface of the workpiece. The average thickness of the layer is around 30 µm at the area facing the electrode front and around 15 µm for the side surface of the machined cavity. This is an expected result since the sparking occurs between the electrode tip and the bottom of the workpiece. This thickness is in agreement with the result published by Tsai [19], he found that the thickness of the recast layer is around 25 µm using Cu metal electrode and Cu-Cr composite electrode with a medium carbon steel. Guu [131] found that the thickness of the recast layer at various EDM conditions are in the range of 10-30 µm.

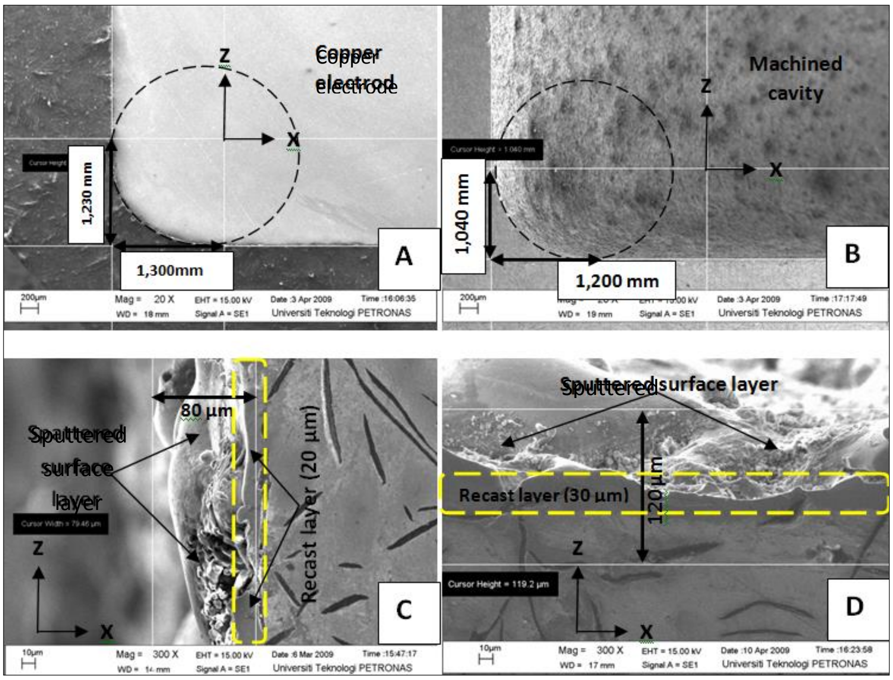

Figure 5.14 FESEM images of Copper electrode corner wear (A), the machined cavity (B), the recast layer of the cavity side surfaces (C), and the recast layer (D)

5.3. Machining of Cemented Tungsten Carbide using Cu electrode

Cemented Tungsten carbide is one of the highest resistant materials to abrasive wear due to its high hardness value of 1500 Vickers and low thermal expansion. In addition, it has a relatively low electrical and thermal conductivity. These properties make the machining of this material using conventional technique impossible. The results show that the proper selection of machining conditions is important to be able to machine cemented Tungsten carbide using die-sinking EDM. This result also mentioned by Purtas [132]. The hardness of WC-Co alloys primarily depends on the grain size of tungsten carbide particles and cobalt content. The difficulty of machining cemented WC using EDM derived from the high thermal stress generated was due to the very low thermal conductivity and thermal expansion in addition to the high melting point and hardness. For more about the properties of cemented Tungsten carbide, Upadhyasa [114].

Table 5.4 L9 Taguchi orthogonal array including the observed values of MRR (mg/min), EW (mg/min), TWR, and Ra (µm)

	L9(3**4) Taguchi Orthogonal Array				Machining results			
	Peak current code [Amp]	Pulse On-time code [µs]	Pulse Off-time code [µs]	Gap voltage code [Volt]	MRR (mg./min)	EW (mg/min)	TWR (%)	Ra (µm)
Exp-1	3.2 [12]	6 [64]	4 [16]	10 [80]	3.80	0.70	18.30	6.8
Exp-2	3.2 [12]	7 [128]	5 [32]	11 [110]	6.10	1.20	19.40	2.9
Exp-3	3.2 [12]	8 [256]	6 [64]	12 [150]	6.10	1.40	23.00	3.1
Exp-4	3.4 [14]	6 [64]	5 [32]	12 [150]	6.20	1.50	24.40	5.9
Exp-5	3.4 [14]	7 [128]	6 [64]	10 [80]	4.30	1.00	22.40	3.3
Exp-6	3.4 [14]	8 [256]	4 [16]	11 [110]	4.80	1.30	26.80	3.7
Exp-7	3.5 [15]	6 [64]	6 [64]	11 [110]	2.50	0.40	15.60	11.8
Exp-8	3.5 [15]	7 [128]	4 [16]	12 [150]	3.00	0.50	17.70	4.7
Exp-9	3.5 [15]	8 [256]	5 [32]	10 [80]	5.60	1.30	23.80	3.8

Table 5.5 The mean averages of MRR, EW, TWR, and Ra.

Variables	levels	MRR (mg/min)	EW (mg/min)	TWR (%)	SR (µm)
peak current	1	5.30	1.10	20.23	4.2667
	2	5.10	1.30	24.53	4.3000
	3	3.70	0.70	19.03	6.7667
Pulse on time	1	4.20	0.90	19.43	8.1667
	2	4.50	0.90	19.83	3.6333
	3	5.50	1.30	24.53	3.5333
Pulse off-time	1	3.90	0.80	20.93	5.0667
	2	6.00	1.30	22.53	4.2000
	3	4.30	0.90	20.33	6.0667
Gap voltage	1	4.60	1.00	21.5	4.6333
	2	4.50	1.00	20.6	6.1333
	3	5.10	1.10	21.7	4.5667

Table 5.6 The values of the sum of square and the percentage contribution of variables on machining responses derived from ANOVA

	MRR (mg/min)		EW (mg/min)		TWR (%)		Ra (µm)	
	SS	SS (%)	SS	SS (%)	SS	SS (%)	SS	SS (%)
Peak current	4.68	0.10	0.45	0.01	9.54	33.10	12.34	20.70
pulse on time	2.94	0.06	0.41	0.01	13.85	31.83	42.03	70.51
Pulse off-time	7.38	0.16	0.42	0.01	5.69	5.12	5.24	8.78
Gap voltage	4540.66	99.67	4540.66	99.97	100.00	29.95	0.00	0.01
	4555.66	100.00	4541.94	100.00	129.09	100.00	59.60	100.00

The experimental layout of L9 Taguchi orthogonal array [OA] used including the main observed values of MRR (mg/min), EW (mg/min), TWR, and Ra (µm) machining responses is shown in Table 5.6. The analyses of variance (ANOVA) including the mean average of the machining responses and the percentage contribution (SS %) are shown Table 5.5 and Table 5.6 respectively.

The experimental work was conducted on oil die sinking EDM machine of type Mitsubishi EA series model BRN-51748. The MRR and electrode wear (EW) were measured using (mass different/machining time) in (mg/min) and the tool wear ratio (TWR) measured as the percentage of the ratio (EW/MRR). The surface roughness constant (Ra) is measured using Mitutoyo surface roughness tester by taking the average of 10 readings at different lines on the surface of the cavity parallel to the axis of the machined cylinder. The quality characteristics of MRR were calculated based on ‘the higher is better’ and the other results calculated based on ‘the smaller the better’.

5.3.1. Material Removal Rate (MRR in mg/min)

The Percentage Contribution of variables on MRR and the main effect are shown in Figure 5.15. The Figure shows that pulse off-time, peak current, and the Pulse On-time are the most significant variables contribute on the observed values of MRR (mg/min). The effect of gap voltage is negligible. This result contradicts with the observation during machining; where the machining process at high voltage shows clear instability of machining process. These difficulties can be explained according to the experimental observation during machining process as follow; the increase in gap voltage leads to the fragmentation of small particles from the workpiece due to high thermal stress.

When this fragmented particle drops into the discharge gap, the machining process shows a high degree of carbon formation by dielectric disintegration, high rate of bubble formation with combustion. During that, the machining process shows reverse reading on CNC monitor and some time the machine auto stop due to uncontrolled condition. Thus, the gap voltage should be set at levels lower than 150 volts. Gap voltage higher than that is the main source of crack initiation and fragmentation. The main-effects chart of MRR (mg/min) in Figure 5.16 indicates that higher MRR required lower setting of peak current, higher pulse On-time and gap voltage. The effect of pulse Off-time on the value of MRR is not clear where it shows that the material removal rate is higher when the pulse Off-time is set at 32 µs. The effect of pulse Off-time on MRR is not stable. This might be referred to the effect of the interaction between variables which we not included in this design of experiment.

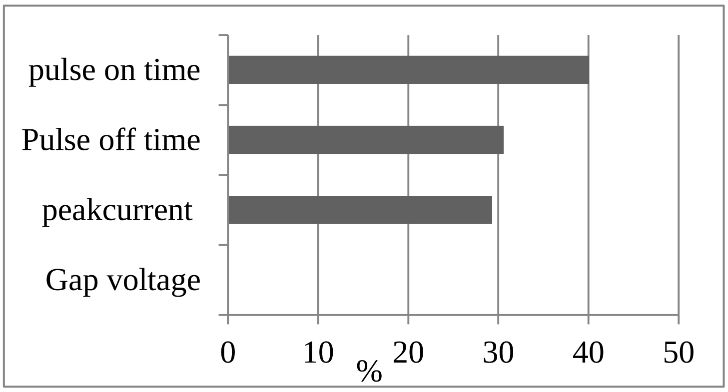

Figure 5.15 Contribution of machining variables on MRR (mg/min) of cemented Tungsten carbide using Copper electrode

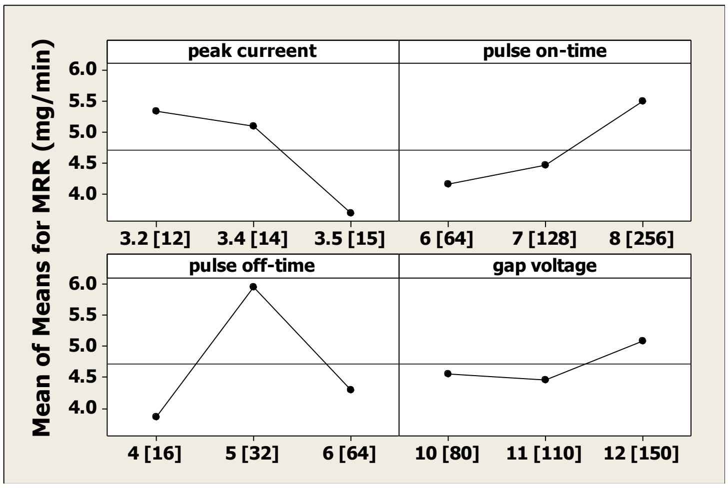

Figure 5.16 The main effect plot of MRR (mg/min) for cemented Tungsten carbide using Copper electrode

5.3.2. Electrode Wear (EW in mg/min)

Figure 5.17 shows that the percentage contribution of Gap voltage on the values of EW is negligible. As mentioned section 5.3.2.2, this result can be referred to the fragmentation of small particles from the workpiece, which is cuts as a new electrode tip leading to machining process between the new tip electrode and the work piece. At the same time, the effects of peak current, pulse off-time, and pulse On-time are significant. The contribution of peak current on EW is more significant than the MRR. The main effects chart of Figure 5.18 shows that the electrodes wear decreases with peak current and increases with the increase of pulse On-time and gap voltage. Lower electrode wear can be obtained by setting the pulse on time, pulse Off-time and the gap voltage at a lower level and at the same time the peak current should be set at higher level.

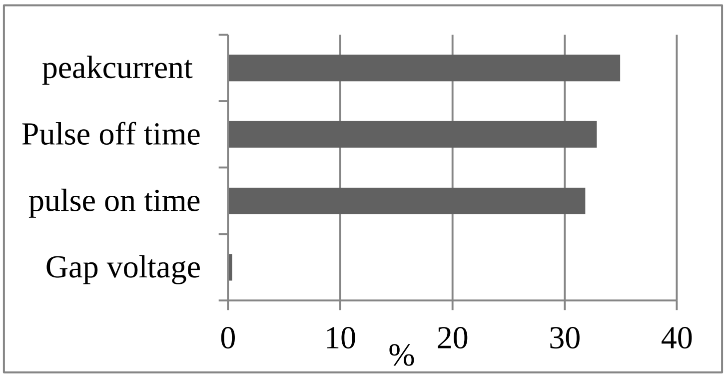

Figure 5.17 Contribution of machining variables on EW (mg/min) of cemented Tungsten carbide using Copper electrode

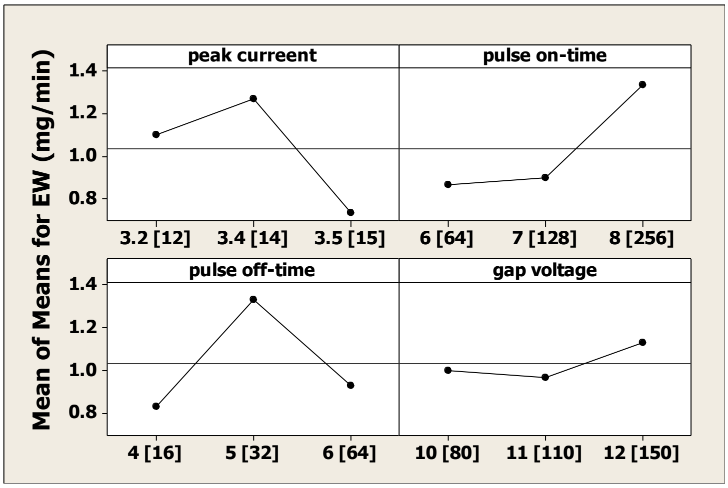

Figure 5.18 The main effect plot of EW (mg/min) for cemented Tungsten carbide using Copper electrode

5.3.3. Tool Wear Ratio (TWR %)

It is important to decrease the TWR to improve the surface tolerance. As shown in Figure 5.19, the most important variables that can contribute on the value of the tool wear ratio are the pulse off-time, peak current, and pulse on time. The contribution of gap voltage is insignificant. As shown in Figure 5.20 of the main effect plot of tool wear ratio. It is necessary to set the peak current and the gap voltage at higher level to reduce the value of TWR, meanwhile longer pulse On-time is better.

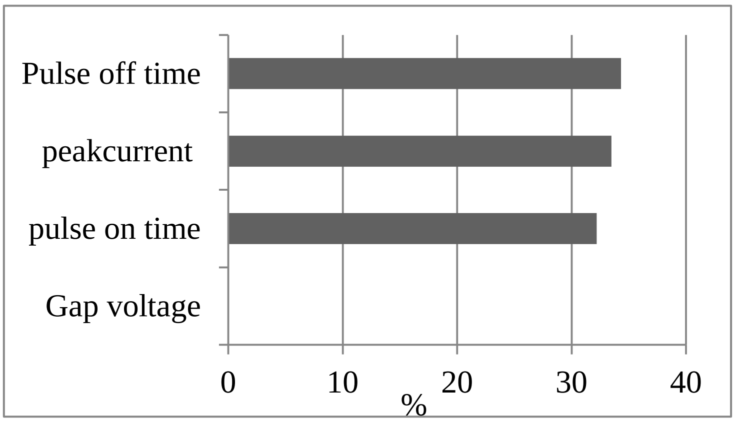

Figure 5.19 Contribution of machining variables on TWR (%) of cemented Tungsten carbide using Copper electrode

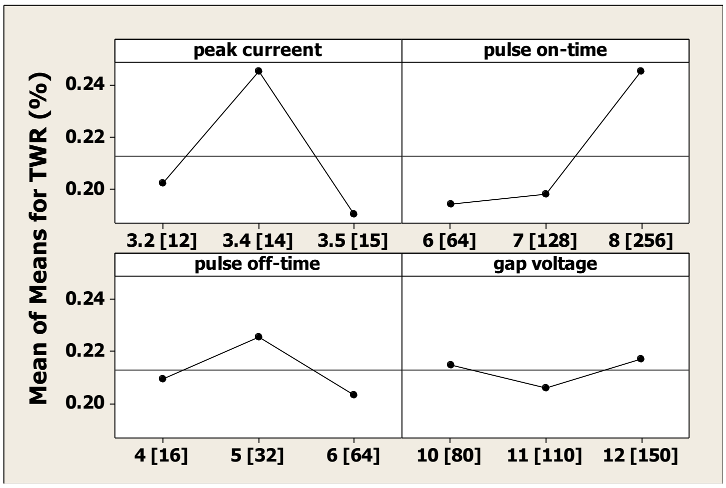

Figure 5.20 The main effect plot of TWR (%) for cemented Tungsten carbide using Copper electrode

5.3.4. Surface Roughness Ra (µm)

Figure 5.21 shows that the most important variable influencing the surface roughness are the pulse On-time and peak current followed by pulse off-time. This result is in agreement with the study of Jahan [133], he found that the surface characteristics are mostly depending on the discharge energy during machining (VIt_{on}) and also influenced by the electrode material. The main effects chart of Figure 5.22 indicates that the surface roughness can be reduced by using low peak current and longer pulse on-time. This result is in agreement with Puertas [132] where he mentioned that in order to obtain a good surface roughness in the case of Tungsten carbide, low values should be used for both peak current and gap voltage.

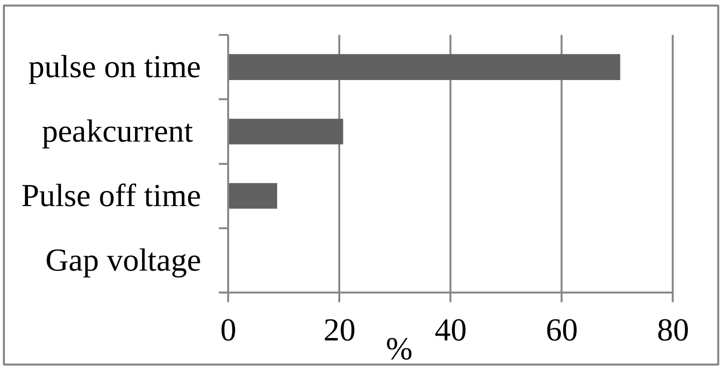

Figure 5.21 Contribution of machining variables on RA (µm) of cemented Tungsten carbide using Copper electrode

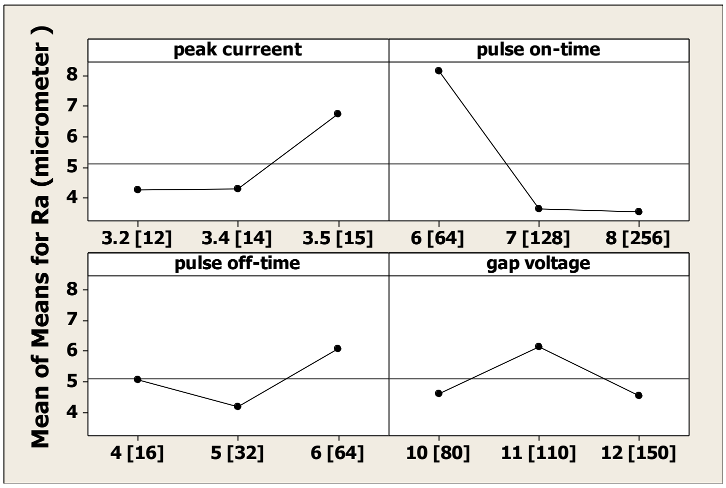

Figure 5.22 The main effect plot of Ra (µm) for cemented Tungsten carbide using Copper electrode

5.3.5. Microstructure

Further investigation carried out using optical and FESEM microscopes. The effects of machining condition on metallurgical and surface morphology of the heat-affected layer under the surface of the machined areas were inspected. According to the observations during machining, the high gap voltage and Pulse On-time setting show a turbulence machining with flaming and even short cut. This observation is confirmed by the contribution of variables on MRR and EW in section 5.1.2.1

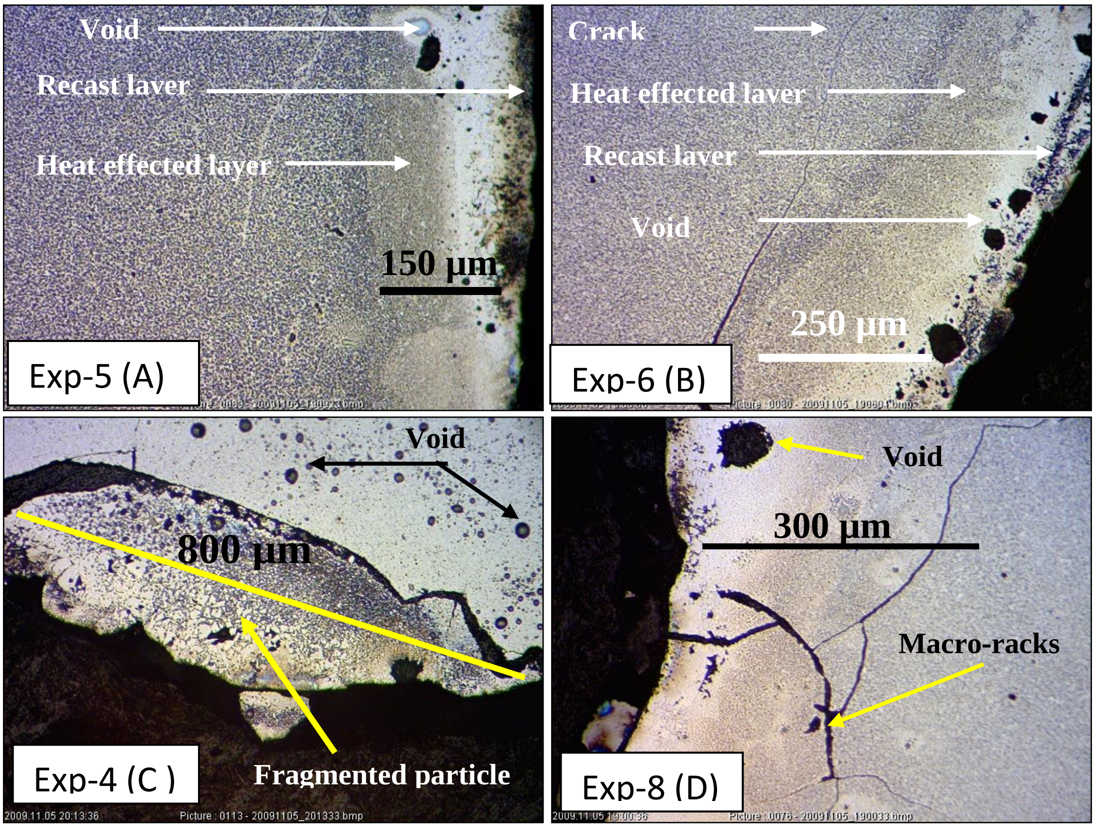

Figure 5.23 Optical images show the structure of the machined surface of cemented Tungsten carbide (WC-6% Co)

Figures 5.23 (A, B, C, and D) show the optical image of the machined surface of cemented Tungsten carbide for Exp-4, Exp-5, Exp-6, and Exp-8. The total thicknesses of the affected layers include the recast layer and the heat-affected layer is in the range 150-300 µm depending on the setting of the gap voltage and Pulse On-time. Due to the rapid heating and cooling process of ceramic, which is brittle, the thermal stresses can exceed the ultimate tensile strength of the material. This will initiate a micro-crack, which enlarges rapidly to form macro-crack, which in turn propagates rapidly leading to fragmentation of small parts. This result confirmed by the optical microstructure of Exp-4 and Exp-8 of Figure 5.23 where the macro-crack and the fragmented particles can be seen clearly. This result also mentioned by Hung [120].

The FESEM images of the machined surface of Tungsten carbide in Figure 5.24 shows the effect of crack propagation and fragmentation of particles on the quality of the machined cavity. The quality of the machined cavity depends on the machining condition and on the workpiece material. The cracks and the fragmentation of small parts from the surface highly affect the surface roughness and the surface tolerance where the depth of the gaps on the surface ranges from 100 µm to 400 µm. It can also be seen that the level of surface damage is higher in front of the electrode tip.

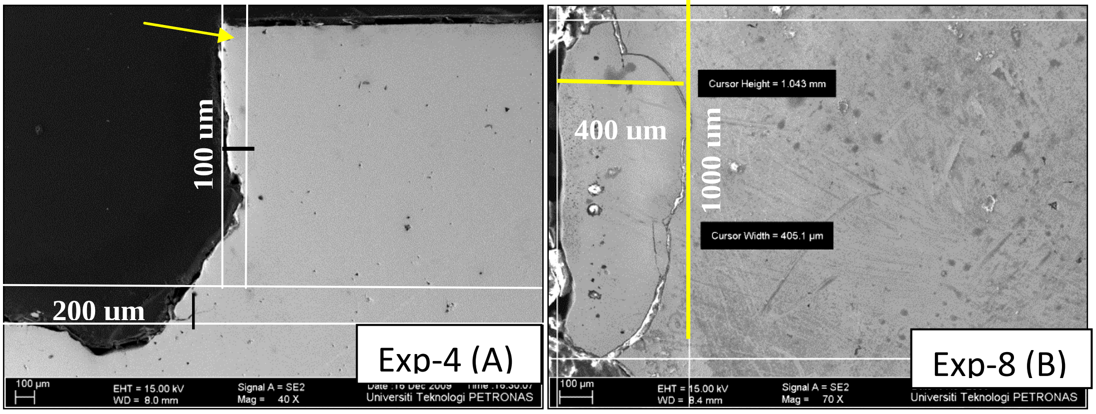

Figure 5.24 FESEM images of the internal edge of the machined cemented Tungsten carbide

One of the most important observations during machining is that the CNC reading changes from negative to positive and the machining process becomes turbulence with bubbles and flaming. This can be referred to the presence of the fragmented particles, which can be bigger than the discharge gap (0.01 mm). When this fragmented particle drops into the discharge gap and attached into the electrode surface and becomes a new tip electrode as shown if Figure 5.25, the machining process will continue between the workpiece and the new electrode tip leading to the formation of layered particles mainly consisted of carbon as shown in EDX profile in Figure 5.27. Figure 5.26 (A, B, and C) is the optical images show the structure of material removed from the electrode tip at different magnifications. Meanwhile, Figure 5.26 (D) is the FESEM images of the same material. Under these conditions the machining process can take longer time without any overall progress on MRR and EW. Many works on machining cemented Tungsten carbide were carried out using different electrode materials confirm the presence of the damaged layer Lee [41] observes that there is a clear EDM damaged layer on the workpiece and the degree of the damage and the amount of micro-cracks increase with the peak current and pulse duration. He concluded that very low values of peak current and pulse duration are necessary to remove the micro-cracks. Jahan [133] also mentioned that the surface structure mainly depends on pulse on–time but also is influenced by the properties of the electrode material.

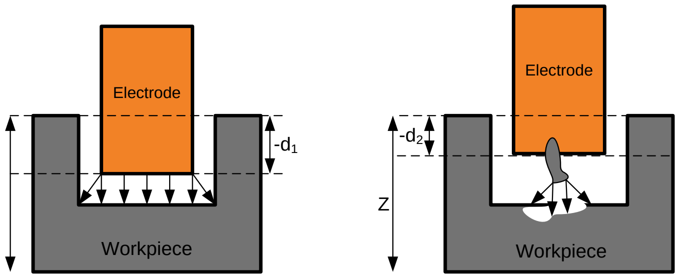

Figure 5.25 Schematic diagram show the effect of fragmented particles on machining process

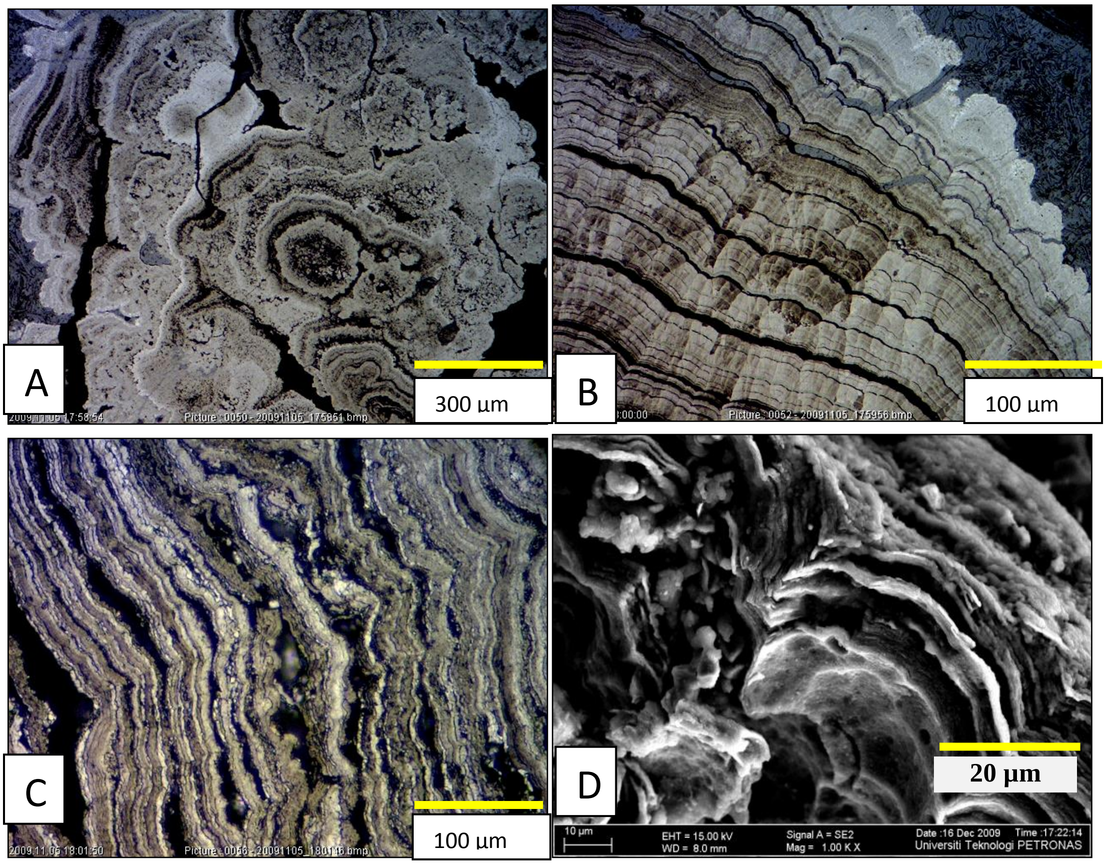

Figure 5.26 (A), (B), and (C) are the optical images and (D) is the FESEM image of the material found attached to the electrode tip and prevent machining process

The periodical structure of this material indicates that this structure formed during the discharge sequence. Each layer built up from sub layers with an average thickness of a single layer in the range of 10 µm. The composition of this material was analyzed using energy-dispersive X-ray spectroscopy (EDX) as shown in Figure 5.27 and the result shows that the basic structures of this material as mentioned earlier are carbon and oxygen. Neither the electrode material nor Tungsten was detected.

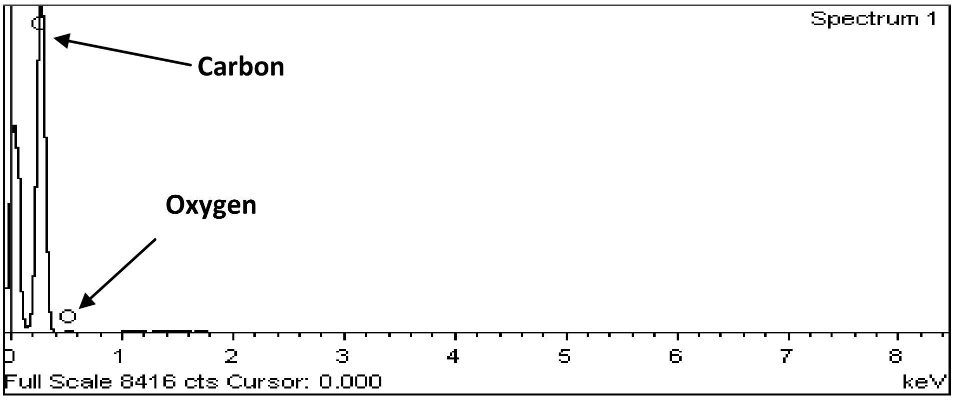

Figure 5.27 EDX spectrum of the material removed from the electrode tip

5.4. Machining of Hardened Die Steel using Cu-W Electrode

5.5. Hardening

Hardening is an important step to improve the strength (hardness) of material. When the steel is heated above A1, the crystal structure will change from BCC of the ferrite or pearlite to FCC of austenite, which can contain more carbon up to 2.0%. Quenching austenite structure can influence the mechanical properties such as hardness, yield strength, and tensile elongation. When austenite is cooled slowly, the austenite grain will break down depending on whether it is a low or high carbon steel to form; (Austenite +ferrite) → (ferrite + pearlite) for low carbon steel % (0-0.8), or (austenite +cementite) → (cementite +pearlite) for high carbon steel % (08-2.0)

In order to fix the fine-grained austenite structure, direct hardening was used as shown in Figure 5.28 which follow according to Hans [113]. The sample was heated to 1150^{o}C for 2 h, quenched in air followed by tempering to 750^{0}C and quenched in oil.

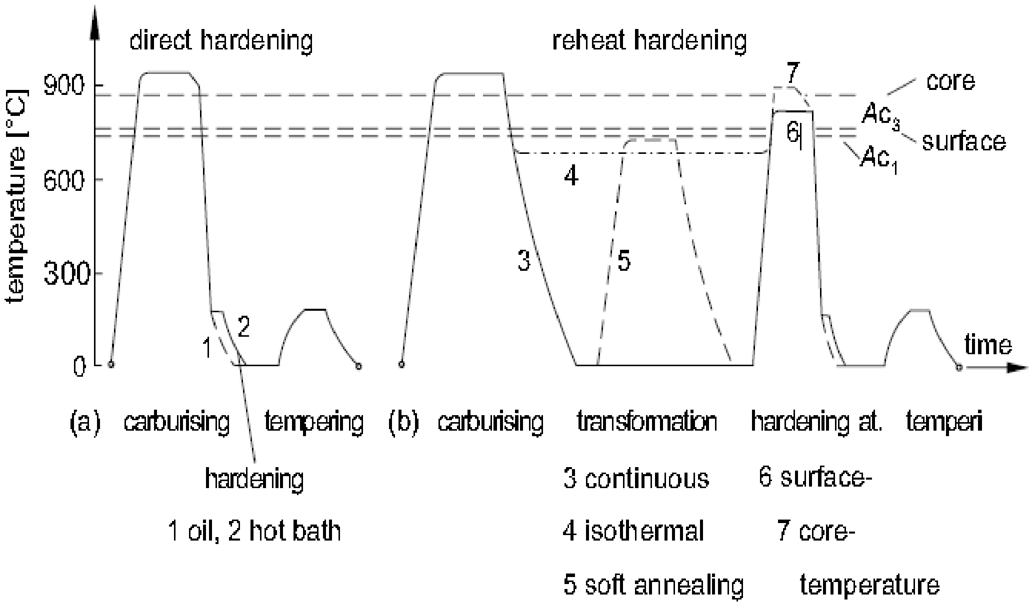

Figure 5.28 (a) Direct hardening from the carburizing temperature in oil or a hot bath. (b) Reheat hardening with refining of the grain size by cooling below Ac1 and subsequent hardening from the surface or core temperature Hans [113].

Figure 5.29 (A) and (B) shows the effect of hardening on microstructure of die steel. Figure 5.29 (A) shows a few crystallized austenite grains distributed in a pearlite matrix before hardening and the structure after hardening in Figure 5.29 (B) shows a few cementite grain distributed in a fully recrystallized austenite matrix Bruse [134].

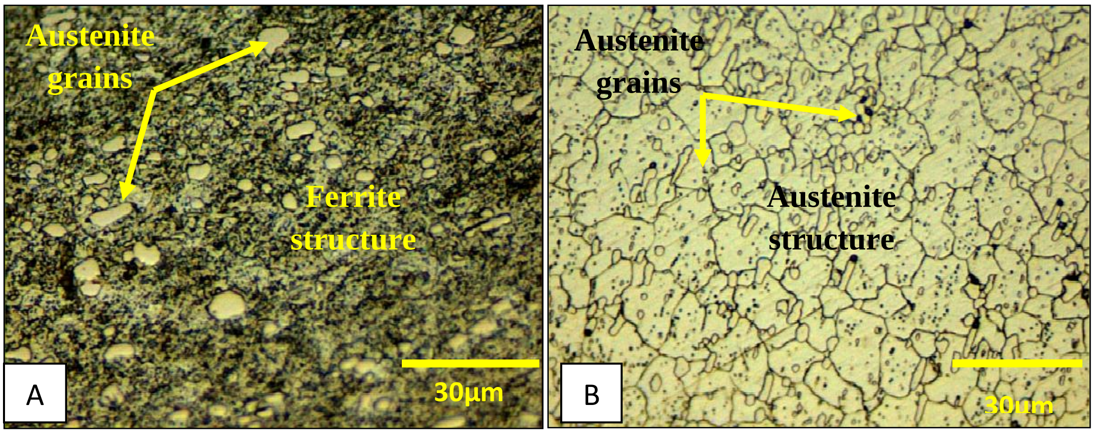

Figure 5.29 Optical images of die steel before hardening (A) show a Few prior Austenite grains distributed inside ferrite structure and after hardening (B) shows an Austenite grains dominate the structure with few pearlite structures.

5.6. Data Analysis

Table 5.7 The experimental layout of mixed mode L16 Taguchi orthogonal array and the observed values of MRR (mg/min), EW (mg/min), TWR, and Ra (µm)

L16 Taguchi orthogonal array				Machining results			
	Peak current Code[Amp]	Pulse On-time Code[µsec]	Gap Voltage Code[Volt]	MRR (mg/min)	EW (mg/min)	TWR (%)	Ra (µm)
Exp-1	1.5 (5.5)	4 (16)	0 (80)	5.80	0.46	7.93	2.61
Exp-2	1.5 (5.5)	5 (32)	0 (80)	13.60	0.74	5.44	2.04
Exp-3	1.5 (5.5)	6 (64)	1 (110)	51.10	1.29	2.52	2.24
Exp-4	1.5 (5.5)	7 (128)	1 (110)	6.20	0.11	1.77	1.61
Exp-5	2.5 (10)	4 (16)	0 (80)	101.80	7.03	6.91	3.6
Exp-6	2.5 (10)	5 (32)	0 (80)	122.00	5.66	4.64	4.06
Exp-7	2.5 (10)	6 (64)	1 (110)	110.40	4.17	3.78	4.68
Exp-8	2.5 (10)	7 (128)	1 (110)	118.80	1.56	1.31	3.4
Exp-9	3.5 (15)	4 (16)	1 (110)	172.20	11.67	6.78	4.58
Exp-10	3.5 (15)	5 (32)	1 (110)	202.10	9.04	4.47	4.96
Exp-11	3.5 (15)	6 (64)	0 (80)	195.70	6.66	3.40	4.94
Exp-12	3.5 (15)	7 (128)	0 (80)	231.00	4.56	1.97	6.01
Exp-13	4.5 (25)	4 (16)	1 (110)	300.70	19.36	6.44	5.03
Exp-14	4.5 (25)	5 (32)	1 (110)	221.90	11.13	5.02	7.69
Exp-15	4.5 (25)	6 (64)	0 (80)	369.20	12.68	3.43	4.71
Exp-16	4.5 (25)	7 (128)	0 (80)	219.30	6.82	3.11	8.36

Table 5.8 The mean averages of MRR (mg/min), EW (mg/min), TWR, and Ra (µm)

Variables	levels	Mean of MRR (mg/min)	Mean of EW (mg/min)	Mean of TWR (%)	Mean of Ra (µm)
peak current	1	19.00	0.70	3.68	2.13
	2	113.00	4.60	4.07	3.94
	3	200.00	8.00	4.00	5.12
	4	278.00	12.50	4.50	6.45
pulse on time	1	145.00	9.60	6.62	3.96
	2	140.00	6.80	4.86	4.69
	3	182.00	7.90	4.34	4.14
	4	144.00	3.30	2.29	4.85
gap voltage	1	315.00	11.20	3.56	9.08
	2	296.00	14.60	4.93	8.55

Table 5.9 The sum of square (SS) and percentage contribution (SS%) of variables

Variables	MRR (mg/min)		EW (mg/min)		Ra (µm)	
	SS	SS (%)	SS	SS (%)	SS	SS (%)
peak current	149.20	28.30	0.30	28.23	40.42	11.42
pulse on time	4.50	0.86	0.10	8.07	2.18	0.62
gap voltage	0.37	70.84	0.70	63.71	311.39	87.97
	154.07	100.00	1.10	100.01	353.99	100.01

5.6.1. Material Removal Rate (mg/min)

The percentage contribution of machining variables on MRR of Figure 5.30 shows that the most effective variables on the MRR are the gap voltage. Peak current and pulse On-time contributes by less than 1%. This result seems like it contradict with the result in section 5.1.2.1 where the contribution of gap voltage on MRR (mg/min) of cemented Tungsten carbide using Copper electrode is negligible. The main-effects chart of Figure 5.31 indicates that the MRR (mg/min) linearly increases with peak current but the effect of pulse On-time is not stable.

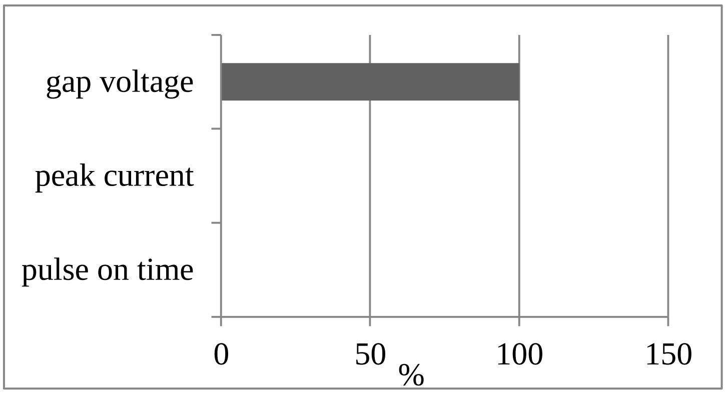

Figure 5.30 Contribution of machining variables on MRR (mg/min) for hardened die steel using Cu-W electrode

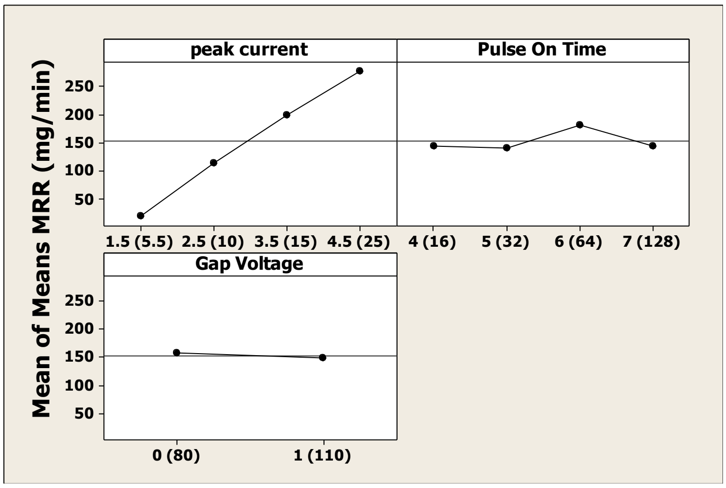

Figure 5.31 The main effect plot of MRR (mg/min) for hardened die steel using Cu-W electrode

It was observed during machining that any increase in Gap voltage creates an unstable machining process with a high degree of carburization leading to an increase in cracks enlargement as shown in Figures 5.23 and 5.24. Due to this, a carbon particle formed in the gap between the electrode and the workpiece, which consequently can stop the machining process. In order to continue the machining process, this particle must be removed and the electrode tip and the workpiece must be cleaned to remove the carbon particles and the black carbon layer. The proof is evident from EDX analysis in figure 2.27.

5.6.2. Electrode Wear

The percentage contribution of variables on the EW (mg/min) in Figure 5.32 shows that the Gap voltage is the most important variable that contributes on EW (mg/min) by 60% followed by peak current and Pulse On-time.

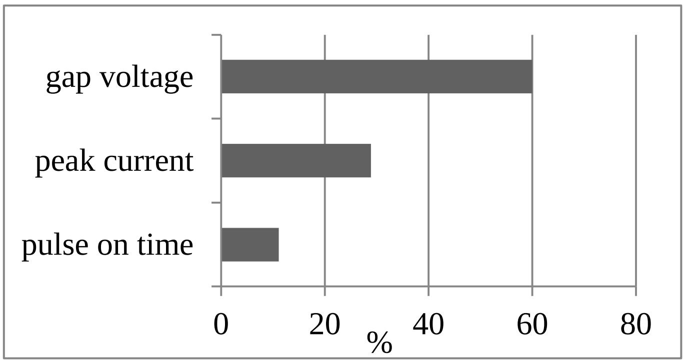

Figure 5.32 Contribution of machining variables on EW (mg/min) for hardened die steel using Cu-W electrode

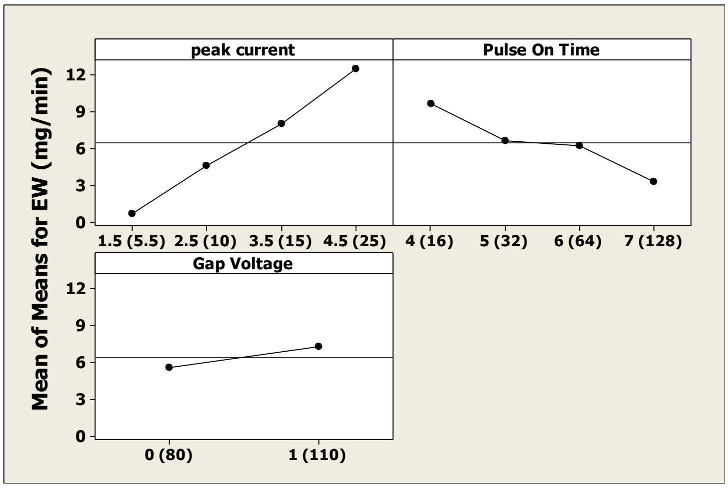

Figure 5.33 The main effect plot of EW (mg/min) for hardened die steel using Cu-W electrode

The main effects plot of Figure 5.33 shows that the electrodes wear increases with peak current and Gap voltage but decreases with Pulse On-time. Lower electrode wear can be obtained by setting the peak current and the gap voltage at lower level at the same time, and pulse On-time should be set at higher level. This result is in agreement with the conclusion of researches conducted by [35], [135] and [2].

5.6.3. Tool Wear Ratio TWR (%)

The percentage of EW (mg/min) relative to the MRR (mg/min) which is called the tool wear ratio used because it links EW with MRR. In general, as the MRR increases the EW and surface roughness will increase. Figure 5.34 shows that the most contributed variable on the TWR (%) is the gap voltage followed by pulse on-time. The main effect plot of TWR of Figure 5.35 the value of the TWR can be reduced mainly by increasing the pulse On-time and the gap voltage but the effect of pulse On-time is more significant.

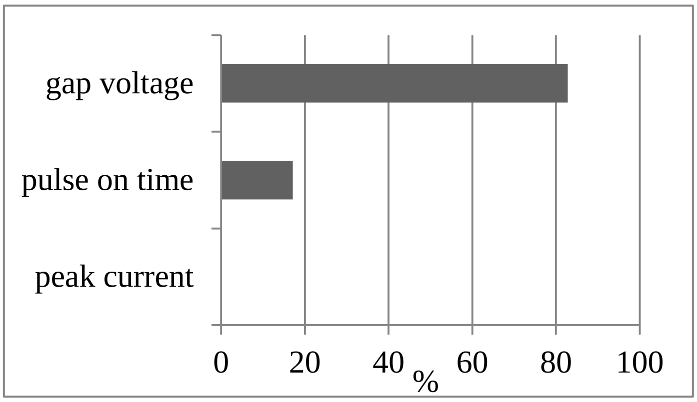

Figure 5.34 Contribution of machining variables on TWR (%) for hardened die steel using Cu-W electrode

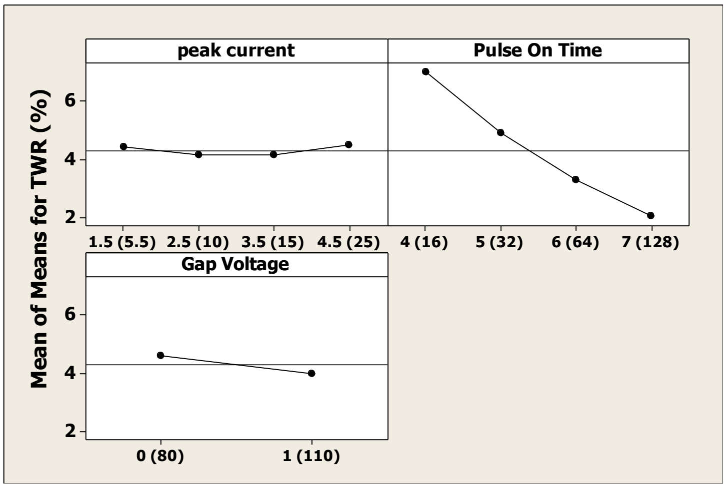

Figure 5.35 The main effect plot of TWR (%) for hardened die steel using Cu-W electrode

5.6.4. Surface Roughness Ra (µm)

Figure 5.36 shows that the most important variable influencing the surface roughness are Gap voltage, which contributed by 87% followed by peak current. As expected, the main effects plot of surface roughness as a function of machining variables in Figure 5.37 shows that the value of Ra (µm) linearly increases with peak current but decreases with gap voltage. The effects of pulse On-time on surface roughness are not obvious. The negative effect of Pulse On-time on Ra (µm) can be referred to the effect of longer pulse On-time on amount of material that can be melt and re-solidified from the workpiece which can create bigger crater size. The size of the crate is directly related to the discharge area; meanwhile the shape (topography) of the crater is related to the amount of the discharge (peak current and the discharge gap). This result is in agreement with the conclusion derived by [83] and [136].

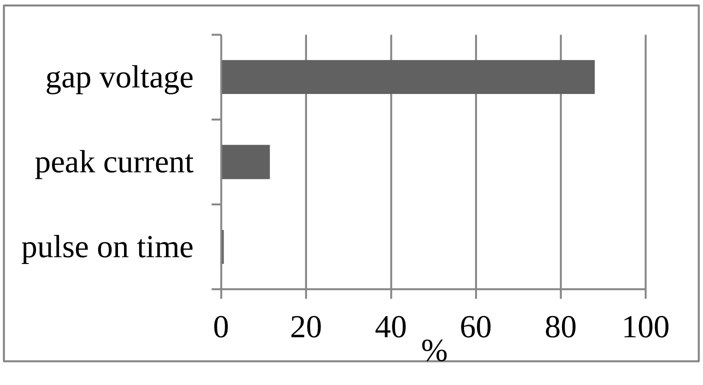

Figure 5.36 Contribution of machining variables on Ra (µm) for hardened die steel using Cu-W electrode

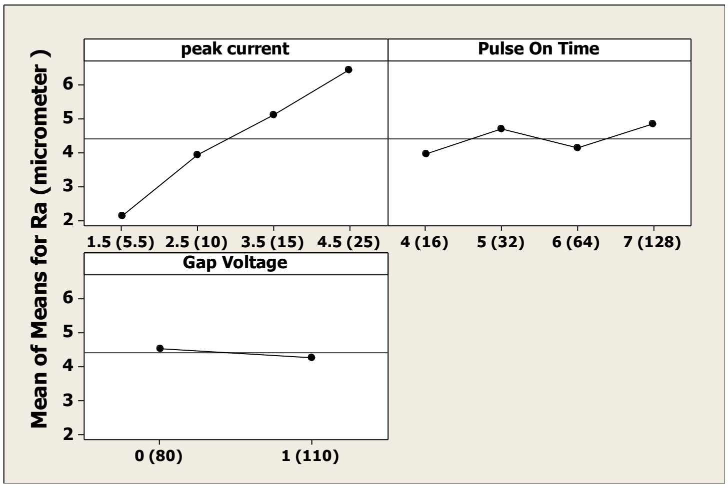

Figure 5.37 The main effect plot of Ra (µm) for hardened die steel using Cu-W electrode

5.6.5. Estimated Result at Optimum Condition and Confirmation Test

The analysis of the machining results shows that the maximum MRR (mg/min) can be achieved by setting the peak current at higher levels (3-4) (15-25 Ampere), pulse On-time also at high levels 3-4 (64-128 µs) and gap voltage at level 0 (80 volt). Lower EW value can be achieved by setting peak current at 1-2 (5.5-10 Amp), pulse On-time at 3-4 (64-128 µs) and gap voltage at level 0 (80 volt). Optimal setting for lower Surface roughness requires setting of peak current and gap voltage at lower levels. It is better to use the index TWR (%) to determine the optimal setting of the machining variables because lower TWR represents the Lower EW with respect to the MRR. Thus, the optimal settings of parameters can be shown in Table 5.10

Table 5.10 variables setting for optimal MRR (mg/min), EW (mg/min), and Ra (µm)

	Peak current code (ampere)				Pulse On-time code (µs)				Gap voltage code (volt)	
MRR (mg/min)	1.5 (5.5)	2.5 (10)	3.5 (15)	4.5 (25)	4 (16)	5 (32)	6 (64)	7 (128)	0 (80)	1 (110)
EW (mg/min)	1.5 (5.5)	2.5 (10)	3.5 (15)	4.5 (25)	4 (16)	5 (32)	6 (64)	7 (128)	0 (80)	1 (110)
RA (µm)	1.5 (5.5)	2.5 (10)	3.5 (15)	4.5 (25)	4 (16)	5 (32)	6 (64)	7 (128)	0 (80)	1 (110)

The predicted values in of MRR (mg/min), EW (mg/min) and the Ra (µm) according to the selected variables setting were calculated using equation 5.1 Roy [86].

$$\hat{Y}_{prd} = \bar{Y} + \sum_{i}^{n} (\hat{y}_{opt} - \bar{Y}) \qquad (5.1)$$

Where; $\hat{Y}_{prd}$ is the predicted means average, $\bar{Y}$ the overall experimental means average, and $\hat{y}_{opt}$ the mean averages of response at the selected setting of variables.

The predicted values tested experimentally using Cu-W electrode on hardened die steel at the same variables setting used to calculate the predicted values. This confirmation test is important to measure the variation between the predicted values and the confirmation test and the degree of confident. The analysis carried out using 1-sample t-test because the population standard deviation is unknown and the number of confirmation test (sample size) is limited. Table 5.11 shows the predicted values, the confirmation test, and the 1-sample t-test result.

Table 5.11 The 1-sample t-test of the predicted values and confirmation test of MRR, EW, and Ra at two different current setting

Peak current 2.5 (10 A), Pulse On-time 5(32 µs), and Gap voltage 0(80 volt)					1-sample t-test analysis			
	Test-1	Test-2	Test-3	Test-4	Mean	St Dev	SE Mean	95% CI
Predicted value of MRR (mg/min)	105.00	105.00	105.00	105.00	105.00	0.00	0.00	(105.00, 105.00)
Confirmation test of MRR (mg/min)	130.00	140.00	150.00	150.00	142.50	9.57	4.79	(127.27, 157.73)
Percentage of the difference (%)	18.18	27.27	36.36	36.36				
Predicted value EW (mg/min)	4.00	4.00	4.00	4.00	4.00	0.00	0.00	(4.00, 4.00)
Confirmation test of EW (mg/min)	6.40	6.20	7.50	7.70	6.95	0.76	0.38	(5.74, 8.16)
Percentage of the difference (%)	60.00	55.00	87.50	92.50				
Predicted value of Ra (µm)	4.35	4.35	4.35	4.35	4.35	0.00	0.00	(4.35, 4.35)
confirmation test of Ra (µm)	6.66	4.80	7.88	5.32	6.17	1.39	0.69	(3.96, 8.37)
Percentage of the difference (%)	54.88	11.63	83.26	23.72				

Peak current 3.5 (15 A), Pulse On-time 5(32 µs), and Gap voltage 0(80 volt)			1-sample t-test analysis			
	Test -1	Test -2	Mean	St Dev	SE Mean	95% CI
Predicted value of MRR (mg/min)	192.00	192.00	192.00	0.00	0.00	(192.00, 192.00)
Confirmation test of MRR(mg/min)	200.00	190.00	195.00	7.07	5.00	(131.47, 258.53)
Percentage of the difference (%)	36.36	0.00				
Predicted value EW(mg/min)	7.33	7.33	7.33	0.00	0.00	(7.33, 7.33)
Confirmation test of EW (mg/min)	10.70	10.80	10.75	0.07	0.05	(10.15, 11.38)
Percentage of the difference (%)	87.50	92.50	73.75			
Predicted value of Ra(µm)	4.30	4.30	4.30	0.00	0.00	(4.30, 4.30)
confirmation test of Ra (µm)	7.88	5.32	6.60	1.81	1.28	(-9.66, 22.86)
Percentage of the difference (%)	83.26	23.72	43.40			

The number of confirmed test (sample size) can influence the quality of the result. In manufacturing, testing many samples is not always manageable due to feasibility, time consuming and cost. The range of the derived values that contain the value of an unknown population parameter is known as interval of Confidence (CI). Table 5.11 shows the 1-sample t-test results for confirmation test at two different peak current setting.

For MRR at high peak current setting (3.5, 5, 0), the percentage error of confirmation test from the predicted value is in the range 18-36 with standard deviation (SD) equal 7.07%. The average of the predicted values 195 (mg/min) lays inside the interval of confidence (CI) equal (131,47–258,53). The Mean values of EW and Ra show percentage errors equal to 73.75 and 43.4 respectively with SD equal 0.759% and 1.386%. The equivalent interval of confidence are (5.742, 8.158), (3.959, 8.371) respectively.

In general, the 1-sample t-test for MRR, EW, and Ra at lower peak current setting (2.5, 5, and 0) shows higher standard deviation SD for MRR, EW and Ra. The SD, which is a measure of machining stability for all machining responses are less than 10. On the other hand, the interval of confidence CI (95%) is better at higher peak current setting.

5.7. Design and Manufacturing the New EDM Tool Electrode

The common EDM electrodes are; Copper alloy, Graphite, Tungsten and Copper-Tungsten composite. The drawback of Copper is due to its poor wear. Copper-Tungsten Cu-W powder metallurgy electrode shows the highest wear resistance and it is the preferred electrode for machining carbide. Tungsten grade in Cu-W electrode can reach up to 80%W. This electrode is manufactured by compaction of the micro size Tungsten particles followed by sintering at temperature over 2700^{0}C before infiltration with Copper. This makes Copper-Tungsten electrode the most expensive EDM electrode. The high hardness and melting point of Tungsten lead to difficulties in creating the desired electrode shape.

This part is aimed at synthesizing a new EDM tool electrode material using ball milling. Ball milling and mechanical alloying technique is a promising simple process in manufacturing due to the need of special composite material, which cannot be produced by conventional process. Milling experiment was designed using milling time and the different composition of WC, Si, and Ti powder as milling variables. Taguchi design of experiment being one of the most applicable techniques in quality improvement was adopted as the main statistical tool for design and analysis of experiment.

Before milling, the elemental powder were characterized for their particle size, shape, microstructure and chemical contamination using Malvern particle size analyzer, FESEM, and XRD studies were carried out using Bruker AXS D8. The tap density, green density and sintered density were measured using Ultrapycnometer 1000 v2.2, with helium gas at 19 psi and room temperature. Ball milling experiments were conducted under normal atmospheric condition using Fritsch PULVERISETTE 5 planetary ball mill keeping the milling conditions at one hour cycle duration, rotation speed at 300 Rev/min and the ball powder ratio fixed at 12:1.

The milled powders were also characterized for their particle size, microstructure, contamination, and densities using the same equipment. Consolidation was carried out via cold pressing at 740 MPa using CARVER Auto pallet hydraulic press machine. Sintering was carried out in argon environment at 950^{o}C for 120 min using high temperature furnace model LINO VWK-135-S.The flow rate of argon is 16.66 cm^{3}/sec. The hardness was measured in Rockwell B using AFARI 206 RTO hardness tester and the heat conduction was measured using the unsteady state heat transfer measurement model HT17.

5.7.1. Characterization of the Elemental Powder

Specification received from the supplier shows that the composition of the elemental powder material used in this research is as follows; a 99% pure electrolytic Copper powder (Cu) with an average particle size of 10 µm, an agglomerated Tungsten carbide (WC) powder of >99% with 3 µm average particle size of. Silicon powder used is 99% purity with an average particle size of 11 µm. The Titanium powder used is 99% purity with an average particle size of 15 µm. For further investigation, FESEM, XRD, and TEM were used and the results are as shown in section 5.7.1.1-5.7.1.3.

5.7.1.1. FESEM Analysis of the Elemental Powder

The microstructure of Copper, Tungsten carbide, Silicon, and Titanium are shown in Figure 5.38. The structure shows a rounded Copper powder with an average particles size of 8 µm. The average particles size of the agglomerated Tungsten carbide is 3-µm meanwhile the average particles size of Silicon particles is around 10 µm for the bigger particle and submicron for the fine particles. Titanium is regular in shape with average particles size equal to 10 µm.

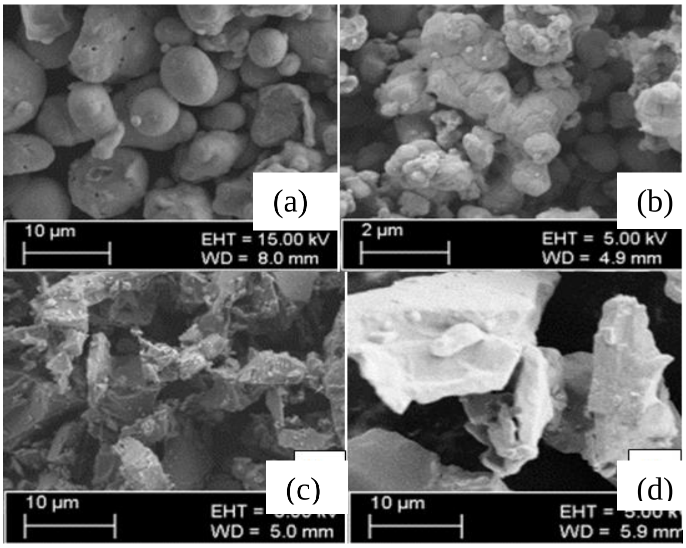

Figure 5.38 FESEM images of (a) Cu, (b) WC, (c) Si, and (d) Ti. powder

5.7.1.2. XRD Analysis of the Elemental Powder

The crystal structure of this elemental powder was analyzed using XRD. The plot of scattering intensity versus 2θ angle of the elemental powder of Cu, WC, Ti, and Si using Cu-Ka (1.5418740Å) are shown in Figure 5.39. Table 5.12 is the data analyses of XRD calculated using the distance between planes of atoms (d) and brag Bragg's equation. The spacing between nearest neighbors (a) using the planes constant [hkl], and the thickness of crystallite (t) using Scherer's Formula.The crystal structure of Copper is FCC with lattice constant equal to 3.61 Å.

The thickness of crystallite of the high intensity peak of Copper in the direction [111] is equal to 28.2 nm. The alpha-Tungsten carbide is a hexagonal close packed filled with carbon atoms leading to a six coordinate rhombohedra prismatic shape. This packing shows the lowest lattice constants ranged from 2.06 to 2.47 Å.

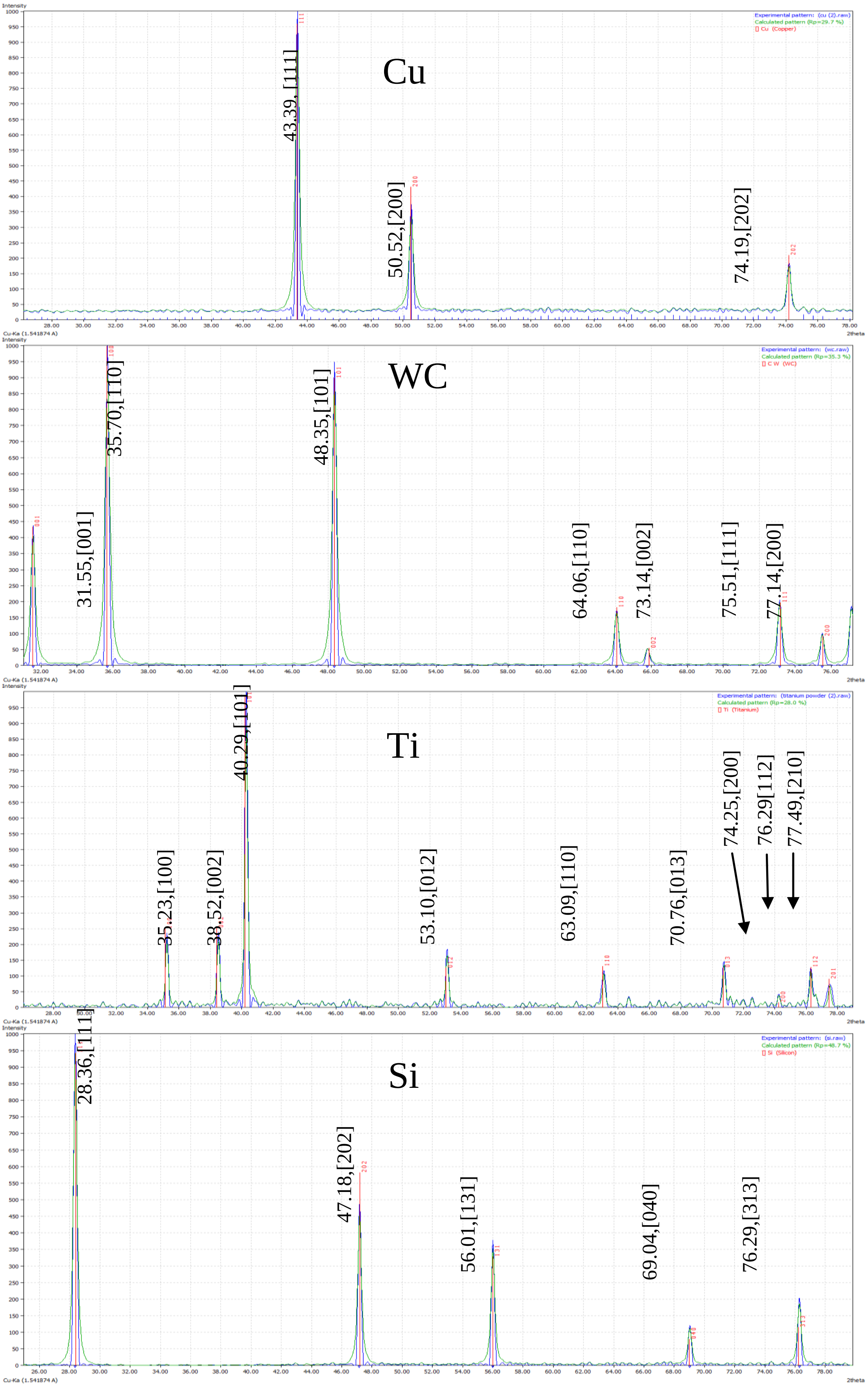

Figure 5.39 The X-ray diffraction pattern of Cu, WC, Ti, and Si (Cu-Ka-1.541814Å)

Table 5.12 The measured lattice constants for the elemental powder

Elements	2theta[°]	Intensity	h	k	L	d [A]	a [A]	t [A]
Cu	43.39	1000	1	1	1	2.09	3.61	282.18
Cu	50.52	363	2	0	0	1.81	3.61	289.91
Cu	74.19	172	2	0	2	1.28	3.62	328.66
WC	31.55	437	0	0	1	2.84	2.84	272.47
WC	35.70	1000	1	1	0	2.52	3.56	275.46
WC	48.35	954	1	0	1	1.88	2.66	287.39
WC	64.06	180	1	1	0	1.45	2.06	309.24
WC	73.14	210	0	0	2	1.29	2.59	326.42
WC	75.51	103	1	1	1	1.26	2.18	331.57
WC	77.14	190	2	0	0	1.24	2.47	335.29
Ti	35.23	232	1	0	0	2.55	2.55	412.66
Ti	38.52	236	0	0	2	2.34	4.68	416.61
Ti	40.29	1000	1	0	1	2.24	3.17	418.93
Ti	53.10	182	0	1	2	1.72	3.86	439.64
Ti	63.09	119	1	1	0	1.47	2.08	461.45
Ti	70.76	147	0	1	3	1.33	4.21	482.29
Ti	76.29	126	1	1	2	1.25	3.06	499.99
Ti	77.49	78	2	1	0	1.23	2.75	504.18
Si	28.36	1000	1	1	1	3.15	5.45	270.45
Si	47.18	481	2	0	2	1.93	5.45	286.10
Si	56.01	373	1	3	1	1.64	5.45	296.96
Si	69.04	120	0	4	0	1.36	5.44	318.18
Si	76.29	201	3	1	3	1.25	5.44	333.34

The thickness of crystallite for 1000 and 954 intensity peaks is 27.5 and 28.7 nm, which is the same as that for Copper. Titanium shows a thickness of crystallite equal to 41.89 nm for the 1000 intensity peak, which is the largest one, compared to the other element. Since α-Ti is a hexagonal close pack, its lattice constant varies from one direction to other, it is equal to 3.86 Å in the direction [101] of the 1000 intensity peak. Silicon is a diamond structure with the lattice constant a=5.44 Å and the equivalent thickness of crystallite (t) for 1000 intensity is equal to 27 nm.

5.7.1.3. TEM Analysis of the Elemental Powder of Cu, WC, Ti, and Si

TEM was used to analysis the structure of the elemental powder at high resolution. This was used to confirm the crystal structure concluded from XRD data such as the thickness of crystallite, defect, orientation, and composition. The TEM images of Cu, WC, Ti, and Si are shown in Figures 5.40 and 5.41.

Figure 5.40 (a) shows the oriented and ordered lattice interference fringe for Cu with a lattice constant equal to 4Å which is bigger than the one calculated from XRD data for FCC Cu in the direction [111] but close to that of [202] as shown in Table 5.12.

TEM images of Tungsten carbide are shown in Figure 5.40 (b). The structure reveals that the analyzed sample mainly without real or apparent crystalline (amorphous structure) with a few crystalline structures distributed. The lattice constant of the detected crystal structure is around 4.5Å, which varies from that shown in Table 5.12.

TEM images in Figure 5.40, which is selected from of a series of five images for Ti and Si. The analyzed TEM image of Ti confirms that the thickness of crystallite is longer than that of Copper and Tungsten carbide, the size of the lattice constant of Ti is 4Å, which is the same as that calculated using XRD data for the 1000 intensity peak at [101]. Silicon on the other hand does not show any crystalline structure.

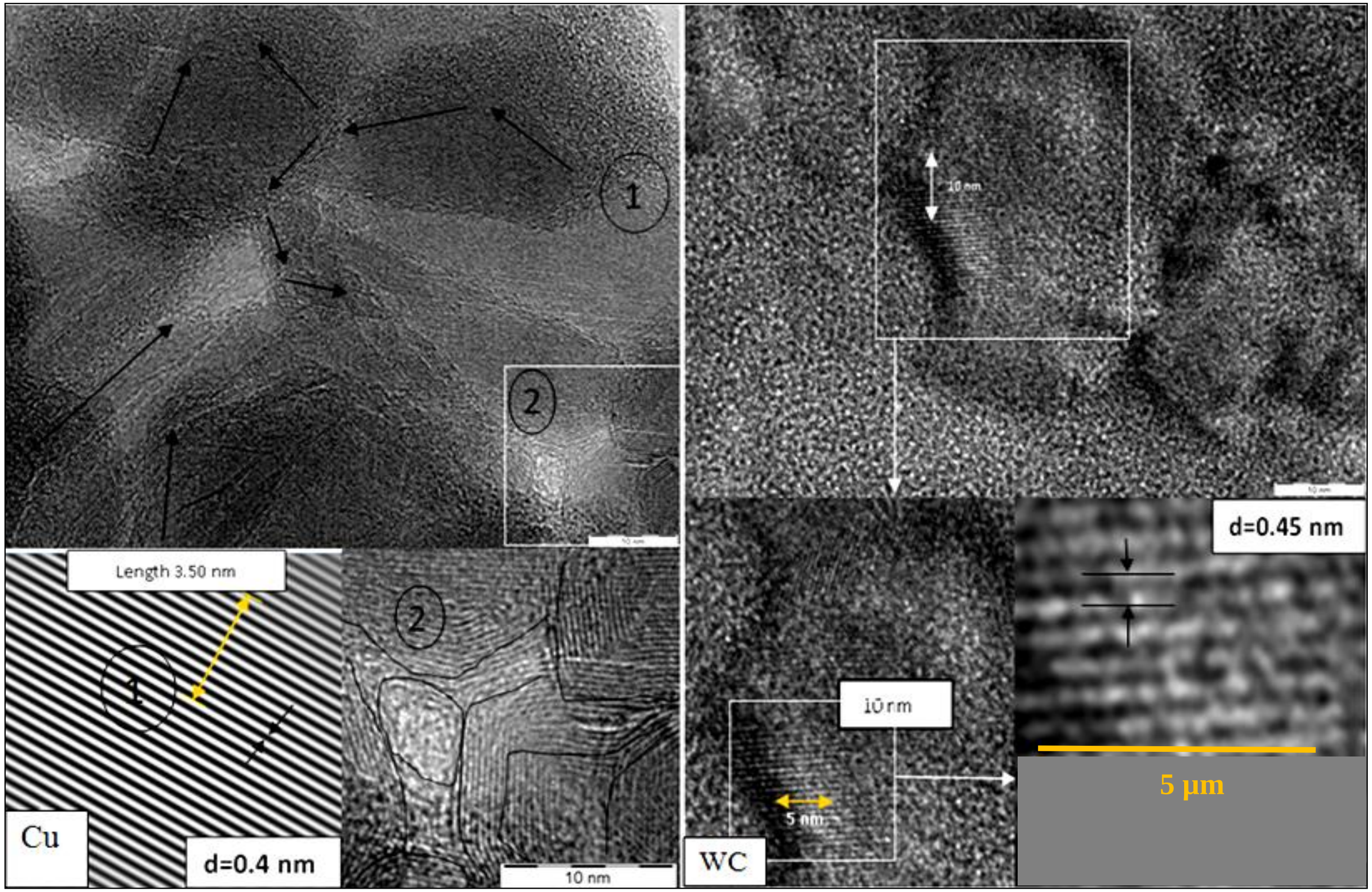
(a)

(b)

Figure 5.40 Transmission electron microscope images of the elemental powder Copper and Tungsten carbide

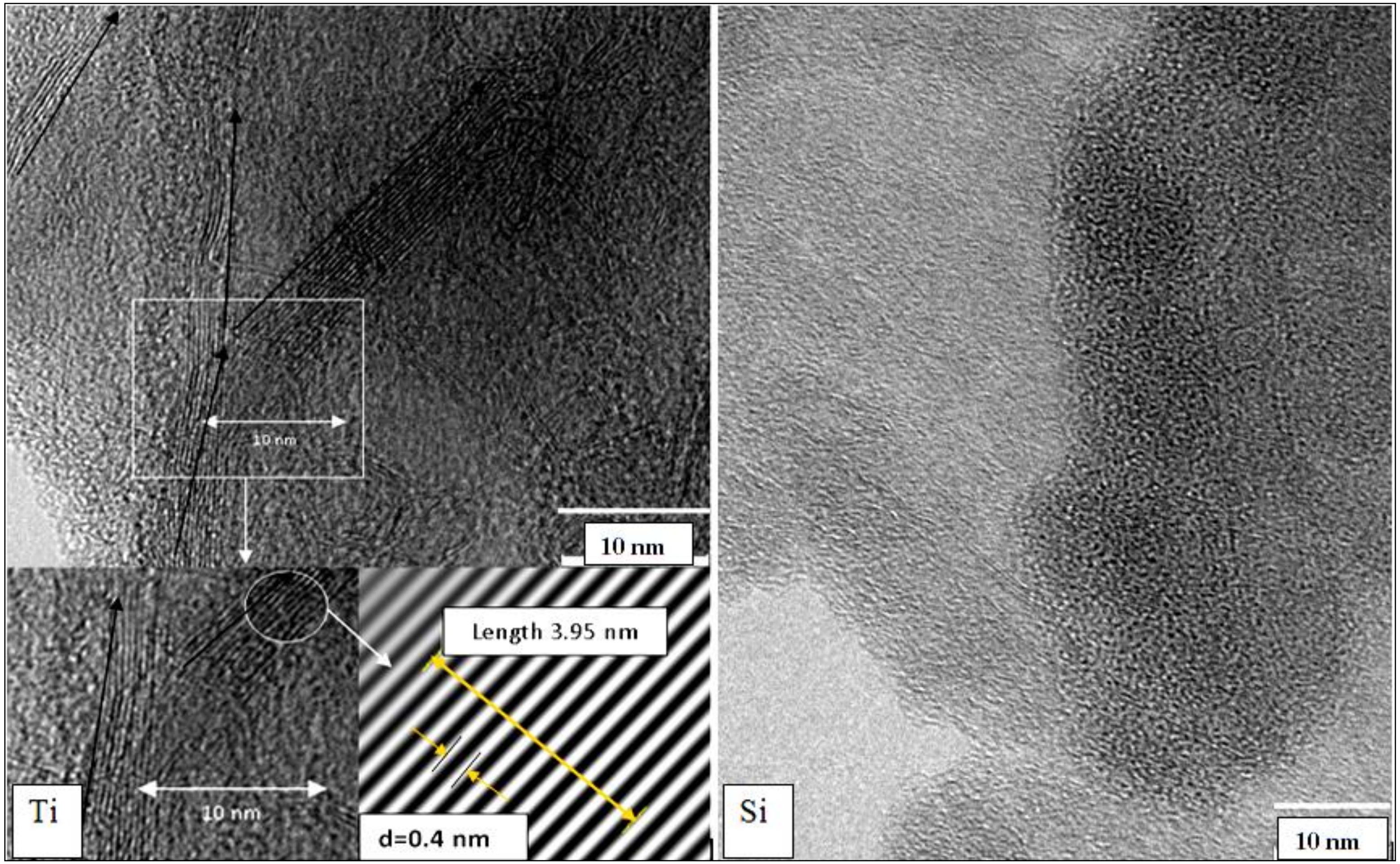

Figure 5.41 Transmission electron microscope images of the elemental powder of Titanium and Silic

5.7.2. Synthesizing and Characterization of Cu-WC-Si using Ball Milling

Milling experiments are designed using L16 Taguchi orthogonal using milling time, Tungsten carbide content, and Silicon constant as milling variables. All the three variables fixed at four levels as shown in Table 5.13. The main measured properties of the milled powder after milling are the tap density (ρ_{tap}) , green densities (ρ_{gr}), porosity of green compact, and compressibility (Φ). After sintering, the properties measured are sintered density ($\rho_{\sin t}$), porosity after sintering, densification (Ψ), hardness, and thermal decay constant. The analysis carried out to measure the effect of milling variables on these properties using the analysis of variants ANOVA and the results of the mean averages are shown in Table 5.14. The sum of square SS and the percentage contribution SS (%) of tap density, green density and the compressibility are shown in Tables 5.15.

Table 5.13 The experimental layout of L16 Taguchi orthogonal array by three variables all at four levels including the observed values of the theoretical density (ρ_{theo}), tap density (ρ_{tap}) , green densities (ρ_{gr}), porosity of green compact, compressibility (Φ), sintered density ($\rho_{\sin t}$), porosity after sintering, densification (Ψ), hardness, and thermal decay constant.

L16 Taguchi orthogonal array by three variables all at four levels				Milling results before sintering					Milling results after sintering				
	Milling time (h)	WC (wt %)	Si (wt %)	ρ_{theo} (g/cm^3)	ρ_{tap} (g/cm^3)	ρ_{gr} (g/cm^3)	Green porosity (%)	Φ (%)	$\rho_{\sin t}$ (g/cm^3)	Sintered porosity (%)	Ψ (%)	Hardness (HRB)	Thermal decay constant (b) s^{-1}
Exp-1	5	0	0	8.90	7.68	7.45	16.29	-2.99	7.24	18.65	-14.48	26	3.45
Exp-2	5	15	0.75	9.21	8.00	7.50	18.57	-6.25	7.75	15.85	14.62	26	4.35
Exp-3	5	30	1.5	9.54	8.40	7.99	16.25	-4.88	7.73	18.97	-16.77	15	4.09
Exp-4	5	45	2.25	9.89	8.16	8.62	12.84	5.64	8.38	15.27	-18.9	22	
Exp-5	10	0	0.75	8.72	7.44	7.12	18.35	-4.30	6.94	20.41	-11.25	18	6.38
Exp-6	10	15	0	9.41	7.89	7.81	17.00	-1.01	6.56	30.29	-78.13	1	2.72
Exp-7	10	30	2.25	9.33	8.29	7.96	14.68	-3.98	7.52	19.40	-32.12	11	6.43
Exp-8	10	45	1.5	10.13	8.35	8.52	15.89	2.04	8.66	14.51	8.7	14	6.46
Exp-9	15	0	1.5	8.54	7.26	6.96	18.50	-4.13	7.15	16.28	12.03	13	6.43
Exp-10	15	15	2.25	8.82	7.34	7.44	15.65	1.36	7.61	13.72	12.32	11	7.29
Exp-11	15	30	0	9.99	8.35	8.12	18.72	-2.75	7.71	22.82	-21.93	38	5.01
Exp-12	15	45	0.75	10.38	8.76	8.5	18.11	-2.97	8.25	20.52	-13.3	34	4.74
Exp-13	20	0	2.25	8.37	7.65	6.83	18.40	-10.72	7.25	13.38	27.27		5.73
Exp-14	20	15	1.5	9.01	8.22	7.34	18.53	-10.71	7.75	13.98	24.55	9	5.04
Exp-15	20	30	0.75	9.76	8.48	7.87	19.36	-7.19	7.85	19.57	-1.06	26	5.1
Exp-16	20	45	0	10.65	8.87	8.10	23.94	-8.68	8.33	21.78	9.02	42	5.24

Table 5.14 The mean averages of tap density, green density, and compressibility

Variables		Tap densities (g/cm^3)	Green densities (g/cm^3)	Compressibility Φ (%)	Green porosity (%)	Sintered porosity	Densification (%)	Hardness (HRB)	Decay constant (1/s)
Milling time (h)	5	8.060	7.890	-2.12	15.99	17.19	-8.88	22.25	.96
	10	7.992	7.853	-1.81	16.48	21.15	-28.20	11.00	5.50
	15	7.928	7.755	-2.12	17.74	18.33	-2.72	24.00	5.87
	20	8.305	7.535	-9.33	20.06	17.18	14.95	19.25	5.28
WC (wt %)	5	7.508	7.090	-5.54	17.89	17.18	3.4	14.25	5.50
	10	7.863	7.523	-4.15	17.44	18.46	-6.66	11.75	4.85
	15	8.380	7.985	-4.70	17.25	20.19	-17.97	22.25	5.16
	20	8.535	8.435	-0.99	17.70	18.02	-3.62	28.00	5.48
Si (wt %)	5	8.197	7.870	-3.86	18.99	23.39	-26.38	26.75	4.10
	10	8.170	7.748	-5.18	18.60	19.09	-2.75	26.00	5.14
	15	8.057	7.702	-4.42	17.29	15.94	7.13	12.75	5.5
	20	7.860	7.713	-1.93	15.39	15.94	-2.86	11.00	6.48

Table 5.15 The sum of square of density, green density, and compressibility derived from ANOVA

Tap densities (g/cm^3)		Green densities (g/cm3)		Compressibility (%)		Green porosity (%)		Sintered density		Sintered porosity (%)		Densification (%)		Hardness (HRB)		b (1/s)	
SS	SS (%)	SS	SS (%)	SS	SS (%)	SS	SS	SS	SS	SS	SS	SS	SS	SS	SS	SS	SS
0.33	0.02	0.30	0.02	160	22.79	39.69	54.99	0.36	8.59	42.1	18.97	380	52.93	398	14.08	0.00	3.15
1045.00	50.05	967.06	50.10	283	40.32	0.93	1.29	3.52	84	19.3	8.70	949	13.22	673	23.81	0.02	29.89
1042.00	49.93	963.09	49.89	259	36.89	31.55	43.72	0.27	6.60	160.	72.33	243	33.85	175	62.11	0.04	66.97
2087.00	100.00	1930	100.00	703	100.00	72.179	100.00	4.15	100.00	221	100.00	718	100.0	282	100.00	0.0618	100.00

5.7.2.1.Effect of Milling Variables on Tap Density (g/cm3) of Cu-WC-Si

The contribution of milling variables on tap density shows in Figure 5.42 indicates that that the tap density majorly affected by the compositions on milled powder. The effect of milling variables on tap density is negligible. The main effect plot of tap density in Figure 5.43 shows that the tap density increases with Tungsten carbide and decreases with Silicon content. This trend is also expected since Tungsten carbide density is six times higher in density than Silicon density. The tap density slightly decreases with time and then start to increase after 15 h.

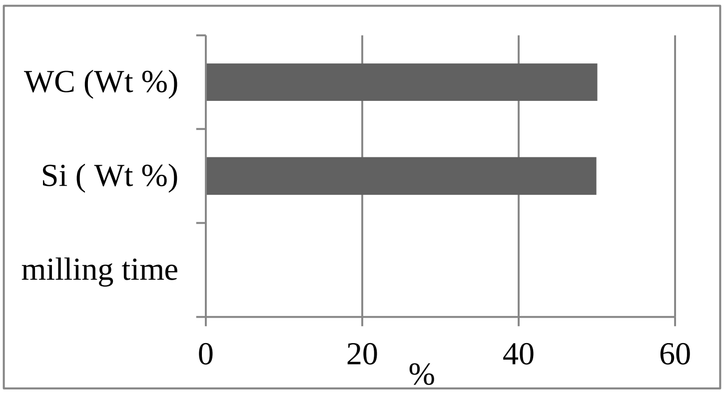

Figure 5.42 Contribution of milling variables on Tap density of milled Cu-WC-Si powder

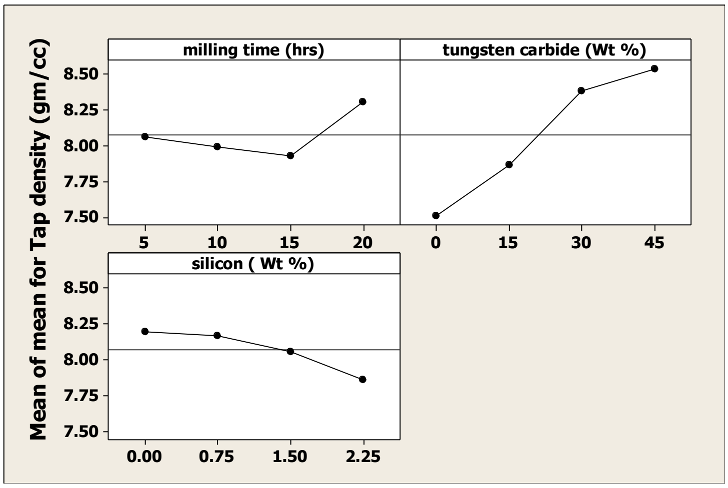

Figure 5.43 The main effect plot of tap density (g/cm^3) versus milling time, Tungsten content (wt %), and Silicon (wt %)

5.7.2.2.Effect of Milling Variables on Green Density (g/cm^3) of Cu-WC-Si

The contribution of variables on the densities of powder after compaction (Green density) in Figure 5.44 show that the green density mostly influenced by the Tungsten carbide and Silicon content. The main effect plot in Figure 5.45 indicates that the green density increases with the Tungsten carbide content because it is a high density material 14 (g/cm^3) and decreases with Silicon 2.3 (g/cm^3). With longer milling time the green density decreases or in other word the porosity will increases. In the early stages of the milling process, the brittle powder (Si) easily fragmented and the ductile metal powder (Cu) particles are flattened leading to this is referred to as lamellar structure. With continued milling, the microstructure refinement by fracturing and agglomeration by cold welding will continue leading to bigger and harder particles. Deformation this harder particle under cold compaction is difficult.

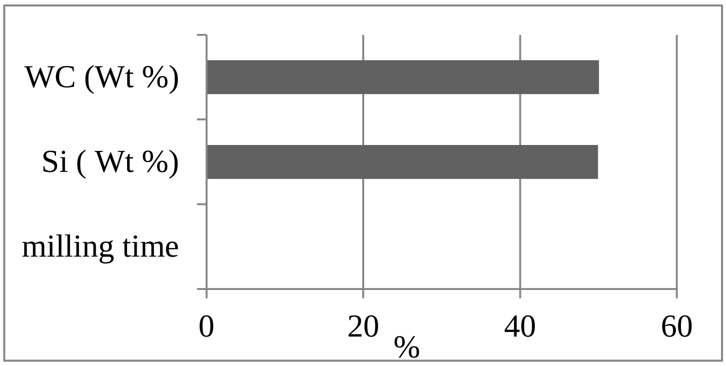

Figure 5.44 Contribution of milling variables on Green density of milled Cu-WC-Si powder

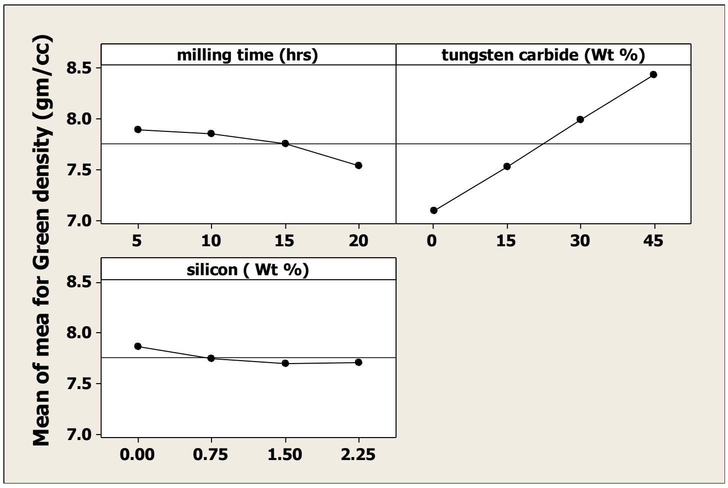

Figure 5.45. The main effect plot of Green density (g/cm^3) versus milling time, Tungsten content (wt %), and Silicon (wt %)

5.7.2.3.Effect of Milling Variables on the Compressibility (%) of Cu-WC-Si

The behaviour of density change under cold compaction from tap density to green density was measured by the compressibility parameter. The higher value of compressibility means the higher final density (lower porosity). The compressibility is measured as the percentage of density change from tap density to green relative to the targeted theoretical density. Figure 5.46 shows that the value of compressibility mainly effected by Tungsten carbide followed by Silicon content and milling time. The main effect plot of compressibility in Figure 5.47 shows that the compressibility increases with Tungsten carbide and Silicon but decreases with milling time. The effect of milling time is significant after 15 h milling time. The improvement in compressibility by silicon can be referred the ease of fracture make silicon powder works as a lubricant.

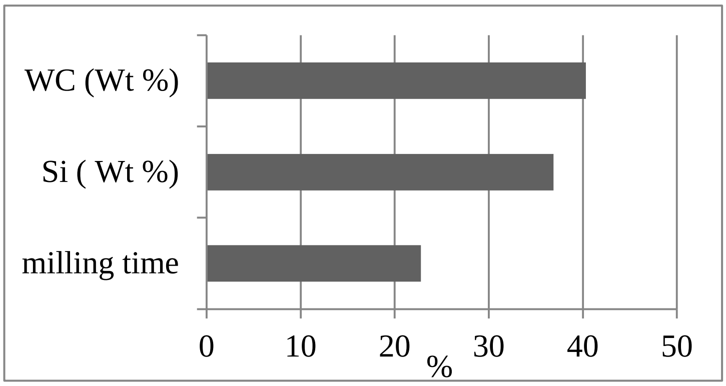

Figure 5.46 Contribution of milling variables on Compressibility (%) of milled Cu-WC-Si powder

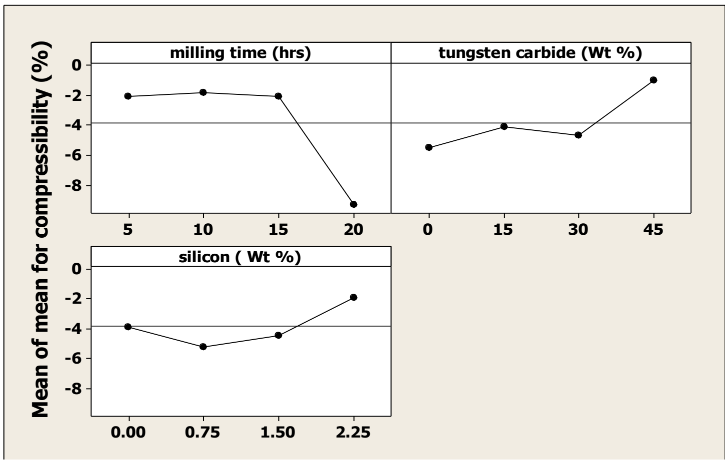

Figure 5.47 The main effect plot of Compressibility (%) versus milling time, Tungsten content (wt %), and Silicon (wt %)

Negative compressibility means that the tap density of the free powder is higher than the green density after compaction. This can be related to the technique used to measure the densities. The pycnometer measures the density by measuring the volume that can be occupied by helium gas which in turn will be used to measure the correct volume occupied by powder or solid sample inside. The penetration of gas primarily depends on type of gas, gas pressure, type of pores and temperature. After compaction, some of the pores can be closed inside the green compact where the pycnometer gas cannot penetrate and as a result, the measured volume will be less than the real volume (higher density). This can be seen in Figure 5.46.

5.7.2.4.Effect of Milling Variables on the Porosity (%) of Cu-WC-Si

The Contribution of milling variables on the Porosity of the Green compact shown in Figure 5.48 indicates that the porosity is mainly affected by milling time followed by Silicon content. The effect of Tungsten carbide content on the porosity is less than three percent. The main effect plot of the porosity of green compact shown in Figure 5.49 indicates that this porosity increase with milling time up to 16% after 15 h milling and around 20% after 20 h milling. Silicon content reduces the value of porosity from 19% at zero Silicon content to around 15% at 2.25 wt% of Silicon. The effect of Tungsten carbide shows that the porosity of green compact remains around 17.5% for all Tungsten carbide content.

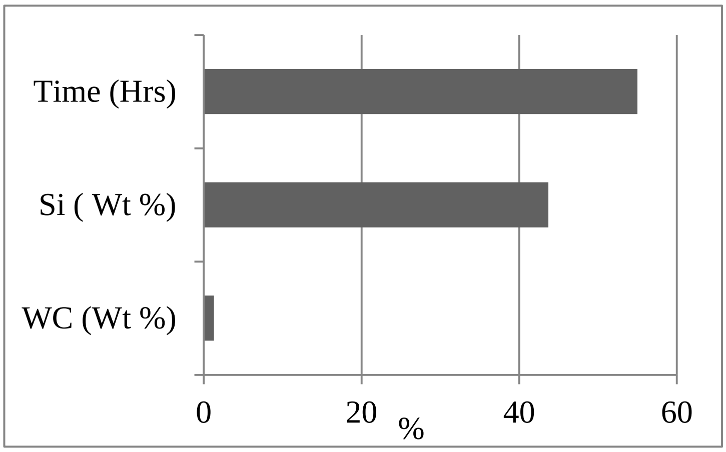

Figure 5.48 Contribution of milling variables on the Porosity of Cu-WC-Si Green compact

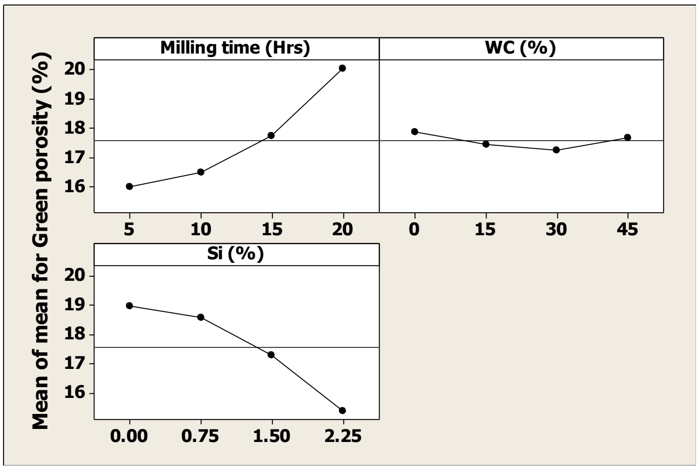

Figure 5.49 The main effect plot of Green porosity (%) versus milling time, Tungsten content (wt %), and Silicon (wt %)

The positive effect of Silicon on the porosity of green compact can be referred to the ease of fracture of Silicon particle under compaction, which in turn increases the slipping point and reordering. Figure 5.50 is a schematic diagram showing the effect of the closed pore on the volume reading and it is confirmed by Figure 5.51.

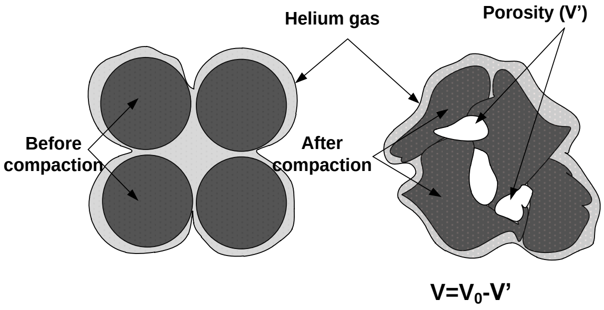

Figure 5.50 The effect of the closed pore on volume reading of pycnometer

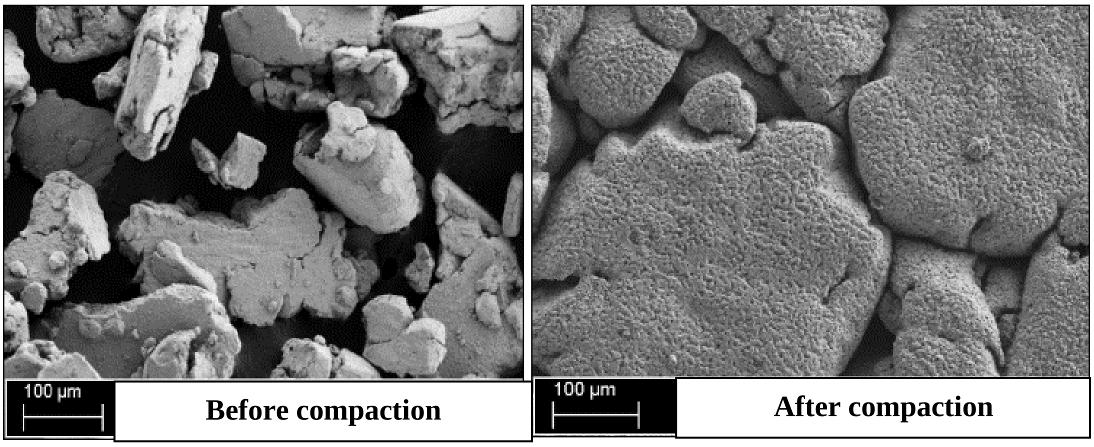

Figure 5.51 FESEM images show the milled powder before and after compaction

5.7.2.5.FESEM of Ball milled Cu-WC-Si Powder

Refer to Table 4.4, Figure 5.52 is the FESEM images of milled powder for experiments 1-4 at three different magnifications. The four experiments are all milled for 5 h. The images reveal that the particle sizes of the milled powder do not depend on milling time but it depends on the amount and properties of milled powder.

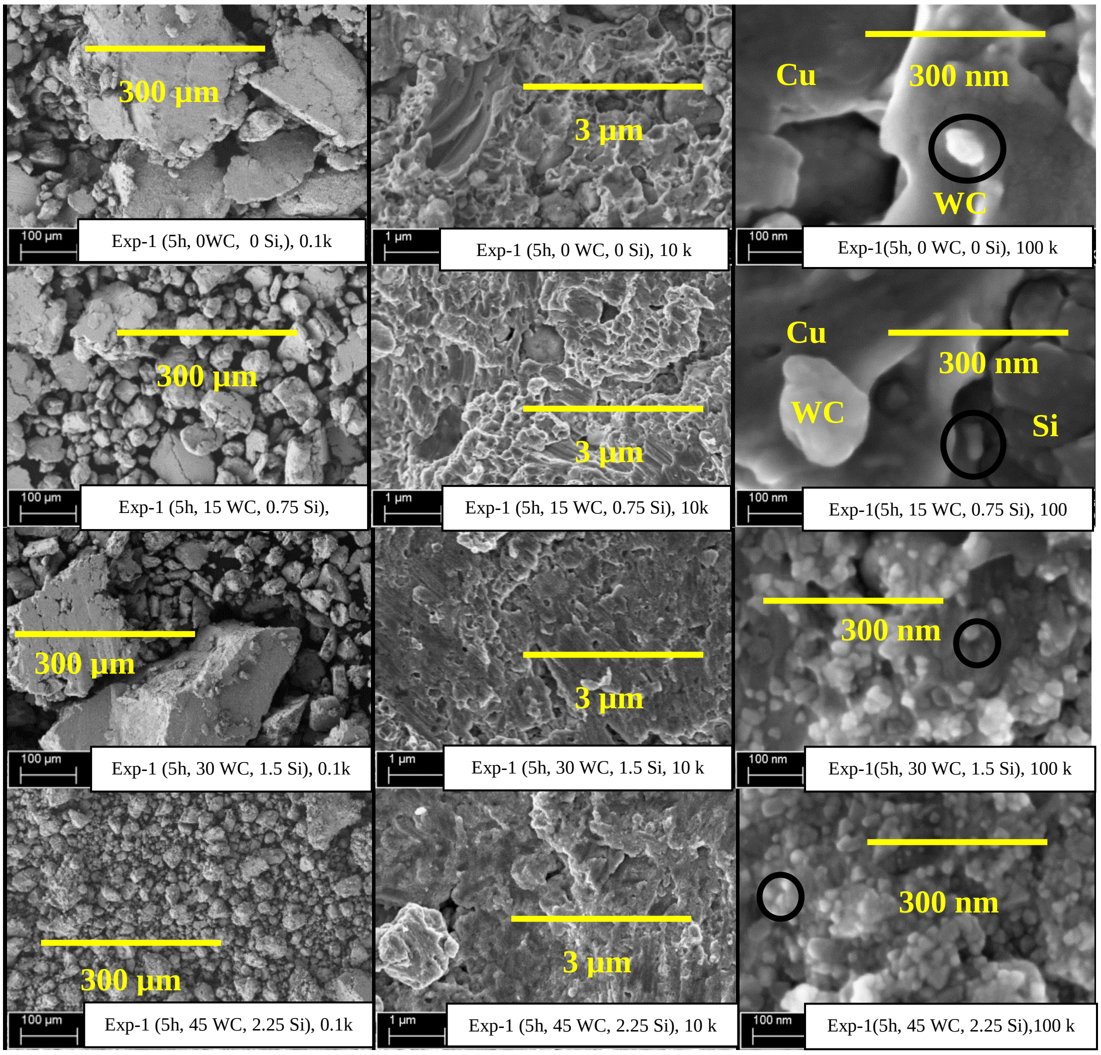

Figure 5.52 FESEM images of 5 h milled powder from Exp-1 to Exp-4 at three different magnification [low (0.1k), midrange (10k), and high (100k)]

The granular-size of the milled powder decreases with increases in the amount of Silicon as shown in image Exp-4 where Silicon content is maximum (2..25 Si wt%). In Exp-1, Exp-2 and Exp-3, Copper content which is the ductile phase is more than Exp-4 and that is why the milled particle size is bigger. The higher magnification images show that after 5 h milling time, a nanosize particle with less than 50 µm achieved. The 10k magnification shows a good homogenization with some closed and channelled pored can be seen. The high magnification FESEM images (100k) in Figure 5.53 of Cu-WC-Si powder milled for 15 h show a high surface oxide. This is an expected result; since the surface energy is inversely proportional to reduction in particle size and will contribute to the total driving force for reaction according to this relation $G_{total} = G_v = G_s$, Where; G_v is molar free energy and G_s is the surface energy.

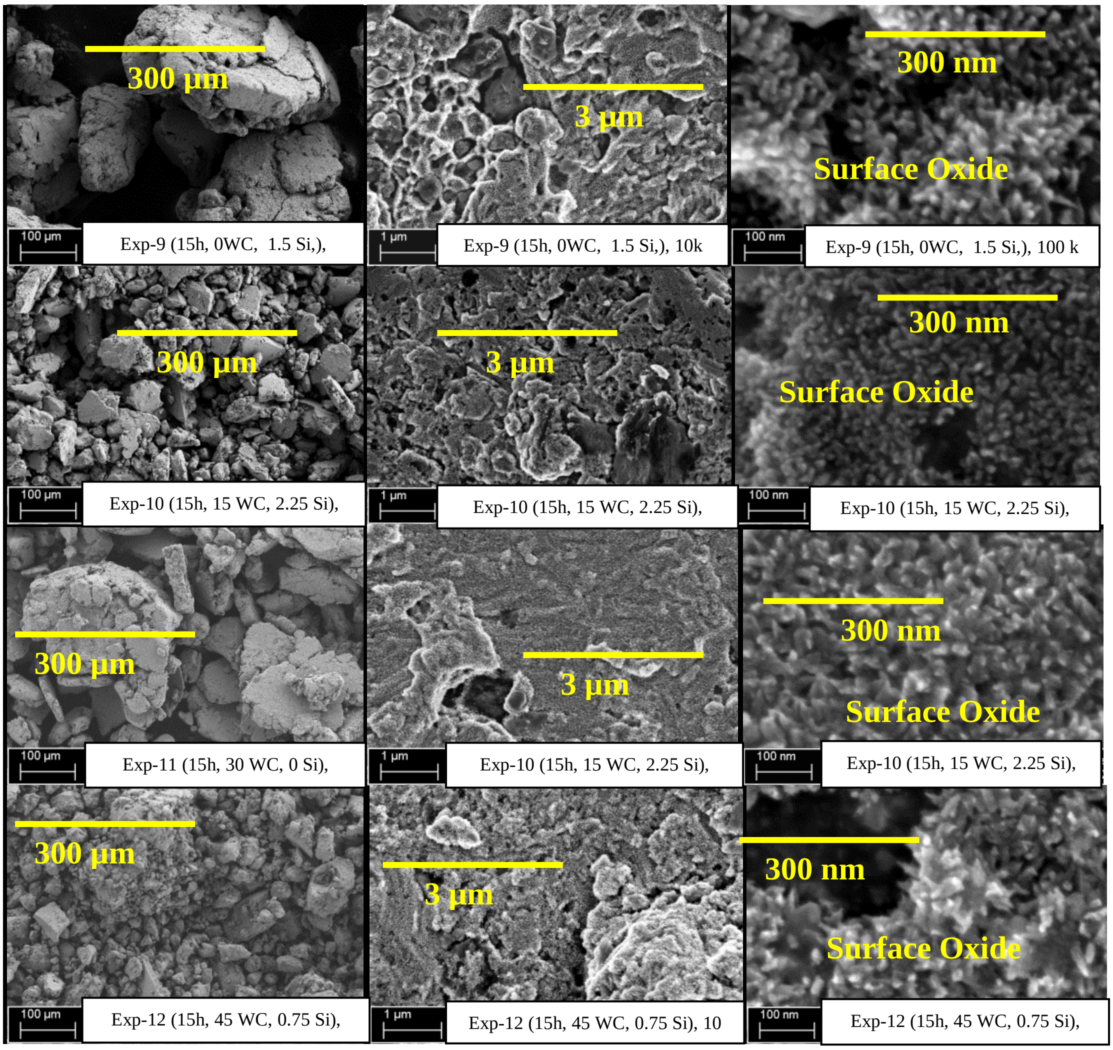

Figure 5.53 FESEM images of the 15 h milled powder from Exp-9 to Exp-12 at three different magnification [low (0.1k), midrange (10k), and high (100k)]

The granular-size of the milled powder also increases with decreasing of WC and Si as can be seen from 0.1k magnification images of Exp-9 (minimum WC) and Exp-11 (lower Si). The Energy dispersion X-ray EDX of the milled powder for the 15 h milled powder of Exp-10 (Cu+15%WC+2.25%Si) taken at the wall area (spectrum 1), Area 2 and Area 3 are as circled in Figure 5.54. It is clear that after 15 h milling time, that this surface oxide and contamination by zirconium are detected.

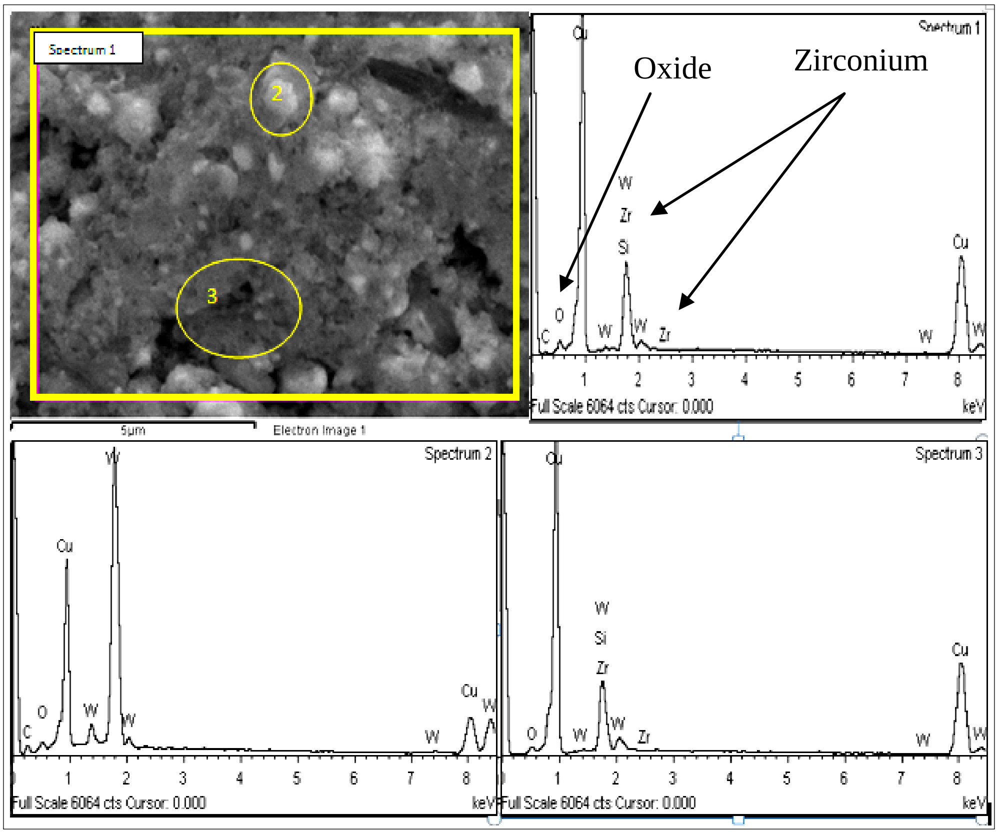

Figure 5.54 EDX analysis at different area on the 10 h milled powder of Exp-10 (Cu+15%WC+2.25%Si).

5.7.2.6.XRD Analysis of Bal- milled Cu-WC-Si Powder

Figure 5.55 is the XRD pattern of the milled Cu-WC-Si powder aligned with the spectrum of the XRD pattern elemental of powder. Measurement was carried out on milled powder of experiments 1-8 and the pattern compared with the pattern of the elemental powder as shown in Figure 5.32. The two high intensity peaks of Copper belonging to (43.39, [111]) and (50.52, [200]) as well as the four highest intensity peaks of Tungsten carbide along (31.55, [001]), (35.70, [110]), (48.35, [101]), and (64.06, [110]) are detected. Two peaks of Silicon belonging to (47.18, [202]) and (56.01, [131]) are also detected. All the detected peaks of milled powder, which belongs to the higher energy, are identical to the elemental powder. The low energy peak belongs to WC at (73.14, [002]), WC (75.51, [111]) are overlapped with that belonging to Cu at (74.19, [202]), WC (77.14, [200]),

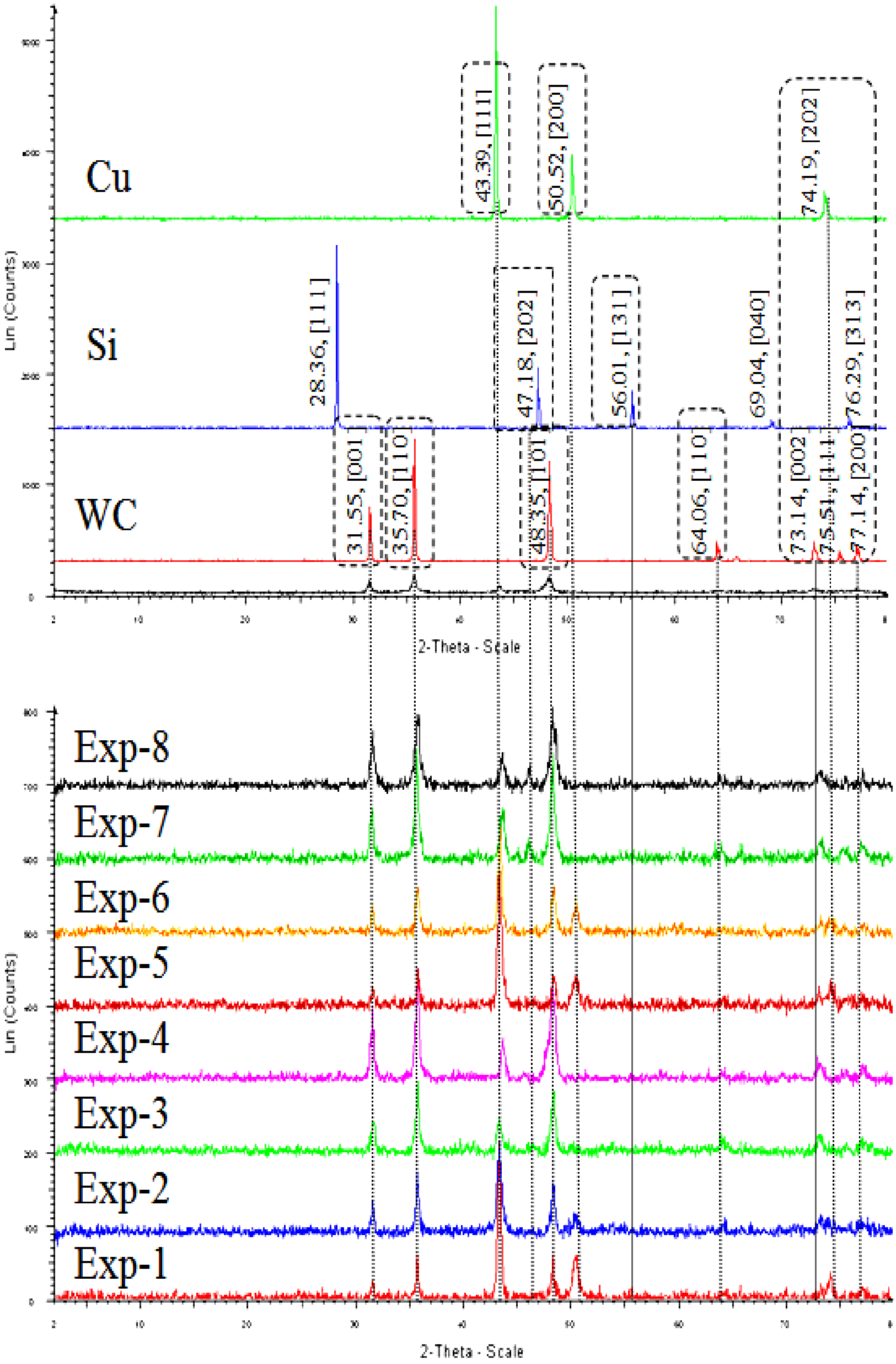

Figure 5.55 XRD pattern of the milled powder aligned with the spectrum of "as revived" powder

5.7.3. Consolidation of Cu-WC-Si Milled Powder

Liquid phase sintering was carried out by sintering the green compact at 1200^{0}C, which is greater than the melting point of Copper. The Powder was placed into the cylindrical cast iron mold of 13 mm diameter and a wall thickness of 2 mm at temperature 1200^{0}C in an atmosphere of helium gas for 2 h. Figures 5.56 A, B, C, and D are the optical microstructure of the liquid phase sintered Cu-WC-Si taken at the boundary between the powder and the mold.

The microstructure of the contact layers between the compact and the internal surface of the die show that Copper liquid phase moves out from the compact region and interact with the internal surface of the mold material (cast iron) leading to a formation of thick intermetallic layers. The average thicknesses of these layers exceed 100 µm. the failure of liquid phase sintering creates a high degree of porosity and a lack in the electrically conductive materials.

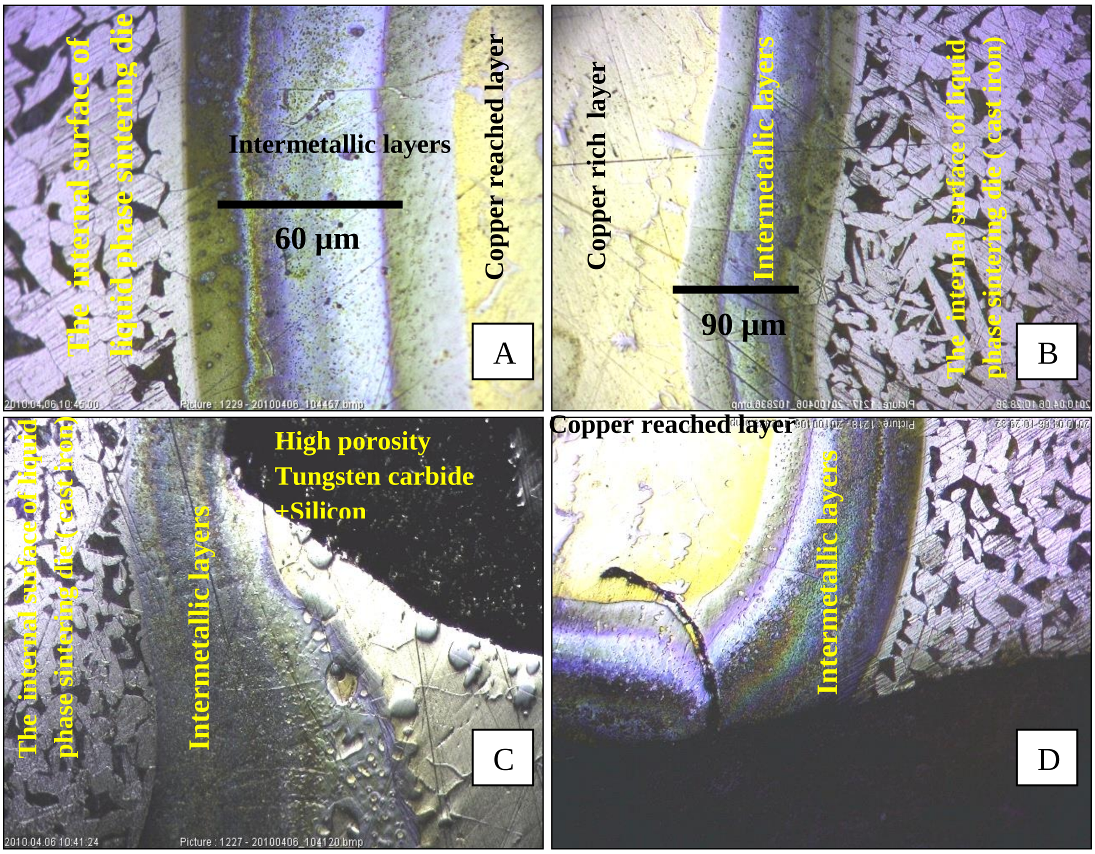

Figure 5.56 (A), (B), (C), and (D) are the optical microscopic images taken at the boundary between the mold (cast iron) and the liquid phase Cu-WC-Si composite sintered at 1200 ^{0}C for 2 h.

5.7.3.1.Sintered Density of Cu-WC-Si Composite Electrode

Consolidation was carried out via cold compaction at 740 MP followed by sintering at 950 ^{o}C for 2 h. Figure 5.57 shows that the sintered density mainly depends on Tungsten carbide content followed by milling time. The densification during sintering depends on the amount of material that can be moved by diffusion mechanism at the grain boundary. The main effect plot of sintered density in Figure 5.58 shows that the mean average of sintering density increased with increasing with Tungsten carbide and Silicon content. The improvement in sintered density with Silicon content can be referred to the chemical stability, which is improved by the presence of Silicon. Sintered density slowly decreases with milling time up to 10 h and then increases with time. This can be explained by the effect of contamination from the milling medium (zirconia) on the density.

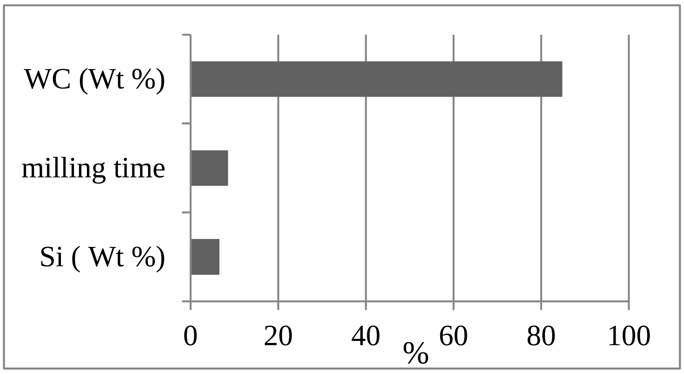

Figure 5.57 Contribution of milling variables on density (g/cm^3) of sintered Cu-WC-Si composite electrode

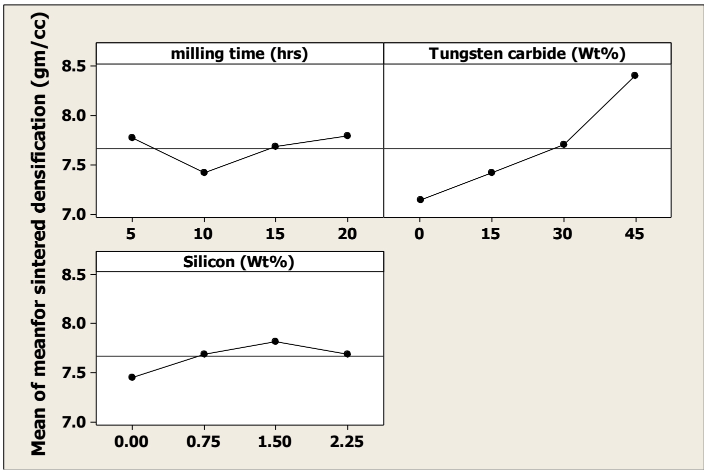

Figure 5.58 The main effect plot of sintered density versus Tungsten %, Silicon %, and milling time

5.7.3.2.Densification of Cu-WC-Si Composite During Sintering

This parameter is measured as the percentage of improvement achieved in density (green-sintered) during sintering relative to the theoretical density. As shown in Figure 5.59, the value of densification parameter is mainly affected by milling time and Silicon followed by Tungsten carbide content. the main effect plot of the densification in Figure 5.60 indicates that the densification becomes positive only after 15 h milling time and also at Silicon content more that 1.5 Wt %. The negative effect of WC on densification during sintering can be referred to the low solubility of Tungsten carbide with Copper. Milling time improves homogenization and particle size reduction. Meanwhile Silicon improves the chemical stability and reduces the agglomeration of milled particles and cold welding with milling medium.

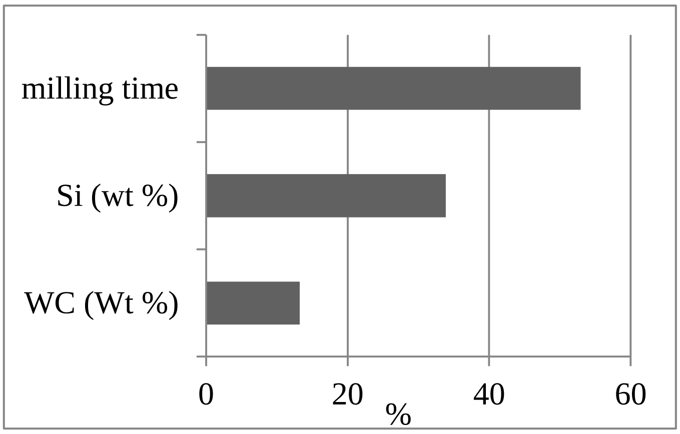

Figure 5.59 Contribution of milling variables on the densification (%) of sintered Cu-WC-Si composite electrode

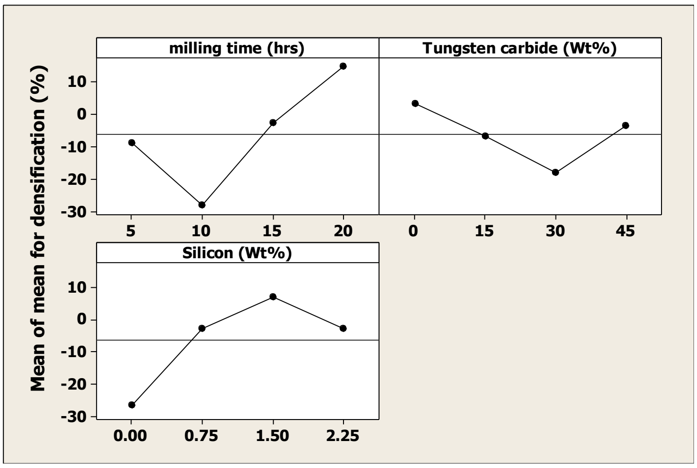

Figure 5.60 The main effect plot of sintered density versus Tungsten %, Silicon %, and milling time

5.7.3.3.The Porosity of Cu-WC-Si Composite after Sintering

Figure 5.61 shows the contribution of variables on the porosity after sintering. The most important variables contribute on the porosity after sintering is the Silicon content followed by milling time. As it mentioned in section 5.3.3.2, the low contribution of Tungsten carbide can be referred to the high melting point of WC and the low solubility of WC with Copper.

The main effect plot of the porosity of Cu-WC-Si after sintering is shown in Figure 5.62. The porosity in general decreases with Silicon content milling time. The porosity of Cu-WC-Si after sintering also increases with the Tungsten carbide content up to 30 wt% but it decreases at 45 wt%.

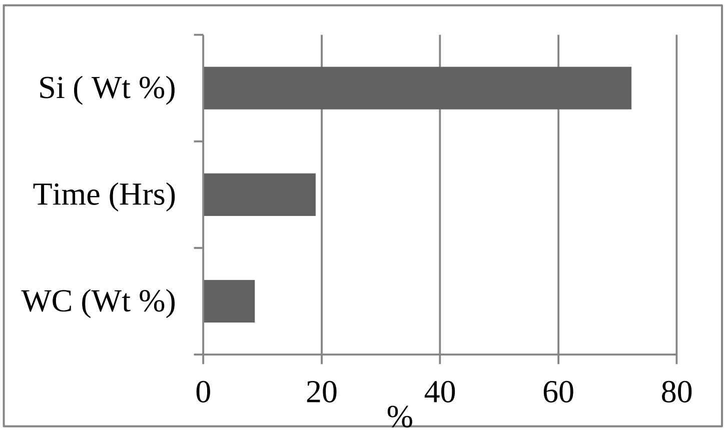

Figure 5.61 Contribution of milling variables on porosity (%) of sintered Cu-WC-Si composite electrode

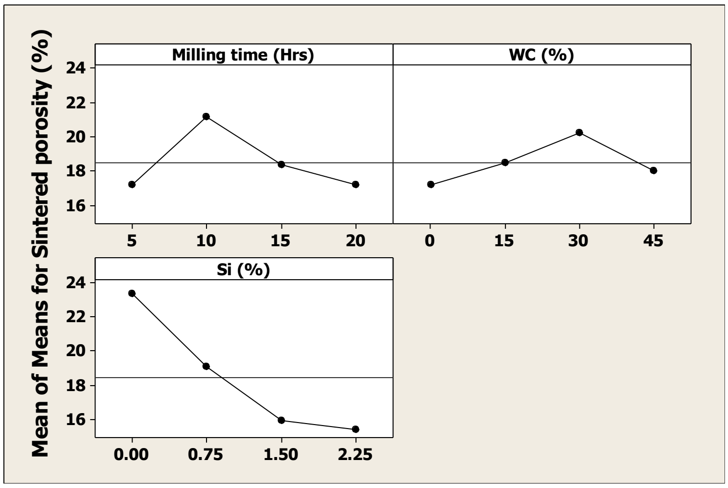

Figure 5.62 The main effect plot of sintered porosity versus Tungsten %, Silicon %, and milling time

5.7.3.4.Hardness

Figure 5.63 shows that the Silicon contributes by more than 60% on hardness followed by Tungsten carbide. The high contribution of Silicon on hardness can be referred to the weaknesses of bonding. Since this material will be used for electric contact as an EDM electrode, the reduction in hardness is not the objective.

Figure 5.64 shows that the main effect plot of hardness after sintering negatively affected by Silicon where the hardness increases with Tungsten carbide and decreases with Silicon because tungsten is a brittle material meanwhile tungsten carbide is a hard material. The hardness of sintered Cu-WC-Si decreases from 27 (HRB) without Silicon to around 12 (HRB) with 2.25 wt % Si. On the other hand it is increased from 12 (HRB) when WC content is 15 wt% to around 27 (HRB) at 45 wt% WC.

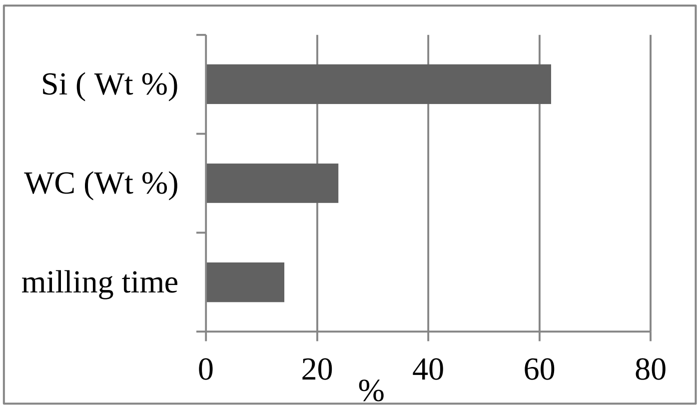

Figure 5.63 Contribution of milling variables on hardness (RB) of sintered Cu-WC-Si composite electrode

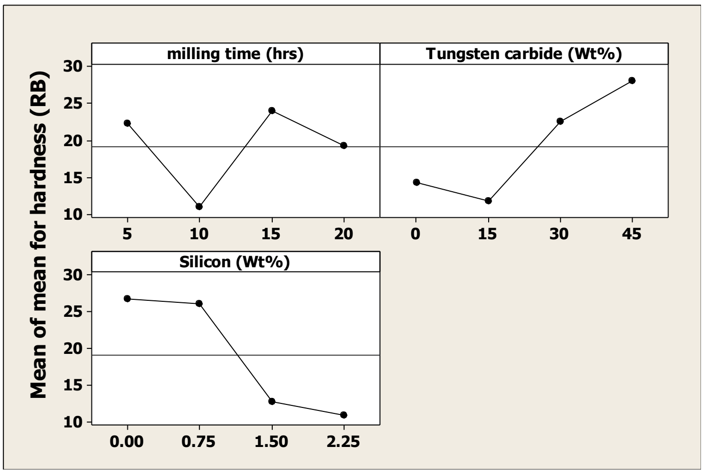

Figure 5.64 The main effect plot of hardness of sintered samples versus Tungsten Wt %, Silicon Wt %, and milling time

5.7.3.5.Heat Conduction

The rate of heat transfer through the electrode material during machining is one of the main required properties for good electrode performance. Poor heat transfer will store the heat inside the electrode because the heating rate by sparking is higher than the cooling rate by dielectric liquid leading to many negative effects on the performance. This will increase the electrode wear resistance. Unsteady state heat conduction test is used to measure the heat conduction mode by measuring the difference between the temperature of the electrode core and the hot water surrounding the electrode. The plot of dimensionless temperature ϴ versus time of pure Copper and three detected Cu-WC-Si electrode is shown in Figures 5.65 up to Figure 5.68. The results show an exponential decay of ϴ with time as shown in equation 5.2.

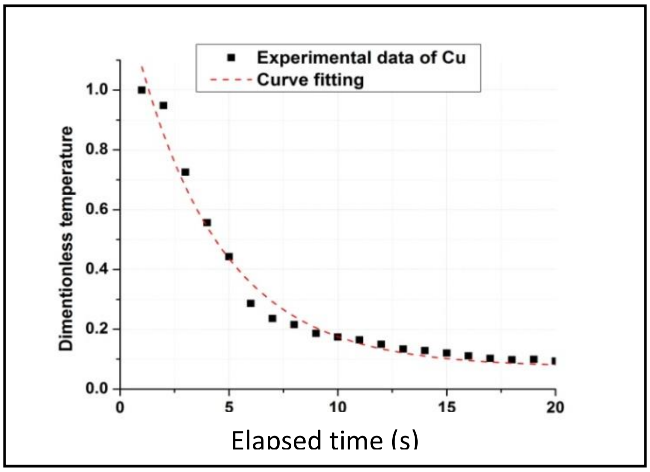

Figure 5.65 Unsteady state heat conduction of pure Copper electrode

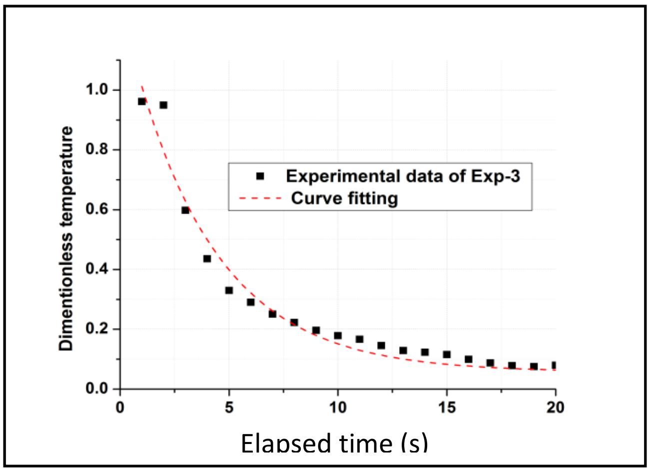

Figure 5.66 Unsteady state heat conduction of Cu+30WC+1.5Si composite electrode

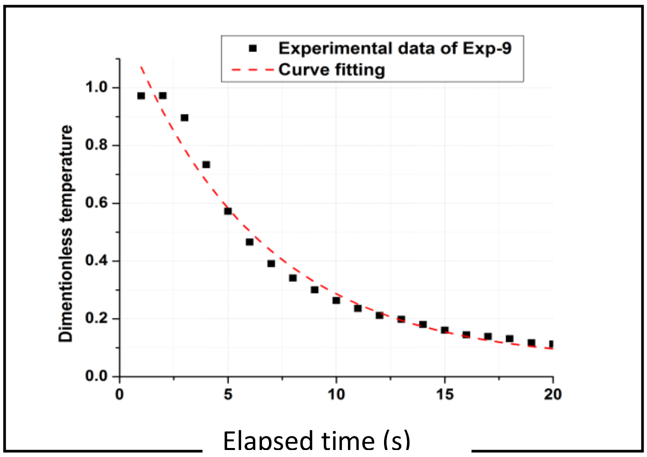

Figure 5.67 unsteady state heat conduction of 5 Cu+30WC+1.5Si electrode

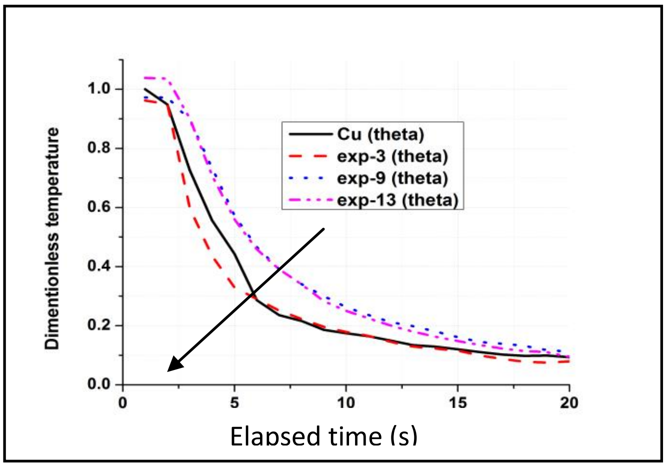

Figure 5.68 Unsteady state heat conduction mode for different electrode material

$$y(t) = y_0 + A exp(-bt) \tag{5.2}$$

Where y_0 is the dimensionless temperature at t=0, A is the normalization constant, and b are the decay constants. According to the general solution of lumped model of unsteady state heat transfer, the decay constant is given as follows;

$$b = (\alpha h A_S / k.V) = (h A_S / \rho V.c_p) \tag{5.3}$$

Where k is the thermal conductivity, V is the volume of mass m, A is surface area, ρ is density, and Cp is the specific heat capacity. According to this model, b is the most important constant in this relation because it represents the thermal properties. The analysis of the results indicates that all samples reach steady state after

30 seconds. Within this period, the variation of fitting curves depends on the decay constant b.

5.7.3.6.The Thermal Decay Constant b (1/s) of Cu-WC-Si Electrode

Figure 5.69 shows that the effects of electrode materials on the decay constant b are more significant that milling time. The main effect plot of the decay constant in Figure 5.70 indicates that the decay constant increases with milling time, Tungsten carbide content, and Silicon content. The decay constant increases with milling time up to 15 h and then decrease but still higher than at the lower milling time. Thus, lower decay constant can be achieved at a lower milling time, lower Silicon content and 15 wt% Tungsten carbide content. Lower Tungsten carbide and Silicon content mean higher Copper content. On the other hand, lower milling time can reduce the contamination and degree of oxidation.

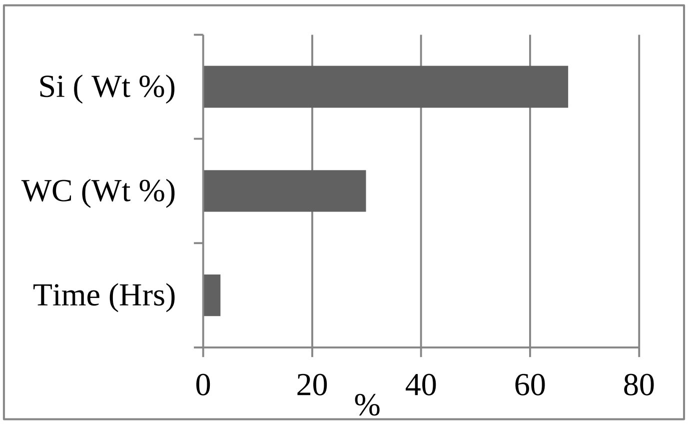

Figure 5.69 Contribution of milling variables on thermal decay constant (1/s) of Cu-WC-Si composite electrode

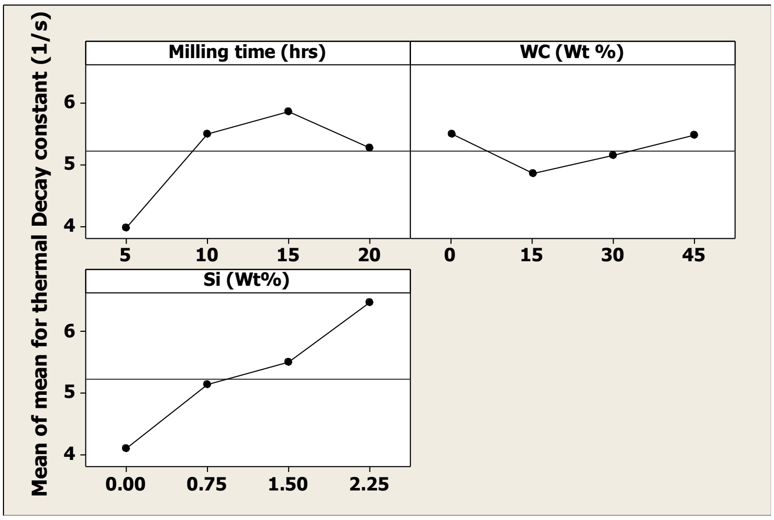

Figure 5.70 The main effect plot of thermal decay constant (1/s) of sintered Cu-WC-Si composite electrode versus milling time (h), Tungsten (wt %), and Silicon (wt %)

5.7.3.7.FESEM Images of Cu-WC-Si Composite after Sintering

Figure 5.71 is the FESEM images analysis carried out to reveal the effect of sintering on the microstructure of Cu-WC-Si electrode material. The images of Exp-1 (B) in, which is represent zero Tungsten carbide and Silicon content shows high oxide at grain boundaries. The amount of this oxide is reduced by adding 0.75 % Si as shown by FESEM image of Exp-5 (B). The images of Exp-8, which represents Cu-45%WC+1.5% Si milled for 10 h shows the higher porosity and lower contact area. This result confirms the results mentioned in section 5.3.2.4 where the porosity increases with milling time.

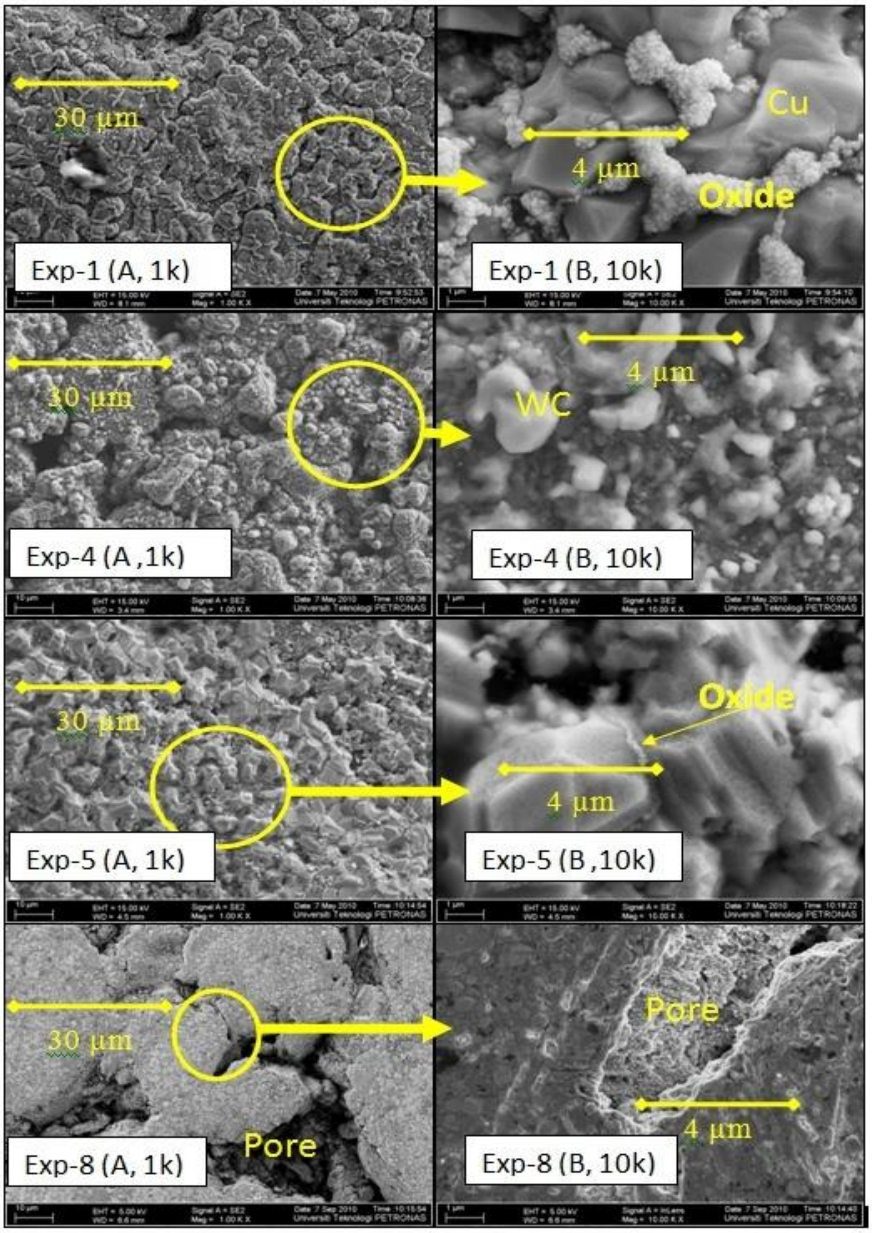

Figure 5.71 FESEM imager of selected samples after sintering at 950^{o}C for 120 min

5.7.4. Synthesizing of Cu-WC-Ti Composite using Ball Milling

Table 5.16 is the layout of experiment designed by L8 Taguchi orthogonal array using milling time, Tungsten carbide content, and Silicon content as milling variables. All variables set at two levels.

Table 5.16 L8 Taguchi orthogonal array by three variables all fixed at two levels

	Milling Time (h)	Tungsten carbide Wt %	Titanium Wt %
Exp-1	5	20	5
Exp-2	5	20	5
Exp-3	5	40	10
Exp-4	5	40	10
Exp-5	10	20	10
Exp-6	10	20	10
Exp-7	10	40	5
Exp-8	10	40	5

5.7.4.1.FESEM Images of Cu-WC-Ti Composite after Sintering

Figure 5.72 shows the FESEM micrographs of a selected Cu-WC-Ti milling powder at low 0.1K and high 50K magnifications. The low magnification images were taken to show the effect of milling variables and milled particle size and higher magnification images were taken to show the effect of milling variables on particle size reduction and homogenization.

The average particle sizes of milled powders range from 20 µm to 300 µm. Generally, the particle size decreases as milling time and Copper content increases. The granular particle size of Experiments 1, which is milled for 5 h, is bigger because it contains more Copper (ductile) than other experiment. The higher magnification images show that the smallest particle size achieved by milling after five and 10 h are around 40-60 nm. This results show that particle size reduction by ball milling has a limitation. Particles sizes reduction by milling is limited by size of milling balls, size of milling medium as well as the composition. This result in agreement with Giulemany [57] and also mentioned by Lee and Tian [61, 64].

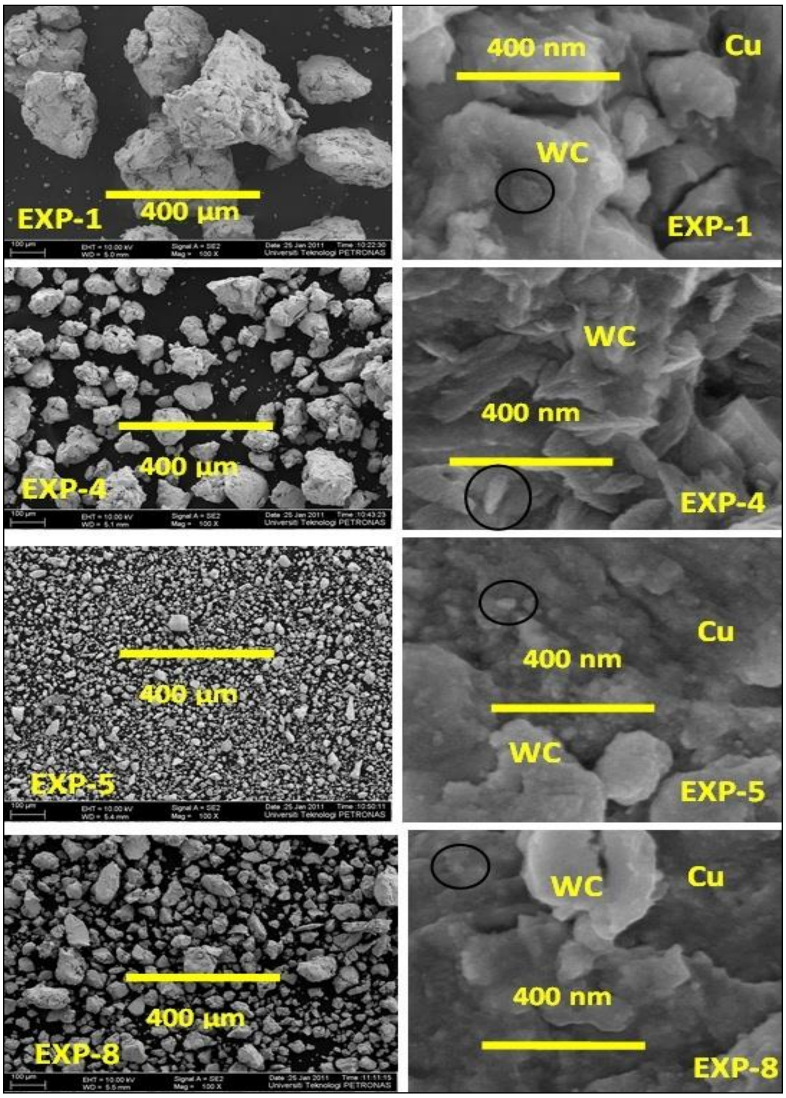

Figure 5.72 FESEM images of selected Cu-WC-Ti milled powder at 0.1k and 50k magnification

5.7.4.2.XRD of Ball milled Cu-WC-Ti Composite after Sintering

Figure 5.73 is the X-ray diffraction patterns of the elemental Cu, WC, and Ti powder. The lower part represents the diffraction patterns of Exp-1 to Exp-4 of the milled Cu-WC-Ti. The data analysis of XRD data are shown in Table 5.17. This data is the d-spacing between planes of atoms, the distance between nearest neighbors (a) and the thickness of crystallite (t) of the milled powder Cu-WC-Ti Exp-3 from. The d-spacing of the elemental powder ranges from 1.2 to 2.8 Å and the crystallite thickness ranges from 282Å for Copper and 500Å for Titanium. The XRD data of the 5 h milled Cu-WC-Ti of Exp-3 is shown in Table 5.17. According to baker [137], the binary phase diagrams of Cu-Ti, C-Ti, W-Si shows that these compositions are miscible at the temperatures of 900^{0}C, 2700^{0}C and 860^{0}C respectively. The d-spacing between planes of atoms is still in the same range but the thickness of crystallite decreases to the range 204 - 251 Å.

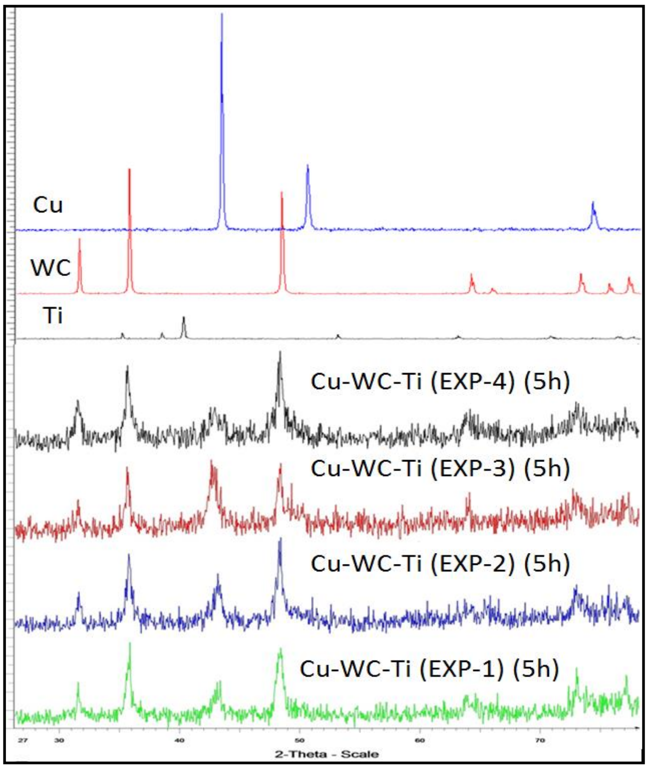

Figure 5.73 XRD pattern of the milled Cu-WC-Ti powder aligned with the spectrum of the pattern of elemental powder

Table 5.17 XRD data analyses of Exp-3 from Cu-WC-Ti milling plane

	2theta[°]	Intensity (I/I_o)	d[A]	a [A]	t [A]
WC	31.56	539.45	2.83	2.83	204.36
WC	35.69	964.91	2.52	3.56	206.59
Ti	38.41	247.13	2.34	4.69	208.24
Ti	40.11	239.97	2.25	3.18	209.34
Cu	43.45	552.45	2.08	3.61	211.68
WC	48.44	998.48	1.88	2.66	215.62
Cu	50.25	413.34	1.82	3.63	217.19
Ti	53.63	241.34	1.71	3.82	220.33
Ti	70.67	214.28	1.33	4.22	241.02
WC	72.95	652.03	1.30	2.59	244.51
Ti	74.51	322.79	1.27	2.55	247.02
WC	77.06	493.78	1.24	2.48	251.33

5.7.4.3.TEM Images of Milled Cu-WC-Ti Composite

Figure 5.74 is the Transmission electrode microscope analysis of Exp-2 and Exp-3 from the milled Cu-WC-Ti powder. The composition of Exp-2 is Cu-20 %WC-5%Ti and for Exp-3 is Cu-40 %WC-10%Ti. In both images, the thickness of crystallite decreases where the average thickness detected is less than 200 Å. This result confirms the reduction of the thickness of crystalline calculated from XRD data. The change can be as a result of the stored energy of the amorphous, and some meatastable phase created. This agreed with the work of Alam [46]. The distances between the lines of the detected periodical structure are in the range from 2.2Å to 6Å. This is different from the range mentioned earlier in Table 5.17.

Phase formation during mechanical alloying of Ti-Si system studied by [61] where he found that the mechanical alloying a mixture of elemental powders led to the formation of TiSi2 equilibrium compound, while when starting from Si + TiH1.924, a metastable phase was formed. The metastable phase completely transforms to TiSi2 when the mechanically alloyed powder is annealed at temperatures above 800 °C. He concludes that the kinetics related to the different phase transitions depending on the starting powder mixture are discussed.

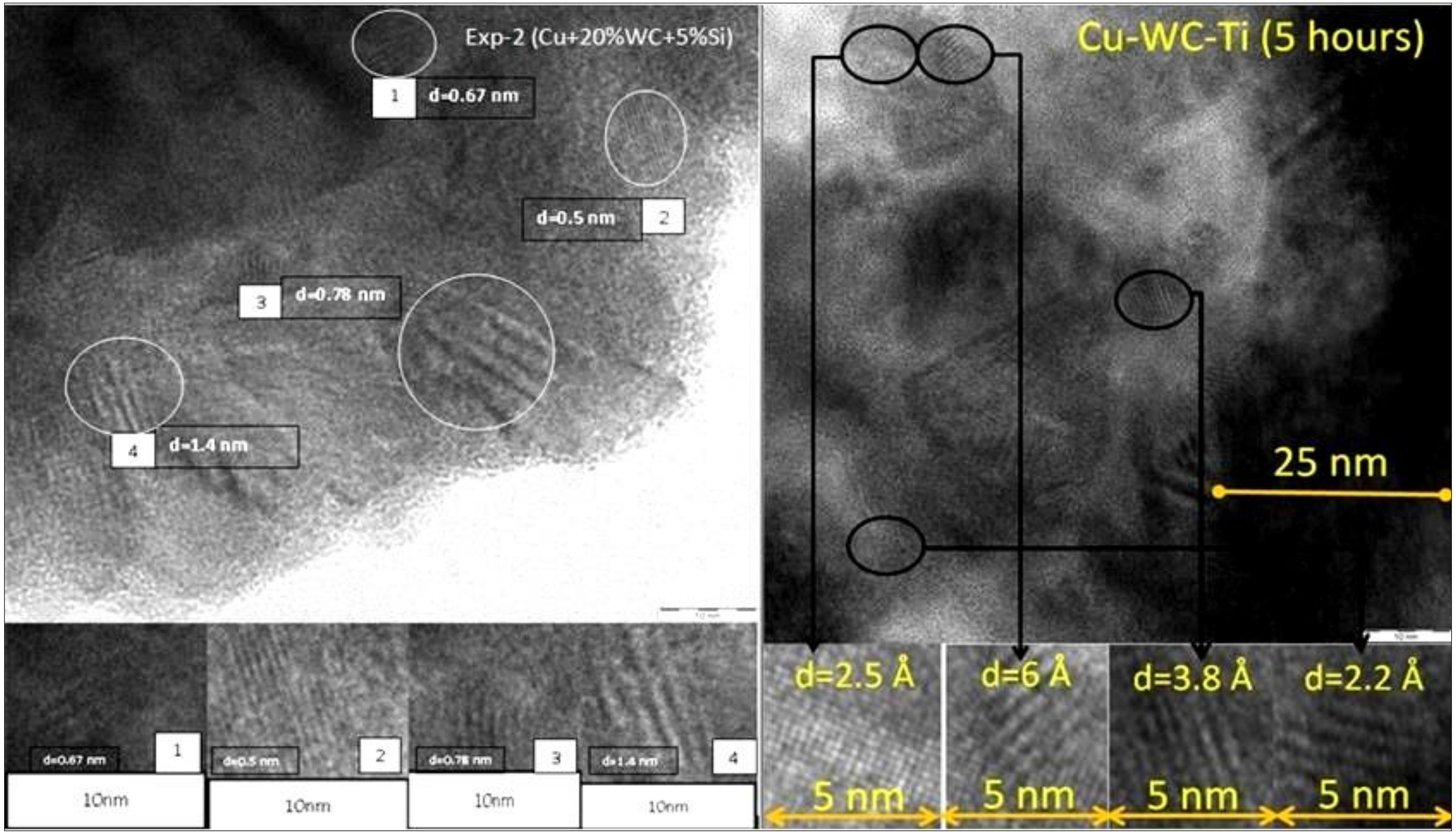

Figure 5.74 TEM micrograph of the 5 h milled Cu-20 %WC-5%Ti and Cu-40 %WC-10%Ti

5.7.5. Synthesizing of Ball milled Cu-WC-Ti-Si

Cu-WC-Ti-Si nanocomposite materials are synthesized using planetary ball milling. Ti and Si additives were used due the good solubility. Characterization was carried out using SEM, XRD, and TEM. Over 99% purity elemental powder of Cu, WC, Ti, and Si powder was mixed and milled using planetary ball milling. Milling experiment was designed using L8 Taguchi orthogonal array as shown in Table 5.18. Milling was carried out at a standard pressure room temperature in air environment.

Table 5.18 L8 Taguchi orthogonal array by four variables all fixed at two levels

	Milling Time (h)	WC (Wt %)	Ti (Wt %)	Si (Wt %)
Exp-1	5	20	10	0
Exp-2	5	20	20	1
Exp-3	5	40	10	1
Exp-4	5	40	20	0
Exp-5	10	20	10	1
Exp-6	10	20	20	0
Exp-7	10	40	10	0
Exp-8	10	40	20	1

5.7.5.1.FESEM Images of Cu-WC-Ti-Si Composite after Sintering

Figure 5.75 is the FESEM images of selected samples of the milled powder of Cu-WC-Ti-Si composite at 0.1k and 50k magnification. The low magnification images show the milled particles sizes ranges from few µm up to 200 µm.

In general, the 10 h milled powder show smaller particle size than 5 h milled powder. The higher magnification images show the fracture of Tungsten carbide particles by ball milling. The sizes of these particles are in the range from 50 nm to 500 nm. Since milling medium is Tungsten carbide, these particles could be eroded from the milling medium. The black circuit shows the smallest achieved nanoparticle size embedded in the Copper reach area. The lower limit of these particle sizes is independent of milling time; these results explain the low contribution of milling time on particle size reduction.

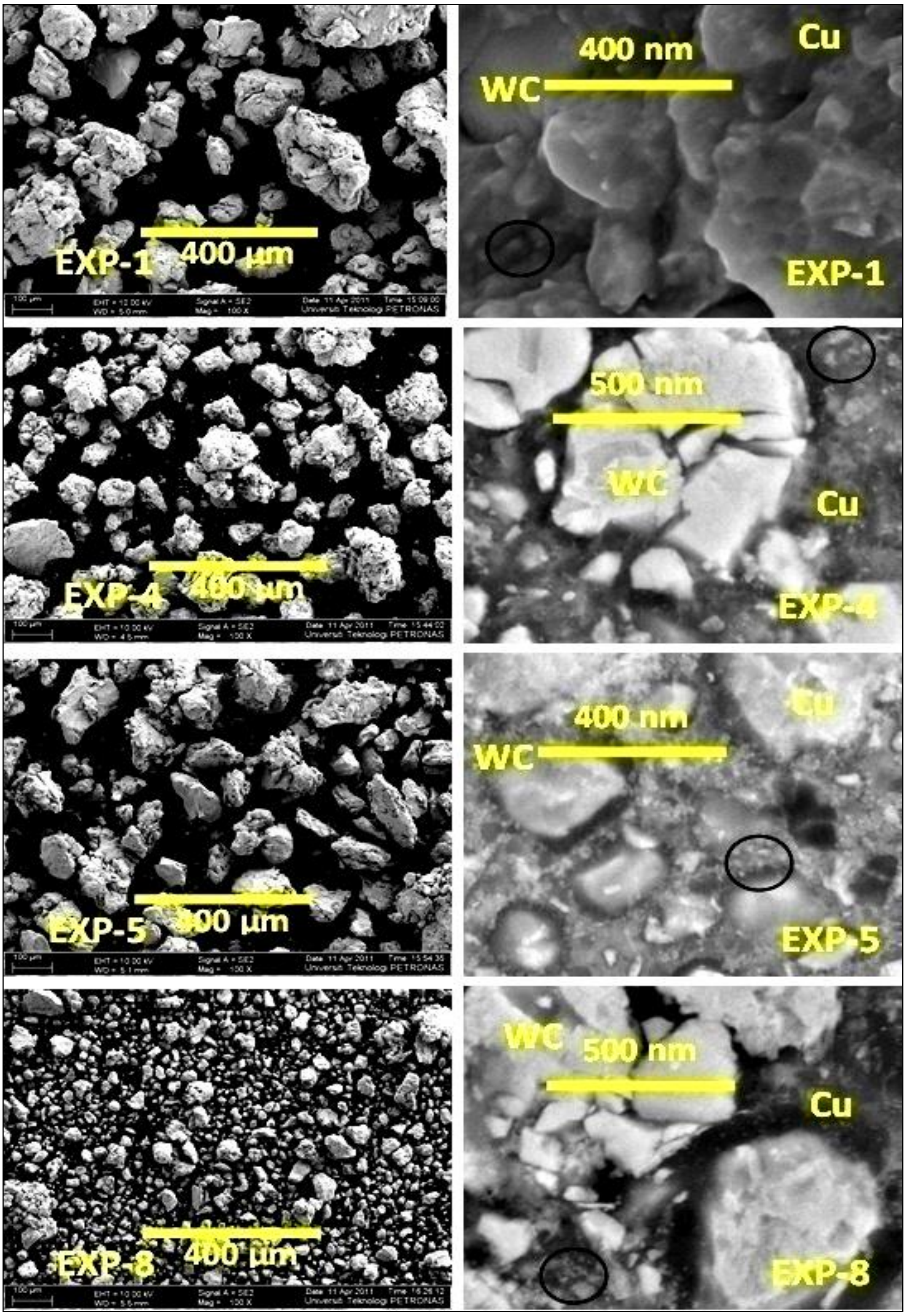

Figure 5.75 FESEM images of the milled powder of EXP-1&2 (milled for 5 h) and EXP-5&8 (milled for 10 h)

5.7.5.2.TEM Images of Cu-WC-Ti-Si Composite after Sintering

Figure 5.76 shows the TEM images of 5 h milled Cu+40%WC+10%Ti+1%Si. The analysis shows an amorphous structure with small crystalline structure distribution. The average d-spacing of the detected crystal structure as shown here is 2.47 nm, which probably belongs to Tungsten carbide.

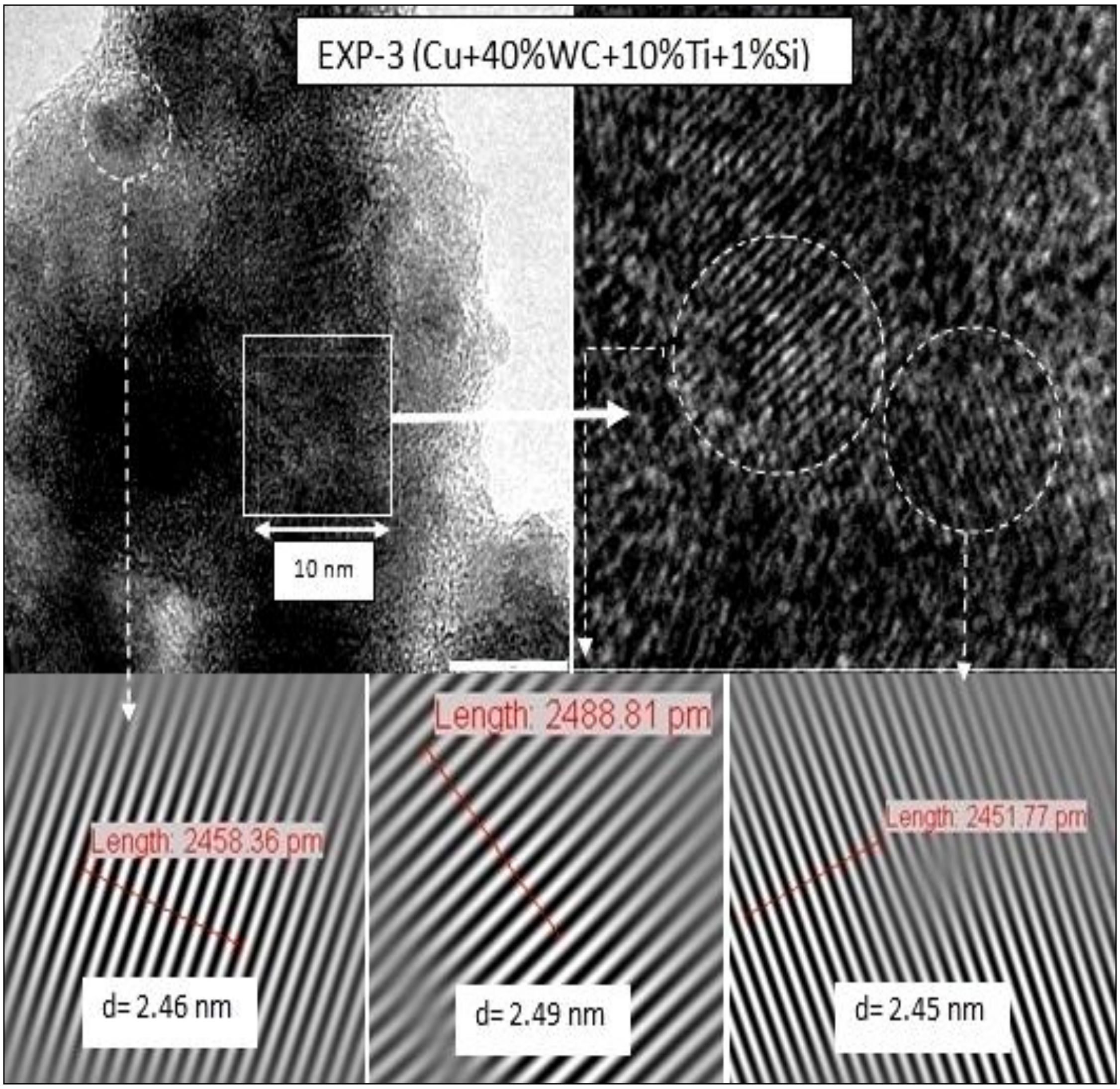

Figure 5.76 TEM images of 5 h milled Cu+40%WC+10%Ti+1%Si

5.7.1. The Performance of New Electrode on Machining of Hardened Die Steel

The performance of the developed EDM tool electrode is tested on machining of hardened die steel at the same machining variables setting as shown in Table 5.19. This setting is the optimal setting, which shows low variation and better interval of confidence (CI,95%) . The machining results achieved at this setting using Cu-W electrode are MRR= 195 (mg/min), EW=10.75 (mg/min), and TWR=5.51 %.

Table 5.19 Machining setting used to test the performance of new electrode

Machining factors	Factors setting (Codes)	Factors setting (Explicit unit)
Power circuit type	TP	
Auxiliary power	0	
Polarity	+	
Peak current	3.5	15 amp
Pulse On-time	5	23 µsec
Pulse of time	4	16 µsec
Gap voltage	0	80 volts
Electric discharge	11	2.5 m/min
Jump up distance	2	0.4 mm
Jump down time	3	150 ms
Condenser selection	0	
Machining adjustment	80	
Servo voltage	0	
OP sensitivity	8	
Dielectric pressure	4	
Flushing mode	45^o	

5.7.1.1. Performance of Cu-WC-Si Electrode on Machining of Die Steel

Table 5.21 shows the measured MRR (mg/min) and EW (mg/min) using Cu-WC-Si composite electrode at setting shown in Table 5.20. The electrode performance was characterized by measuring the material removal rate MRR (mg/min), the electrode wear EW (mg/min), and the tool wear ratio TWR (%). The results compared with that achieved by using the conventional Cu+80%W electrode. The improvement measured as the percentage of the difference between the targeted value achieved by Cu-W electrode and the value achieved by the new electrode relative to the targeted value.

Table 5.20 The machining results (MRR, EW, and TWR) achieved by using Cu-WC-Si EDM electrode compared with the machining results achieved by using Cu-W electrode [MRR= 195 (mg/min), EW=10.75 (mg/min), and TWR=5.51 %] at the same machining condition

L16 Taguchi orthogonal array by three variables all at four levels				Machining results using Cu-WC-Si electrode			Percentage improvement in MRR, EW, and TWR		
	Milling time (h)	WC wt %	Si wt %	MRR (mg/min)	EW (mg/min)	TWR (%)	MRR (+ve is better)	EW (-ve is better)	TWR (-ve is better)
Exp-1	5	0	0.00	219.00	6.80	3.11	12.31	-36.74	-43.56
Exp-2	5	15	0.75	222.00	11.10	5.00	13.85	3.26	-9.26
Exp-3	5	30	1.50	369.00	12.70	3.44	89.23	18.14	-37.57
Exp-4	5	45	2.25	301.00	19.40	6.45	54.36	80.47	17.06
Exp-5	10	0	0.75	202.00	9.00	4.46	3.59	-16.28	-19.06
Exp-6	10	15	0.00	231.00	4.60	1.99	18.46	-57.21	-63.88
Exp-7	10	30	2.25	170.00	6.40	3.76	-12.82	-40.47	-31.76
Exp-8	10	45	1.50	196.00	0.50	0.26	0.51	-95.35	-95.28
Exp-9	15	0	1.50	6.00	0.70	11.67	-96.92	-93.49	111.80
Exp-10	15	15	2.25	14.00	1.30	9.29	-92.82	-87.91	68.60
Exp-11	15	30	0.00	51.00	11.70	22.94	-73.85	8.84	316.33
Exp-12	15	45	0.75	172.00	1.60	0.93	-11.79	-85.12	-83.12
Exp-13	20	0	2.25	119.00	0.10	0.08	-38.97	-99.07	-98.55
Exp-14	20	15	1.50	6.00	4.20	70.00	-96.92	-60.93	1170.42
Exp-15	20	30	0.75	110.00	5.70	5.18	-43.59	-46.98	-5.99
Exp-16	20	45	0.00	112.00	7.00	6.25	-42.56	-34.88	13.43

Table 5.21 The mean averages of MRR (mg/min) and EW (mg/min) versus milling time and electrode composition

Variables	Levels	MRR (mg/min)	EW (mg/min)	TWR (%)
Milling time (h)	5	277.75	12.50	4.50
	10	199.75	5.13	2.60
	15	60.75	3.83	11.53
	20	86.75	4.25	19.80
Tungsten carbide (Wt %)	5	136.50	4.15	5.14
	10	118.25	5.30	21.05
	15	175.00	9.13	8.80
	20	195.25	7.13	3.46
Silicon (Wt %)	5	153.25	7.53	8.55
	10	176.50	6.85	3.88
	15	144.25	4.53	21.06
	20	151.00	6.80	4.94

Table 5. 22 the sum of square SS and the percentage contribution SS (%) of variables on the MRR, EW, and TWR achieved by using Cu-WC-Si electrode

	MRR (mg/min)		EW (mg/min)		TWR (%)	
	SS	SS (%)	SS	SS (%)	SS	SS (%)
Time (h)	122420	87.53	200.34	79.84	774.17	29.50
WC (wt %)	15070.25	10.77	30.005	11.95	816.72	31.12
Si (wt %)	2362.5	1.69	20.56	8.19	1033.47	39.38
Total	139852.75	100	250.91	100	2624.35	100

Tables 5.22 and 5.23 shows the mean averages and the sum of square SS, and the percentage contribution SS (%) of Tungsten carbide, Silicon content, and milling time on MRR (mg/min) of Cu-WC-Si composite electrode. The results achieved by this electrode are comparable with the conventional Cu-W electrode for milling time less than 10 h. The electrode wear on the other hand improved with milling time over 5 h.

a. MRR (mg/min) Achieved by using Cu-WC-Si Electrode at Optimal Setting

Figure 5.77 shows that the most significant parameters that make a significant impact on the MRR (mg/min) achieved by using Cu-WC-Si electrode are milling time followed by Tungsten carbide content. The main effect plot of the MRR (mg/min) achieved by this electrode in Figure 5.78 indicates that MRR decreases milling time and increases with Tungsten carbide content. The effect of Silicon content of the performance of Cu-WC-Si electrode in the case of MRR is insignificant.

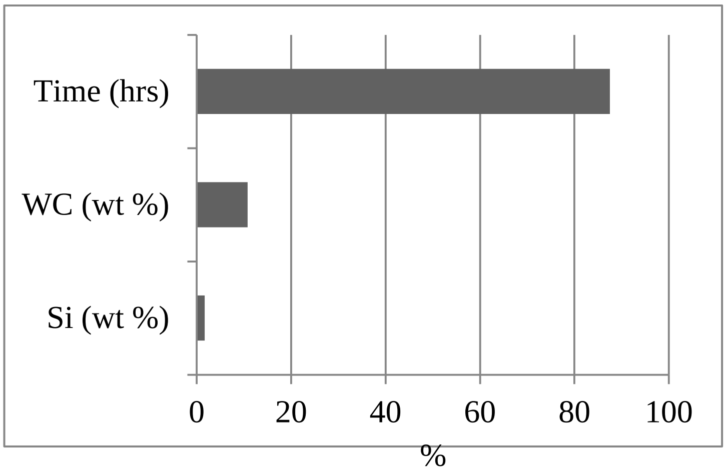

Figure 5.77 Contribution of milling variables on MRR (mg/min) of Cu-WC-Si electrode

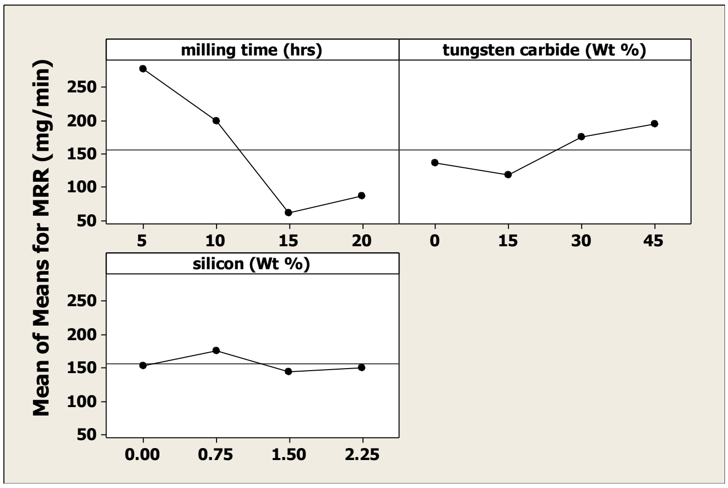

Figure 5.78 The main effect plot of MRR (mg/min) of Cu-WC-Si composite electrode versus milling time (h), Tungsten (wt %), and Silicon (wt %)

b. EW (mg/min) Achieved by using Cu-WC-Si Electrode at Optimal Setting

Figure 5.79 shows the percentage contribution of milling variables of Cu-WC-Si electrode on the EW (mg/min) is same as that on MRR. The effect of Silicon content on EW is slightly more than that in MRR. The main effect plot in Figure 5.80 show that the electrode wear decreases milling time from 12 (mg/min) at 5 h milling time to 4 (mg/min) after 20 h milling time. The electrodes wear also decrease with Silicon content. It decreases from 7 (mg/min) without Silicon to 4 (mg/min) with 1.5 % Si content. The electrodes wear decreases with Tungsten carbide content.

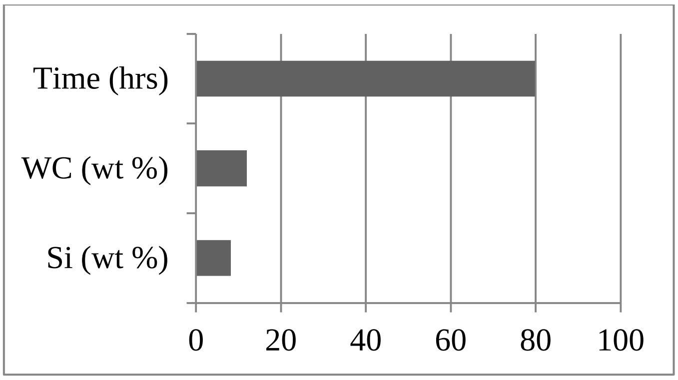

Figure 5.79 Contribution of milling variables on EW (mg/min) of Cu-WC-Si

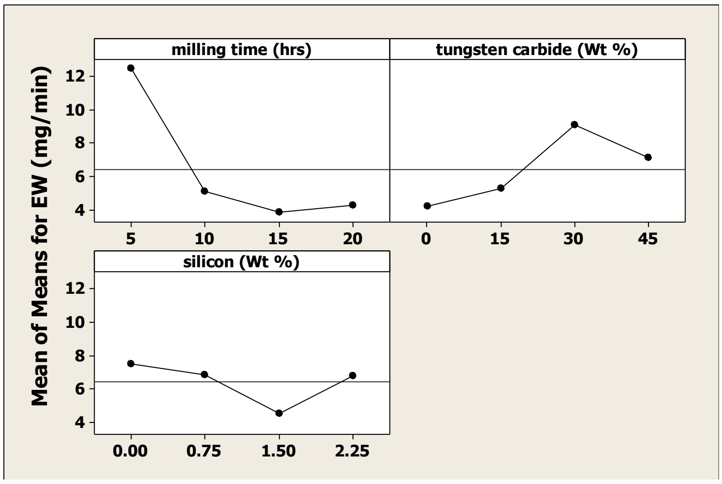

Figure 5.80 The main effect plot of EW (mg/min) of Cu-WC-Si composite electrode versus milling time (h), Tungsten (wt %), and Silicon (wt %)

c. TWR (%) of Cu-WC-Si Electrode At Optimal Setting

Figure 5.81 shows that the TWR of Cu-WC-Si electrode 40% influenced by the Silicon content and by 30% for both Tungsten carbide and milling time.

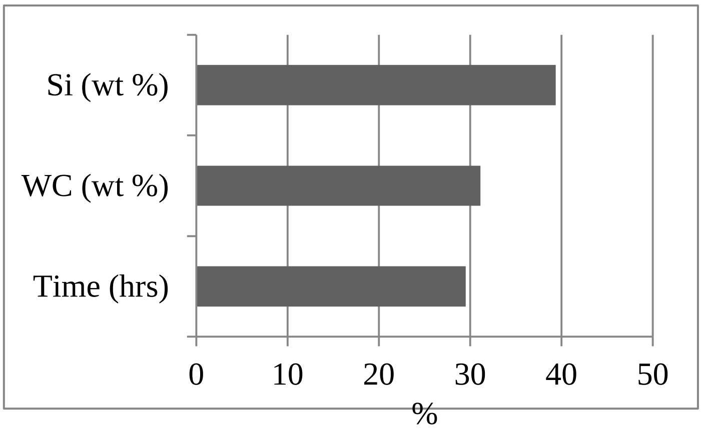

Figure 5.81 Contribution of milling variables on TWR (%) of Cu-WC-Si electrode

The main effect plot in Figure 5.82 show that the TWR (%) increases with milling time and decreases with Tungsten carbide content. The minimum tool wear ratio can be achieved at 10 h milling time, 45 wt% of WC, and lower Silicon content.

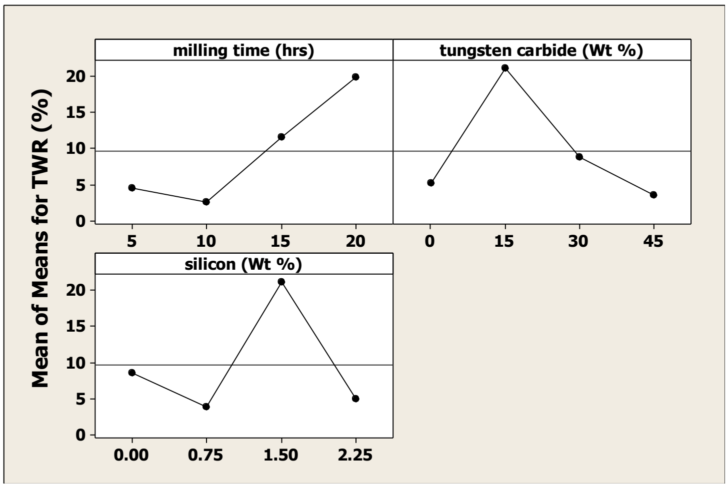

Figure 5.82 The main effect plot of TWR (%)) of Cu-WC-Si composite electrode versus milling time (h), Tungsten (wt %), and Silicon (wt %)

5.7.1.2.The Performance of Cu-WC-Ti Electrode on Machining of Die Steel

The performance of Cu-WC-Ti was tested under the same conditions and the results is compared with the machining results achieved by using Cu-W electrode [MRR= 195 (mg/min) and EW=10.75 (mg/min) %] at the same machining condition as in Table 5.24. The measured values and the percentage of improvement in MRR (g/min), EW (mg/min) of this electrode with respect to Cu-W electrode are shown below in Table 5.24. in general, the MRR (mg/min) using the new developed Cu-WC-Ti electrode is less than the targeted value achieved by using Cu-W electrode. The percentage of the decrease in MRR (mg/min) from that achieved by Cu-W electrode at the same machining condition is in the range (83-98) %. Meanwhile, the electrode wear shows a clear improvement where the negative sign indicates that the electrode wear of Cu-WC-Ti is less than that of Cu-W electrode at the same machining variables setting. The electrode wear improvements are in the range (31 to 89) % from the value of the electrode wear achieved by a Cu - W electrode. Table 5.25 is the MRR (mg/min), EW (mg/min), and the TWR (%) achieved by using Cu-WC-Ti electrode. Table 5.26 is sum of square SS and the percentage contribution of variables SS (%).

Table 5.23 The MRR (mg/min), EW(mg/min), and the TWR (%) achieved by using Cu-WC-Ti electrode compared with the machining results achieved by using Cu-W electrode [MRR= 195 (mg/min) and EW=10.75 (mg/min) %] at the same machining condition

L8 Taguchi orthogonal array by three variables all fixed at two levels				Machining results using Cu-WC-Ti in (mg/min)			Percentage of improvement in MRR, EW and TWR		
	Time (h)	WC wt %	Ti wt %	MRR (mg/min)	EW (mg/min)	TWR (%)	MRR (+ve is better)	EW (-ve is better)	TWR (Smaller is better)
Exp-1	5	20	5	32.45	7.40	22.80	-83.36	-31.16	313.79
Exp-2	5	20	5	17.42	1.48	8.50	-91.07	-86.23	54.26
Exp-3	5	40	10	79.60	3.76	4.72	-59.18	-65.02	-14.34
Exp-4	5	40	10	42.25	4.85	11.48	-78.33	-54.88	108.35
Exp-5	10	20	10	2.58	4.08	158.14	-98.68	-62.05	2770.05
Exp-6	10	20	10	20.84	1.13	5.42	-89.31	-89.49	-1.63
Exp-7	10	40	5	16.54	2.77	16.75	-91.52	-74.23	203.99
Exp-8	10	40	5	6.25	1.67	26.72	-96.79	-84.47	384.94

Table 5.24 The mean averages of MRR (mg/min) and EW (mg/min) and TWR (%) of Cu-WC-Ti versus milling time and electrode composition

Variables	Levels	MRR (mg/min)	EW (mg/min)	TWR (%)
Milling time (h)	5	4.30	4.73	11.88
	10	1.55	2.14	51.76
Tungsten carbide (wt %)	20	1.18	3.52	48.71
	40	1.68	3.26	14.92
Titanium (wt %)	5	0.89	3.33	18.69
	10	1.96	3.45	44.94

Table 5.25 the sum of square SS and the percentage contribution SS (%) of variables on the MRR, EW, and TWR achieved by using Cu-WC-Ti electrode

	MRR (mg/min)		EW (mg/min)		TWR (%)	
	SS	SS (%)	SS	SS (%)	SS	SS (%)
Time (h)	1969.10	60.32	7.68	97.88	3181.06	46.48
WC (wt %)	636.35	19.49	0.14	1.72	2284.61	33.38
Si (wt %)	659.03	20.19	0.03	0.40	1378.05	20.14
Total	3264.47	100.00	7.85	100.00	6843.72	100.00

a. MRR (mg/min) Achieved by using Cu-WC-Ti Electrode at Optimal Setting

The contribution of milling time and composition of Cu-WC-Ti composite are shown in Figure 5.83. Milling time is the most significant factor influencing the values of MRR where it contributes by 60%.

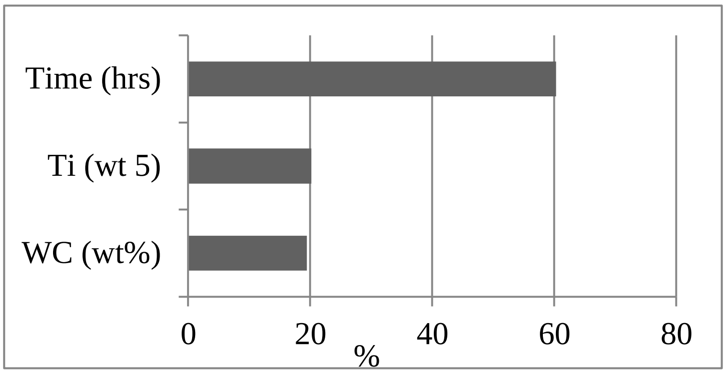

Figure 5.83 Contribution of milling variables on MRR (mg/min) of Cu-WC-Ti electrode

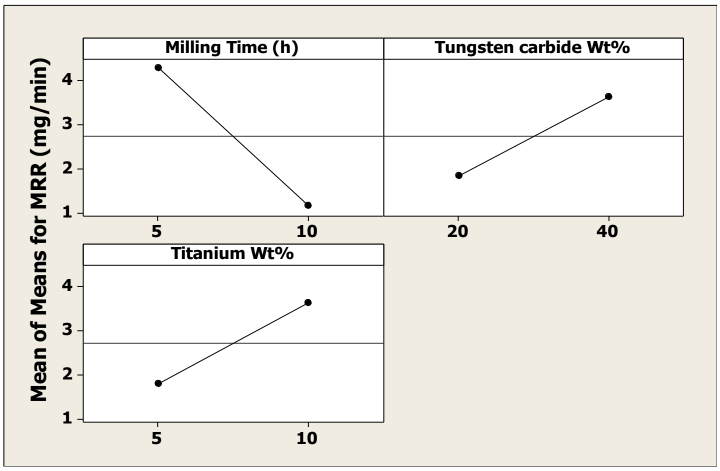

Figure 5.84 The main effect plot of MRR (mg/min) of Cu-WC-Ti composite electrode versus milling time (h), Tungsten (wt %), and Titanium (wt %)

The main effect plot of MRR shown in Figure 5.84 indicates that The MRR increases with Tungsten carbide and Titanium but decrease with milling time. The value of MRR reduced from 4.4 (mg/min) for 5 h milling time to 1.2 (mg/min) for 10 h milling time electrode. This can be referred to the affect of contamination and porosity where both increases with milling time.

b. EW (mg/min) Achieved by using Cu-WC-Ti Electrode at Optimal Setting

The contribution of milling variables on the values of EW (mg/min) shown in Figure 5.85 indicates that milling time is the most important variable influencing the EW value where it contributes by 97.88 %. The main effect plot of EW (mg/min) in Figure 5.86 shows that the electrode wear reduced from 4.4 (mg/min) for 5 h milling time to 2.2 (mg/min) after 10 h milling time. This can be referred to the effect of milling time on the increase in contamination by WC from the mill medium (low conductivity) and the decrease of copper content (high conductivity). The electrodes wear decreases with Tungsten carbide and increases with Titanium.

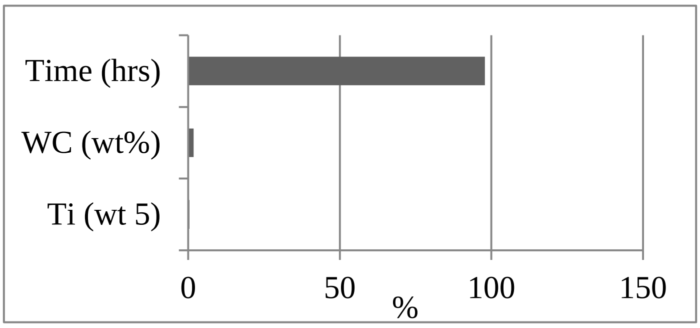

Figure 5.85 Contribution of milling variables on EW of Cu-WC-Ti electrode

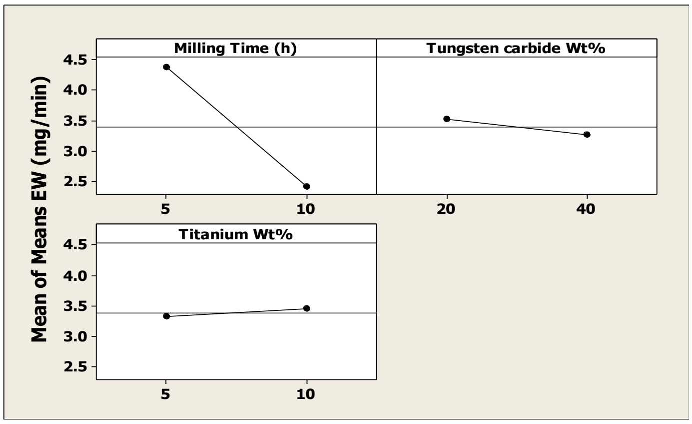

Figure 5.86 The main effect plot of EW (mg/min) of Cu-WC-Ti composite electrode versus milling time (h), Tungsten (wt %), and Titanium (wt %)

c. TWR (%) of Cu-WC-Ti Electrode At Optimal Setting

Figure 5.87 shows that the milling time and Tungsten carbide are the most significant variable influencing the value of the TWR for Cu-WC-Ti electrode. Milling time contributes by more than 45%. The percentage of contribution from Titanium is 20% and Tungsten carbide contributes by 35%. The main effect plot of EW (mg/min) in Figure 5.88 shows that the TWR (%) increases with milling time and Titanium but decreases with Tungsten carbide content. The minimum tool wear ratio can be achieved at 5 h milling time, 40 wt% of WC, and 5 wt% of Titanium. The increases of TWR by Titanium additive mean that Titanium contributes more on the improvement in MRR than the reduction in EW.

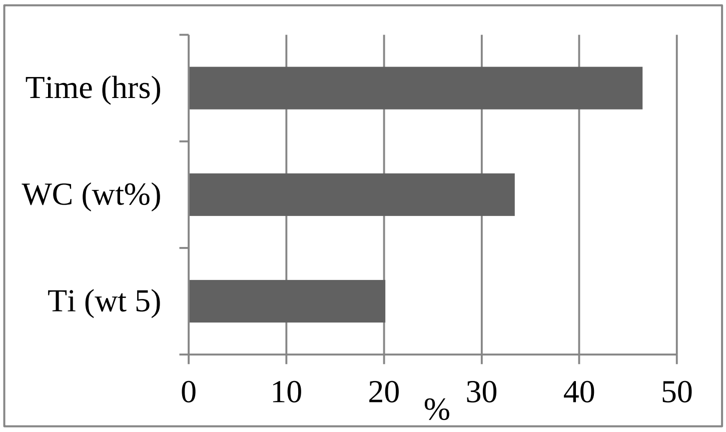

Figure 5.87 Contribution of milling variables on TWR (%) of Cu-WC-Ti electrode

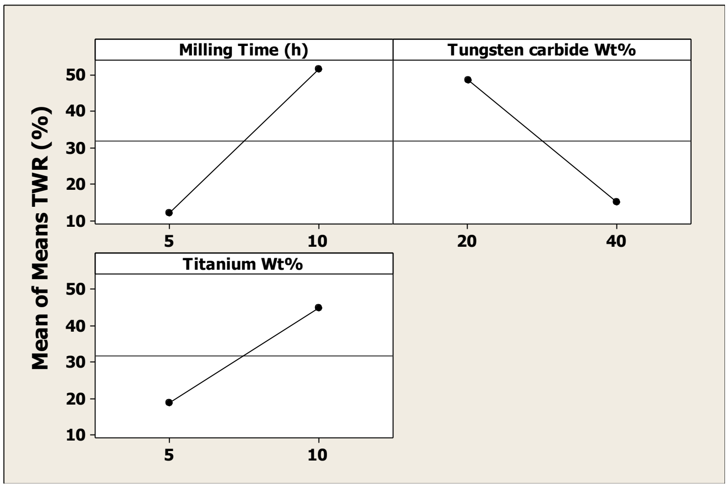

Figure 5.88 The main effect plot of TWR (%) of Cu-WC-Ti composite electrode versus milling time (h), Tungsten (wt %), and Titanium (wt %)

5.7.1.3.The Performance of Cu-WC-Ti-Si Electrode on Machining of Die Steel

The performance of Cu-WC-Ti-Si composite electrode was tested on diesinker EDM at the same machining conditions as in Table 5.22. The MRR (mg/min), EW (mg/min), and TWR (%) achieved by using this electrode are shown in Table 5.27. In general, The MRR (mg/min) achieved by using this electrode is less than that of Cu-W electrode where the sign of improvement is negative except the 10 h milled Cu+10%WC+20%Ti composite electrode where it showed 2% positive improvement. The EW of Cu-WC-Ti-Si electrode is lower than that of Cu-W electrode under same machining condition. The exception is the 5 h milled Cu-10%WC+10%Ti where it show an electrode wear less than that of Cu-W electrode this can be explained by the higher copper content (80%) which is characterized by higher thermal wear. The MRR (mg/min) by using Cu-WC-Ti-Si decreases by (15-98) % from the targeted level achieved by Cu-W electrode under the same machining condition. Meanwhile, the percentage improvement of the Cu-WC-Ti-Si composite electrode is ranged from 14% to 95%.

Table 5.26 The machining results (MRR and EW) achieved by using Cu-WC-Ti-Si electrode compared with the machining results achieved by using Cu-W electrode [MRR= 195 (mg/min) and EW=10.75 (mg/min) %] at the same machining condition

L8 Taguchi orthogonal array by four variables all fixed at two levels					Machining results using Cu-WC-Ti-Si in (mg/min)			Percentage improvement in MRR and EW		
	Milling Time (h)	WC (wt %)	Ti (wt %)	Si (wt %)	MRR (mg/min)	EW (mg/min)	TWR (%)	MRR (+ve is better)	EW (-ve is better)	TWR (%)
Exp-1	5	20	10	0	165.48	11.86	7.17	-15.14	10.33	30.13
Exp-2	5	20	10	1	36.74	9.21	25.07	-81.16	-14.33	354.99
Exp-3	5	40	20	0	9.99	0.46	4.65	-94.88	-95.72	-15.61
Exp-4	5	40	20	1	25.33	0.90	3.57	-87.01	-91.63	-35.21
Exp-5	10	20	20	0	198.80	7.40	3.72	1.95	-31.16	-32.49
Exp-6	10	20	20	1	17.72	1.93	10.91	-90.91	-82.05	98.00
Exp-7	10	40	10	0	37.93	1.28	3.38	-80.55	-88.09	-38.66
Exp-8	10	40	10	1	32.96	0.68	2.07	-83.10	-93.67	-62.43

Table 5.27 The mean averages of MRR (mg/min) and EW (mg/min) and TWR (%) for Cu-WC-Ti-Si electrode

Variables	Levels	MRR (mg/min)	EW (mg/min)	TWR (%)
Milling time (h)	5	59.39	5.61	10.11
	10	71.85	2.82	5.02
Tungsten carbide (wt %)	5	104.70	7.60	11.72
	10	26.55	0.83	3.14
Titanium (wt %)	5	68.28	5.76	9.42
	10	62.96	2.687	5.71
Silicon (wt %)	5	103.05	5.25	4.73
	10	28.19	3.18	10.40

Table 5.28 the sum of square SS and the percentage contribution SS (%) of variables on the MRR, EW, and TWR achieved by using Cu-WC-Ti-Si electrode

	MRR (mg/min)		EW (mg/min)		TWR (%)	
	SS	SS (%)	SS	SS (%)	SS	SS (%)
Time (h)	310.81	1.31	15.54	11.53	51.93	18.43
WC (wt %)	12210.56	51.34	91.68	68.00	137.93	48.95
Ti (wt %)	56.52	0.24	19.03	14.11	27.54	9.77
Si (wt %)	11207.54	47.12	8.57	6.35	64.39	22.85
Total	23785.42	100.00	134.81	100.00	281.78	100.00

a. MRR (mg/min) Achieved by using Cu-WC-Ti-Si Electrode at Optimal Setting

Figure 5.89 shows that the contribution of Tungsten carbide and Silicon content are more significant than that of milling time. In other word, the value of MRR (mg/min) achieved by using Cu-WC-Ti-Si composite electrode mainly influenced by the composition of electrode material. The effect of Titanium is negligible. The main effect plot in Figure 5.90 indicates that the MRR clearly decreases with increasing the Tungsten carbide and Silicon content but increase with longer milling time. Moreover, the MRR increased with milling time. But decreases with Tungsten carbide and Silicon content. The negative effect of WC can be related to the lake of bonding due to low sintering temperature, high porosity, and low conductivity. The negative effect of WC, Ti, and Si on MRR can be referred to the reduction in electrical conductivity due to the reduction in Copper content. The positive effect of milling time is related to the reduction in particle size, homogenization, and low porosity.

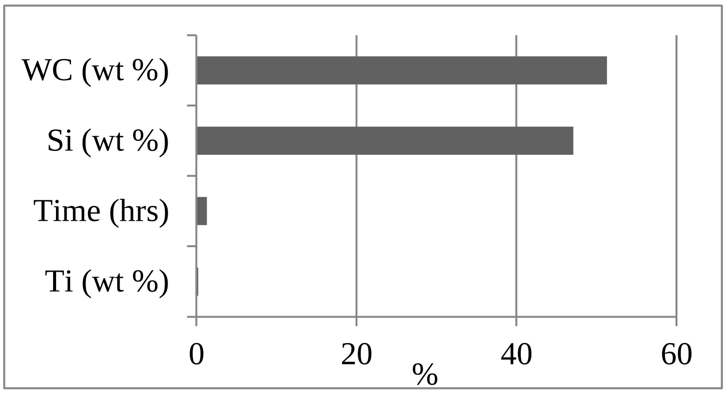

Figure 5.89 Contribution of milling variables on MRR (mg/min) of Cu-WC-Ti-Si electrode

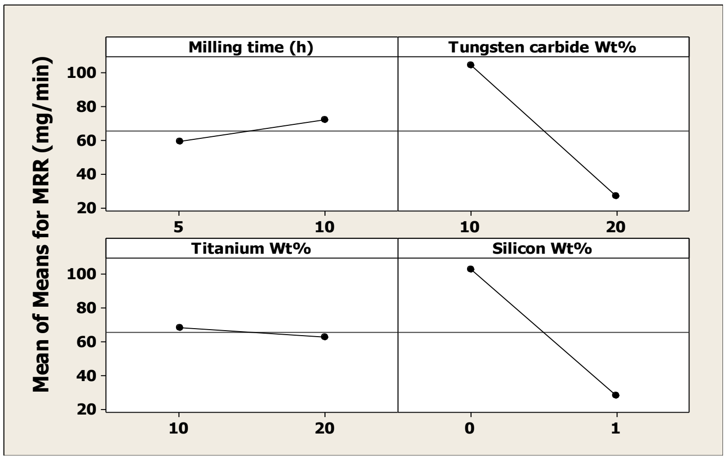

Figure 5.90 The main effect plot of MRR (mg/min) of Cu-WC-Ti-Si composite electrode versus milling time (h), Tungsten (wt %), and Silicon (wt %)

b. EW (mg/min) Achieved by using Cu-WC-Ti-Si Electrode at Optimal Setting

As shown in Figure 5.91, the electrode wear of Cu-WC-Ti-Si composite electrode during machining of hardened die steel mainly influenced by milling time followed by the values of Silicon, Titanium, and tungsten carbide content respectively. This effect of milling variables on EW is the reverse of that shown on MRR.

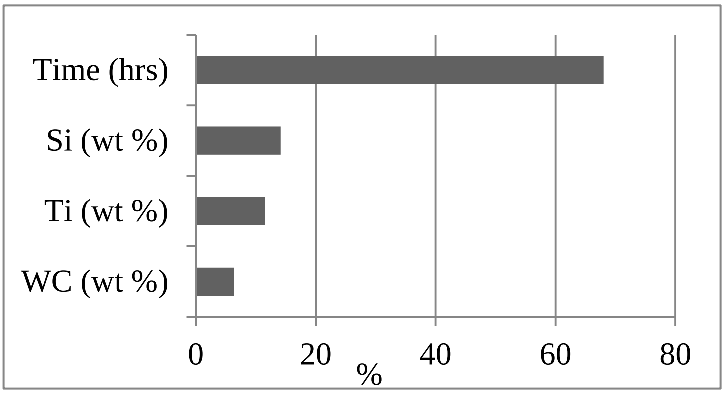

Figure 5.91 Contribution of milling variables on EW (mg/min) of Cu-WC-Ti-Si electrode

The main effect plot of EW (mg/min) in Figure 5.92 indicates that the electrode wear decreases with milling time, Tungsten carbide content, Titanium content, and Silicon content. The positive effect of milling variables on the EW can be referred to the reduction in electrical conductivity due to the reduction in Copper content in combining with porosity which leads to low discharge efficiency. The second point is the contamination by Tungsten carbide from the milling medium (bowl and balls) which might reduce the overall electrical conductivity and increases the porosity.

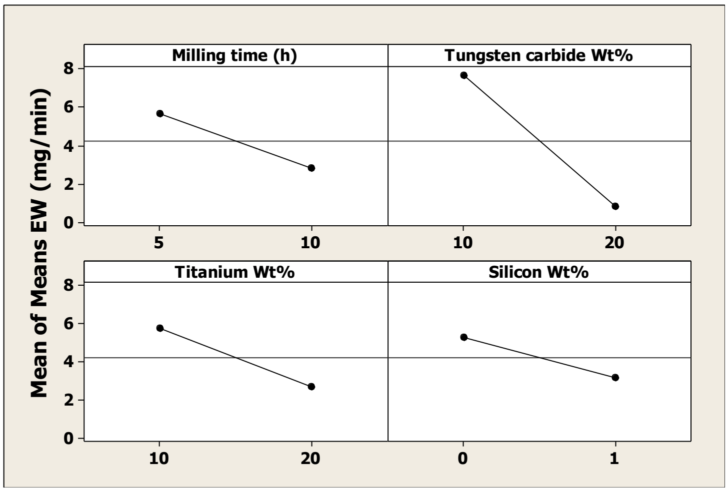

Figure 5.92 The main effect plot of EW (mg/min) of Cu-WC-Ti-Si composite electrode versus milling time (h), Tungsten (wt %), and Silicon (wt %)

c. TWR (%) of Cu-WC-Ti-Si Electrode At Optimal Setting

Figure 5.93 is show the Contribution of variables on the TWR (%) of Cu-WC-Ti-Si composite electrode during machining of hardened die steel at optimal setting. Milling time show the most significant contribution followed by the weight percent (wt %) of WC, Ti, and Si. How the TWR affected by these factors can be observed by means of the main effect plot shown in Figure 5.94.

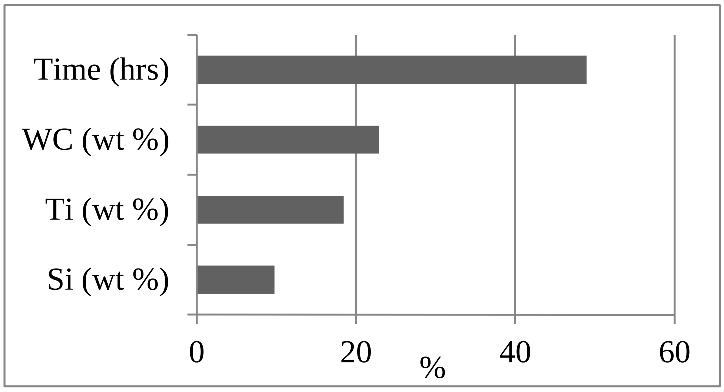

Figure 5.93 Contribution of milling variables on TWR (%) of Cu-WC-Ti-Si electrode

The TWR (%) decreases with increasing the milling time, Tungsten carbide wt%, and Titanium wt%. The presence of Silicon in Cu-WC-Ti-Si composite makes an increase the value of TWR. This means that the negative contribution of Silicon on decreasing the MRR (mg/min) is more than the improvement of EW (mg/min). This can be referred to the reduction on the electrical conductivity which in turn reduces the discharge efficiency.

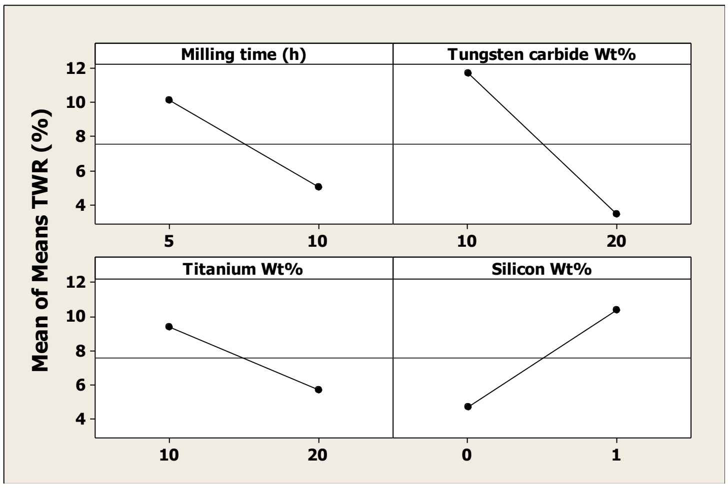

Figure 5.94 The main effect plot of TWR (%) of Cu-WC-Ti-Si composite electrode versus milling time (h), Tungsten (wt %), and Silicon (wt %)

5.7.1.4.Microstructure of Electrode and Workpiece after Machining

Figures 5.95, 5.96, 5.97, and 5.98 are the FESEM images of the electrode surface before and after machining, and the equivalent surface of the machined workpiece. Four out of the sixteen Cu-WC-Si composite electrodes was selected to show the effect of electrode surface on discharge efficiency and the surface roughness of the machined area. The selected experiments are EXP-1, Exp-4, Exp-8, and EXP-9, which are representing the 5, 10, and 15 h milling time. The FESEM of the electrode and the work-piece surface morphology of Exp-1 illustrated in Figure 5.48 showed a homogenous distribution of re-solidified molten electrode material due to homogenous discharge efficiency. The morphology of the machined surface shows big craters with few elevated edges. In general, the size of the crater on the machined surface is directly related to the consolidated particle size of the electrode. On the other hand, the shape of the sputtered layer and the degree of contamination is directly related to the bonding strength of electrode material. Higher Copper content electrodes (Exp-1 and Exp-9) show homogenous distribution of the re-solidified layer. Meanwhile the higher Silicon content shows a lake of the re-solidified layer due to the poor of discharge efficiency.

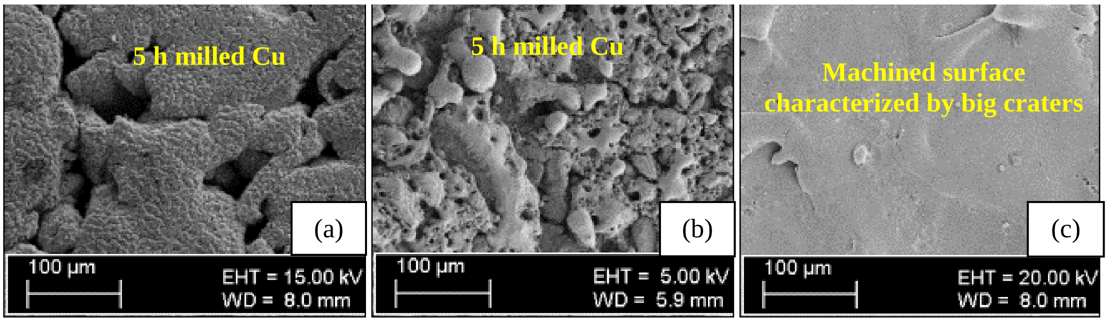

Figure 5.95 FESEM images of 5 h milled (Cu+0% WC+ 0% Ti+ 0% Si) electrode before machining (a), after machining (b), and the machined workpiece (c)

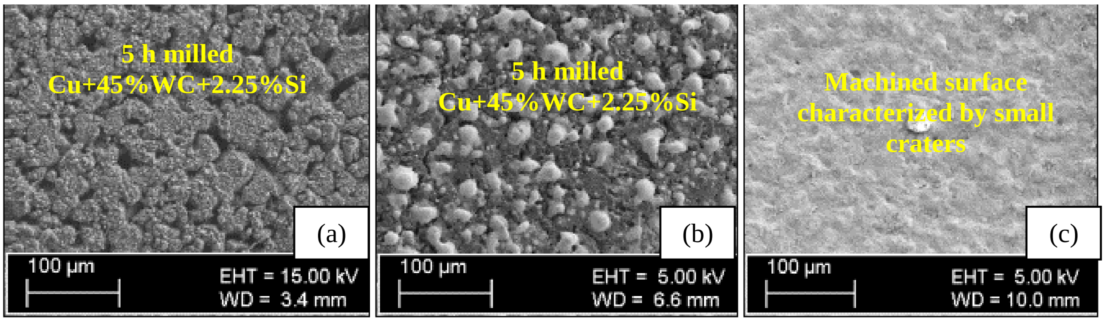

Figure 5.96 FESEM images of 5 h milled (Cu+45%WC+2.25%Si) electrode before machining (a), after machining (b), and the machined workpiece (c)

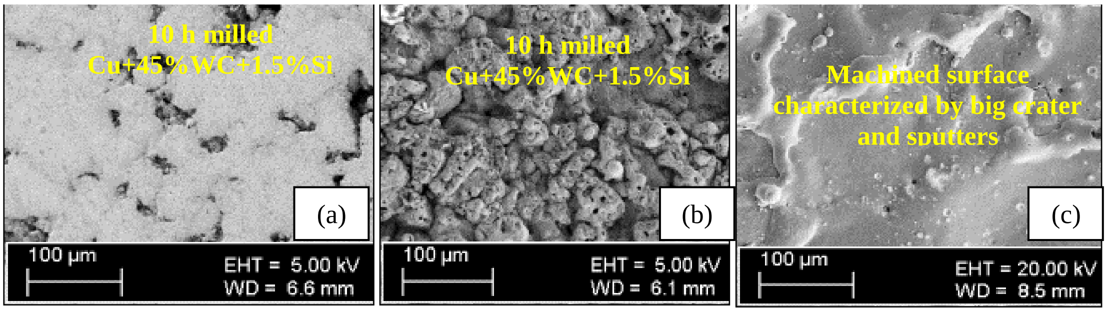

Figure 5.97 FESEM images of 10 h milled (Cu+45%WC+1.5%Si) electrode before machining (a), after machining (b), and the machined workpiece (c)

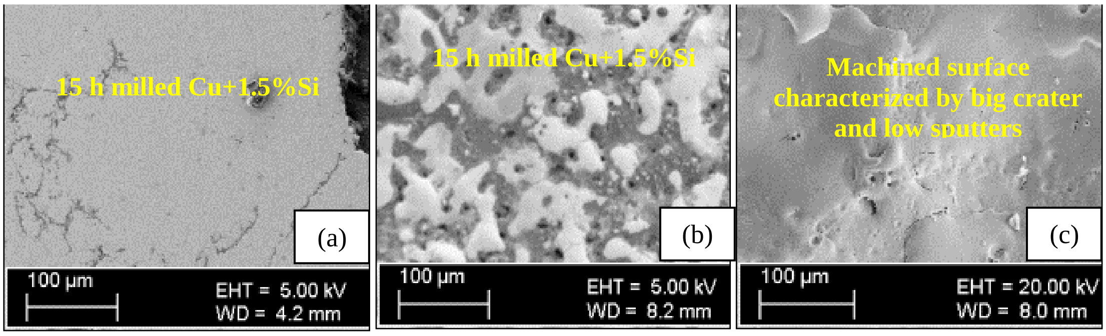

Figure 5.98 The FESEM images of 15 h milled (Cu+1.5%Si) electrode before machining (a), after machining (b), and the machined workpiece (c)

Table 5. 29 consolidate table show the relation between electrode manufacturing variables and machining results for different electrode

Electrode materials	Manufacturing variables						Machining results		
	Time (h)	Cu wt %	W wt %	WC wt %	Si wt %	Ti wt %	MRR (mg/min)	EW (mg/min)	TWR (%)
Cu-W		20.00	80	-	-	-	195.00	10.75	5.51
Cu-WC-Si	5	100.0	-	0	0.00	-	219.00	6.80	3.11
	5	84.25	-	15	0.75	-	222.00	11.10	5.00
	5	68.50	-	30	1.50	-	369.00	12.70	3.44
	5	52.75	-	45	2.25	-	301.00	19.40	6.45
	10	99.25	-	0	0.75	-	202.00	9.00	4.46
	10	85.00	-	15	0.00	-	231.00	4.60	1.99
	10	67.75	-	30	2.25	-	170.00	6.40	3.76
	10	53.50	-	45	1.50	-	196.00	0.50	0.26
	15	98.50	-	0.00	1.50	-	6.00	0.70	11.67
	15	82.75	-	15	2.25	-	14.00	1.30	9.29
	15	70.00	-	30	0.00	-	51.00	11.70	22.94
	15	54.25	-	45	0.75	-	172.00	1.60	0.93
	20	97.75	-	0	2.25	-	119.00	0.10	0.08
	20	83.50	-	15	1.50	-	6.00	4.20	70.00
	20	69.25	-	30	0.75	-	110.00	5.70	5.18
	20	55.00	-	45	0.00	-	112.00	7.00	6.25
Cu-WC-Ti	5	95.00	-	20	-	5	32.45	7.40	22.80
	5	94.25	-	20	-	5	17.42	1.48	8.50
	5	88.50	-	40	-	10	79.60	3.76	4.72
	5	87.75	-	40	-	10	42.25	4.85	11.48
	10	89.25	-	20	-	10	2.58	4.08	158.1
	10	90.00	-	20	-	10	20.84	1.13	5.42
	10	92.75	-	40	-	5	16.54	2.77	16.75
	10	93.50	-	40	-	5	6.25	1.67	26.72
Cu-WC-Ti	5	70.00	70	20	0.00	10	165.48	11.86	7.17
	5	69.00	69	20	1.00	10	36.74	9.21	25.07
	5	40.00	40	40	0.00	20	9.99	0.46	4.60
	5	39.00	39	40	1.00	20	25.33	0.90	3.55
	10	60.00	60	20	0.00	20	198.80	7.40	3.72
	10	59.00	59	20	1.00	20	17.72	1.93	10.89
	10	50.00	50	40	0.00	10	37.93	1.28	3.37
	10	49.00	49	40	1.00	10	32.96	0.68	2.06

CHAPTER 6

CONCLUSIONS AND RECOMMENDATIONS

6.1. Conclusions

Parametric analysis of oil die-sinker EDM process has been done using Cu and Cu-W electrodes on hardened material. The machining experiments were designed based on Taguchi quality improvement technique. Process optimization was then carried out using analysis of variance and the predicted values were compared with experimental values showing little or no difference. The following points are the conclusions from the analysis of the results:

1- Experimental work was carried out on the machining of gray cast iron using Copper electrode. The results show that, peak current, pulse On-time, working voltage, and Pulse Off-time are the most significant factors that contributed to MRR, EW, and Ra. The machining of cemented Tungsten carbide revealed that the gap voltage is the main variable that controls the machining process. The gap voltage must be set to 80 volts or lower to be able to machine this material. The cracks size and the fragmented particles were found to be directly linked to high gap voltage setting. The machining process of cemented Tungsten carbide in the presence of fragmented particles led to the formation of layered carbon particle.

2- By using high-energy ball milling of different combinations of Cu, WC, Si, and using milling time and composition as milling variables conditions, particle size of less than 50 nm were achieved and clear change in the thickness of crystalline and d-spacing are observed using XRD. Using TEM for further investigation, it discovered that a few crystalline structures were randomly distributed inside the amorphous structure with the thickness of crystalline less than that of the elemental powder. The detected crystalline structure using TEM shows that the distance between any two neighbour (d-spacing) are in the ranges 2.5Å - 6Å, which vary from that of the elemental powder (around 6Å).

3- The performance of the newly developed electrode on the machining of hardened material can be concluded as follows by observing the table 2.29.

  - As shown in section 5.7.1.1, the MRR achieved by using the 5 h and 10 h milling time for Cu-WC-Si composite electrode was improved by 1% to 90% depending on milling time and composition. The EW improved at milling time longer than 10 h by 9%-95% regardless of the composition. The best TWR was achieved by using the 5 h and 10 h milling time electrode.
  - The result of section 5.7.1.2 show that the MRR achieved by all compositions of 5 h and 10 h milling time for Cu-WC-Ti composite electrode are reduced by 83% to 98% from the value achieved by using Cu-W electrode under the same machining condition. Conversely, the EW is improved by 31% to 89% from that achieved by using Cu - W electrode. The TWR of this electrode is less than that of Cu-W and Cu-WC-Si electrode.
  - Section 5.7.1.3 show that the MRR achieved by using 5 h and 10 h milling time of Cu-WC-Ti-Si composite electrode was less than that of Cu-W electrode, which was reduced by 15% to 95%. The contribution composition on MRR is more significant compared with milling time. The EW is improved by 14% to 95% compared to the values achieved by using Cu-W electrode under the same machining variable setting. The TWR increases with milling time and the amount of Titanium, but decreases with Tungsten carbide content. The minimum tool wear ratio can be achieved using the 5 h milled Cu+ 40% WC+ 5% Ti.

Out of the three new developed electrodes, Cu-WC-Si shows the best performance in machining of hardened material where it shows the highest MRR and lowest TWR compared to that achieved by conventional Cu-W electrode. Less than wt % 1.5 Si is enough to improve milling process and chemical stability. Ti additive is not advisable as binder because it reduce the performance of Cu-WC-Ti and Cu-WC-Si-Ti. In other words, the best combination for higher MRR, low EW and TWR is the 10 h milled Cu-45WC-1.5Si.

6.2. Scope for future work

From the analysis of the results obtained from the current work, several possible extensions to the research can be suggested as follows:

1. Optimization of machining of cemented Tungsten carbide using diesinker EDM is a big challenge. For further experimental investigation, it is important to take into consideration the interaction between variables. This in turn requires using higher level Taguchi orthogonal array that would help in selecting the best machining parameter setting combination for higher MRR and low EW and surface roughness. Peak current, pulse on time, gap voltage and dielectric pressure may be used as the main variables.

2. Apart from that, the current research show that the MRR using the new developed Cu-WC-Ti electrode is poorer than Cu-W electrode; however the EW is better. Hence, further work may focus more on developing Cu-W-Ti, Cu-W-Fe composite using low energy ball milling for longer milling time to reduce the effect of contamination from milling medium.

3. The current work was done using dry air as milling environment. It would be interesting to introduce other milling process parameters gases such as milling environment. It is expected that inert gas may be helpful in the surface oxide reduction.

6.3. Summary of Research Contribution

The research work of EDM recently focused mainly on different aspects to improving the material removal rate, electrode wear, and surface roughness. In the area of developing a new EDM electrode material, this research innovating a new modified Copper tungsten composite material for use as an EDM electrode and also can be used spot welding electrode or high voltage electrical contact material. The results research contribution can be summarized as follows;

In the area of synthesizing a novel EDM electrode material, one of his most significant contributions is the use of Tungsten carbide in replacement of tungsten which soluble with copper and productive relative to the cost. Tungsten carbide is more efficient than the most popular high melting point temperature.

Cu-WC electrode with Silicon additive that is relatively high melting point, good in thermal conductivity, and can form an electrically conductive silicide shows better milling process. Silicon played as a binder and as self-lubricant. This is clear from the reduction in granular particle size after milling which is in turn improve the compressibility. Silicon content reduces the value of porosity from 19% at zero Silicon content to around 15% at 2.25 wt% of Silicon.

Silicon additive also improves the chemical stability by reducing the surface oxidation during milling and the oxide at grain boundary after sintering. The amount of this oxide is reduced by adding 0.75 % Si.

The performance of Cu-WC-Si electrode on machining of hardened die steel show some improvement in MRR than that achieved by Cu-W electrode at a lower milling time where it reduces the cost of copper by sticking and cold welding with milling medium.

Titanium additive which is conductive and higher in temperature than silicon create a serious problem during welding where the lost of powder by cold welding with milling medium is increased. Regaining this powder require higher milling energy for few second which is in turn increase the contamination by milling medium material.

REFERENCES

[1] R. Kern, "Sinker Electrode Material Sellection " *Technical Report,* p. 6, 2008

[2] A. Khan, "Electrode wear and material removal rate during EDM of aluminum and mild steel using copper and brass electrodes," *The International Journal of Advanced Manufacturing Technology,* vol. 39, pp. 482-487, 2008.

[3] H.-T. Lee, F.-C. Hsu, and T.-Y. Tai, "Study of surface integrity using the small area EDM process with a copper–tungsten electrode," *Materials Science and Engineering: A,* vol. 364, pp. 346-356, 1/15/ 2004.

[4] K. L. Aas, "Performance of two graphite electrode qualities in EDM of seal slots in a jet engine turbine vane," *Journal of Materials Processing Technology,* vol. 149, pp. 152-156, 2004.

[5] Y. Tang, J. Hong, H. Zhou, and B. Lu, "A new technique for the fabrication of graphite EDM electrodes," *Journal of Materials Processing Technology,* vol. 166, pp. 199-204, 2005.

[6] M. T. Kunieda, Tsutomu. Nakano, Shintaro, "Improvement of Dry EDM Characteristics Using Piezoelectric Actuator," *CIRP Annals - Manufacturing Technology,* vol. 53, pp. 183-186, 2004.

[7] Q. H. D. Zhang, R. Zhang, J. H. Zhang, Q. B., "An investigation of ultrasonic-assisted electrical discharge machining in gas," *International Journal of Machine Tools and Manufacture,* vol. 46, pp. 1582-1588, 2006.

[8] A. Abdullah and M. Shabgard, "Effect of ultrasonic vibration of tool on electrical discharge machining of cemented tungsten carbide (WC-Co)," *The International Journal of Advanced Manufacturing Technology,* vol. 38, pp. 1137-1147, 2008.

[9] T. T. Endo, Takayuki. Mitsui, Kimiyuki, "Study of vibration-assisted micro-EDM--The effect of vibration on machining time and stability of discharge," *Precision Engineering,* vol. 32, pp. 269-277, 2008.

[10] K. M. T. Shu, G. C., "Study of electrical discharge grinding using metal matrix composite electrodes," *International Journal of Machine Tools and Manufacture,* vol. 43, pp. 845-854, 2003.

[11] L. D. Li, C. Atkinson, J. Giedl-Wagner, R. Helml, H. J., "Sequential Laser and EDM Micro-drilling for Next Generation Fuel Injection Nozzle Manufacture," *CIRP Annals - Manufacturing Technology*, vol. 55, pp. 179-182, 2006.

[12] M. Y. Kunieda, Masahiro. Taniguchi, Norio, "Electrical Discharge Machining in Gas," *CIRP Annals - Manufacturing Technology*, vol. 46, pp. 143-146, 1997.

[13] C. C. Kao, J. Tao, and A. J. Shih, "Near dry electrical discharge machining," *International Journal of Machine Tools and Manufacture,* vol. 47, pp. 2273-2281, 2007.

[14] J. Tao, "Investigation of dry and near-dry electrical discharge milling processes," phd, Mechanical engineering, University of Michigan, Michigan, 2008.

[15] Y.-C. L. Lin, Ho-Shiun, "Machining characteristics of magnetic force-assisted EDM," *International Journal of Machine Tools and Manufacture,* vol. 48, pp. 1179-1186, 2008.

[16] Y.-C. C. Lin, Yuan-Feng. Wang, Der-An. Lee, Ho-Shiun, "Optimization of machining parameters in magnetic force assisted EDM based on Taguchi method," *Journal of Materials Processing Technology,* vol. 209, pp. 3374-3383, 2009.

[17] H. M. F. Zaw, J. Y. H. Nee, A. Y. C. Lu, L., "Formation of a new EDM electrode material using sintering techniques," *Journal of Materials Processing Technology,* vol. 89-90, pp. 182-186, 1999.

[18] L. W. Li, Y. S. Fuh, J. Y. H. Lu, Li, "Effect of TiC in copper-tungsten electrodes on EDM performance," *Journal of Materials Processing Technology,* vol. 113, pp. 563-567, 2001.

[19] H. C. Y. Tsai, B. H. Huang, F. Y., "EDM performance of Cr/Cu-based composite electrodes," *International Journal of Machine Tools and Manufacture,* vol. 43, pp. 245-252, 2003.

[20] H. P. Dürr, Rolf. Eleser, Nuri Saad, "Rapid tooling of EDM electrodes by means of selective laser sintering," *Computers in Industry,* vol. 39, pp. 35-45, 1999.

[21] J. L. Zhao, Yue. Zhang, Jianhua .Yu, Chengye .Zhang, Youliang, "Analysis of the wear characteristics of an EDM electrode made by selective laser

sintering," *Journal of Materials Processing Technology,* vol. 138, pp. 475-478, 2003.

[22] D. Gu and Y. Shen, "Processing and microstructure of submicron WC-Co particulate reinforced Cu matrix composites prepared by direct laser sintering," *Materials Science and Engineering: A,* vol. 435-436, pp. 54-61, 2006.

[23] P. K. D. V. C. Yarlagadda, Periklis .Subramanian, Vijay S., "Feasibility studies on the production of electro-discharge machining electrodes with rapid prototyping and the electroforming process," *Journal of Materials Processing Technology,* vol. 89-90, pp. 231-237, 1999.

[24] D. E. H. Dimla, N. Rothe, H., "Investigation of complex rapid EDM electrodes for rapid tooling applications," *The International Journal of Advanced Manufacturing Technology,* vol. 23, pp. 249-255, 2004.

[25] A. E. W. B. Rennie, Chris E. Bennett, Graham R., "Electroforming of rapid prototyping mandrels for electro-discharge machining electrodes," *Journal of Materials Processing Technology,* vol. 110, pp. 186-196, 2001.

[26] M. B. Monzón, A. N. Marrero, M. D. Hernández, N. Hernández, P. Aisa, J., "Validation of electrical discharge machining electrodes made with rapid tooling technologies," *Journal of Materials Processing Technology,* vol. 196, pp. 109-114, 2008.

[27] C. C. Hsu, D. Lai, M. Tzou, G., "EDM electrode manufacturing using RP combining electroless plating with electroforming," *The International Journal of Advanced Manufacturing Technology,* vol. 38, pp. 915-924, 2008.

[28] J. M. Ferreira, Artur. Alves, Nuno, "Rapid tooling aided by reverse engineering to manufacture EDM electrodes," *The International Journal of Advanced Manufacturing Technology,* vol. 34, pp. 1133-1143, 2007.

[29] P. M. Lonardo and A. A. Bruzzone, "Effect of Flushing and Electrode Material on Die Sinking EDM," *CIRP Annals - Manufacturing Technology,* vol. 48, pp. 123-126, 1999.

[30] J. Ferreira, "A study of die helical thread cavity surface finish made by Cu-W electrodes with planetary EDM," *The International Journal of Advanced Manufacturing Technology,* vol. 34, pp. 1120-1132, 2007.

[31] B. Ekmekci, "Residual stresses and white layer in electric discharge machining (EDM)," *Applied Surface Science,* vol. 253, pp. 9234-9240, 2007.

[32] P. J. Govindan, Suhas S., "Experimental characterization of material removal in dry electrical discharge drilling," *International Journal of Machine Tools and Manufacture,* vol. 50, pp. 431-443, 2010.

[33] N. S. Mohri, Masayuki. Furuya, Masanori. Saito, Nagao. Kobayashi, Akira, "Electrode Wear Process in Electrical Discharge Machinings," *CIRP Annals - Manufacturing Technology,* vol. 44, pp. 165-168, 1995.

[34] J. Marafona and C. Wykes, "A new method of optimising material removal rate using EDM with copper-tungsten electrodes," *International Journal of Machine Tools and Manufacture,* vol. 40, pp. 153-164, 2000.

[35] S. H. L. Lee, X. P., "Study of the effect of machining parameters on the machining characteristics in electrical discharge machining of tungsten carbide," *Journal of Materials Processing Technology,* vol. 115, pp. 344-358, 2001.

[36] N. Mohri and T. Tani, "Micro-pin Electrodes Formation by Micro-Scanning EDM Process," *CIRP Annals - Manufacturing Technology,* vol. 55, pp. 175-178, 2006.

[37] R. S. Garg, K. Sachdeva, Anish. Sharma, Vishal. Ojha, Kuldeep. Singh, Sharanjit, "Review of research work in sinking EDM and WEDM on metal matrix composite materials," *The International Journal of Advanced Manufacturing Technology,* vol. 50, pp. 611-624, 2010.

[38] B. Ekmekci, "White Layer Composition, Heat Treatment, and Crack Formation in Electric Discharge Machining Process," *Metallurgical and Materials Transactions B,* vol. 40, pp. 70-81, 2009.

[39] B. T. Ekmekci, A. Erman. Erden, Abdulkadir, "A semi-empirical approach for residual stresses in electric discharge machining (EDM)," *International Journal of Machine Tools and Manufacture,* vol. 46, pp. 858-868, 2006.

[40] J. L. Simao, H. G. Aspinwall, D. K. Dewes, R. C. Aspinwall, E. M., "Workpiece surface modification using electrical discharge machining," *International Journal of Machine Tools and Manufacture,* vol. 43, pp. 121-128, 2003.

[41] S. H. L. Lee, Xiaoping, "Study of the surface integrity of the machined workpiece in the EDM of tungsten carbide," *Journal of Materials Processing Technology,* vol. 139, pp. 315-321, 2003.

[42] H.-T. H. Lee, Fu-Chuan. Tai, Tzu-Yao, "Study of surface integrity using the small area EDM process with a copper-tungsten electrode," *Materials Science and Engineering A,* vol. 364, pp. 346-356, 2004.

[43] P. R. Soni, *Mechanical Alloying Fundamentals and Applications*: Cambridge International Science Publishing, 2001.

[44] T. S. Raghu, R. Ramakrishnan, P. Rama Mohan, T. R., "Synthesis of nanocrystalline copper-tungsten alloys by mechanical alloying," *Materials Science and Engineering A,* vol. 304-306, pp. 438-441, 2001.

[45] Y. Q. Li, Xuanhui. Zheng, ZhouShun. Lei, Changmin. Zou, Zhiqiang. Yu, Shu, "Properties of W-Cu composite powder produced by a thermo-mechanical method," *International Journal of Refractory Metals and Hard Materials,* vol. 21, pp. 259-264, 2003.

[46] S. N. Alam, "Synthesis and characterization of W-Cu nanocomposites developed by mechanical alloying," *Materials Science and Engineering: A,* vol. 433, pp. 161-168, 2006.

[47] Y. Y. Li, Shu, "Thermal-mechanical process in producing high dispersed tungsten-copper composite powder," *International Journal of Refractory Metals and Hard Materials,* vol. 26, pp. 540-548, 2008.

[48] M. O. Yusoff, Radzali. Hussain, Zuhailawati, "Mechanical alloying and sintering of nanostructured tungsten carbide-reinforced copper composite and its characterization," *Materials & Design,* vol. 32, pp. 3293-3298, 2011.

[49] A. Yamamoto, T. Kusano, T. Seki, and T. Okutomi, "Vaporization of carbon from Cu-WC contact during arc discharge in vacuum," *Plasma Science, IEEE Transactions on,* vol. 27, pp. 915-922, 1999.

[50] M. S. Shunmugam, P. K. Philip, and A. Gangadhar, "Improvement of wear resistance by EDM with tungsten carbide P/M electrode," *Wear,* vol. 171, pp. 1-5, 1994.

[51] H. Z. a. S. B. Jamaludin, "Studies on Mechanical Alloying of Copper-Tungsten Carbide Composite for Spot Welding Electrode," *Journal of Materials Engineering and Performance,* vol. 18, pp. 1059-9495, 2009.

[52] E. M. Ahmadi, M. Sadrnezhaad, S. K., "W-15 wt%Cu nano-composite produced by hydrogen-reduction/sintering of WO3-CuO nano-powder," *International Journal of Refractory Metals and Hard Materials,* vol. 28, pp. 441-445, 2010.

[53] Y. V. L. Baikalova, O. I., "Solid state synthesis of tungsten carbide in an inert copper matrix," *Journal of Alloys and Compounds,* vol. 297, pp. 87-91, 2000.

[54] L. S. Zhang Hentt, Su YuchangfS, Wang Unglingf, Wu Iijunf, I n Zhaoshengt: and Zhang Bangweit$, "Synthesis and stability of amorphous Cu 60 Ti 40-x Zr x alloys by mechanical alloying," *Journal of Physics: Condensed Matter,* vol. 5, p. 477, 1993.

[55] P. K. Šebo, Š. Štefánik, P. Korb, G., "Influence of Ti and Zr on the bond strength between carbon rod and Cu-Ti and/or Cu-Zr alloys," *Journal of Materials Science,* vol. 35, pp. 503-507, 2000.

[56] A. Evirgen, Öveçoglu, M. Lütfi, "Characterization investigations of a mechanically alloyed and sintered Al-2 wt%Cu alloy reinforced with WC particles," *Journal of Alloys and Compounds,* vol. 496, pp. 212-217, 2010.

[57] S. D. J.M. Guilemany, J. Nin, and J.R. Miguel, "Study of the Properties of WC-Co Nanostructured Coatings Sprayed by High-Velocity Oxyfuel," *Journal of Thermal Spray Technology,* vol. 14(3), p. 7, 2005.

[58] P. F. Feng, Akhtar. Wang, Xiaohong. Humail, Islam S. Qu, Xuanhui, "Mechanically activated reactive synthesis of refractory molybdenum and tungsten silicides," *International Journal of Refractory Metals and Hard Materials,* vol. 26, pp. 173-178, 2008.

[59] K. G. Gan, Mingyuan, "The compressibility of Cu/SiCp powder prepared by high-energy ball milling," *Journal of Materials Processing Technology,* vol. 199, pp. 173-177, 2008.

[60] Q. X. W. Wang, X. H. Yang, Y. Fan, Z. K., "Preparation of W-15 wt%Ti prealloyed powders," *International Journal of Refractory Metals and Hard Materials,* vol. 27, pp. 847-851, 2009.

[61] Y.-S. L. Lee, Sung-Man, "Phase formation during mechanical alloying in the Ti-Si system," *Materials Science and Engineering: A,* vol. 449-451, pp. 1099-1101, 2007.

[62] N. P. A. a. S. S. R. A. Khosroshahi, "Effect of Silicon on Nanostructure TiAl(γ) Formation Kinetic via Mechanical Alloying Method," *Journal of Applied Sciences,* vol. 8, pp. 3727-3732, 2008.

[63] Z. Yang, "High energy milling of silicon and graphite mixtures and synthesis of nanostructured silicon nitride/silicon carbide composites," Ph.D, The University of Connecticu, 1999.

[64] H. Tian, "Microstructure and phase evolution in nanocrystalline materials during ball milling," PhD, Materials Science and Engineering, University of Michigan, Michigan, 1999.

[65] H.-E. Schaefer, *Nanoscience The Science of the_Small in Physics Engineering Chemistry Biology and Medicine Nanoscience and Technology* Springer, 2010.

[66] A. B. Saidi, M., "Production of (W, Ti)C reinforced Ni-Ti matrix composites," *Journal of Materials Processing Technology,* vol. 124, pp. 166-170, 2002.

[67] C. H. Hong, Jiecai. Zhang, Xinghong. Meng, Songhe, "Influence of hot pressing on microstructure and mechanical properties of combustion synthesized TiB2-Cu-Ni composite," *Journal of Materials Processing Technology,* vol. 183, pp. 445-449, 2007.

[68] Q. T. Dong, Qing. Li, Wenchao, "Al2O3-TiC-ZrO2 nanocomposites fabricated by combustion synthesis followed by hot pressing," *Materials Science and Engineering: A,* vol. 475, pp. 68-75, 2008.

[69] H. El-hofy, *Advanced Machining Processes: Nontraditional and Hybrid Machining Processes*: McGraw-Hill Professional, 2005.

[70] S. M. A Lissaman, *Principles of Engineering Manufacture,* 3rd ed.: V. Chiles, S. C. Black and Elsevier Science Ltd., 1996.

[71] B. J. A, "ELECTRICAL DISCHARGE MACHINING," in *Modem manufacturing processes* ed: Industrial Press Inc, 1991.

[72] P. F. M. Ostwald, Jairo, *Manufacturing Processes and Systems (9th Edition)*: John Wiley & Sons, 1997.

[73] E. A. B. Avallone, Theodore. Sadegh, Ali M., *Marks' Standard Handbook for Mechanical Engineers (11th Edition)*: McGraw-Hill, 2008.

[74] W. Grzesik, *Advanced Machining Processes of Metallic Materials Theory, Modelling and Applications*: Elsevier Science, 2008.

[75] b. fleming, *How to book Electrical Discharge Machining,* 4th ed.: fleming publication 2005.

[76] E. C. Jameson, *electrical discharge machining*: Elman C. Jameson and the Society of Manufacturing Engineers, 2001.

[77] R. Bartnikas, *Electrical Insulating Liquids (Engineering Dielectrics, Vol 3) (v. 3)*: ASTM International, 1994.

[78] V. F. K. Vasily Y. Ushakov, S. M. Korobeynikov, *Impulse Breakdown of Liquids (Power Systems)*: Springer-Verlag Berlin Heidelberg 2007.

[79] S. K. Saha, "Experimental Investigation of the Dry Electric Discharge Machining (Dry EDM) Process," Msc, Department of Mechanical Engineering, Indian Institute of Technology Kanpur, Kanpur, 2008.

[80] W. S. Rudolf F. Graf, *Encyclopedia of Electronic Circuits Volume 1*: McGraw-Hill/TAB Electronics, 1985.

[81] H. Frohlich, *Theory of Dielectrics Dielectric Constant and Dielectric Loss (Monographs on the Physics and Chemistry of Materials)* OXFORD 1949.

[82] G. G. Raju, *Dielectrics in Electric Fields (Power Engineering, 19)*: Marcel Dekker, Inc., 2003.

[83] M. A. R. K. M. M. Rahman, K. Kadirgama M. M. Noor and Rosli A. Bakar, "Modeling of Material Removal on Machining of Ti-6Al-4V through EDM using Copper Tungsten Electrode and Positive Polarity " *World Academy of Science, Engineering and Technology* 2010.

[84] B. E.-H. a. D. M. ROY, *SERVICE DESIGN FOR SIX SIGMA / A Road Map for Excellence*: John Wiley & Sons, Inc, 2005.

[85] K. Y. B. S. El-Haik, Design for Six Sigma-A Roadmap for Product Development McGraw-Hill, 2009.

[86] r. K. ROy, *A Primer on the Taguchi Method* van nostland reinhold, 1990.

[87] U. Eşme*, "application of taguchi method on the optimization of resistance spot welding process," *The Arabian Journal for Science and Engineering*, vol. 34, 2009.

[88] C.Suryanarayana, *Mechanical alloying and milling* vol. 46, 2001.

[89] C. Suryanarayana, *Non-equilibrium Processing of Materials (Pergamon Materials Series)*: Pergamon, 1999.

[90] J. R. Davis, *Alloying: Understanding the Basics (06117G)*: ASM International, 2001.

[91] C. Suryanarayana, *Mechanical Alloying and Milling*: Marcel Dekker, 2004.

[92] M. S. El-Eskandarany, *Mechanical Alloying for Fabrication of Advanced Engineering Materials*: William Andrew Publishing/Noyes, 2001.

[93] M. S. El-Eskandarany, *Mechanical Alloying For Frabrication of Advanced Engineering Materials*: Noyes Publications, 2001.

[94] R. M. German, *Powder Metallurgy and Particulate Materials Processing*: Metal Powder Industries Federation, 2005.

[95] A. U. a. G. S. Upadhyaya, *powder metallurgy science technology and materials*: Universities Press (India) Private Limited 2011.

[96] G. S. Upadhyaya, *POWDER METALLURGY TECHNOLOGY*: CAMBRIDGE INTERNATIONAL SCIENCE PUBLISHING, 2002.

[97] E. S. Lassner, Wolf-Dieter, *Tungsten - Properties, Chemistry, Technology of the Element, Alloys, and Chemical Compounds*: Springer - Verlag, 1985.

[98] MATABASE. (2012, 5/8/2012). *Tungsten*. Available: http://www.matbase.com/material/non-ferrous metals/other/tungsten/properties

[99] E. A. Savrun, H. Del, "Electrically conductive tungsten silicide coatings for EMI/RFI shielding of optically transparent windows," *Journal of Materials Science,* vol. 33, pp. 2893-2897, 1998.

[100] B. W. Sell, J. Pomplun, K. Sänger, A. Schumann, D. Krautschneider, W., "Interface characteristics between tungsten silicide electrodes and thin dielectrics," *Microelectronic Engineering,* vol. 55, pp. 197-203, 2001.

[101] W. A. James F. Shackelford, *CRC Materials Science and Engineering Handbook, Third Edition*: Taylor & Francis, 2001.

[102] G. Sade, J. Pelleg, and V. Ezersky, "Titanium silicide formation in bilayer barrier structure," *Microelectronic Engineering,* vol. 33, pp. 317-323, 1997.

[103] A. T. S. Wee, A. C. H. Huan, T. Osipowicz, K. K. Lee, W. H. Thian, K. L. Tan, and R. Hogan, "Surface and interface studies of titanium silicide formation," *Thin Solid Films,* vol. 283, pp. 130-134, 1996.

[104] S. Gummadi, M.E.S, "Determination of milling time and energy requirements to produce fine sized titanium silicide particles using an attritor," MSc, The Faculty of the College of Graduate Studies, Lamar University, Beaumont, 2005.

[105] V. P. Smolej, S . Kaysser, W A, "Rearrangement During Liquid Phase Sintering of Large Particles " *Powder Metall. Int,* vol. 14, pp. 34-36, 1982.

[106] S. V. N. N. a. P. R. Rao, "Phase Diagrams of Binary 'rungs ten Alloys (Copper-Tungsten)," ed. Calcutta: Indian Institute of Metals, 1991, pp. 76-79.

[107] A. International, *ASM Handbook, Volume 3: Alloy Phase Diagrams (Asm Handbook)* ASM International, 1992.

[108] H. U. Fujiwara, Yukitomi. Awasthi, Alok. Krishnamurthy, Nagaiyar. Garg, Sheo Parkash, "Determination of the standard free energies of formation for tungsten silicides by EMF measurements using lithium silicate liquid electrolyte," *Journal of Alloys and Compounds,* vol. 391, pp. 307-312, 2005.

[109] K. P. Sufryd, Norbert. Riani, Paola. Richter, Klaus W. Cacciamani, Gabriele, "Experimental investigation of the Cu–Si phase diagram at x(Cu)>0.72," *Intermetallics,* vol. 19, pp. 1479-1488, 2011.

[110] X. C. Yan, Y. A., "A thermodynamic analysis of the Cu–Si system," *Journal of Alloys and Compounds,* vol. 308, pp. 221-229, 2000.

[111] F. L.-H. Hernandez-Santiago, Victor M.. Saucedo-Muñoz, Maribel L.. Dorantes-Rosales, Hector J., "Gibbs-Thomson relationship for the precipitation in Cu-Ti alloys," *Materials Characterization,* vol. 58, pp. 303-306, 2007.

[112] D. D. Bozic, O. Dimcic, B. Cvijovic, I. Rajkovic, V., "The combination of precipitation and dispersion hardening in powder metallurgy produced Cu-Ti-Si alloy," *Materials Characterization,* vol. 59, pp. 1122-1126, 2008.

[113] W. T. Hans Berns, *Ferrous Materials: Steel and Cast Iron*: Springer, 2008.

[114] G. S. Upadhyasa, *cemented tungsten carbide*. kunpur: Noyes Publications, 1998.

[115] T. innovations. (2011, 2011-12-06 15:43:07 Tuesday, December 06, 2011). *Electrical or thermal condutivity, resistivity, density and melting point*. Available: http://www.tibtech.com/conductivity.php

[116] E. ToolBox. (2011, Tuesday, December 13, 2011). *Tools and Basic Information for Design, Engineering and Construction of Technical Applications*.

[117] ASM, *ASM Handbook, Volume 20 - Materials Selection and Design*: ASM International, 1997.

[118] ASM, *ASM Handbook Volume 09 - Metallography And Microstruct*: ASM INTERNATIONAL, 1985.

[119] W. H. T. Perrin Walker, *CRC handbook of metal etchants*: CRC Press in Boca Raton 1991.

[120] K.-Y. H. Kung, Jenn-Tsong. Chiang, Ko-Ta, "Material removal rate and electrode wear ratio study on the powder mixed electrical discharge machining

of cobalt-bonded tungsten carbide," *The International Journal of Advanced Manufacturing Technology,* vol. 40, pp. 95-104, 2009.

[121] M. B. Pradhan, Chandan, "Neuro-fuzzy and neural network-based prediction of various responses in electrical discharge machining of AISI D2 steel," *The International Journal of Advanced Manufacturing Technology,* 2010.

[122] R. K. Roy, *Overview Design Of Experiments Taguchi (Product Details)*: Wiley, John & Sons, Incorporated, 2001.

[123] G. E. Totten, *Steel Heat Treatment: Metallurgy and Technologies (Steel Heat Treatment Handbook, Second Edition)*: CRC, 2006.

[124] (2012, july 2012). *Eagle Alloys Corporation*. Available: http://www.eaglealloys.com/t-tungsalloyscopper.html

[125] MatWeb. Your Source for Materials Information [Online]. Available: http://www.matweb.com/

[126] n. S. f. M. Rudolf Steiner, *ASM Handbook Volume 1: Properties and Selection: Irons, Steels, and High-Performance Alloys (06181)* ASM International, 1190.

[127] E. Lifshin, *X-ray Characterization of Materials*: WILEYVCH, 1999.

[128] Y. A. Cengel, *HEAT AND MASS TRANSFER: A PRACTICAL APPROACH*, 3rd ed.: McGraw-Hill Education (Asia), 2006.

[129] LAMET, *Asm Handbook: Volume 8 Mechanical Testing and Evaluation (Asm Handbook)* ASM International, 2000.

[130] M.-T. Y. K.-Y. H. C.-Y. Lo, "A study on electrode wear sensing and compensation in Micro-EDM using machine vision system," *Int J Adv Manuf Technol* p. 9, 2009.

[131] Y. H. H. Guu, H. Chou, C. Y. Deng, C. S., "Effect of electrical discharge machining on surface characteristics and machining damage of AISI D2 tool steel," *Materials Science and Engineering A,* vol. 358, pp. 37-43, 2003.

[132] I. L. Puertas, C. J. Álvarez, L., "Analysis of the influence of EDM parameters on surface quality, MRR and EW of WC-Co," *Journal of Materials Processing Technology,* vol. 153-154, pp. 1026-1032, 2004.

[133] M. P. W. Jahan, Y. S. Rahman, M., "A study on the fine-finish die-sinking micro-EDM of tungsten carbide using different electrode materials," *Journal of Materials Processing Technology,* vol. 209, pp. 3956-3967, 2009.

[134] A. O. B. Bruce L. Bramfitt, *ASM International; Metallographer's Guide Practices and Procedures for Irons and Steels*: ASM International, 2001.

[135] C. C. Y. Wang, Biing Hwa .Chow, Han Ming Suzuki, Yasuo, "Cutting austempered ductile iron using an EDM sinker," *Journal of Materials Processing Technology,* vol. 88, pp. 83-89, 1999.

[136] K.-T. Chiang, "Modeling and analysis of the effects of machining parameters on the performance characteristics in the EDM process of Al2O3+TiC mixed ceramic," *The International Journal of Advanced Manufacturing Technology,* vol. 37, pp. 523-533, 2008.

[137] H. Baker and H. Okamoto, "ASM Handbook, Volume 03 - Alloy Phase Diagrams," ed: ASM International, 1992.

PUBLICATIONS

INDEX JOURNAL

[1]. A.T.Z. Mahamat, A.M.A. Rani and Patthi Husain, “Machining of Cemented Tungsten Carbide using EDM”, Journal of Applied Sciences 11 (10): 1784-1790, 2011. “http://scialert.net/abstract/?doi=jas.2011.1784.1790”

[2]. A.T.Z. Mahamat, A.M.A. Rani and Patthi Husain, “Synthesize of Cu-WC-Ti metal composite by using planetary ball milling”, International Journal of Engineering and Applied Sciences 6 2012: 278-282.

“https://www.waset.org/journals/ijeas/v6/v6-51.pdf”

[3]. Al Tidjani Zakaria Mahamat, Ahmad Majdi Abdul-Rani and Patthi Hussain, “ Characterization of bal- milled Cu-WC-Ti-Si composite”, Asian Journal of Scientific Research, under Science Alert”, Accepted 26 July 2012.

INTERNATIONAL CONFERENCE

[1]. Al Tidjani Zakaria Mahamat, Ahmad Majdi Abdul Rani, Patthi Husain, “Machining of cemented Tungsten carbide using Copper electrode”, international Conference on Plant Equipment and Reliability (ICPER-2010), 15 – 17 June 2010, Kuala Lumpur, Malaysia

[2]. Al Tidjani Zakaria Mahamat, Ahmad Majdi Abdul Rani, Patthi Husain, “Synthesize of Cu-WC-Si Composite by using Planetary Ball Milling”, international Conference on Advance of Material & Nanotechnology II (ICAMN-2010), 29 November -01December 2010, Kuala Lumpur, Malaysia.

[3]. Al Tidjani Zakaria Mahamat, Ahmad Majdi Abdul Rani, Patthi Husain, “Synthesize of Cu-WC-Ti metal composite by using planetary ball milling”, 3rd CUTSE international Conference (3rd CUTSE-2011), 8th-9th November 2011, Curtin/ Sarawak, Malaysia.

[4]. Al Tidjani Zakaria Mahamat, Ahmad Majdi Abdul Rani, Patthi Husain, “Synthesizing and characterization of bal- milled Cu-WC-Ti-Si nanocomposite”, international Conference on Production, Energy and Reliability (ICPER-2012), 12th-14th June 2012, Kuala Lumpur, Malaysia.

[5]. A.M. Abdul-Rani , AL Tidjani Zakaria Mahamat, “Analysis on Cu-WC-Si as Electrode for Ad-vancement in EDM”, 15th International Conference on Advances in Materials & Processing Technologies (AMPT-2012), 23-26 September 2012, Wollongong, Australia.

NATIONAL CONFERENCE

[1]. Al Tidjani Zakaria Mahamat, Ahmad Majdi Abdul Rani, Patthi Husain, “Electro Discharge Machining by using Modified Copper-Tungsten Electrode”, National postgraduate Conference (NPC 2009), 25-26 march 2009, Tronoh Perak , Malaysia.

[2]. Al Tidjani Zakaria Mahamat, Ahmad Majdi Abdul Rani, Patthi Husain, “Electro Discharge Machining by using Modified Copper-Tungsten Electrode”, National postgraduate Conference (NPC 2011), 19th-20th September 2011, Tronoh Perak, Malaysia.